Ölmez Nalcıoğlu Ö et al. JOTCSA. 2025; 12(4): 197-206.

**RESEARCH ARTICLE**

JOURNAL of the TURKISH CHEMICAL SOCIETY
SECTION: A
CHEMISTRY

TURKISH CHEMICAL SOCIETY

# Synthesis of New Azoquinolone: Evaluation of Structural, Spectral Properties, and Antimicrobial Activity

**Öznur Ölmez Nalcıoğlu[1*], Mehtap Yakut[2], Ayşe Gül Caniklioğlu[3]**

[1]Department of Mathematics and Science Education, Science Education, Giresun University Faculty of Education, 28200, Giresun, Türkiye.
[2]Department of Chemistry, Ankara University Faculty of Science, 06100, Ankara, Türkiye.
[3]Department of Primary Education, Elementary School Teacher Education, Giresun University Faculty of Education, 28200, Giresun, Türkiye.

**Abstract:** A new azo dye containing quinolone (QANB) was synthesized by the ring-opening of pyranoquinolone (PQ), which was obtained from N-ethyl aniline and diethyl malonate. Surprisingly, we determined that under strong base conditions, azo coupling occurred at the 8-position of the quinolone group rather than at the 3-position of the pyroquinolone ring. Structure of 3-[1-ethyl-4-hydroxy-8-(4-nitro-phenylazo)-2-oxo-1,2-dihydro-quinolin-3-yl]-3-hydroxy-acrylic acid (QANB) was elucidated by $^{1}$H NMR, $^{13}$C NMR, $^{13}$C NMR DEPT, $^{13}$C NMR APT, 2D NMR ($^{1}$H-$^{1}$H COSY and $^{1}$H-$^{13}$C HMQC) and HRMS Analyses. Moreover, we investigated the antimicrobial activity of QANB on eight different bacteria and two different yeasts. The disc diffusion method and the minimum inhibitory concentration value determination (MIC) were used for antimicrobial activity. QANB demonstrated broad-spectrum antibacterial activity against both Gram-positive and Gram-negative bacteria. However, it has effectively shown activity against *Entereobacter aerogenes (E. aerogenes)*, which causes pneumonia, sepsis, urinary tract infections, and wound infections. QANB also showed significant activity against *Candida albicans (C. albicans)*. The fact that QANB is much more effective against *C. albicans* than nystatin, which is widely used as an antifungal drug, supports the idea that this compound can be used as a potential antifungal drug.

**Keywords:** Quinolone, Pyranoquinolone, Azo dyes, Antibacterial activity, Antifungal activity, *Candida albicans*.

**Submitted:** June 13, 2025. **Accepted:** September 25, 2025.

**Cite this:** Ölmez Nalcıoğlu Ö, Yakut M, Caniklioğlu AG. Synthesis of New Azoquinolone: Evaluation of Structural, Spectral Properties, and Antimicrobial Activity. JOTCSA. 2025;12(4): 197-206.

**DOI:** https://doi.org/10.18596/jotcsa.1719222

***Corresponding author's E-mail:** oznur.olmez@giresun.edu.tr

## 1. INTRODUCTION

Quinolones are prominent heterocyclic compounds in scientific and clinical research (1). Nalidixin, a quinolone antibiotic, was discovered for the first time by Lesher in 1962 (2). After this discovery, the number of antibiotic quinolones has crucially increased due to high potency, a broad spectrum of activity, potentially low incidence of side effects (1), good absorption after oral administration, and excellent bioavailability (3). Quinolones are classified into four generations according to their antibiotic activity with structural modifications. They are first, second, third, and fourth-generation antibiotics (3). Quinolones are also used in medicinal applications such as anti-tubercular (4), anti-malarial (5), anti-HIV (6), anti-cancer (7), and antifungal (8).

Azo dyes are widely used in textiles, cosmetics, optics, electronics, food, material science, and pharmaceutical industries (9,10). They have recently gained interest in advanced materials in the areas of high technology, supramolecular systems, and chemical sensors (11,12). Besides their applications, they also have biological properties such as antibacterial, antifungal, cytotoxic, anticancer, and antiproliferative (13,14).

The bioactive properties of the target derivatives have improved by incorporating the heterocyclic moiety into the azo dye scaffold. Azo dyes based on heterocycles are widely used in pharmaceuticals and drug development but remain under-reported. Bearing the heterocyclic structure of azo compounds has recently attracted considerable attention due to their increased biological activity potential (15). Azo compounds containing heterocyclic moieties are used as prodrugs in cancer treatment and as markers in diagnosis, by enabling the detection of cancer tumors through fluorescence off-on imaging of tumor hypoxia (16). Li et al. have reported that the azo dye-based fluorescence probe that detects $H_2S$ for biological applications has excellent selectivity, sensitivity, and biocompatibility (17).

Bacterial pathogens such as *Staphylococcus aureus*, *Enterococcus faecalis*, *Enterobacter aerogenes*, and *Salmonella enterica* can cause various infections, including those of the respiratory, urinary tract, bloodstream, skin, and soft tissues. These pathogens pose a threat to public health worldwide, causing a wide range of illnesses, from mild infections to fatal diseases such as pneumonia, salmonellosis, typhoid fever, and sepsis (18). Quinolone antibiotics have a wide range of clinical applications due to their effective function against bacterial pathogens. Over time, overuse of quinolone antibiotics can result in bacterial pathogens developing mutations that confer resistance to quinolones, and such pathogens are referred to as antimicrobial resistance (AMR) pathogens (19-21). According to a systematic analysis conducted from 1990 to 2021, bacterial AMR is associated with approximately 4.71 million deaths worldwide; 1.14 million of these deaths are reported to be due to infections caused by resistant bacteria (22). The emergence of AMR in quinolone antibiotics has led to the development of new types of antibiotics. Modification of the quinolone core by adding different substituent groups at the N-1, C-6, C-7, and C-8 positions alters their antimicrobial activity, pharmacokinetics, and metabolic properties, leading to a better understanding of the structure-activity relations (SARs) in quinolone compounds. To improve SAR, the addition of specifically selected substituent groups at these important positions of the quinolone core has enabled the targeting of specific pathogenic bacteria and improved the pharmacokinetics of quinolone compounds (2). However, some fungal species pose significant threats to human health and agricultural products; for example, they cause infectious diseases in humans and plants (23). Due to the continuous increase in invasive fungal infections (IFI), it is estimated that more than 6.5 million people worldwide are exposed to life-threatening fungal infections and that approximately 2.5 million people die each year because of these infections (24). The World Health Organization (WHO) published a fungal priority pathogens list (WHO FPPL) in 2022 to strengthen the global response to the increase in IFI threatening public health and to antifungal resistance. According to this report, *Candida albicans* is a pathogen classified as a critical priority group, while *Candida parapsilosis* is classified as a high-priority group. These two pathogen types cause invasive candidiasis, a life-threatening condition with a mortality rate ranging from approximately 20% to 50% (25). A report published by the WHO in 2025 stated that the global repertoire of antifungal drugs used to treat severe fungal infections is critically limited and that some fungal species have developed resistance to existing antifungal drugs (26). Furthermore, drug-resistant fungal infections continue to be an economic burden (19,23). To combat pathogens effectively, the pursuit of advanced research and development is essential for obtaining antimicrobial agents with enhanced efficacy and a broader spectrum of activity. Therefore, the development of novel compounds with dual antibacterial and antifungal activity is of paramount importance. Azoquinolones, with their unique structural features and potential bioactivity, represent promising candidates in this context.

In this study, we aimed to obtain an azo compound containing a pyranoquinolone moiety and expected azo coupling to occur at the 3-position of pyranoquinolone. Surprisingly, the experimental results showed a different product than expected. The NMR analyses revealed an unexpected ring-opening reaction, indicating that the products obtained were of azoquinolone structure. This transformation provides a new perspective on the reactivity of the pyranoquinolone skeleton under azo coupling conditions and suggests an alternative synthetic route for producing functional heterocyclic dyes. Herein, we have reported a new azo dye containing the quinolone moiety (QANB). The azo coupling occurred at the 8-position on the quinolone ring instead of the 3-position of the pyranoquinolone, contrary to what is described in the literature (27-29). We have introduced the ring-opening product resulting from the diazotization of the pyrano-quinolone and the azo coupling to the quinolone. The structural analysis of QANB has been comprehensively presented by $^1$H NMR, $^{13}$C NMR, $^{13}$C NMR DEPT, $^{13}$C NMR APT, and 2D NMR ($^1$H-$^1$H COSY and $^1$H-$^{13}$C HMQC). Besides, the antibacterial and antifungal properties of QANB have been evaluated.

## 2. EXPERIMENTAL SECTION

### 2.1. Materials and Instruments

FTIR spectra were performed with a Bruker Tensor 27 FT−IR spectrometer in KBr pellets in the range 4000−400 cm$^{-1}$. $^1$H NMR (400 MHz), $^{13}$C NMR (100 MHz), $^{13}$C NMR DEPT-135, $^{13}$C NMR APT, 2D NMR ($^1$H-$^1$H COSY and HMQC) spectra were recorded using a Bruker Avance DPX-400 NMR spectrometer and an Agilent Technologies 400 MHz Spectrometer. NMR samples were carried out at room temperature in 5 mm NMR tubes, and the chemical shifts were recorded as δ (ppm) using TMS, which is the internal standard. MS spectra were obtained with ionization of solid samples by direct electron impact (DEI) in a DI unit. The LC-MS TOF electrospray ionization technique (Agilent Technologies 6230-A) was used to record the HRMS data. Melting points were detected by uncorrected open capillaries with STUART Melting Point SMP30.

### 2.2. Synthesis of 6-Ethyl-4-hydroxy-6H-pyrano[3,2-c]quinoline-2,5-dione (PQ)

6-Ethyl-4-hydroxy-2H-pyrano[3,2-c] quinoline-2,5-dione (PQ) was prepared by the condensation of *N*-ethyl aniline (1 mol, 125 mL) and diethyl malonate (2 mol, 303 mL) according to the literature methods (30,31). The compound was recrystallized from DMF. An orange solid m.p: 254-255 °C, Yield: 99%. $^1$H NMR (400 MHz, DMSO-$d_6$, δ, ppm): 13.18 (1*H*, s, *OH*), 8.30 (1H, dd, J = 8.0; 2.0 Hz, Ar-*H*), 7.74 (1H, t, *J* = 8.8 Hz, Ar-*H*), 7.48–7.19 (2H, m, Ar-*H*), 5.61 (1H, s, *H3*), 4.36 (2H, q, *J* = 7.6 Hz, $CH_2$), 1.36 (3H, t, *J*

=8.0 Hz, –$CH_3$). m/z (EI, 70 eV): 257 ($M^+$, 83.92), 229 ($M^+$ -$CH_2$=$CH_2$, 100), 77 ($C_6H_5$+, 51.08).

### 2.3. Synthesis of 3-[1-ethyl-4-hydroxy-8-(4-nitro-phenylazo)-2-oxo-1,2-dihydro-quinolin-3-yl]-3-hydroxy-acrylic acid (QANB)

p-Nitroaniline (0,138 g; 1 mmol) was dissolved in conc. HCl (3 mL) at room temperature, and the mixture was cooled down to -5 °C in a salt/ice bath. $NaNO_2$ solution (0.10 g; 1.454 mmol) was slowly added to the solution within 30 min. Diazonium solution was kept at -5 °C for 1 h. 6-Ethyl-4-hydroxy-6H-pyrano[3,2-c]quinoline-2,5-dione (PQ) (0.257 g; 1 mmol), which was synthesized according to literature (30,31), was dissolved in 20 mL 10% NaOH and cooled in a salt/ice bath. Diazonium solution was slowly added to this solution. The mixture was stirred for 3 h at 0 °C, and then it was stirred overnight at room temperature. Acetic acid was added to the solution until the pH>6. The orange precipitate formed in the yellow solution. The orange product was filtered off, washed with water, and dried in air. The crude product was recrystallized from ethanol-ethyl acetate. The orange crystals (QANB) were filtered off, washed with EtOH, and dried under vacuum overnight. (Yield: 160 mg, 43%; decomp. > 123°C).

FTIR (KBr; ν $cm^{-1}$): 3499, 3441, 3275 (O-H); 3080, 3027 (Ar-*H*); 2982, 2934 (aliphatic *C-H*); 1740, 1676 (*C=O*); 1640, 1603 (*C=C*); 1553 and 1327 (Ar-*OH*); 1443 (*N=N*); 1269, 1248, 1269 and 1107 (*C-O*). $^1$H NMR (400 MHz, DMSO-$d_6$, δ, ppm): 13.52 (1H, br, *OH*); 12.40 (1H, br, *CO-OH*); 9.20 (br, *OH*); 8.23 (1H, d, $J_{1\text{-}2}$ = 8.8 Hz, *H*-14 and *H*-16); 8.18 (1H, d, $J_{1\text{-}2}$ = 7.2 Hz, *H*-5); 7.90 (1H, br, *H*-6); 7.82 (1H, br, *H*-6'); 7.62 (1H, d, $J_{1\text{-}2}$ = 7.2 Hz, *H*-5'); 7.55 (1H, br, *H*-7); 7.33 (2H, m, *H*-13 and *H*-17); 5.65 (1H, s, *H*-10); 4.41 (2H, m, *H*-18); 4.28-4.19 (m, *H*-18'); 1.31-1.28 (3H, m, *H*-19); 1.18-1.06 (m, *H-19*'). $^{13}$C NMR (400 MHz, DMSO-$d_6$, ppm): δ 169.1 (*C*-2), 162.7 (*C*-9), 160.9 (*C*-11), 159.4 (*C*-15), 149.4 (*C*-12), 141.4 (*C*-8 or *C*-8a), 138.1 (*C*-4), 134.9 (*C*-6), 126.4 (*C*-14/*C*-16), 124.6 (*C*-7), 124.3 (*C*-5), 116.5 (*C*-6'), 114.0 (*C*-13/*C*-17), 113.7 (*C*4a), 99.9 (*C*-3), 90.3 (*C*-10), 37.8 (*C*-18), 13.1 (*C*-19). Molecular Weight (calcd.): 424.36. HRMS: *m/z* calcd. for $C_{20}H_{16}N_4O_7$ $[M\text{-}CO_2\text{+}H]^+$ 381.1191, found 381.1181.

### 2.4. Antimicrobial Activity Evaluations

#### *2.4.1. Microorganisms*

Microorganisms used during the study are provided by the Giresun University Medicine Faculty and Arts and Sciences Faculty Microbiology Laboratory culture collection. In this study as Gram (+) bacteria species, *Staphylococcus aureus* (*S. aureus*) (ATCC 29213), *Enterococcus faecalis* (*E. faecalis*) (ATCC 29212), *Bacillus subtilis* (*B. subtilis*) (ATCC 6633), *Gordonia rubripertincta* (*G. rubripertincta*); and as Gram (-) bacteria species, *Proteus vulgaris* (*P. vulgaris*) (ATCC 13315), *Klebsiella pneumoniae* (*K. pneumoniae*) (ATCC 700603), *Enterobacter aerogenes* (*E. aerogenes*) (CMM 2531) and *Salmonella enterica* (*S. enterica*) (ATCC 14028) are used. In addition, as yeast species, *Candida albicans* (*C. albicans*) (FMC 17) and *Candida parapsilosis* (*C. parapsilosis*) (ATCC 22019) are used.

#### *2.4.2. Determination of antimicrobial activity of QANB*

30 mg/mL of the sample was sterilized by passing through 0.45 µM filters. The prepared sample was applied to the microorganisms studied by using the disc diffusion method. For bacteria in Mueller Hinton Broth (MHB), for yeasts in Sabouraud Dextrose Broth (SDB), overnight cultures were prepared, and 200 µL of suspension containing $10^8$ CFU / mL of bacteria-yeast was added to the Mueller Hinton Agar (MHA) (to test bacteria) and Sabouraud Dextrose Agar (SDA) (to test yeast). Sterile discs with a diameter of 6 mm were placed on the MHA (for bacteria) and SDA (for yeasts) and some of the discs on the petri were impregnated with 20 µL of different compounds and only one of them was treated with DMSO (negative control), streptomycin (for bacteria) and nystatin (for yeasts) were added as positive control on the same petri. After incubating the cultured petri dishes for 1 hour in the refrigerator, the bacteria were incubated at 37 °C for 24 h, and the fungi at 27 °C for 48 h. The inhibition zones were measured in millimeters (32). The tests were carried out with three replicates each time. The results were shown in Table 2.

#### *2.4.3. Determination of minimum inhibitory concentration (MIC) of QANB*

96 well-plates were used for determining the MIC values of the sample. The sample was dissolved to obtain a final concentration of 10 mg/mL. 95 µL MHB was added to each well. Serial dilutions were prepared after adding 100 µL of the sample to the first well. Finally, 5 µL of microorganism suspension was inoculated into the tubes and incubated at 37 °C overnight, and the MIC values were recorded. The tests were performed in three replicates (33). The results were summarized in Table 3.

## 3. RESULTS AND DISCUSSION

### 3.1. Synthesis

Some azo dyes based on the pyranoquinolinone moiety were reported as coupling products at the 3-position of PQ with diazonium salts in pyridine (27,28). Soliman and Yahia reported the coupling product at the 3-position of PQ with 2,5-difluoroanilin diazonium salt in $Na_2CO_3$ solution (29). We aimed at the synthesis of an azo dye based on a pyranoquinolone moiety, which was carried out with p-nitroaniline diazonium salt and PQ in NaOH media. We expected the coupling at the 3-position to be like previous studies (27-29). However, the NMR result of the product (QANB) showed that there was no coupling at the 3-position of PQ. We found that azo coupling was accomplished at the 8-position of PQ with 4-nitroanilin diazonium salt under strong base conditions, probably due to keto-enol tautomer equilibrium of PQ under these conditions. Moreover, PQ may have undergone ring-opening during the reaction or purification process. According to previous reports, quinolone derivatives can be obtained via hydrolysis and ring-opening of the pyran ring fused to PQ under basic conditions (34-36). The proposed mechanism for the ring-opening reaction of PQ is shown in Scheme 3. In this study, the azo coupling reaction was conducted at -5 °C. An electron-withdrawing group (p-$NO_2$) may have caused the ring-opening reaction. We here have reported the synthesis and comprehensive structural characterization of QANB using $^{1}H$ NMR, $^{13}C$ NMR, $^{13}C$ NMR-APT, and 2D NMR ($^{1}H$-$^{1}H$ COSY, $^{1}H$-$^{13}C$ HMQC). $^{1}H$-$^{13}C$ HMBC spectrum could not be obtained. The synthesis route and structure of QANB are presented in Scheme 1.

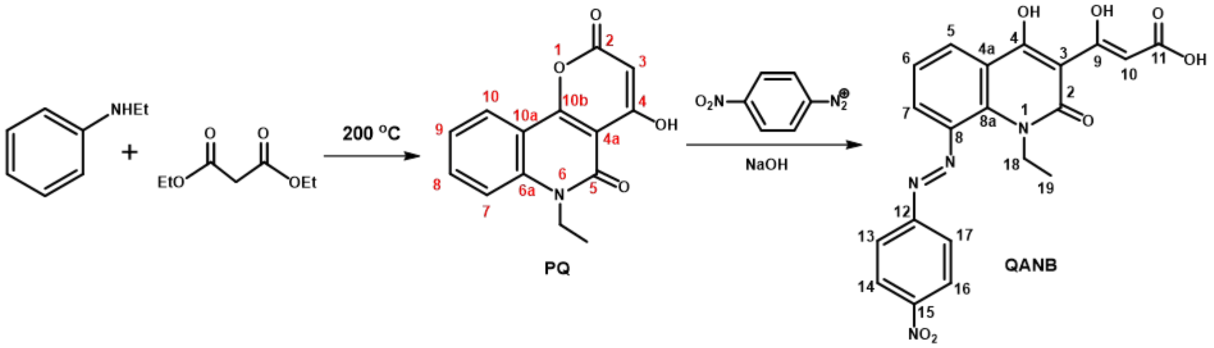

**Scheme 1:** Synthesis route of compound QANB.

### 3.2. The FTIR Results of QANB

In this study, OH bands of QANB were observed as three different bands in the range of 3499-3275 cm$^{-1}$. The aromatic C-H band was recorded at 3080 cm$^{-1}$. Alkyl C-H peaks were observed in the range of 2982-2859 cm$^{-1}$. Socrates reported that the C=O group of α, β-unsaturated aliphatic carboxylic acids has a very strong band in the range of 1715-1690 cm$^{-1}$ (37). Moreover, Ibrahim et al reported at 1727 cm$^{-1}$ due to the peak $C=O_{carboxy}$ group of the quinolinone derivative formed by ring-opening reaction of pyranoquinolinone. They were also reported at 1673 cm$^{-1}$ peak attributed to the $C=O_{quinolinone}$ (34). In the FTIR spectrum of QANB, the band recorded at 1740 cm$^{-1}$ for C=O indicates that ring opening occurs, and carboxylic acid is formed. Besides, Mirsadeghi et al reported that strong bands in the region 1687-1625 cm$^{-1}$ of the azo quinolone dyes originate from the 2-carbonyl of quinolone moiety (38). Similarly, in this work, the C=O group in the 2-position of the quinolinone ring was also recorded at 1676 cm$^{-1}$. The other bands were observed at 1640 cm$^{-1}$ and 1602 cm$^{-1}$ for aromatic C=C, at 1553 (asymmetric stretching vibration) and 1327 cm$^{-1}$ (symmetric stretching vibration) for Ar-$NO_2$, 1443 cm$^{-1}$ for -N=N-, 1269 and 1107 cm$^{-1}$ for C-O. The FTIR spectra of the PQ and QANB are presented in S1 of the SI.

### 3.3. The NMR Results of QANB

The structure of the new QANB was characterized by $^{1}H$ NMR, $^{13}C$ NMR, $^{13}C$ NMR APT, $^{13}C$ NMR DEPT-135, $^{1}H$-$^{1}H$ COSY, and $^{1}H$-$^{13}C$ HMQC spectroscopy. NMR spectra were presented in S2-S12 of the SI. Table 1 shows that the $^{1}H$ and $^{13}C$ NMR chemical shifts, numbered according to Scheme 1, correlate with the $^{1}H$-$^{13}C$ HMQC spectrum. $^{1}H$ NMR chemical and $^{13}C$ NMR shifts presented in this section are designated according to Scheme 1 (see S2-S4 in the SI).

According to the $^{1}H$ NMR spectra of compound QANB in DMSO-$d_6$, O-H peaks were monitored at 13.52 ppm and 9.20 ppm (see S2 in the SI). The $^{1}H$-$^{13}C$ HMQC spectrum (see S11-S12) showed that the OH peak attached to C-4 at 9.20 ppm correlates with 138.10 ppm in the $^{13}C$ NMR (S3-S4). The C-4 quaternary peak is negative in the APT spectra (S5-S6), and there is no signal in the DEPT spectra (S7-S8). OH-peak observed at 13.52 ppm belongs to C-9 and forms an intermolecular hydrogen bond with the COOH group. C-9 peak recorded at 162.7 ppm phased down in the $^{13}C$ NMR APT. In the $^{1}H$ NMR and $^{1}H$-$^{1}H$ COSY spectrum of QANB, the doublet peak, which was observed at 8.23 ppm with coupling $J_{1\text{-}2}$ = 8.80 Hz, was coupled to the peak at 7.3 ppm (see S9-S10 in the SI). The peaks at 8.23 ppm belong to C-14 and C-16 on the phenyl ring. The $^{1}H$-$^{13}C$ HMQC spectrum showed that these peaks correlate with 126.4 ppm in the $^{13}C$ NMR (S11-12). The other phenyl peaks, which are observed at 7.33 ppm, belong to C-13 and C-17. The $^{1}H$-$^{13}C$ HMQC spectrum showed that these peaks correlate with 114.0 ppm in the $^{13}C$ NMR. The peaks which belong to the quinoline ring were recorded in the range of 8.18-7.55 ppm. In the $^{1}H$-$^{13}C$ HMQC spectrum, the protons of the quinolone ring were determined that the H-5 doublet peak ($J$ = 7.2 Hz) observed at 8.18 ppm correlates with the peak at 124.3 ppm of C-5, H-6 broad signal (δ 7.90 ppm) correlates with the peak at 134.9 ppm of C-6, H-7 broad signal (δ 7.55 ppm) correlates with 124.6 ppm of C-7 peak. The presence of positive methine peaks (C-H) on both $^{13}C$ NMR ATP and $^{13}C$ NMR-DEPT spectra has contributed to these results. Hasani et al. reported that exchangeable proton signals appear broader than non-exchangeable ones, suggesting that the exchange process occurs in the slow-intermediate regime (39). In addition, the broad signal (δ 7.82 ppm) may be related to the H-6' proton, while the distorted doublet (δ 7.62 ppm; $J$ = 7.2 Hz) may be associated with the H-5' proton in the $^{1}H$ NMR spectrum. The presence of both a distorted and a well-defined doublet ($J$ = 7.20 Hz) for the same proton may be attributed to the keto-enol tautomeric equilibrium in the $^{1}H$ NMR spectrum in DMSO-$d_6$. In the $^{1}H$–$^{1}H$ COSY spectrum of QANB, the broad signal corresponding to H-6′ (7.82 ppm) exhibited correlations with the H-5′ signal at 7.61 ppm (Fig. 1a). The possible tautomeric forms of QANB in the solvent medium are depicted in Scheme 2. The H-18 protons of -$CH_2$ attached quinolone recorded at 4.41 ppm correlated with the peaks in the range of 1.31-1.28 ppm of H-19 in the $^{1}H$-$^{1}H$ COSY spectrum and the peak at 37.8 ppm of C-18 in the $^{1}H$-$^{13}C$ HMQC spectrum (Fig. 1b). The H-19 protons belonged to the methyl group ($CH_3$), correlated with the carbon peak at 13.1 ppm in the $^{1}H$-$^{13}C$ HMQC spectrum (Table 1). In addition, the $^{1}H$ NMR spectrum revealed peaks with 4.28-4.18 and 1.18-1.06 ppm ranges, associated with alkyl peaks attached to the nitrogen in the quinoline ring. As illustrated in Scheme 2, these peaks can be attributed to H-18' and H-19', respectively. Notably, the H-18′ protons (4.28–4.18 ppm) exhibited correlations with H-19′ signals (1.18–1.06 ppm) in the $^{1}$H–$^{1}$H COSY spectrum, confirming their spatial proximity (see S9, in the SI). In the $^{3}$C NMR APT and DEPT spectra, while C-18 peaks (methylene) were phased down, C-19 peaks (methyl) were phased up. The quaternary peaks were phased down in the $^{13}$C NMR APT spectra, and no signal in the $^{13}$C NMR DEPT spectra. The quaternary peaks appeared for C-2, C-9, C-11, C-15, and C-4 in the range of 169.1-138.1 ppm, while C-12, C-8a/C-8 peaks, which appeared as weak peaks in the $^{13}$C NMR, were not observed in the $^{13}$C NMR APT spectra. As the HMBC spectrum gave no results on the instrument, we were certainly unable to identify the quaternary peaks in the range of 169.1-135.95 ppm. The other quaternary peaks were observed at 113.7 ppm for C-4a and 99.9 ppm for C-3. They are negative in the $^{13}$C NMR APT spectra. It may be related to the broad signal H-6' proton observed at 7.82 ppm and the doublet (Scheme 2).

| | Positions | | | | | | | | | | | |
|---|---|---|---|---|---|---|---|---|---|---|---|---|
| | **H-5** | **H-6** | **H-7** | **H-10** | **H-13** | **H-14** | **H-16** | **H-17** | **H-18 -CH$_2$** | **H-19 -CH$_3$** | **C-4 -OH** | **C-9 -OH** | **C-11 -OH (COOH)** |
| **$\delta_H$** | 8.18 (d, *J* =7.2) | 7.90 (br) | 7.55 (br) | 5.65 (s) | 7.33 (m) | 8.23 (d, *J*=8.8) | 8.23 (d, *J* =8.8) | 7.33 (m) | 4.41 (m) | 1.31-1.28 (m) | 13.52 (s) | 9.20 (s) | 12.40 (s) |
| **$\delta_C$** | 124.3 | 134.9 | 124.6 | 90.3 | 114.0 | 126.4 | 126.4 | 114.0 | 37.8 | 13.1 | 138.1 | 162.7 | 169.1 |
| **HMQC** | C-5 | C-6 | C-7 | C-10 | C-13 | C-13 | C-16 | C-17 | C-18 | C-19 | ND | C-9 | ND |

ND: Not determined

**Table 1.** $^{1}$H and $^{13}$C NMR data (δ, ppm; *J*, Hz), HMQC correlations of dye QANB in DMSO-$d_6$.

**(a)** **(b)**

**Figure 1: a)** Expansion of $^{1}$H-$^{1}$H COSY spectrum for QANB in DMSO-$d_6$ **b)** Expansion of $^{1}$H-$^{13}$C HMQC spectrum for QANB in DMSO-$d_6$.

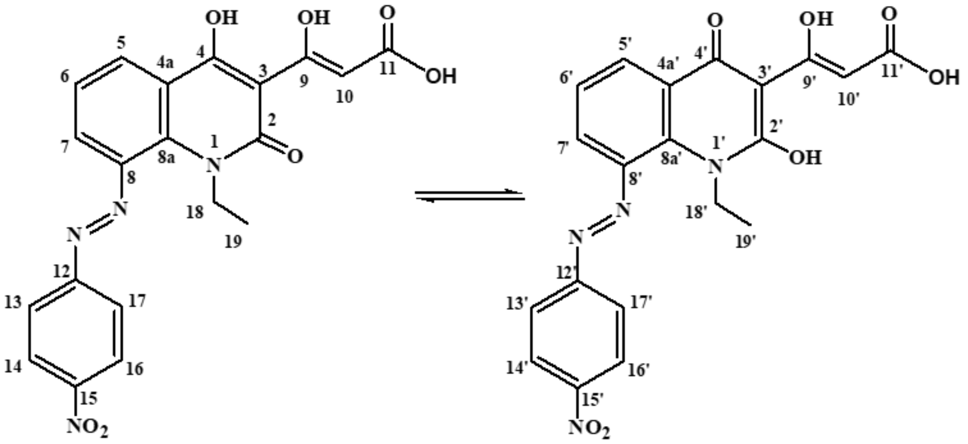

**Scheme 2:** Keto-enol tautomers of QANB.

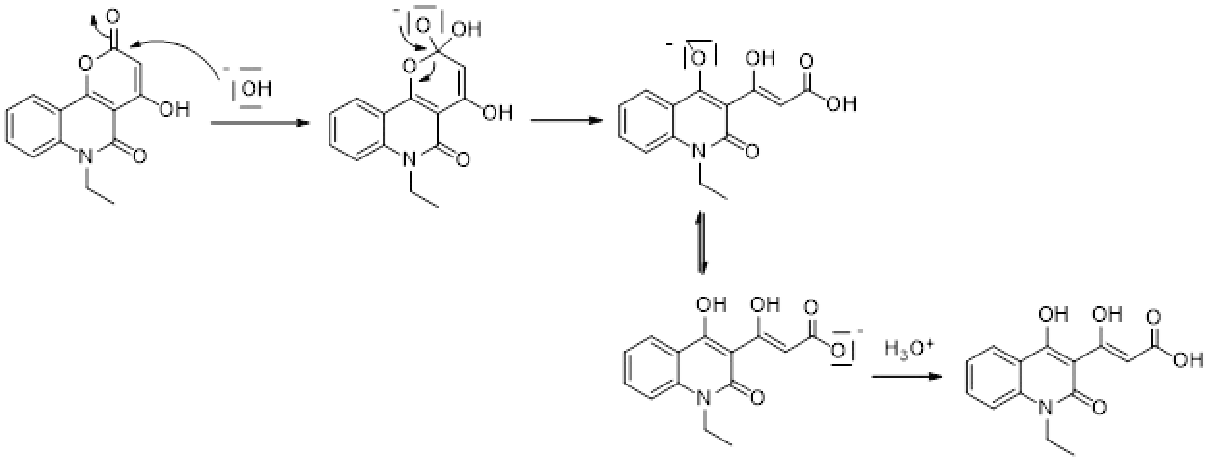

**Scheme 3:** Ring-opening reaction mechanism of PQ under strong base conditions.

### 3.4. Antimicrobial Activity

In this study, the antimicrobial activities of a quinolone derivative molecule, QANB, were identified by using the disc diffusion method on eight different bacteria and two different yeasts.

It has been determined from the tests that QANB has different antimicrobial activity, ranging from 13 mm to 33 mm against various bacteria and yeasts. The largest zone diameter for bacteria was measured against *E. aerogenes* with a diameter of 22 mm, and the largest zone diameter for yeasts was measured against *C. albicans* with a diameter of 33 mm. The antimicrobial activities of QANB are shown in Fig. 2. The antibacterial activity of QANB against selected Gram-positive and Gram-negative bacteria is demonstrated in S14–S15 of the SI.

Our sample, QANB, exhibited the same effect as standard antibiotics on some bacteria used in the tests, while showing greater activity than antibiotics on some other bacteria. Also, the antifungal effect of QANB on *C. albicans* was determined to be notably more active than the standard nystatin (Table 2). According to the results obtained, our sample, QANB, can be evaluated as an alternative to standard antibiotics (streptomycin, tetracycline) and antifungal (nystatin) for some tested bacteria and fungi.

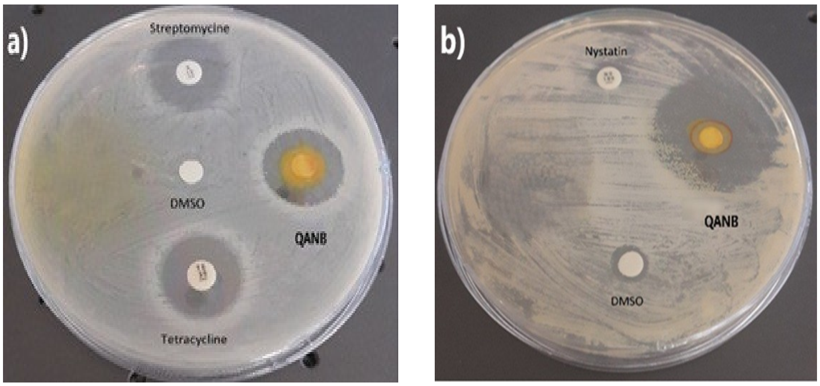

**Figure 2:** Antibacterial activity on *E. aerogenes* (a) and antifungal activity on *C. albicans* (b) of QANB.

**Table 2:** Inhibition zones of QANB, standard antibiotics, and standard antifungal.

| | | **QANB** | **DMSO** | **Str** | **Nys** | **Tet** |
|---|---|---|---|---|---|---|
| Gram (+) bacteria | *B. subtilis* | 18 | ---- | 16 | U | 18 |
| | *S. aureus* | - | ---- | 24 | U | 19 |
| | *E. faecalis* | 20 | ---- | 29 | U | 28 |
| | *G. rubripertincta* | 19 | ---- | 17 | U | 27 |
| Gram (-) bacteria | *E. aerogenes* | 22 | ---- | 20 | U | 20 |
| | *S. enterica* | 20 | ---- | 15 | U | 20 |
| | *P. vulgaris* | 13 | ---- | 21 | U | 17 |
| | *K. pneumoniae* | - | ---- | 19 | U | 14 |
| Yeasts | *C. albicans* | 33 | ---- | U | 9 | U |
| | *C. parapsilosis* | - | ---- | U | 23 | U |

**Str:** Streptomycin**, Nys:** Nystatin**, Tet:** Tetracycline, **U:** Untested**,**
**(-):** No inhibition**, DMSO:** Dimethyl sulfoxide

The lowest level of an antimicrobial that suppresses the visible growth of a microorganism after an overnight incubation period is known as the minimum inhibitory concentration (MIC) (40). For QANB, the MIC values determined against the bacteria in which the zone diameter measured over 10 mm during antibacterial activity determination are shown in Table 3 (41). The lowest MIC value was determined on *E. faecalis* with 625 µg/mL. The MIC values of QANB against the tested bacterial strains ranged from 1250 to 2500 µg/mL (Table 3).

**Table 3.** MIC values of QANB (µg/mL).

| **Microorganisms** | | **QANB** |
|---|---|---|
| | | **MIC values (µg/mL)** |
| Gram (+) bacteria | *B. subtilis* | 2500 |
| | *E. faecalis* | 625 |
| | *G. rubripertincta* | 1250 |
| Gram (–) bacteria | *E. aerogenes* | 2500 |
| | *S. enterica* | 2500 |
| | *P. vulgaris* | 2500 |

Quinolones are broad-spectrum antibiotics that have been used in medicine and veterinary medicine since the 1960s in the treatment of many infections (42,43). Various quinolone derivative molecules were prepared and evaluated by researchers against bacteria and yeasts. Turan-Zitouni et al. synthesized new naphthyridine hydrazone derivatives, and they tested new compounds for their antimicrobial activities (44). It was determined that the antifungal activity of the synthesized compounds was quite high. It was also observed that the antibacterial activities of the related compounds were higher on some bacteria compared to streptomycin. In our study, we found similar results. The synthesized QANB demonstrated significant antifungal activity against *C. albicans* and showed measurable inhibitory effects against selected bacterial species.

Mohammed observed that one of the compounds formed inhibition zones with diameters of 12, 15, 16, and 17 mm against *Proteus vulgaris*, *Staphylococcus hominis*, *Staphylococcus epidermidis*, *Streptococcus hemolyticus*, *Klebsiella pneumoniae*, *Staphylococcus aureus* (ATCC 25923), and *Staphylococcus aureus* in his study on the synthesis of new diazo dyes derived from 2, 4-dihydroxy quinoline (45).

In another study, Yahyazadeh and Yousefi synthesized some novel heteroaryl azo dyes derived from 8-chloro-4-hydroxy-2-quinolone. They tested the dyes for their antibacterial activities on four different bacteria. It was determined that all but three of the eight synthesized compounds exhibited antibacterial activity (46).

Rufchahi et al. synthesized a series of azo dyes by coupling diazotized p-substituted aniline derivatives with 8-methyl-4-hydroxy-2-quinolone at the 3-position. These compounds were evaluated for their antibacterial activity against *Bacillus subtilis*, *Micrococcus luteus*, *Salmonella enterica*, and *Pseudomonas aeruginosa* (47). The antibacterial activities of the p-nitro (p-$NO_2$) derivative against *S. enterica* and *B. subtilis* were selected for comparison with QANB. According to these results, the p-nitro derivative exhibited an 8 mm inhibition zone against *S. enterica*, comparable to standard antibiotics such as Tetracycline (inhibition zone of 7 mm) and Erythromycin (inhibition zone of 8 mm). In our study, QANB with azo substitution at the 8-position showed a significantly larger inhibition zone of 20 mm, while Streptomycin, a commonly used standard, exhibited an inhibition zone of 15 mm. While Rufchahi et al. reported that *B. subtilis* showed resistance to the p-nitro derivative, this study found that QANB was more effective against *B. subtilis* than streptomycin (16 mm), with an inhibition zone of 18 mm (47). These findings suggest that shifting the azo bond from the 3-position to the 8-position can significantly increase the antibacterial potential. This supports the SAR perspective that positional substitution within the quinolone skeleton plays a critical role in biological performance.

As shown in the literature, most quinolone derivatives show effective antimicrobial activity. The results obtained in our study also support this situation. Therefore, the antimicrobial effects of QANB suggest that these valuable properties warrant further investigation.

## 4. CONCLUSION

In this study, 6-ethyl-4-hydroxy-2H-pyrano[3,2-c]quinoline-2,5-dione (PQ) was prepared by condensation of *N*-ethyl aniline and diethyl malonate. The new azo dye bearing a quinolone moiety (QANB) was obtained from PQ. Azo dye formed at the 3-position of PQ in pyridine medium, as reported in the literature (28). However, we obtained a different result from previous studies. We have reported that PQ gives the coupling at the 8-position on the quinolone ring instead of the 3-position of the pyranoquinolone in the strong base medium with the diazonium salt of p-nitroaniline, followed by a ring-opening reaction. The strong basic condition may have increased the contribution of the keto-enol tautomer of the PQ, leading to azo coupling occur at the 8-position. QANB was elucidated by FTIR, NMR ($^{1}$H NMR, $^{13}$C NMR, $^{13}$C NMR DEPT, $^{13}$C NMR APT, $^{1}$H-$^{1}$H COSY, and $^{1}$H-$^{13}$C HMQC), and mass spectroscopy. Its antimicrobial activity was tested on four different Gram-positive and Gram-negative bacteria. According to these results, QANB exhibited antibacterial activity against *B. subtilis, E. faecalis,* and *G. rubripertincta* (Gram-positive), as well as *E. aerogenes, S. enterica,* and *P. vulgaris* (Gram-negative). Notably, it significantly demonstrated the activity against *E. aerogenes*, which causes pneumonia, sepsis, urinary tract infections, and wound infections. According to the results obtained by applying the disc diffusion method, MIC evaluation tests were also performed for bacteria with zones of inhibition ≥10 mm. The lowest MIC value was observed for *E. faecalis* with 625 µg/mL. The MIC values of QANB against the tested bacterial strains ranged from 1250 to 2500 µg/mL. QANB also showed significant activity against *C. albicans*. The fact that QANB is more effective against *C. albicans* than nystatin, which is widely used as an antifungal agent, supports that this compound can be used as a potential antifungal drug. Additionally, QANB demonstrated broad-spectrum antibacterial activity against both Gram-positive and Gram-negative bacteria, indicating its potential as a candidate for third-generation antibiotics in the future.

## 5. CONFLICT OF INTEREST

### Declaration of generative AI and AI-assisted technologies in the writing process

During the preparation of this work, the authors used the AI-powered tools DeepL, Grammarly, and Copilot to improve the language and readability of the text. After using these tools, the authors reviewed and edited the content as needed and took full responsibility for the publication’s content.

## 6. ACKNOWLEDGEMENTS

The authors are grateful to Giresun University Central Research Laboratory (GRUMLAB) and the Giresun University Biology Department for their technical support during the antimicrobial study.

### CRediT authorship contribution statement

**Öznur Ölmez Nalcıoğlu:** Conceptualization, Performed Experiments, Methodology, Validation, Investigation, Data Curation, Writing-Original Draft, Writing-Review&Editing, Visualization. **Mehtap Yakut:** Performed Experiments, Methodology, Investigation, Writing-Review&Editing. **Ayşe Gül Caniklioğlu:** Methodology, Validation, Investigation, Data Curation, Visualization, Writing-Original Draft, Writing-Review&Editing.

## 7. REFERENCES

1. Andersson MI, MacGowan AP. Development of the quinolones. J Antimicrob Chemother [Internet]. 2003 May 1;51(90001):1–11. Available from: <URL>.

2. Andriole VT. The quinolones: Past, present, and future. Clin Infect Dis [Internet]. 2005 Jul 15;41(Supplement_2):S113–9. Available from: <URL>.

3. Oliphant CM, Green GM. Quinolones: A comprehensive review. 2002;65(3):455–64. Available from: <URL>.

4. Liu X, Deng J, Xu Z, Lv ZS. Recent advances of 2-Quinolone-based derivatives as anti-tubercular agents. Anti-Infective Agents [Internet]. 2018 May 3;16(1):4–10. Available from: <URL>.

5. Fan YL, Cheng XW, Wu JB, Liu M, Zhang FZ, Xu Z, et al. Antiplasmodial and antimalarial activities of quinolone derivatives: An overview. Eur J Med Chem [Internet]. 2018 Feb;146:1–14. Available from: <URL>.

6. Wang R, Xu K, Shi W. Quinolone derivatives: Potential anti-HIV agent—development and application. Arch Pharm (Weinheim) [Internet]. 2019 Sep 5;352(9):1900045. Available from: <URL>.

7. Gao F, Zhang X, Wang T, Xiao J. Quinolone hybrids and their anti-cancer activities: An overview. Eur J Med Chem [Internet]. 2019 Mar;165:59–79. Available from: <URL>.

8. Zhang B. Quinolone derivatives and their antifungal activities: An overview. Arch Pharm (Weinheim) [Internet]. 2019 May 25;352(5):1800382. Available from: <URL>.

9. Singh PK, Singh RL. Bio-removal of azo dyes: A review. Int J Appl Sci Biotechnol [Internet]. 2017 Jun 29;5(2):108–26. Available from: <URL>.

10. Khan MN, Parmar DK, Das D. Recent applications of azo dyes: A paradigm shift from medicinal chemistry to biomedical sciences. Mini-Reviews Med Chem [Internet]. 2021 Jun;21(9):1071–84. Available from: <URL>.

11. Arslan Ö, Aydıner B, Yalçın E, Babür B, Seferoğlu N, Seferoğlu Z. 8-Hydroxyquinoline based push-pull azo dye: Novel colorimetric chemosensor for anion detection. J Mol Struct [Internet]. 2017 Dec;1149:499–509. Available from: <URL>.

12. Ölmez Nalcıoğlu Ö, Kılıç E, Haspulat Taymaz B, Kamış H. Synthesis of new azobenzo[c]cinnolines and investigation of electronic spectra and spectroelectrochemical behaviours. Spectrochim Acta Part A Mol Biomol Spectrosc [Internet]. 2021 Dec;263:120175. Available from: <URL>.

13. Ali Y, Hamid SA, Rashid U. Biomedical applications of aromatic azo compounds. Mini-Reviews Med Chem [Internet]. 2018 Oct 12;18(18):1548–58. Available from: <URL>.

14. Şener N, Mohammed HJA, Yerlikaya S, Celik Altunoglu Y, Gür M, Baloglu MC, et al. Anticancer, antimicrobial, and DNA protection analysis of novel 2,4-dihydroxyquinoline dyes. Dye Pigment [Internet]. 2018 Oct;157:11–9. Available from: <URL>.

15. Mezgebe K, Mulugeta E. Synthesis and pharmacological activities of azo dye derivatives incorporating heterocyclic scaffolds: a review. RSC Adv [Internet]. 2022;12(40):25932–46. Available from: <URL>.

16. Kumari R, Sunil D, Ningthoujam RS, Kumar NA. Azodyes as markers for tumor hypoxia imaging and therapy: An up-to-date review. Chem Biol Interact [Internet]. 2019 Jul;307:91–104. Available from: <URL>.

17. Li X, Cheng J, Gong Y, Yang B, Hu Y. Mapping hydrogen sulfide in rats with a novel azo-based fluorescent probe. Biosens Bioelectron [Internet]. 2015 Mar;65:302–6. Available from: <URL>.

18. Pandey N. Bacterial pathogenesis. In: Microbes of Medical Importance [Internet]. Iterative International Publishers, Selfypage Developers Pvt Ltd; 2024. p. 3–28. Available from: <URL>.

19. Sati H, Carrara E, Savoldi A, Hansen P, Garlasco J, Campagnaro E, et al. The WHO bacterial priority pathogens list 2024: A prioritisation study to guide research, development, and public health strategies against antimicrobial resistance. Lancet Infect Dis [Internet]. 2025 Sep;25(9):1033–43. Available from: <URL>.

20. Tang K, Zhao H. Quinolone antibiotics: Resistance and therapy. Infect Drug Resist [Internet]. 2023 Feb;16:811–20. Available from: <URL>.

21. Pham TDM, Ziora ZM, Blaskovich MAT. Quinolone antibiotics. Medchemcomm [Internet]. 2019;10(10):1719–39. Available from: <URL>.

22. Naghavi M, Vollset SE, Ikuta KS, Swetschinski LR, Gray AP, Wool EE, et al. Global burden of bacterial antimicrobial resistance 1990–2021: A systematic analysis with forecasts to 2050. Lancet [Internet]. 2024 Sep;404(10459):1199–226. Available from: <URL>.

23. Li K, Guo J, Liang R, Wang X, Chen Q, Wang J, et al. A review on antifungal activity of plant essential oils. Phyther Res [Internet]. 2025 Aug 9;39(8):3736–61. Available from: <URL>.

24. Liao H, Liu M, Wang M, Zhang D, Hao Y, Xie F. Exploring the potential of s-Triazine derivatives as novel antifungal agents: A review. Pharmaceuticals [Internet]. 2025 May 7;18(5):690. Available from: <URL>.

25. WHO. WHO fungal priority pathogens list to guide research, development and public health action [Internet]. 2022. Available from: <URL>.

26. WHO. WHO issues its first-ever reports on tests and treatments for fungal infections [Internet]. 2025. Available from: <URL>.

27. Soliman HN, Yahia IS. Synthesis and technical analysis of 6-butyl-3-[(4-chlorophenyl)diazenyl]-4-hydroxy-2H-pyrano[3,2-c] quinoline-2,5(6H)-dione as a new organic semiconductor: Structural, optical and electronic properties. Dye Pigment [Internet]. 2020 May;176:108199. Available from: <URL>.

28. Saeed AM, AlNeyadi SS, Abdou IM. Anticancer activity of novel Schiff bases and azo dyes derived from 3-amino-4-hydroxy-2H-pyrano[3,2-c]quinoline-2,5(6H)-dione. Heterocycl Commun [Internet]. 2020 Dec 31;26(1):192–205. Available from: <URL>.

29. Soliman H, Yahia I. Structure, properties, and thermal behavior of chemically synthesized 3-((2,5 Difluorophenyl)diazenyl)-6-ethyl-4-hydrox-2H-pyrano[3,2-c]quinoline-2,5(6H)-dione as new brand organic materials: Antimicrobial activity. Egypt J Solids [Internet]. 2023 Aug 1;45(1):1–23. Available from: <URL>.

30. Yakut M, Yılmaz M, Pekel T, Erkan S, Katırcı R, Biçer E. Manganese(III) acetate-based radical cyclization reactions for pyranocoumarin and pyranoquinoline compounds: Synthesis, DFT and molecular docking studies. ChemistrySelect [Internet]. 2022 Nov 25;7(44):e202202787. Available from: <URL>.

31. Aly AA, Nieger M, Bräse S, Bakheet MEM. X-ray structure analyses of 4-Hydroxy-1-Methylquinolin-2(1H)-One, 6-Ethyl-4-Hydroxy-2 H-Pyrano[3,2-c]Quinoline-2,5(6H)-Dione, (E)-4-(2-Benzylidene-Hydrazineyl)Quinolin-2(1H)-One and Diethyl (E)-2-(2-(1-Methyl-2-Oxo-1,2-Dihydro-Quinolin-4-yl)Hydrazineylidene) Succinate. J Chem Crystallogr [Internet]. 2023 Mar 4;53(1):38–49. Available from: <URL>.

32. Murray PR, Baron EJ, Jorgensen JH, Landry ML, Pfaller MA. Manual of clinical microbiology [Internet]. Washington: ASM Press; 2007. Available from: <URL>.

33. Yiğit D, Yiğit N, Aktaş E, Özgen U. Ceviz (*Juglans regia* L.)'in antimikrobiyal aktivitesi. Türk Mikrobiyoloji Cemiy Derg [Internet]. 2009;39(1–2):7–11. Available from: <URL>.

34. Ibrahim MA, Hassanin HM, Gabr YAA, Alnamer YAS. Novel heterocyclic derivatives of pyrano[3,2-c]quinolinone from 3-(1-ethy1-4-hydroxy-2-oxo-2(1H)-quinolin-3-yl)-3-oxopropanoic acid. Eur J Chem [Internet]. 2010 Sep 30;1(3):195–9. Available from: <URL>.

35. Ismail MM, Othman ES, Mohammed HM. Synthesis and cyclization reactions with quinolinyl

keto esters. I. chemical reactivity of quinolinyl beta-keto ester and quinolinyl alpha,beta-unsaturated ketones. Chem Pap [Internet]. 2005;59:117–26. Available from: <URL>.

36. Abass M, Othman ES. Chemistry of substituted quinolinones. III. synthesis and reactions of some novel 3-pyrazolyl-2-quinolinones. Synth Commun [Internet]. 2001 Jan 20;31(21):3361–76. Available from: <URL>.

37. Socrates G. Infrared and raman characteristic group frequencies: Tables and charts [Internet]. John Wiley & Sons; 2001. 1 p. Available from: <URL>.

38. Mirsadeghi FA, Rufchahi EM, Zarrabi S. Spectral characterization and computational studies of some new synthesized 3-arylazo-4-hydroxybenzo[h]quinolin-2(1H)-one dyes. J Mol Struct [Internet]. 2022 Nov;1268:133726. Available from: <URL>.

39. Hasani M, Nordstierna L, Martinelli A. Molecular dynamics involving proton exchange of a protic ionic liquid–water mixture studied by NMR spectroscopy. Phys Chem Chem Phys [Internet]. 2019;21(39):22014–21. Available from: <URL>.

40. Andrews JM. Determination of minimum inhibitory concentrations. J Antimicrob Chemother [Internet]. 2001 Jul 1;48(suppl_1):5–16. Available from: <URL>.

41. Sati SC, Khulbe K, Joshi S. Antibacterial evaluation of the himalayan medicinal plant *Valeriana wallichii* DC. (Valerianaceae). Res J Microbiol [Internet]. 2011;6(3):289–96. Available from: <URL>.

42. Webber M, Piddock LJV. Quinolone resistance in *Escherichia coli*. Vet Res [Internet]. 2001 May;32(3/4):275–84. Available from: <URL>.

43. Ruiz J. Mechanisms of resistance to quinolones: target alterations, decreased accumulation and DNA gyrase protection. J Antimicrob Chemother [Internet]. 2003 May 1;51(5):1109–17. Available from: <URL>.

44. Turan-Zitouni G, Altıntop MD, Özdemir A, Demirci F, Mohsen UA, Kaplancikli ZA. Yeni naftiridin hidrazon türevleri ve anti-mikrobiyal aktiviteleri. Cukurova Med J [Internet]. 2014 Jun 1;39(2):234–9. Available from: <URL>.

45. Mohammed HJA. 2, 4-dihidroksi kinolin türevi yeni diazo boyarmaddelerin sentezi ve antimikrobiyal özelliklerin incelenmesi. 2018.

46. Yahyazadeh A, Yousefi H. Synthesis, spectral features and biological activity of some novel hetarylazo dyes derived from 8-chloro-4-hydroxyl-2-quinolone. Spectrochim Acta Part A Mol Biomol Spectrosc [Internet]. 2014 Jan;117:696–701. Available from: <URL>.

47. Moradi Rufchahi EO, Pouramir H, Yazdanbakhsh MR, Yousefi H, Bagheri M, Rassa M. Novel azo dyes derived from 8-methyl-4-hydroxyl-2-quinolone: Synthesis, UV–vis studies and biological activity. Chinese Chem Lett [Internet]. 2013 May;24(5):425–8. Available from: <URL>.

Journal of the Turkish Chemical Society Section A: Chemistry
TURKISH CHEMICAL SOCIETY

# A Direct Synthesis Route of Thermally Expanded Graphene for Electrically Conductive PEEK Polymer Composites with Environmental Assessment Analysis

**Semih Doğan**[1*]

[1]Sabanci University, Integrated Manufacturing Technologies Research and Application Center & Composite Technologies Center of Excellence, Manufacturing Technologies, Istanbul, 34906, Türkiye.

**Abstract:** This study presents a rapid and chemical-free synthesis of thermally expanded graphene (TEG), which is a lightweight carbon material, via 5-minute single-step thermal exfoliation of commercially available expandable graphite. The resulting TEG exhibits ultralow density of 0.0195 g/mL and a significant volumetric expansion ratio (32-fold), indicative of a porous network structure. Structural analyses confirmed the effective removal of oxygen-containing groups (C/O ratio increased from 4.7 to 79.0), restoration of conjugated graphitic domains ($I_{2D}/I_G$ value of 0.57), the material's thermal robustness (single major decomposition stage beginning at 595 °C), and the formation of wrinkled layers with microholes resulting from gas release. Importantly, a life cycle assessment (LCA) revealed a moderate global warming potential (0.0233 kg $CO_2$-eq/g), substantially lower than that of reduced graphene oxide (rGO) and carbon nanotubes (CNTs). For the first time, TEG was incorporated into polyetheretherketone (PEEK) to fabricate conductive polymer composites, achieving an electrical conductivity of 0.003381 S/cm at 10 wt.% loading. These findings highlight TEG as a sustainable and high-performance conductive filler for advanced thermoplastic applications in polymer matrices.

**Keywords:** Expandable graphite, Volumetric expansion, Polymer composite, Electrical conductivity, Life cycle assessment.

**Submitted:** June 18, 2025. **Accepted:** September 19, 2025.

**Cite this:** Doğan S. A Direct Synthesis Route of Thermally Expanded Graphene for Electrically Conductive PEEK Polymer Composites with Environmental Assessment Analysis. JOTCSA. 2025;12(4): 207-20.

**DOI:** https://doi.org/10.18596/jotcsa.1722180

***Corresponding author's E-mail:** semih.dogan@sabanciuniv.edu

## 1. INTRODUCTION

The development of electrically conductive polymer composites has been at the center of materials science these days, especially for flexible electronics, sensors, energy storage devices, and EMI shielding applications (1-3). One of the most significant advantages of conductive polymer composites is their processability and versatility, enabling the integration of conductivity into complex-shaped components through polymer processing techniques. High-performance thermoplastic polymers like polyether ether ketone (PEEK) offer superior mechanical and thermal properties, but PEEK is inherently non-conductive (4). Therefore, conductive fillers play a pivotal role in transforming insulating polymers into functional materials with the ability to conduct electricity. The efficiency of a conductive filler is not only based on intrinsic electrical conductivity but also on morphology, aspect ratio, surface area, and polymer matrix compatibility (5). Conductive fillers enable the development of composites with tailored electrical properties by introducing a percolating network of conductive pathways within the polymer matrix. For this purpose, traditional conductive fillers such as carbon nanotubes (CNT), reduced graphene oxide (rGO), and graphene nanoplatelets (GNP) are widely used to achieve conductivity with various polymers at relatively low filler loadings (6-8). Nevertheless, their effective incorporation into polymer matrices suffers from issues like agglomeration and poor interfacial bonding (9). To overcome these challenges, graphite-based fillers like thermally expanded graphene oxide (TEGO), which has a porous and worm-like structure, are desirable due to high electrical conductivity ($10^6$ - $10^8$ S/m), large specific surface area (40-200 $m^2$/g), and mechanical stability (10). Furthermore, when incorporated into a wide range of polymer matrices, conductive filler enhances the electrical conductivity in the fabrication of advanced composites (11).

As environmental concerns continue to shape the future of material development, it is crucial to explore sustainable alternatives to traditional manufacturing methods. Thus, conventional synthesis routes such as the Hummers' method for the preparation of graphene oxide and reduced graphene oxide are based on harsh chemical oxidation routes, which are environmentally hazardous and time-consuming (12). Hence, these nanomaterials often lead to materials with low conductivity due to structural defects. Moreover, the multi-step nature of these methods gives rise to scalability and inconsistent product quality. Furthermore, uniform dispersion and percolation of graphene derivatives within viscous, high-temperature polymers such as PEEK remain major engineering challenges (13). In particular, inadequate filler dispersion and poor interface compatibility can lead to insufficient electrical performance and weak structural integrity (14) These limitations result in the development of high-performance, electrically conductive polymer composites using graphene-based fillers remaining hindered by processing constraints and material inefficiencies.

In the conventional approach, thermally exfoliated graphite and graphene are synthesized from flake graphite through a two-step process involving both chemical and thermal treatments. For instance, Singh *et al*. prepared thermally exfoliated graphene oxide (TEGO) from graphite through a chemical and thermal process, with a pore size of 2.9 mm and a pore volume of 1.2 cm$^3$/g for hydrogen storage applications (15). To address these challenges, the direct thermal expansion method for synthesizing TEGO is advantageous due to its simplicity, speed, environmental friendliness, and scalability (16). Furthermore, it avoids the complications and safety concerns associated with chemical exfoliation and oxidation, making it a more practical and sustainable route for producing graphite-based fillers suitable for the production of conductive composite materials (17). Herein, expandable graphite flakes, as a potential alternative, present a sustainable and scalable method for synthesizing TEGO, as it allows rapid expansion under thermal treatment without the extensive use of harsh chemicals, thereby reducing environmental impact and enabling cost-effective, large-scale production (18). In one study conducted by Bao *et al*., expanded graphite was rapidly prepared in a muffle furnace at 800 °C for 2 min. In addition, this material showed excellent EMI shielding performance of 85 dB and high electric conductivity of 7153 S/m (19). In another study, Son *et al*. investigated the synthesis of thermal exfoliation of expandable graphite to optimize expansion volume and interlayer spacing. The expandable graphite sample treated at 600 °C for 30 min exhibited optimal structural and electrochemical performance, with a high reversible capacity of 338 mAh g$^{-1}$ (20).

Morphologically, TEGO exhibits a vermicular and worm-like structure characterized by high porosity and a substantial specific surface area ranging from 40 to 200 m$^2$/g. Electrically, TEGO demonstrates remarkable conductivity, with values reported between 10$^6$ and 10$^8$ S/m (21) TEGO's worm-like and porous structure is attributed to the restoration of the conjugated π-electron system, which facilitates electron transport. In addition, TEGO can easily disperse with polymers such as polypropylene and is also compatible with polycarbonates, polycaprolactones, and polycaprolactams (22). For instance, Tarannum *et al*. displayed that thermally expanded graphite (EG)/polyetherimide (PEI) composite increased the electrical conductivity up to 969 Sm$^{-1}$ at 10 wt% EG compared to neat PEI (1.2x10$^{-17}$ Sm$^{-1}$) (23). In another study, Mohammad *et al*. showed that a thermally expanded graphite/polysulfone composite achieved a high electrical conductivity of 52.9 S/cm at a filler concentration of 70 wt% (24).

While CNT and rGO have been widely investigated in various polymer systems, systematic research on TEG-filled PEEK composites remains limited, particularly in terms of electrical performance. To the best of my knowledge, no previous work has systematically evaluated the incorporation of directly synthesized TEG as a conductive filler at different loading ratios within PEEK. As an example of only expanded graphite, Goyal *et al*. reported that expanded graphite/PEEK composite at 5 wt% and 10 wt% filler loadings enhanced the electrical conductivity to around 3.24 S/cm and 12.3 S/cm, respectively (25). Moreover, TEG has been studied in other polymer matrices, such as epoxy, where it is mixed directly with hardeners and dispersed by sonication (26), but such a direct incorporation method and systematic evaluation in PEEK has not yet been reported. In this context, this study aims to bridge this gap by evaluating the electrical and structural performance of PEEK composites filled with directly synthesized TEGO at varying concentrations.

Life cycle assessment (LCA) studies on graphite-filler materials for evaluating the environmental impacts associated with the production process emerged as a pivotal methodology. For instance, Surovtseva *et al*. examined that the traditional synthetic graphite production via the Acheson process had a high global warming potential of 13.8 kgCO$_2$-eq/kg (27). In contrast, Engels *et al*. showed that natural graphite production in China showed lower impacts at 9.6 kgCO$_2$-eq/kg (28). Thus, a critical aspect of this assessment involved the environmental impacts of graphite mining, which can lead to deforestation, water pollution, and soil degradation.

This study demonstrates a direct and efficient route to synthesize TEG from commercially available expandable graphite via a single-step thermal expansion process. Unlike conventional approaches, this method achieves complete exfoliation under thermal shock conditions, making it both scalable and environmentally benign. To the best of our knowledge, this is the first systematic investigation of TEG incorporation into a high-performance thermoplastic PEEK, at different loadings (5 and 10 wt%) to fabricate conductive composites. The study not only demonstrates the feasibility of producing lightweight and electrically conductive PEEK/TEG composites but also provides direct evidence of the concentration-dependent improvement in electrical conductivity. Furthermore, the environmental profile of the synthesis route was rigorously assessed through LCA, providing quantitative insights into its global warming potential and benchmarking its footprint against conventional carbon-based fillers such as rGO and CNTs. By integrating a rapid and scalable synthesis route, advanced functional performance, and comprehensive environmental evaluation, this work advances the state of the art in graphene-based composite research. It establishes TEG as a cost-effective, sustainable, and industrially relevant filler, thereby offering strong potential for deployment in next-generation polymer-based engineering applications, including aerospace, automotive, and electronic sectors.

## 2. EXPERIMENTAL SECTION

### 2.1. Materials

Expandable graphite flakes (material code: 808121, > 300 µm, +50 mesh) were procured from Sigma-Aldrich (Germany) and utilized as the primary carbon precursor for the production of thermally expanded graphene (TEG). Polyetheretherketone (PEEK) granules with a particle size of 6 mm and a density of 1.31 g/cm³ were obtained from Eurotec Engineering Plastics in Türkiye to prepare polymer composites.

### 2.2. Synthesis of TEG

A mass of 5.0 g of expandable graphite was placed in a crucible and subjected to direct thermal exfoliation using an ash furnace. The thermal exfoliation process was carried out under an argon atmosphere at 1000 °C for 5 min, with a controlled heating rate and an argon flow rate maintained at 5 L/min to facilitate the expansion of the graphite structure. Following the thermal exfoliation process, 1.2 g of TEG was obtained as the final product.

### 2.3. Preparation of TEG Reinforcement PEEK Composites

In the initial step, 95 g of PEEK granules were subjected to ball milling to reduce their particle size and enhance their dispersibility. The milled PEEK powder was then dry-mixed with 5 g of TEG using a mechanical stirrer at room temperature for 15 min to ensure homogeneous distribution of the components. The resulting powder mixture was transferred into a mold and subjected to compression molding using a hydraulic press located adjacent to the Fourier transform infrared system for 1 min. A uniaxial pressure of 10 tons was applied to form thin pellets. Finally, the pressed pellets were thermally treated in a furnace by heating to 390 °C for 30 min, followed by a controlled cooling process to stabilize the composite structure. TEG-PEEK composites were prepared by incorporating TEG into the PEEK matrix at different weight percentages. 5 wt.% TEG-PEEK composite was initially fabricated, followed by the preparation of 10 wt.% TEG-PEEK composite using the same processing method, as seen in Scheme 1.

### 2.4. LCA Studies

The carbon footprint to produce TEG from expandable graphite through a thermal process was evaluated by life-cycle assessment (LCA) according to the ISO 14040 and 14044 standards. The analysis was performed using Ecoinvent-3 allocation cutoff by classification (system library) in Simapro software (9.3.0.2 version). Global ReCiPe 2016 v1.1 midpoint method (Hierarchist perspective) was employed in order to analyze a broad spectrum of environmental impacts for the life cycle impact assessment (LCIA). These included contributions to climate change and global warming potential (GWP), as well as depletion of the stratospheric ozone layer. Additional indicators addressed the formation of ground-level ozone and its effects on human health and ecosystems, as well as the generation of fine particulate matter contributing to air pollution. This approach enabled a detailed evaluation of the environmental profile of TEG production, facilitating the identification of key impact hotspots within the thermal exfoliation process.

### 2.5. Characterization Techniques

Fourier Transform Infrared (FT-IR) spectroscopy was performed using a Thermo Scientific IS10 spectrometer equipped with an ATR accessory. Spectra were recorded over the 4000–800 cm$^{-1}$ range to identify and characterize the functional groups present in the samples. X-ray diffraction (XRD) analysis was conducted using a GNR Explorer diffractometer equipped with a Cu Kα radiation source (λ = 1.5406 Å). Scans were carried out over a 2θ range of 10° to 80° to evaluate the crystallinity and identify the phases present in the samples. Raman spectroscopy was employed to investigate the molecular structure and vibrational characteristics of the samples using a Renishaw inVia Reflex Raman microscope. Measurements were performed at ambient temperature using a 532 nm excitation laser, with spectra collected in the 100–3200 cm$^{-1}$ range. X-ray photoelectron spectroscopy (XPS) was utilized to determine the chemical and elemental composition of the samples using a Thermo Scientific K-Alpha spectrometer. Survey and high-resolution spectra were acquired to analyze elemental states and surface chemistry. Thermogravimetric analysis (TGA) was performed to assess the thermal stability and decomposition characteristics of the materials using a Mettler Toledo TGA/DSC 3+ thermal analyzer. The samples were heated at a rate of 10 K/min over a temperature range of 25°C to 1000°C, with an oxygen flow rate of 50 mL/min. Optical microscopy (OM) analysis was conducted using a Nikon Eclipse LV100ND microscope. The materials were examined under lenses at different magnifications (50x and 100x). Surface morphology was examined using a ZEISS Cross Beam 350 Gemini II Focused Ion Beam-Scanning Electron Microscope (FIB-SEM). Electrical conductivity measurements of the TEG–PEEK composites were performed using a Tektronix DMM 4020 5½-digit digital multimeter, a high-precision instrument capable of accurately measuring voltage, current, and resistance.

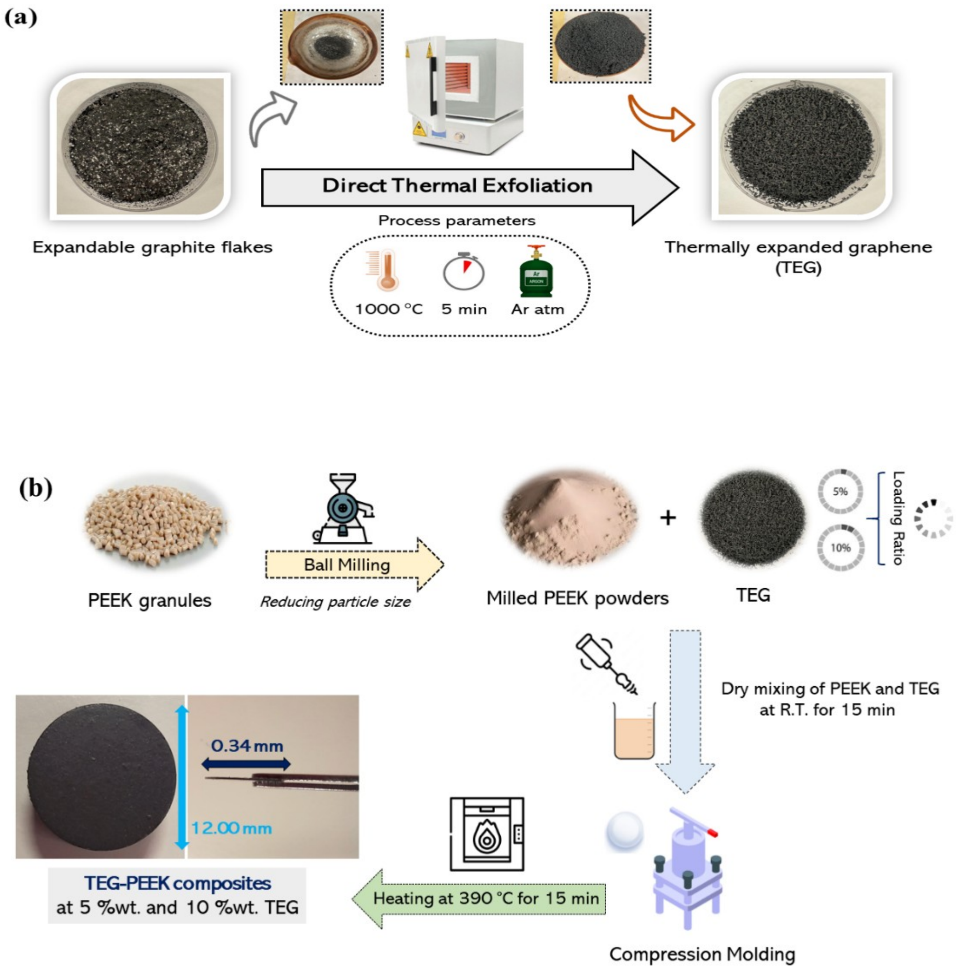

**Scheme 1:** Schematic illustration of (a) the synthesis of TEG from expandable graphite and (b) the preparation of 5 %wt. and 10 %wt. TEG-PEEK composites.

## 3. RESULTS AND DISCUSSION

### 3.1. Physicochemical Property Evaluation of TEG

Volume expansion is a critical phenomenon in graphitic materials, particularly due to their anisotropic layered structure (29). To analyze the impact of expansion on material performance and stability, the volume expansion behavior of graphitic materials was examined. Scheme 2 presents a comparative analysis of the volumetric changes observed in expandable graphite and TEG, as measured in a 25 mL graduated cylinder. In Scheme 2a, expandable graphite occupied a smaller volume, indicating its compact layered structure prior to expansion. In contrast, Scheme 2b demonstrates the dramatic volume increase of TEG, a result of rapid gas evolution during exfoliation, which separates the graphene layers and forms a low-density, highly porous structure.

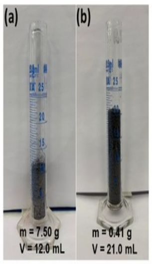

**Scheme 2:** Volume expansion of (a) expandable graphite and (b) TEG.

Density is an essential physical property that reflects the degree of exfoliation and internal structure changes in graphitic materials (30). Measuring the bulk density provides quantitative support for the morphological transformation observed during thermal treatment (31). Table S1 presents the comparative bulk density measurements of expandable graphite and TEG by using the displacement method in a graduated cylinder.

**Table 1:** Expansion characteristics of TEG.

| **Expansion Ratio (density)** | **ρ-Expandable graphite/ρ-TEG** | **ρ-Expandable graphite** | **ρ-TEG** |
|---|---|---|---|
| | 32.05 | 0.6250 g/mL | 0.0195 g/mL |

The expansion ratio in graphitic materials is a critical parameter that reflects how much the material increases in volume upon thermal treatment. A high expansion ratio indicates effective exfoliation and layer separation, which results in a substantial increase in specific surface area and porosity (32). The expanded morphology also facilitates enhanced ion intercalation and surface functionalization (33). The density-based expansion ratio was calculated to evaluate the structural transformation and functional performance of TEG. Table 1 presents the expansion characteristics of TEG. The results showed that TEG expanded approximately 32 times in volume per gram compared to the expandable graphite. This reflected the significant increase in volume due to extensive exfoliation and porosity introduced during the thermal expansion process.

### 3.2. Structural Characterization of TEG

FT-IR analysis was employed to investigate the thermal modifications of TEG, and the functional groups present in expandable graphite. The objective of this analysis was to evaluate the chemical transformation occurring during the thermal exfoliation process and to confirm the reduction in oxygen-containing groups, which are typically introduced during the process. FT-IR spectra of expandable graphite and TEG are presented in Fig. 1a. FT-IR spectra revealed several distinct absorption bands between expandable graphite and TEG. Expandable graphite exhibited prominent absorption bands (34,35). A broad band at 3369 $cm^{-1}$ was attributed to O–H stretching vibrations, indicating the presence of hydroxyl groups. The peaks at 2991 $cm^{-1}$ and 2882 $cm^{-1}$ corresponded to C–H stretching, suggesting aliphatic hydrocarbon groups. A strong absorption band at 1755 $cm^{-1}$ was assigned to C=O stretching vibrations, typically associated with carboxylic groups. C=C stretching band appeared at 1637 $cm^{-1}$ by reflecting the presence of conjugated double bonds within the graphite structure. Additionally, two bands at 1199 $cm^{-1}$ and 1060 $cm^{-1}$ were observed and attributed to C–O stretching, indicating the presence of alkoxy and epoxy groups. On the other hand, the FT-IR spectra of TEG showed a marked reduction in the intensity of the oxygen-related bands, indicating the successful removal of these groups during thermal exfoliation. Remarkably, O–H and C=O bands disappeared, confirming the deoxygenation of the nanomaterial. C–H stretching bands at 2991 $cm^{-1}$ and 2878 $cm^{-1}$ were still present by suggesting hydrocarbon moieties (36). C=C stretching peaks at 1593 $cm^{-1}$ and 1486 $cm^{-1}$ became more pronounced, indicative of the restoration of the conjugated $sp^2$ carbon network (19). A common spectral peak at 2330-2334 $cm^{-1}$ was also observed in both materials, attributed to atmospheric $CO_2$ (37). Overall, FT-IR analysis demonstrated that thermal exfoliation of expandable graphite led to the reduction of oxygen-containing groups (O–H, C=O, and C–O), thus confirming the restoration of conjugated C=C bonds characteristic of graphitic structures.

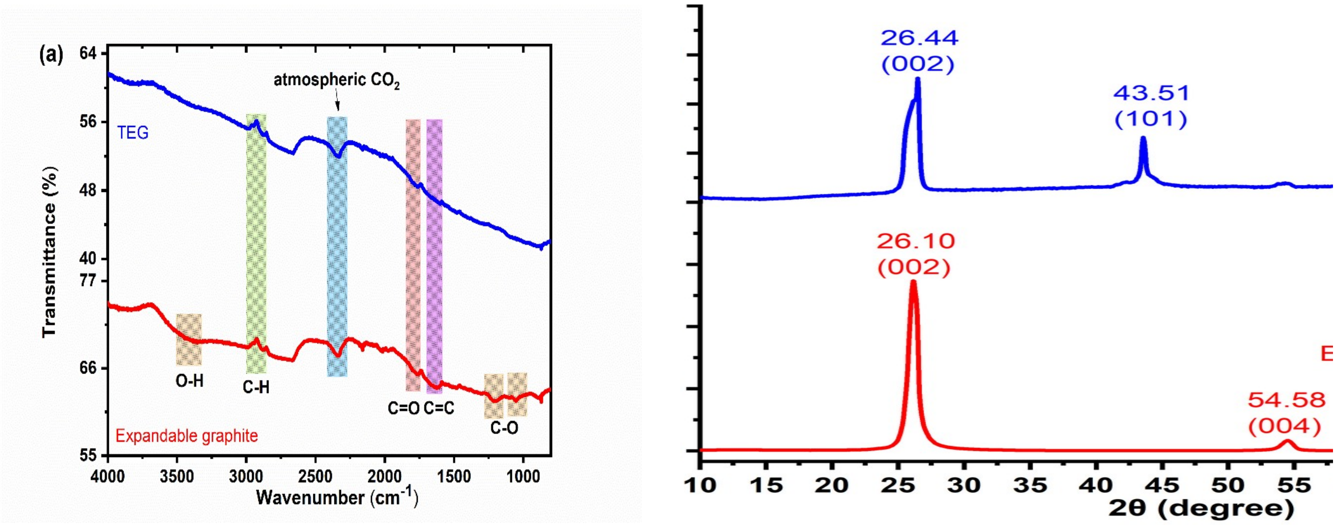

**Figure 1:** (a) FT-IR spectra and (b) XRD patterns of expandable graphite and TEG.

XRD analysis was performed to evaluate the crystalline structure of expandable graphite and TEG, as shown in Fig. 1b. The XRD pattern of expandable graphite exhibited two sharp and intense diffraction peaks. The strong peak at $2\theta = 26.10°$ corresponded to the (002) plane of graphite. Another peak observed at $2\theta = 54.58°$ was assigned to the (004) plane, further confirming the crystallinity of the expandable graphite (20). After thermal exfoliation, the XRD pattern of TEG showed notable changes. The (002) diffraction peak shifted slightly to $2\theta = 26.44°$ and exhibited a significant decrease in intensity accompanied by broadening. This behavior suggested a decrease in the stacking order of the graphene layers and an increase in structural disorder, attributed to the removal of oxygen-containing functional groups and the expansion process (38). In addition, a new peak emerged at 2θ = 43.51°, corresponding to the (101) plane, which is indicative of turbostratic carbon structures with randomly oriented graphene layers. The disappearance of the (004) peak at 54.58° in the TEG pattern further indicated the loss of long-range crystalline order.

The crystallite sizes and crystallinity degrees determined from XRD characterization are presented in Table S2. Expandable graphite exhibited a high crystalline degree of 88.8%, reflecting its well-ordered layered structure. The crystallite sizes at 26° and 54° were 82.7 Å and 86.3 Å, respectively. Moreover, TEG showed a substantially reduced crystalline degree of 51.8%. The crystallite size at 26° was slightly larger at 90.1 Å, but a notably large crystallite size (131.2 Å) was observed at 43°, indicating partial restacking or reorganization of layers after thermal exfoliation.

Raman spectroscopy provided essential information regarding the degree of graphitization, defects, and layer thickness in carbon-based materials. Fig. 2a displays Raman spectra of expandable graphite and TEG. Raman spectra of expandable graphite showed two characteristic peaks. The first peak, known as the D band, appeared at 1348 cm$^{-1}$ and is attributed to the breathing modes of sp$^2$ carbon atoms in disordered graphite structures. The second major peak, the G band, was located at 1584 cm$^{-1}$, corresponding to the $E_{2G}$ phonon of sp$^2$ carbon atoms, indicative of an ordered graphitic structure. Furthermore, the presence of a broad 2D band at 2714 cm$^{-1}$ was also noted, providing information about the stacking of graphene layers (39). After thermal exfoliation, significant changes were observed in the Raman spectrum of TEG. The D band remained at 1348 cm$^{-1}$, whereas the G band slightly shifted to 1579 cm$^{-1}$, suggesting partial restoration of the sp$^2$ carbon network and a decrease in defects. In addition, the 2D band also shifted slightly to 2717 cm$^{-1}$, which is consistent with the exfoliation and thinning of graphite layers (40). The intensity ratio of $I_D/I_G$ is widely used to evaluate the degree of disorder or defects within the graphitic structure. A higher $I_D/I_G$ value indicates a greater amount of structural defects and disorder in the carbon lattice, while a lower ratio suggests higher graphitic crystallinity and fewer defects (41,42). For expandable graphite, $I_D/I_G$ was calculated to be 0.47, reflecting a relatively disordered structure due to the presence of functional groups and lattice imperfections introduced during the expansion process. After thermal exfoliation, $I_D/I_G$ value for TEG significantly decreased to 0.13, indicating a substantial reduction in structural defects. This decrease demonstrated that the thermal exfoliation process effectively removed oxygen-containing groups and restored the sp$^2$ carbon network, enhancing the material's structural order and graphitic character (43). Furthermore, expandable graphite exhibited $I_{2D}/I_G$ value of 0.72, suggesting a multilayered graphite structure with significant stacking. After exfoliation, TEG showed a slightly lower $I_{2D}/I_G$ value of 0.57, reflecting the formation of thinner graphene sheets and a partial disruption of the stacked graphite structure.

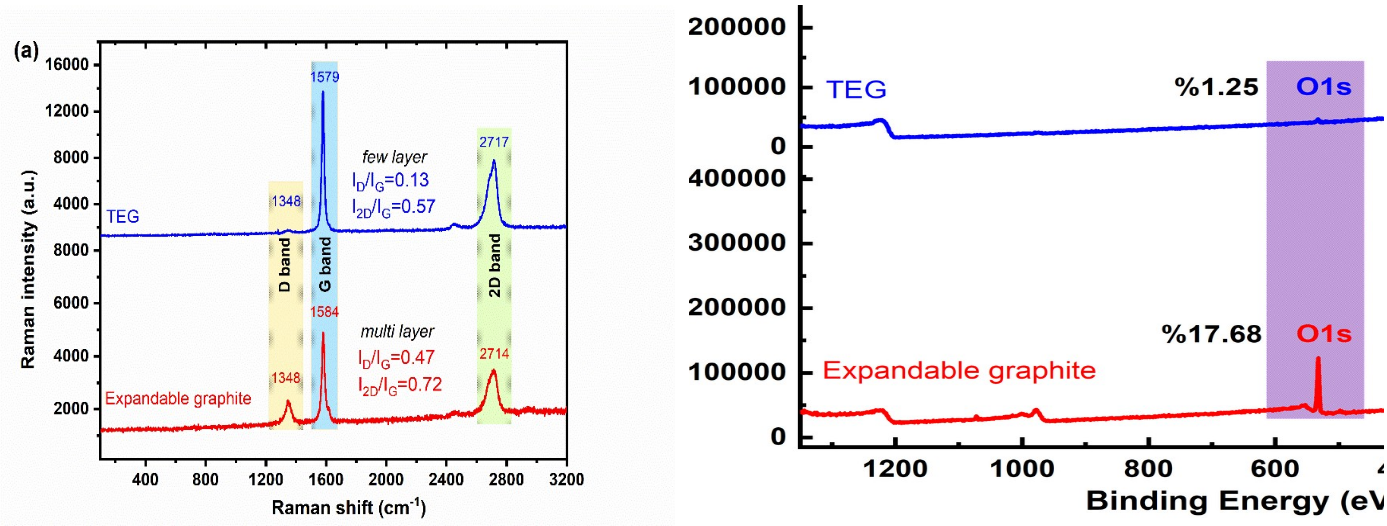

**Figure 2:** (a) Raman spectra and (b) XPS survey scan spectra of expandable graphite and TEG.

The surface chemical composition of expandable graphite and TEG was investigated using XPS. The survey spectra are presented in Fig. 2b by highlighting the presence of the principal elements, carbon (C 1s) and oxygen (O 1s), along with their respective atomic percentages. Expandable graphite exhibited a strong C 1s peak, corresponding to 82.32 %, and a notable O 1s peak, amounting to 17.68 %. The relatively high oxygen content was attributed to the intercalation of oxygen-containing functional groups introduced during the chemical treatment of natural graphite in the preparation of expandable graphite (17). These oxygen functionalities were further confirmed by the deconvoluted C 1s spectrum, which shows prominent peaks corresponding to C–O and C=O bonds (44). The binding energies for the C 1s and O 1s peaks were observed at 284.45 eV and 532.22 eV, respectively. In contrast, TEG demonstrated a significant increase in carbon content to 98.75 %, accompanied by a drastic reduction in oxygen content to 1.25 %. This sharp decrease in oxygen concentration was indicative of the successful thermal reduction and exfoliation of graphite flakes during the heating process (23). The C 1s spectrum of TEG was dominated by a sharp peak near 284.48 eV, attributed primarily to the sp²-hybridized C–C bond. The O 1s peak remains weak and shifted slightly to 532.50 eV, indicating the presence of only trace residual oxygen. The substantial increase in carbon purity and the significant decrease in oxygen functionalities suggested that the thermal exfoliation process not only delaminated the graphite layers but also reduced the material chemically, restoring much of the graphitic sp² carbon network (45). Atomic percentages, calculated C/O ratios and key binding energy positions for the C 1s and O 1s regions are summarized in Table S3. The C/O ratio of TEG was significantly higher than that of expandable graphite, increasing from approximately 4.65 to 79.00 after thermal exfoliation. This dramatic increase in the C/O ratio (ΔC/O=+74.34) confirmed the extensive removal of oxygen-containing groups such as epoxy and carboxyl during the thermal treatment process. This restoration was critical for improving the electrical conductivity of TEGO with minimal residual oxygen functionalities (17).

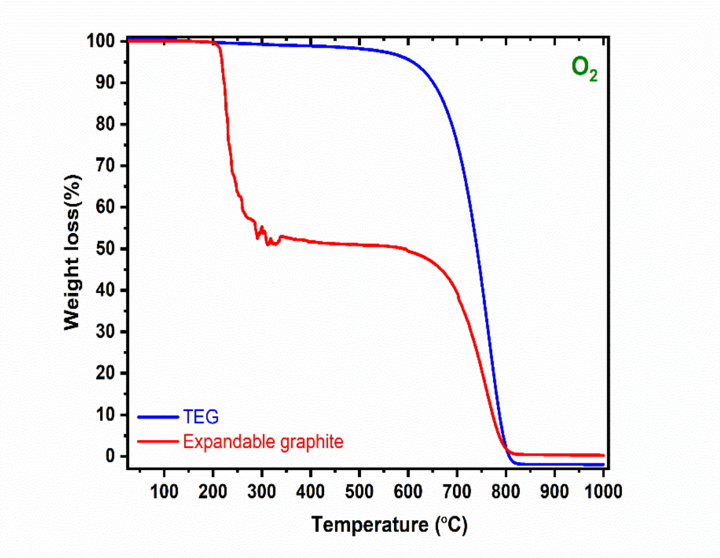

**Figure 3:** TGA curves of expandable graphite and TEG in the presence of oxygen.

TGA thermograms of expandable graphite and TEG are shown in Fig. 3. Weight loss (%) was recorded as a function of temperature from room temperature up to 1000 °C in an oxygen atmosphere. The onset temperature ($T_{on}$) and the maximum decomposition temperature ($T_{dm}$) were determined from DTG curves and are summarized in Table S4. Expandable graphite exhibited a two-step decomposition behavior (18). An initial sharp weight loss was observed between 212–286 °C, corresponding to the expansion process and the release of volatile intercalated species. Beyond 600 °C, a gradual decomposition occurred, associated with oxidation and combustion of the graphitic carbon structure. The material left a residual mass of 0.68% at 1000 °C. On the other hand, TEG displayed only a single major decomposition stage beginning at 595 °C. The weight loss proceeded rapidly until 818 °C. TEG exhibited almost complete combustion, leaving only 0.12% residue at 1000 °C. The low residual mass of 0.12 % in TEG was oxidized.

### 3.3. Microstructure Analysis of TEG

Optical microscopy was employed to examine the morphological textures and internal structure of the carbon-based particles in real time, owing to its capability for non-destructive imaging (46). Fig. 4 displays the optical images of expandable graphite and TEG at a scale of 200 µm and 400 µm by capturing the surface morphology. The optical microscopy image of expandable graphite, as seen in Fig. 4a, revealed a loosely packed and rough surface texture with irregular flake sizes. The morphology was dense packing with minimal interlayer spacing and blocky particles with distinct boundaries, indicative of unexfoliated graphite. The optical microscopy image of TEG in Fig. 4b showed a notable change in morphology. This structure appeared more delaminated and wrinkled, layered with visible sheet-like features.

The morphology of the synthesized TEG was investigated using SEM at different magnifications to elucidate its morphological characteristics and structural transformations upon direct thermal treatment, as shown in Fig. 5.

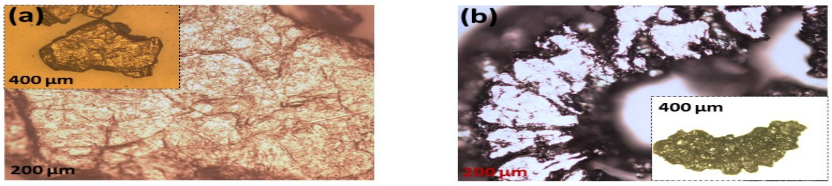

**Figure 4:** Optical microscopy images at 200 µm and 400 µm of (a) expandable graphite and (b) TEG.

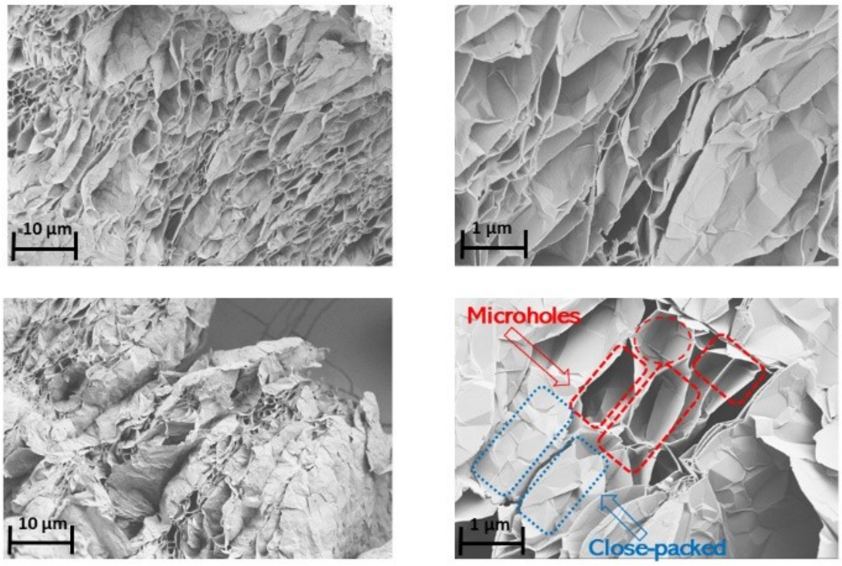

**Figure 5:** SEM images of TEG at two different magnifications (at 10 µm and 1 µm scale bars).

SEM images revealed that expandable graphite consisted of irregularly shaped flake particles with a layered structure (47). TEG was derived from expandable graphite through direct rapid thermal expansion, which simultaneously exfoliated, resulting in a unique microstructure characterized by a highly porous, crumpled morphology. Moreover, TEG exhibited significant morphological changes with a highly crumpled and wrinkled morphology at low magnification (10 µm). The exfoliated sheets were loosely stacked and interconnected, indicative of the violent release of gases such as $CO_2$ during the thermal treatment of expandable graphite, consisting of porous and compacted domains (15). The rapid release of intercalated gases during heating caused the graphite layers to separate and expand, resulting in a worm-like, porous structure (40). The observed morphology confirmed the successful thermal exfoliation of expandable graphite into few-layered graphene oxide sheets with minimal restacking. In addition, at a high magnification (1 µm), the TEG structure displayed thin, wrinkled layers with sharp edges and extensive surface roughness. The structure of TEG was characterized by the formation of microholes, which are indicative of gas release and exfoliation phenomena during thermal treatment. Furthermore, the close-packed regions displayed a compact lamellar arrangement, indicating areas where exfoliation was either incomplete and structurally constrained (48).

### 3.4. Electrical Conductivity Performance of TEG Reinforcement PEEK Composites

The electrical conductivity measurements are critical for confirming the formation of a percolated conductive network by the TEG filler within the PEEK matrix. Furthermore, effective TEG dispersion and interconnectivity contribute significantly to the development of composites suitable for electromagnetic interference (EMI) shielding and flexible structural electronic components (49,50). For this purpose, evaluating the electrical properties of PEEK/TEG composites was critically important, as it directly reflected the influence of the synthesized TEG on the functional performance of the polymer matrix. The incorporation of TEG, synthesized with a high expansion ratio, markedly enhanced the electrical characteristics of the non-conductive PEEK by indicating the development of conductive pathways within the composite.

The electrical performance of PEEK/TEG composites was evaluated by measuring the electrical resistance across samples with two different TEG filler loadings at room temperature. Table S5 presents the electrical properties of PEEK/TEG composites. Neat PEEK exhibited no measurable conductivity, as expected, due to its inherent insulating nature. For the PEEK-5%TEG composite, six resistance measurements were recorded across different sections of the sample, showing values ranging from 343.0 Ω to 508.0 Ω, with an average resistance of 430.83 Ω ± 120.05. The average resistance across both sides of the sample was calculated to be 656.43 Ω·cm, resulting in an electrical conductivity of 0.001523 S/cm. Moreover, PEEK–10% TEG composite demonstrated a more noticeable enhancement in electrical performance. Resistance values across six measured points varied between 117.0 Ω and 420.0 Ω, with an average of 215.50 Ω ± 85.09. The average resistance across both sides was calculated to be 295.78 Ω·cm, corresponding to a significantly improved conductivity of 0.003381 S/cm. Therefore, the overall trend clearly demonstrated that increasing TEG content enhanced electrical conductivity.

Fig. 6a visually highlights how increasing TEG content reduces resistance and enhances conductivity, illustrating the formation of conductive pathways. As TEG content increases, resistance decreases and conductivity improves, indicating the formation of a more continuous conductive network within the polymer matrix. A clear inverse relationship was observed between filler content and electrical resistance, demonstrating that increasing TEG loading promotes the formation of a continuous conductive network. Notably, the PEEK-10%TEG composite exhibited more than double the electrical conductivity compared to the PEEK-5%TEG, suggesting proximity to or attainment of the electrical percolation threshold, as seen in Fig. 6b. This behavior highlighted TEG's effectiveness as a conductive nanofiller and its potential to significantly enhance the functional performance of inherently insulating thermoplastics like PEEK for applications in EMI shielding (51), antistatic materials, and lightweight conductive components (4).

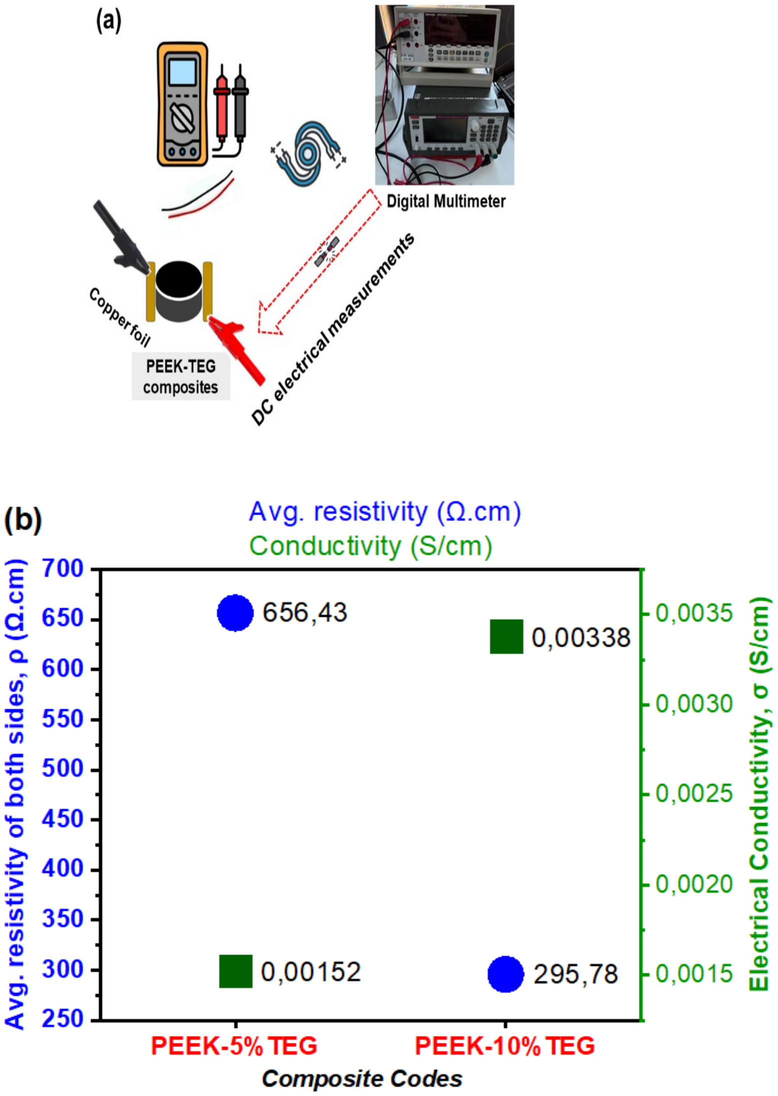

**Figure 6:** (a) Schematic illustration of the electrical conductivity measurement process for PEEK-TEG composites using a digital multimeter and (b) Electrical properties of PEEK/TEG composites at different TEG loadings. The average electrical resistance (Ω·cm) and electrical conductivity (S/m) are shown for PEEK containing 5 wt% and 10 wt% TEG.

### 3.5. Environmental Impact Evaluation of the TEG Production Process by LCA

To understand the energy consumption and environmental impact during the thermal expansion process in TEG synthesis from expandable graphite, LCA studies underscore the importance of specific production conditions such as source of electricity, production scale, and technological efficiency (52,53). The energy input is supplied in the form of electricity, and for industrial-scale batches, the estimated specific energy consumption ranges from 2.5 to 4.0 MJ/kg of expandable graphite (27). LCA analysis provided a comparative study of the environmental impact of selected graphene-based nanomaterials, specifically focusing on their GWP. Research on the GWP of various carbon-based filler materials was evaluated and is summarized in Table 2. Herein, TEG exhibited a GWP of 0.0233 kg $CO_2$-eq/g, which is significantly lower than that of conventional graphene derivatives such as GO (0.210–0.320 kg $CO_2$-eq/g) and rGO (0.586 kg $CO_2$-eq/g). CNTs produced via fluidized-bed CVD also present higher emissions (0.480 kg $CO_2$-eq/g), demonstrating the relatively low environmental impact of TEG compared to widely studied carbon nanomaterials. Even when compared to more environmentally conscious alternatives, such as upcycled GO/talc hybrid materials synthesized via catalytic carbonization, which exhibit a GWP of 0.0329 kg $CO_2$-eq/g. Materials with moderately higher GWP values include carbon fiber (PAN-based, 0.024 kg $CO_2$-eq/g), synthetic graphite (0.0593 kg $CO_2$-eq/g), and black carbon (1.055 kg $CO_2$-eq/g) due to energy-intensive processes and fossil-based precursors. Thus, the influence of production methodology on environmental impact is further evident from the comparison among different carbon sources. For instance, GO synthesized via Hummers' method exhibits a higher GWP by highlighting the substantial contribution of chemical processing and energy consumption. Activated carbon derived from biomass demonstrates a relatively decreased GWP (0.0834 kg $CO_2$-eq/g), illustrating how the choice of feedstock and production route can significantly mitigate environmental impact. On the other hand, producing TEG via thermal expansion of expandable graphite has only a moderate GWP of 0.0233 kg $CO_2$-eq/g and minimizes chemical usage and energy demand, providing a sustainable alternative to traditional carbon-based fillers without compromising material performance for a low environmental footprint in composite applications.

**Table 2:** GWP of carbon-based filler materials (per 1 g) at laboratory scale.

| Material Type | Production Methodology | GWP (kg $CO_2$-eq/g) | Ref. |
|---|---|---|---|
| **TEG** | Direct thermal treatment | 0.0233 | This work |
| **GO** | Brodie and Staundenmaier's methods | 0.2100 | (54,55) |
| | Hummers' Method | 0.3200 | |
| **rGO** | Chemical reduction | 0.5860 | (56) |
| **Upcycled GO/talc hybrid** | Catalytic carbonization | 0.0329 | (57) |
| **CNT** | Fluidized-Bed CVD | 0.4800 | (58) |
| **Black carbon** | Fossil fuel soot | 1.055 | (59) |
| **Activated carbon** | Coal-derived from biomass | 0.0834 | (60) |
| **Carbon fiber (PAN-based)** | Oxidation + carbonization | 0.0240 | (61) |
| **Synthetic graphite** | Conventional graphitization | 0.0593 | (62) |

Fig. S1 provides the Sankey diagram, which has a visual breakdown of the life cycle inventory for the production of 1 kg of TEG, highlighting the relative contributions of inputs to its overall GWP. Fig. S2 illustrates the environmental impact breakdown of TEG in a flow diagram, with a specific focus on GWP contributions and energy input. Table S6 outlines the environmental impact profile of TEG production, highlighting its advantages in process simplicity and the elimination of toxic reducing agents. These results emphasize the need for improved sustainability strategies such as the integration of cleaner energy sources, the adoption of green chemistry principles, and the development of closed-loop systems to reduce the environmental footprint of TEG production and enhance its viability as a functional nanomaterial.

## 4. CONCLUSION

This work establishes a strong foundation for the scalable, chemical-free synthesis of TEG and its integration into high-performance polymer matrices. Beyond proving feasibility, the study provides a framework where structural, functional, and environmental aspects are addressed in a unified manner. This process, which eliminated the need for chemical oxidants and reducing agents, resulted in a lightweight, highly porous material with a remarkable 32-fold volumetric expansion and an ultralow density of 0.0195 g/mL. Morphological analyses further revealed highly crumpled and wrinkled layers with microholes, consistent with gas evolution during exfoliation. For the first time, TEG was incorporated into a PEEK matrix to fabricate electrically conductive composites. At 5 wt% filler content, the PEEK/TEG composite achieved an electrical conductivity of 0.001523 S/cm, while further increasing the TEG loading to 10 wt% resulted in a conductivity of 0.003381 S/cm. This concentration-dependent enhancement demonstrates the effectiveness of TEG as a conductive filler and highlights its strong compatibility with high-performance thermoplastics. The ability of TEG to impart electrical conductivity to an otherwise insulating PEEK matrix underscores its potential as a lightweight and sustainable filler for the development of advanced polymer-based materials. Furthermore, the environmental sustainability of the proposed synthesis approach was assessed through a LCA. The results revealed a moderate global warming potential (GWP) of 0.0233 kg $CO_2$-eq/g, which is considerably lower than that of comparable carbon-based materials, including rGO and CNTs.

Moving forward, designing hybrid TEG-based systems incorporating synergistic nanomaterials could enable percolative networks with superior electrical and thermal transport properties. Such strategies will accelerate the translation of PEEK/TEG composites into advanced engineering applications in aerospace, automotive, and electronics, where lightweight, conductive, and sustainable materials are critically needed.

## 5. CONFLICT OF INTEREST

The authors declare that they have no known competing financial interests or personal relationships that could have appeared to influence the work reported in this paper.

## 6. ACKNOWLEDGMENTS

I would like to extend my heartfelt thanks to Prof. Dr. Burcu Saner Okan from Sabancı University, Faculty of Engineering and Natural Sciences, and Integrated Manufacturing Technologies Research and Application Center & Composite Technologies Center of Excellence for her support in providing access to laboratory facilities. In addition, special thanks to Dr. Havva Başkan Bayrak from the same center for her valuable assistance with the Life Cycle Assessment results. For electrical conductivity measurements, I also extend my sincere thanks to Dr. Mohammad Sajad Sorayani Bafqi from Sabancı University.

## 7. REFERENCES

1. Maruthi N, Faisal M, Raghavendra N. Conducting polymer based composites as efficient EMI shielding materials: A comprehensive review and future prospects. Synth Met [Internet]. 2021 Feb 1;272:116664. Available from: <URL>.

2. Tran V Van, Lee S, Lee D, Le TH. Recent developments and implementations of conductive polymer-based flexible devices in sensing applications. Polymers (Basel) [Internet]. 2022 Sep 7;14(18):3730. Available from: <URL>.

3. Namsheer K, Rout CS. Conducting polymers: A comprehensive review on recent advances in synthesis, properties and applications. RSC Adv [Internet]. 2021 Feb 3;11(10):5659–97. Available from: <URL>.

4. Mokhtari M, Archer E, Bloomfield N, Harkin-Jones E, McIlhagger A. A review of electrically conductive poly(ether ether ketone) materials. Polym Int [Internet]. 2021 Aug 2;70(8):1016–25. Available from: <URL>.

5. Zaccone M, Frache A, Torre L, Armentano I, Monti M. Effect of filler morphology on the electrical and thermal conductivity of PP/carbon-based nanocomposites. J Compos Sci [Internet]. 2021 Jul 23;5(8):196. Available from: <URL>.

6. Mehmood Z, Shah SAA, Omer S, Idrees R, Saeed S. Scalable synthesis of high-quality, reduced graphene oxide with a large C/O ratio and its dispersion in a chemically modified polyimide matrix for electromagnetic interference shielding applications. RSC Adv [Internet]. 2024 Mar 4;14(11):7641–54. Available from: <URL>.

7. Niu Y, Zhang Y, Yao J, Wang H. Improving resistance–strain effects of conductive polymer composites modified by multiscale fillers: Short carbon fiber and carbon nanotube. Polym Compos [Internet]. 2024 May 10;45(7):5839–52. Available from: <URL>.

8. Luo X, Yang G, Schubert DW. Electrically conductive polymer composite containing hybrid graphene nanoplatelets and carbon nanotubes: synergistic effect and tunable conductivity anisotropy. Adv Compos Hybrid Mater [Internet]. 2022 Mar 30;5(1):250–62. Available from: <URL>.

9. Wang H, Qu Q, Wang J, Gao J, Yang J, He Y. Recent advances in the dispersion and interfacial characteristics of carbon nanotubes within polyamide composites. Polym Compos [Internet]. 2025 Jun 20;46(9):7763–84. Available from: <URL>.

10. Saner Okan B. Fabrication of multilayer graphene oxide-reinforced high density polyethylene nanocomposites with enhanced thermal and mechanical properties via thermokinetic mixing. Turkish J Chem [Internet]. 2017 Jan 1;41(3):381–90. Available from: <URL>.

11. Qureshi N, Dhand V, Subhani S, Kumar RS, Raghavan N, Kim S, et al. Exploring conductive filler-embedded polymer nanocomposite for electrical percolation via electromagnetic shielding-based additive manufacturing. Adv Mater Technol [Internet]. 2024 Apr 18;9(17):2400250. Available from: <URL>.

12. Kumuda S, Gandhi U, Mangalanathan U, Rajanna K. Synthesis and characterization of graphene oxide and reduced graphene oxide chemically reduced at different time duration. J Mater Sci Mater Electron [Internet]. 2024 Mar 24;35(9):637. Available from: <URL>.

13. Kausar A. Poly(ether ether ketone) nanocomposites with graphene and derivative nanoreinforcements—contemporary scientific paragon and prospering breakthroughs. Polym Technol Mater [Internet]. 2025 May 3;64(7):973–97. Available from: <URL>.

14. Martínez-Gómez A, Quiles-Díaz S, Enrique-Jimenez P, Flores A, Ania F, Gómez-Fatou MA, et al. Searching for effective compatibilizing agents for the preparation of poly(ether ether ketone)/graphene nanocomposites with enhanced properties. Compos Part A Appl Sci Manuf [Internet]. 2018 Oct 1;113:180–8. Available from: <URL>.

15. Singh SB, De M. Effects of gaseous environments on physicochemical properties of thermally exfoliated graphene oxides for hydrogen storage: a comparative study. J Porous Mater [Internet]. 2021 Jun 5;28(3):875–88. Available from: <URL>.

16. Tuna Genç M, Sarilmaz A, Dogan S, Aksoy Çekceoğlu İ, Ozen A, Aslan E, et al. Thermally-exfoliated graphene oxide/ZnO nanocomposite catalysts for photocatalytic hydrogen evolution and antibacterial activities. Int J Hydrogen Energy [Internet]. 2023 Sep 12;48(78):30407–19. Available from: <URL>.

17. Darabut AM, Lobko Y, Yakovlev Y, Rodríguez MG, Veltruská K, Šmíd B, et al. Influence of thermal treatment on the structure and electrical conductivity of thermally expanded graphite. Adv Powder Technol [Internet]. 2022 Dec 1;33(12):103884. Available from: <URL>.

18. Çalın Ö, Kurt A, Çelik Y. Influence of expansion conditions and precursor flake size on porous structure of expanded graphite. Fullerenes, Nanotub Carbon Nanostructures [Internet]. 2020 Aug 2;28(8):611–20. Available from: <URL>.

19. Bao D, Gao Y, Cui Y, Xu F, Shen X, Geng H, et al. A novel modified expanded graphite/epoxy 3D composite with ultrahigh thermal conductivity. Chem Eng J [Internet]. 2022 Apr 1;433:133519. Available from: <URL>.

20. Son DK, Kim J, Raj MR, Lee G. Elucidating the structural redox behaviors of nanostructured expanded graphite anodes toward fast-charging and high-performance lithium-ion batteries. Carbon N Y [Internet]. 2021 Apr 30;175:187–201. Available from: <URL>.

21. Murugan P, Nagarajan RD, Shetty BH, Govindasamy M, Sundramoorthy AK. Recent trends in the applications of thermally expanded graphite for energy storage and sensors – a review. Nanoscale Adv [Internet]. 2021 Nov 9;3(22):6294–309. Available from: <URL>.

22. Classification P. (12) Patent application publication (10) Pub. No.: US 2009/0054581 A1. Vol. 1. 2009.

23. Tarannum F, Danayat S, Nayal A, Muthaiah R, Annam RS, Garg J. Thermally expanded graphite polyetherimide composite with superior electrical and thermal conductivity. Mater Chem Phys [Internet]. 2023 Apr 1;298:127404. Available from: <URL>.

24. Mohammad H, Stepashkin AA, Laptev AI, Tcherdyntsev V V. Mechanical and conductive behavior of graphite filled polysulfone-based composites. Appl Sci [Internet]. 2022 Dec 30;13(1):542. Available from: <URL>.

25. Goyal RK. Cost-efficient high performance polyetheretherketone/expanded graphite nanocomposites with high conductivity for EMI shielding application. Mater Chem Phys [Internet]. 2013 Oct 15;142(1):195–8. Available from: <URL>.

26. Keyte J, Pancholi K, Njuguna J. Recent developments in graphene oxide/epoxy carbon fiber-reinforced composites. Front Mater [Internet]. 2019 Oct 9;6:471696. Available from: <URL>.

27. Surovtseva D, Crossin E, Pell R, Stamford L. Toward a life cycle inventory for graphite production. J Ind Ecol [Internet]. 2022 Jun 14;26(3):964–79. Available from: <URL>.

28. Engels P, Cerdas F, Dettmer T, Frey C, Hentschel J, Herrmann C, et al. Life cycle assessment of natural graphite production for lithium-ion battery anodes based on industrial primary data. J Clean Prod [Internet]. 2022 Feb 15;336:130474. Available from: <URL>.

29. Rahman MM, Nisar U, Abouimrane A, Belharouak I, Amin R. Valuation of anode materials for high-performance lithium batteries: From graphite to lithium metal and beyond. Electrochem Energy Rev [Internet]. 2025 Dec 31;8(1):14. Available from: <URL>.

30. Canseco V, Anguy Y, Roa JJ, Palomo E. Structural and mechanical characterization of graphite foam/phase change material composites. Carbon N Y [Internet]. 2014 Aug 1;74:266–81. Available from: <URL>.

31. Potts JR, Shankar O, Murali S, Du L, Ruoff RS. Latex and two-roll mill processing of thermally-exfoliated graphite oxide/natural rubber nanocomposites. Compos Sci Technol [Internet]. 2013 Jan 24;74:166–72. Available from: <URL>.

32. Goudarzi R, Hashemi Motlagh G. The effect of graphite intercalated compound particle size and exfoliation temperature on porosity and macromolecular diffusion in expanded graphite. Heliyon [Internet]. 2019 Oct 1;5(10):e02595. Available from: <URL>.

33. Chomkhuntod P, Kornnum S, Arayawate S, Wang B, Iamprasertkun P. Ultra-fast electrochemical expansion for rapid enhancement of graphite paper electrode. ACS Phys Chem Au [Internet]. 2025 Jul 23;5(4):318–26. Available from: <URL>.

34. Kmeťová E, Kačík F, Kubovský I, Kačíková D. Effect of expandable graphite flakes on the flame resistance of oak wood. Coatings [Internet]. 2022 Dec 6;12(12):1908. Available from: <URL>.

35. Lan R, Su W, Li J. Preparation and catalytic performance of expanded graphite for oxidation of organic pollutant. Catalysts [Internet]. 2019 Mar 19;9(3):280. Available from: <URL>.

36. Chi B, Yao Y, Cui S, Jin X. Preparation of graphene oxide coated tetradecanol/expanded graphite composite phase change material for thermal energy storage. Mater Lett [Internet]. 2021 Jan 1;282:128666. Available from: <URL>.

37. Mostovoy AS, Yakovlev A V. Reinforcement of epoxy composites with graphite-graphene structures. Sci Rep [Internet]. 2019 Nov 7;9(1):16246. Available from: <URL>.

38. Cakal Sarac E, Haghighi Poudeh L, Berktas I, Saner Okan B. Scalable fabrication of high-performance graphene/polyamide 66 nanocomposites with controllable surface chemistry by melt compounding. J Appl Polym Sci [Internet]. 2021 Mar 10;138(10):49972. Available from: <URL>.

39. Liu Z, Li G, Cui T, Borodin A, Kuhl C, Endres F. A battery-supercapacitor hybrid device composed of metallic zinc, a biodegradable ionic liquid electrolyte and graphite. J Solid State Electrochem [Internet]. 2018 Jan 16;22(1):91–101. Available from: <URL>.

40. Seyyed Monfared Zanjani J, Saner Okan B, Menceloglu Y. Manufacturing of multilayer graphene oxide/poly(ethylene terephthalate) nanocomposites with tunable crystallinity, chain orientations and thermal transitions. Mater Chem Phys [Internet]. 2016 Jun 15;176:58–67. Available from: <URL>.

41. Pereira Junior AAM, dos Santos FKF, de Almeida Araújo F, Leite-Barbosa OS, Altoé L, Veiga-Junior VF. Chemical and structural analysis of graphene oxide reduced with naringenin: A natural product-based alternative. J Mater Res Technol [Internet]. 2025 Jul 1;37:2850–65. Available from: <URL>.

42. Nuriskasari I, Syahrial AZ, Ivandini TA, Sumboja A, Priyono B, Yan Q, et al. Synthesis of graphitic carbon from empty palm oil fruit bunches through single-step graphitization process using K2FeO4-KOH catalyst as lithium ion battery anode. Results Eng [Internet]. 2024 Dec 1;24:103273. Available from: <URL>.

43. Haghighi Poudeh L, Saner Okan B, Seyyed Monfared Zanjani J, Yildiz M, Menceloglu Y. Design and fabrication of hollow and filled graphene-based polymeric spheres *via* core–shell electrospraying. RSC Adv [Internet]. 2015 Oct 26;5(111):91147–57. Available from: <URL>.

44. Wei Q, Xu L, Tang Z, Xu Z, Xie C, Guo L, et al. High-performance expanded graphite from flake graphite by microwave-assisted chemical intercalation process. J Ind Eng Chem [Internet]. 2023 Jun 25;122:562–72. Available from: <URL>.

45. Bannov AG, Ukhina A V., Maksimovskii EA, Prosanov IY, Shestakov AA, Lapekin NI, et al. Highly porous expanded graphite: Thermal shock vs. programmable heating. Materials (Basel) [Internet]. 2021 Dec 13;14(24):7687. Available from: <URL>.

46. Alzoubi M, Khateeb S, Al-Hallaj S. Modeling of compression curves of phase change graphite composites using Maxwell and Kelvin models. J Compos Mater [Internet]. 2016 Apr 29;50(8):1123–35. Available from: <URL>.

47. Focke WW, Muiambo H, Mhike W, Kruger HJ, Ofosu O. Flexible PVC flame retarded with expandable graphite. Polym Degrad Stab [Internet]. 2014 Feb 1;100(1):63–9. Available from: <URL>.

48. Chen X, Xu X, Yi R, Rao D, Guo J, Zhou Y, et al. Surface functional hybridization of expandable graphite towards enhancing flame retardancy and conductivity of PVA solid electrolytes. Appl Surf Sci [Internet]. 2025 Aug 15;700:163244. Available from: <URL>.

49. D’Aloia AG, Bidsorkhi HC, Tamburrano A, Sarto MS. Graphene-based electromagnetic absorbing textiles for 5G frequency bands. In: 2022 IEEE International Symposium on Electromagnetic Compatibility & Signal/Power Integrity (EMCSI) [Internet]. IEEE; 2022. p. 7–11. Available from: <URL>.

50. Oraby H, Naeem I, Darwish M, Senna MH, Tantawy HR. Electromagnetic interference shielding of thermally exfoliated graphene/polyurethane composite foams. J Appl Polym Sci [Internet]. 2022 Nov 5;139(41):e53008. Available from: <URL>.

51. Nan X, Zhang Y, Shen J, Liang R, Wang J, Jia L, et al. A review of the establishment of effective conductive pathways of conductive polymer composites and advances in electromagnetic shielding. Polymers [Internet]. 2024 Sep 7;16(17):2539. Available from: <URL>.

52. Li J, Wang J, Hao Y, Tan H, Shao B, Zhang C. Global evolution of research on life cycle assessment: A data-driven visualization of collaboration, frontier identification, and future trend. Environ Impact Assess Rev [Internet]. 2026 Jan 1;116:108093. Available from: <URL>.

53. Tahir F, Mabrouk A, Al-Ghamdi SG, Krupa I, Sedlacek T, Abdala A, et al. Sustainability assessment and techno-economic analysis of thermally enhanced polymer tube for multi-effect distillation (MED) technology. Polymers (Basel) [Internet]. 2021 Feb 24;13(5):681. Available from: <URL>.

54. Cossutta M, McKechnie J, Pickering SJ. A comparative LCA of different graphene production routes. Green Chem [Internet]. 2017 Dec 11;19(24):5874–84. Available from: <URL>.

55. Munuera J, Britnell L, Santoro C, Cuéllar-Franca R, Casiraghi C. A review on sustainable production of graphene and related life cycle assessment. 2D Mater [Internet]. 2022 Jan 1;9(1):012002. Available from: <URL>.

56. Serrano-Luján L, Víctor-Román S, Toledo C, Sanahuja-Parejo O, Mansour AE, Abad J, et al. Environmental impact of the production of graphene oxide and reduced graphene oxide. SN Appl Sci [Internet]. 2019 Feb 25;1(2):179. Available from: <URL>.

57. Kocanalı A, Baskan-Bayrak H, Menceloglu Y, Saner Okan B. A selective upcycling approach: Growing 2D and 3D graphene oxide structures with size-controlled talc substrates from waste polypropylene with LCA protocols. J Polym Environ [Internet]. 2023 Sep 24;31(9):4052–68. Available from: <URL>.

58. Teah HY, Sato T, Namiki K, Asaka M, Feng K, Noda S. Life cycle greenhouse gas Emissions of long and pure carbon nanotubes synthesized via on-substrate and fluidized-bed chemical vapor deposition. ACS Sustain Chem Eng [Internet]. 2020 Feb 3;8(4):1730–40. Available from: <URL>.

59. Bond TC, Doherty SJ, Fahey DW, Forster PM, Berntsen T, DeAngelo BJ, et al. Bounding the role of

black carbon in the climate system: A scientific assessment. J Geophys Res Atmos [Internet]. 2013 Jun 16;118(11):5380–552. Available from: <URL>.

60. Vilén A, Laurell P, Vahala R. Comparative life cycle assessment of activated carbon production from various raw materials. J Environ Manage [Internet]. 2022 Dec 15;324:116356. Available from: <URL>.

61. Zhang S, Gan J, Lv J, Shen C, Xu C, Li F. Environmental impacts of carbon fiber production and decarbonization performance in wind turbine blades. J Environ Manage [Internet]. 2024 Feb 1;351:119893. Available from: <URL>.

62. Hubynskyi S, Sybir A, Fedorov S, Usenko A, Hubynskyi M, Vvedenska T. Analysis of changes in global warming potential during enrichment and production of battery-grade graphite using electrothermal fluidized bed technology. IOP Conf Ser Earth Environ Sci [Internet]. 2024 May 1;1348(1):012028. Available from: <URL>.

Yanardag R et al. JOTCSA. 2025; 12(4): 221-234. **RESEARCH ARTICLE**

# The Effects of Thiosemicarbazone-based Oxovanadium (IV) Complex on the Lens and Skin Tissues in Streptozotocin-Induced Diabetic Rats and Computational Studies for the Key Target Proteins of the Lens Tissues

**Refiye Yanardag[1]*, Onur Ertik[2], Tulay Bal Demirci[3], Bahri Ulkuseven[3], Sevim Tunali[1]**

[1]Istanbul University-Cerrahpaşa, Faculty of Engineering, Department of Chemistry, Biochemistry Division, Avcilar, 34320, Istanbul, Türkiye.
[2]Bursa Technical University, Faculty of Engineering and Natural Sciences, Department of Chemistry, Yildirim, 16310, Bursa, Türkiye.
[3]Istanbul University-Cerrahpaşa, Faculty of Engineering, Department of Chemistry, Inorganic Chemistry Division, Avcilar, 34320, Istanbul, Türkiye.

**Abstract:** A vanadium compound, 2,4-dihydroxybenzylidene-N(4)-2-hydroxybenzylidene-S-methyl-isothiosemicarbazidato-oxidovanadium(IV) (VOL), was investigated for its possible benefits in the treatment of diabetes-related symptoms. Male Swiss albino rats aged 3 to 3.5 months were used in the study. The animals were randomly assigned to four groups. Experimental diabetes was induced by a single intraperitoneal injection of streptozotocin (STZ) at a dose of 65 mg/kg. The groups were as follows: Group I – healthy control (no treatment); Group II – healthy control rats administered VOL; Group III – STZ-induced diabetic rats; Group IV – STZ-induced diabetic rats treated with VOL. After diabetes was induced, VOL was administered to the rats in Groups II and IV via gavage at a daily dose of 0.2 mM/kg for 12 consecutive days. Based on biochemical results, in lens and skin tissues, reduced glutathione levels, catalase, and superoxide dismutase activities were increased, whereas lipid peroxidation and non-enzymatic glycosylated levels were decreased in VOL-treated diabetic rats. Besides that, enzyme activities in the polyol pathway decreased in the lens tissues of diabetic animals given VOL. The binding affinities of these two enzymes (AR and SDH) to VOL were also investigated using molecular docking based on the conformational state. The results revealed that the use of VOL can be effective in preventing or at least retarding the development of some diabetic ocular and skin complications.

**Keywords:** Diabetes mellitus, Oxidative stress, Lens tissue, Skin tissue, Vanadium complex.

**Submitted:** July 5, 2025. **Accepted:** October 13, 2025.

**Cite this:** Yanardag R, Ertik O, Bal Demirci T, Ulkuseven B, Tunali S. The Effects of Thiosemicarbazone-based Oxovanadium (IV) Complex on the Lens and Skin Tissues in Streptozotocin-Induced Diabetic Rats and Computational Studies for the Key Target Proteins of the Lens Tissues. JOTCSA. 2025;12(4): 221-34.

**DOI:** https://doi.org/10.18596/jotcsa.1734840

***Corresponding author's E-mail:** yanardag@iuc.edu.tr

## 1. INTRODUCTION

Diabetes mellitus (DM), a condition characterized by high blood sugar levels, is a growing global health problem, with its prevalence expected to reach 12.2% (783.2 million people) by 2045 (1). It is well established today that DM induces increased oxidative stress in various tissues, affecting several metabolic pathways such as glycolytic, hexosamine, polyol pathways, and deactivation of the insulin signaling pathway, as well as enhancing the formation of advanced glycation end products (AGE) and activation of protein kinase C (PKC) (2).

Lens and skin are target tissues in DM that are seriously affected by hyperglycemia. Ocular complications such as cataract formation are common in both types of diabetes. High glucose levels in patients induce oxidative stress, which increases protein oxidation and aggregation in lens cells, thereby resulting in a detrimental effect on lens opacity and the development of cataract (3,4). About 30-70% of diabetic patients encounter skin lesions, fungal and bacterial infections, and non-communicable diseases such as lipid necrosis and granuloma annulare (5-7). Since different biochemical processes are occurring in the skin tissue during the diabetic process, a precise molecular etiology for all diabetic skin conditions has not yet been fully clarified (8). However, it is known that diabetic skin may be one of the first organs to show the first signs of diabetes. In some cases, before diabetes is diagnosed, the wound-healing properties of the skin are insufficient, and high blood sugar levels cause the skin barrier function to deteriorate, making the skin dry (xerosis cutis) and prone to infections (7).

In recent years, numerous studies have focused on the relationship between ultra-trace elements such as copper, iron, zinc, vanadium, and selenium and various diseases, including diabetes (9,10). Among these, vanadium and its various compounds have received special attention as potential therapeutic agents for various conditions, including cancer, atherosclerosis, and diabetes (11). Vanadium compounds are generally divided into three main groups: inorganic vanadium salts (vanadate and vanadyl), peroxovanadium complexes, and organic vanadium compounds. While vanadium can exist in more than one oxidation state, under physiological conditions, the pentavalent form ($VO_3^-$) predominates in extracellular fluids, whereas the tetravalent form ($VO^{2+}$) is more prevalent inside cells (12,13). If vanadium remains in the bloodstream for an extended period, it is distributed and stored in various tissues (2). Vanadium species enter the cell through passive diffusion, utilizing various channels such as phosphate or sulfate, or membrane transporters including citrate, lactate, and organic anion transporters (11,14). In this context, vanadium uptake into cells in the form of ligand complexes is increased (15). The hypoglycemic action of vanadium is due to its insulin-mimetic or insulin-enhancing feature. The biochemistry of vanadium compounds involves glucose uptake, through the inhibition of most phosphatases, stimulation of lipogenesis, and inhibition of lipolysis by modulating several key regulators of lipid metabolism, such as enhancing expression of peroxisome proliferator-activated receptor γ (PPARγ) and the activation of AMP-activated protein kinase (AMPK) (16,17). The insulin-mimicking effect of vanadium is primarily due to its inhibitory action, particularly the nonspecific inhibition of protein tyrosine phosphatase 1B (PTP1B). These types of phosphatases are key negative regulators of insulin signaling, and the inhibition of these enzymes may explain why these compounds could potentially act as hypoglycemic agents (18). Since the anti-hyperglycemic effect of different vanadium compounds has recently drawn attention to the impact of vanadium on Alzheimer's disease, also known as type 3 diabetes (19). Vanadium compounds have been shown to effectively enhance glucose uptake in individuals with diabetes mellitus (DM). Experimental studies suggest that vanadium complexes, initially developed as a vanadate analog for DM treatment, may also play a role in regulating amyloid-beta (Aβ) plaque formation associated with Alzheimer's disease (20,21). Additionally, considering the relationship between DM and COVID-19, and in light of their broad biological activity, vanadium compounds are considered promising candidates for future antiviral therapies targeting SARS-CoV-2 infection (17).

In our study, inspired by the insulin-mimetic effects of vanadium and its derivatives in various diabetic models, we aimed to evaluate the therapeutic effect of the VOL complex we synthesized on DM-induced damage to lens and skin tissues by analyzing various biochemical parameters. Additionally, applying molecular docking of VOL to the two target enzymes in the polyol pathway helped us more clearly to investigate the potential role of this compound in DM.

## 2. EXPERIMENTAL SECTION

### 2.1. Preparation of Starting Material and Complex VOL

The starting material is 2,4-dihydroxybenzaldehyde-S-methyl-isothiosemicarbazone to obtain the title complex. This compound was prepared using the previously mentioned methods (22-24). S-methyl-isothiosemicarbazide (1 mmol) was dissolved in ethanol (50 mL). 2,4-dihydroxybenzaldehyde (1 mmol) was added to the thiosemicarbazide solution and refluxed for 4 hours. The cream-colored precipitate was filtered and washed with ethanol. The melting point of the product obtained in 88% yield was 180-181ºC.

Complex VOL, [2,4-dihydroxybenzylidene-N(4)-2-hydroxybenzylidene-S-methyl-isothiosemicarbazidato-oxidovanadium(IV)], was synthesized from the reaction of the starting material, vanadyl sulphate, and 2-hydroxybenzaldehyde (25). The starting material (1mmol) and 2-hydroxybenzaldehyde (1 mmol) were dissolved in 50 mL of ethanol. The mixture was added to the $VOSO_4.5H_2O$ (1mmol) solution in 25 mL of ethanol in a balloon flask, and the homogeneous solution was allowed to stir for 5 hours at room temperature. The brownish-powder product was filtered, and its structure was confirmed by elemental analysis and IR spectrum (Figure 1). Yield 61%, m.p. > 380 °C. μeff: 1.64 BM. Anal. Calc. for $C_{16}H_{13}N_3O_4SV$ (394.3 g mol−1): Found (calc.): C, 48.73 (48.74); H, 3.28 (3.30); N, 10.68 (10.66); S, 8.04 (8.09). UV-Vis (λ nm in DMSO): 245, 315, 352, 418, 800, 958. IR (ATR, cm−1): ν(OH) 3411, ν(C=N) 1605, 1593, 1578, ν(C−O) 1146-1123, ν(V=O) 985, ν(V-O) 477-434.

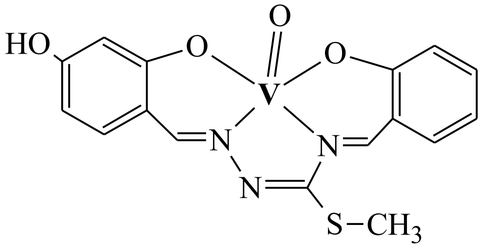

**Figure 1:** 2,4-dihydroxybenzylidene-N (4)-2-hydroxybenzylidene-S-methyl isothiosemicarbazidato-oxidovanadium (IV), [VOL].

### 2.2. Experiment Design and Diabetes Induction

All experimental stages in the study were reviewed and approved by the Istanbul University Animal Care and Use Committee. For that, clinically healthy 3.0–3.5-month-old male Swiss Albino rats were used. The experimental animals were randomly assigned to four groups with the following intraperitoneal (i.p.) injection and oral administration protocols: (1) Control (intact) group (n = 5); (2) Control VOL group, receiving VOL via gavage at a dose of 0.2 mmol/kg/day for 12 days (n = 5); (3) STZ-induced diabetic group, made diabetic through intraperitoneal (i.p.) injection of STZ (n = 6); (4) Diabetic group treated with VOL at the same dose and duration (n = 5). Based on the work of Melchior et al., 3% w/w gum arabic was used in the administration of VOL to the animals (25). On the other hand, induction of experimental diabetes was performed with a freshly prepared solution of STZ dissolved in a cold 0.01 M sodium citrate–hydrochloric acid buffer (pH = 4.5) and applied intraperitoneally with a single dose of 65 mg/kg body weight (26). All rats in the experimental groups developed DM. On the 12th day of the experiment, the animals were fasted overnight and euthanized the following day. All collected lens and skin tissues were immediately frozen and stored at -76℃ until the day of analysis. Fasting blood glucose levels after 18 hours were measured using the method described by Relander and Raiha (1963) (27). Data on blood sugar and weight parameters were previously discussed in our research by Yanardag et al. (2009) (24). A cold saline solution (0.9% NaCl) was employed to prepare 10% (w/v) homogenates for both tissues. Following centrifugation (10,000 g, 4°C, 10 min), the resulting clear supernatant was diluted in appropriate ratios and utilized for all biochemical analyses.

### 2.3. Tissues Non-Enzymatic Oxidative Stress Parameters and Protein Content

The reduced glutathione (GSH) content was measured using the Beutler method, employing Ellman’s reagent (1975) (28). The process measures the SH group reduction capacity, which forms a yellow color with Ellman’s reagent to obtain 5,5’-dithiobis (2-nitrobenzoic acid). Measurements were performed spectrophotometrically at 412 nm, and the results were expressed as nmol GSH/mg protein.

Ledwozyw’s (1986) method was used for lipid peroxidation (LPO) assays (29). Briefly, tissue homogenates treated with thiobarbituric acid are boiled and extracted with *n*-butanol. The obtained colored extracts are measured spectrophotometrically, and the results are expressed as nmol MDA/mg protein.

The thiobarbituric acid method was used to determine lens and skin non-enzymatic glycosylated (NEG) levels (30). Incubating the tissue homogenates with oxalic acid converts the glucose moieties of glycosylated tissue proteins to 5-hydroxymethyl furfural, which is yellow when 2-thiobarbituric acid is added to the reaction medium. The Lowry method was used to measure the tissue homogenates' protein levels, and the results were expressed as nmol fructose/mg protein (31). The activities of the antioxidant enzymes catalase (CAT) and superoxide dismutase (SOD) in lens and skin tissue were determined using the methods of Aebi (1984) (32) and Mylroie et al. (1986) (33).

### 2.4. Lens Tissue Polyol Pathway Enzymes

Hayman and Kinoshita’s (1965) method was used to determine the activity of lens aldose reductase (AR) in the lens tissue (34). After adding phosphate buffer, NADPH, and lens supernatant solutions at appropriate rates, the reaction mixture was started in a sample cuvette by adding DL-glyceraldehyde as a substrate. The final volume was obtained as 1 mL with a pH of 6.2. A double-beam spectrophotometer was used to record absorbance (ΔA) changes at 340 nm for 3 min at 30-second intervals. AR activity was expressed as ΔA/min/g protein. The activity of sorbitol dehydrogenase (SDH) was measured using the method described by Barretto and Beutler (1975) (35). The reaction mixture was prepared by adding 1M Tris (pH 8.0), 50 mM $NAD^+$, 100 mM $MgCl_2$, and diluted lens tissue homogenate. The final volume was made 1 mL with the addition of distilled water. After incubating the mixture at 37°C for 10 minutes, the reaction was initiated by adding a 200 mM sorbitol solution. The increase in absorbance was recorded at 340 nm for 4 minutes at 60-second intervals, and enzyme activity was expressed as U/g protein.

### 2.5. Results Analysis

The unpaired t-test and analysis of variance (ANOVA) were used to analyze the biochemical results, which were calculated using the NCSS statistical software package. Results were expressed as mean ± SD, with $p < 0.05$ considered statistically significant.

### 2.6. Computational Studies

Theoretical calculations for the investigated VOL were performed using the Gaussian 09 program package, applying the density functional theory (DFT) method with the hybrid B3LYP functional and the LANL2DZ basis set (36). For this purpose, the three-dimensional structure of the VOL complex was first drawn using the Avagadro program and then saved in mol2 format. Next, the DFT-based B3LYP method with the standard LANL2DZ basis set was employed to optimize the geometry of the VOL fully. The representations and contributions of the highest occupied molecular orbital (HOMO) and the lowest unoccupied molecular orbital (LUMO) were also calculated. The orbital density distributions of HOMO and LUMO, as well as the molecular electrostatic potential (MEP), were visualized and plotted using GaussView 5.0.

### 2.7. Computational Studies

A molecular docking process was performed for AR and SDH, which are target enzymes in diabetes and lens tissue. Two steps were made for this preparation: i) preparation of proteins and ii) preparation of ligands. In the preparation of proteins, the three-dimensional structures of AR (PDB ID: 1IEI) and SDH (PDB ID: 1PL6) were downloaded from the Protein Data Bank site as PDB files. Molecules other than water and amino acids were deleted, polar hydrogens were added and saved in PDB format to make docking ready (37,38). The structure of the VOL was optimized based on the B3LYP/LANL2D theory using Gaussian 09, and the most stable structure was chosen for docking calculations. In order to understand the inhibitory effect of Complex VOL on target proteins, inhibitor molecules found in AR and SDH structures (Zenarestat - PubChem CID: 5724 and 4-[2-(hydroxymethyl)pyrimidin-4-yl]-N, N-dimethylpiperazine-1-sulfonamide - PubChem CID: 132302, respectively) were re-docked, and it was aimed to compare VOL with standard molecules. For this purpose, standard molecules downloaded from the PubChem site were re-docked by energy minimization using Universal Force Field (UFF) (39). After preparation of proteins and ligands, docking for target proteins was performed using the AMDock program with Autodock 4.2 (40). For AR, X: -6.8, Y: -1.4, Z: 9.3, and for SDH, X: -94.3, Y: 38.3, Z: 33.9, a grid box was determined, and the grid size was entered as 25x25x25—the 3D and 2D interaction of ligands and protein was monitored by using Dassault Systèmes Discovery Studio, 2021.

### 2.8. The Root Mean Square Fluctuation (RMSF) Analysis

Following the identification of the protein-ligand interaction, the stability of the protein-ligand complex was assessed in this work using the CABS-fex 2.0 server and displayed using RMSF (http://biocomp.chem.uw.edu.pl/CABSflex2/index) (41,42).

## 3. RESULTS AND DISCUSSION

### 3.1. Synthesis, UV-Vis, and IR spectroscopy

Complex VOL was gained from the thiosemicarbazone and aldehyde by the template effect of oxovanadium (II) ion. The IR spectrum monitored the formation of the complex. The disappearance of bands attributed to the 2-OH and NH2 groups observed in the starting material and the emergence of bands related to the V=O and V-O vibrations were evidence of the formation of the structure of VOL (25). The imine groups of the starting material were observed at 1608 and 1585 cm$^{-1}$, and the hydroxyl group at 3495 cm-1. Infrared spectrum of VOL showed bands at 1605, 1593, 1578 cm$^{-1}$ attributed to C=N1 and N4=C bands, and in the spectrum of VOL, the stretching and bending bands at 3445, 3337, and 1624 cm$^{-1}$ of amine group disappeared while new bands at 985, 477-434 cm$^{-1}$ assigned to V=O and V-O groups were observed. The UV-Vis spectrum of the VOL complex showed the charge transfer bands at 245, 315, and 352 nm assigned to $\pi \rightarrow \pi^*$ and $n \rightarrow \pi^*$, d-d bands at 418, 800, and 958 nm (25).

The structure and purity of VOL were verified by elemental analysis and thin-layer chromatography (TLC) for the biological tests. The stability of VOL in the gum Arabic solution (the biological medium used in this study) and in a polar solvent (a 1:1 water-DMSO mixture) was investigated by monitoring its UV-Vis spectrum. The absorption and λmax values remained unchanged over a period of 20 days.

### 3.2. VOL Effect on Body Weight and Fasting Blood Glucose Levels of the Experimental Rats

Fasting blood sugar and weight values of the animals used in the study were published in our previous research (24). Here, the weight loss observed in diabetic rats was significantly prevented by VOL treatment administered on days 1, 6, and 12. Similarly, it was found that the increase in blood glucose levels caused by STZ administration was reduced through oral VOL treatment (24).

### 3.3. VOL Effect on Non-Enzymatic Oxidative Stress Parameters Content in the Lens and Skin Tissues of the Experimental Rats

GSH level in diabetic lens tissues was significantly reduced ($p < 0.001$) compared to control rats (Table 1). Significant differences in skin GSH levels were also found among the diabetic and control groups ($p < 0.001$) (Table 2). VOL application to the hyperglycemic rats resulted in a mean increase in the GSH level of both lens and skin tissues in comparison to STZ-induced animals ($p < 0.0001$; $p < 0.0001$) (Table 1; Table 2).

The LPO levels in the lens and skin tissues of the diabetic groups were significantly higher than those of the non-treated control rats ($p < 0.05$; $p < 0.0001$) (Table 1; Table 2). After vanadyl complex administration to diabetic animals, tissue LPO levels significantly decreased compared to untreated diabetic animals ($p < 0.05$; $p < 0.05$) (Table 1; Table 2).

**Table 1:** Lens tissue GSH, LPO, and NEG levels for all groups*.

| **Group** | **GSH (nmol GSH/mg protein)** | **LPO (nmol MDA/mg protein** | **NEG (nmol Fructose/mgprotein)** |
|---|---|---|---|
| **Control** | 12.0 ± 1.8 | 0.5 ± 0.2 | 6.8 ± 0.5 |
| **Control + VOL** | 7.0 ± 1.0 | 0.6 ± 0.1 | 8.8 ± 1.4 |
| **Diabetic** | 4.6 ± 0.4[a] | 0.8 ± 0.2[c] | 49.0 ± 3.8[e] |
| **Diabetic + VOL** | 8.7 ± 1.1[b] | 0.4 ± 0.2[d] | 30.8 ± 7.4[f] |
| **$P_{ANOVA}$** | 0.0001 | 0.005 | 0.0001 |

*Mean ± SD

[a] $p < 0.001$ vs control

[b] $p < 0.0001$vs diabetic group

[c] $p < 0.05$ vs control

[d] $p < 0.05$ vs diabetic group

[e] $p < 0.0001$ vs control

[f] $p < 0.001$ vs diabetic group

**Table 2:** Skin tissue GSH, LPO, and NEG levels for all groups*.

| **Group** | **GSH (nmol GSH/mg protein)** | **LPO (nmol MDA/mg protein)** | **NEG (nmol Fructose/ mg protein)** |
|---|---|---|---|
| **Control** | 19.5 ± 1.1 | 1.4 ± 0.6 | 19.2 ± 2.3 |
| **Control + VOL** | 47.1 ± 7.8 | 1.6 ± 0.1 | 24.6 ± 2.0 |
| **Diabetic** | 12.2 ± 2.5[a] | 2.1 ± 0.1[a] | 35.5 ± 3.7[d] |
| **Diabetic + VOL** | 34.4 ± 1.7[b] | 1.5 ± 0.2[c] | 21.7 ± 3.4[e] |
| **$P_{ANOVA}$** | 0.0001 | 0.076 | 0.0001 |

*Mean ± SD

[a] $p < 0.05$ versus control

[b] $p < 0.0001$ versus the diabetic group

[c] $p < 0.05$ versus the diabetic group

[d] $p < 0.0001$ versus control

[e] $p < 0.001$ versus the diabetic group

A significant increase in the NEG levels was observed in both tissues of diabetic rats in comparison of control group animals ($p < 0.0001$; $p < 0.0001$), whereas in the diabetic group given VOL, this parameter in the same tissues declined significantly in comparison to hyperglycemic group, respectively ($p < 0.001$; $p < 0.001$) (Table 1; Table 2).

### 3.4. VOL Effects on Enzymatic Oxidative Stress Parameters in the Lens and Skin Tissues of Experimental Rats

The activities of CAT in the diabetic lens and skin tissues are lower than those of non-diabetic rats; the differences were statistically significant ($p < 0.001$; $p < 0.0001$) (Table 3; Table 4). After VOL treatment in diabetic rats, catalase (CAT) activity in both tissues showed a statistically significant increase compared to untreated diabetic animals ($p < 0.005$; $p < 0.0001$) (Table 3; Table 4). On the other hand, lens and skin SOD activities were significantly reduced in the diabetic group compared to the non-treated animals ($p < 0.05$; $p < 0.05$) (Table 3; Table 4). Treatment with VOL for 12 days caused an elevation of the SOD activities in diabetic lens and skin tissues ($p < 0.05$; $p < 0.05$) (Table 3; Table 4).

**Table 3:** Lens tissue CAT and SOD activities for all groups *.

| **Group** | **CAT (U/mg protein)** | **SOD (U/mg protein)** |
|---|---|---|
| **Control** | 101.3 ± 3.8 | 1.6 ± 0.1 |
| **Control + VOL** | 106.3 ± 7.8 | 0.7 ± 0.3 |
| **Diabetic** | 85.8 ± 3.6[a] | 1.4 ± 0.1[c] |
| **Diabetic + VOL** | 93.7 ± 3.1[b] | 2.3 ± 0.1[d] |
| **$P_{ANOVA}$** | 0.0001 | 0.001 |

*Mean ± SD

[a] $p < 0.001$ versus control

[b] $p < 0.005$ versus the diabetic group

[c] $p < 0.05$ versus control

[d] $p < 0.05$ versus the diabetic group

**Table 4:** Skin tissue CAT and SOD activities for all groups*.

| Group | CAT (U/mg protein) | SOD (U/mg protein) |
|---|---|---|
| **Control** | 2.3 ± 0.5 | 5.1 ± 0.8 |
| **Control + VOL** | 0.8 ± 0.1 | 5.9 ± 0.4 |
| **Diabetic** | 0.5 ± 0.1[a] | 3.4 ± 0.1[c] |
| **Diabetic + VOL** | 0.8 ± 0.1[b] | 4.6 ± 0.5[d] |
| **P<sub>ANOVA</sub>** | 0.0001 | 0.006 |

*Mean ± SD

[a]p < 0.0001 versus the control

[b]p < 0.0001 versus the diabetic group

[c]p < 0.05 versus the control group

[d]p < 0.05 versus the diabetic group

### 3.5. VOL Effect on Polyol Pathway Enzymes in the Lens Tissue of the Experimental Rats

There was a significant increase in the activities of the enzymes AR and SDH in the lens tissue of the diabetic rats in comparison with the control non-treated rats ($p < 0.0001$; $p < 0.002$). In the diabetic animals given VOL, the polyol pathway enzyme activities were significantly restored in comparison with the diabetic group without any treatment ($p < 0.0001$; $p < 0.003$) (Table 5).

**Table 5:** Lens tissue AR and SDH activities for all groups*.

| Group | AR (U/g protein) | SDH (U/g protein) |
|---|---|---|
| **Control** | 2.9 ± 0.5 | 0.7 ± 0.1 |
| **Control + VOL** | 4.3 ± 0.7 | 1.3 ± 0.6 |
| **Diabetic** | 8.1 ± 1.4[a] | 14.1 ± 0.9[c] |
| **Diabetic + VOL** | 2.3 ± 0.8[b] | 1.6 ± 0.1[d] |
| **P<sub>ANOVA</sub>** | 0.0001 | 0.020 |

*Mean ± SD

[a]p < 0.0001 versus the control

[b]p < 0.0001 versus the diabetic group

[c]p < 0.002 versus control

[d]p < 0.003 versus the diabetic group

### 3.6. Computational Studies

A small Eg ($E_g = E_{LUMO} - E_{HOMO}$) value reflects the reactivity of the complexes, which leads to softness. In contrast, a wide energy gap between HOMO and LUMO complicates electron transfer, resulting in hard compounds (43). The HOMO and LUMO values calculated for VOL were found to be -0.15045 and -0.10921 eV, respectively, and the Eg value was calculated as 0.04124 eV (Figure 2A). The molecular electrostatic potential (MEP) contributes to understanding molecular reactivity, charge distribution, and the locations of electrophilic and nucleophilic assaults in the molecule (44). The red hue represents the largest negative area chosen for electrophilic assault, whereas the blue color represents the positive region preferred for nucleophilic reaction for the VOL (Figure 2B).

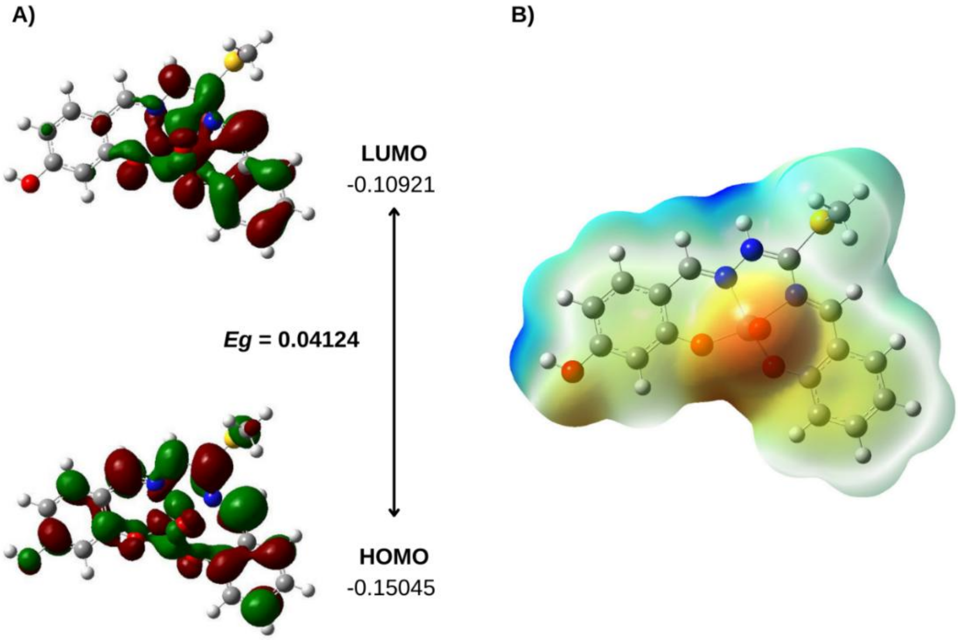

**Figure 2:** A) HOMO-LUMO representation and B) molecular electrostatic potential (MEP) analysis of the VOL.

### 3.7. Molecular Docking Studies

In the *in-vivo* studies, molecular docking was applied to understand whether VOL has potential inhibitory properties for AR and SDH, parameters whose activities decrease when VOL treatment is used, and the binding scores of each target protein are given in Table 6. It was found that the standard molecule Zenarestat (-10.17 kcal/mol) and VOL (-10.04 kcal/mol) had close binding affinities for AR, while for SDH, it was found to have higher binding affinities than the standard molecule (-6.18 kcal/mol) (-7.54 kcal/mol).

**Table 6:** Molecular docking results of the VOL and standards to the target proteins (AR and SDH).

| | AR | | SDH | |
|---|---|---|---|---|
| **Compounds** | **Docking Scores** (kcal/mol) | **Estimated $K_i$** (nM) | **Docking Scores** (kcal/mol) | **Estimated $K_i$** (nM) |
| **VOL** | -10.04 | 43.72 | -7.54 | 2.97 |
| **Zenarestat** | -10.17 | 35.10 | - | - |
| **4-[2-(hydroxymethyl)pyrimidin-4-yl]-N,N-dimethylpiperazine-1-sulfonamide** | - | - | -6.18 | 29.51 |

The 3D and 2D protein-ligand interactions of the interactions of target proteins with VOL and standard molecules are presented in Figure 3. For AR, VAL47, TYR48, TRP111, and CYS298, residues are seen to be molecules that interact in common for both VOL and the standard molecules. However, differences in the interaction with VOL and the standard molecule were detected for TRP111 and CYS298 residues. While hydrogen bonds were observed between these residues and the standard molecule, these interactions were found to be hydrophobic interactions for VOL. When detailed protein-ligand interactions were examined for SDH, it was seen that the interactions were different except for ILE183 and ARG298 residues. While VOL had hydrophobic interactions for ILE183 and ARG298 residues, it was found that the standard molecule formed hydrophobic bonds with ILE183 and hydrogen bonds with ARG298. It can be suggested that these hydrophobic interactions of VOL may have affected the stability of the protein-ligand complexes and resulted in better docking results.

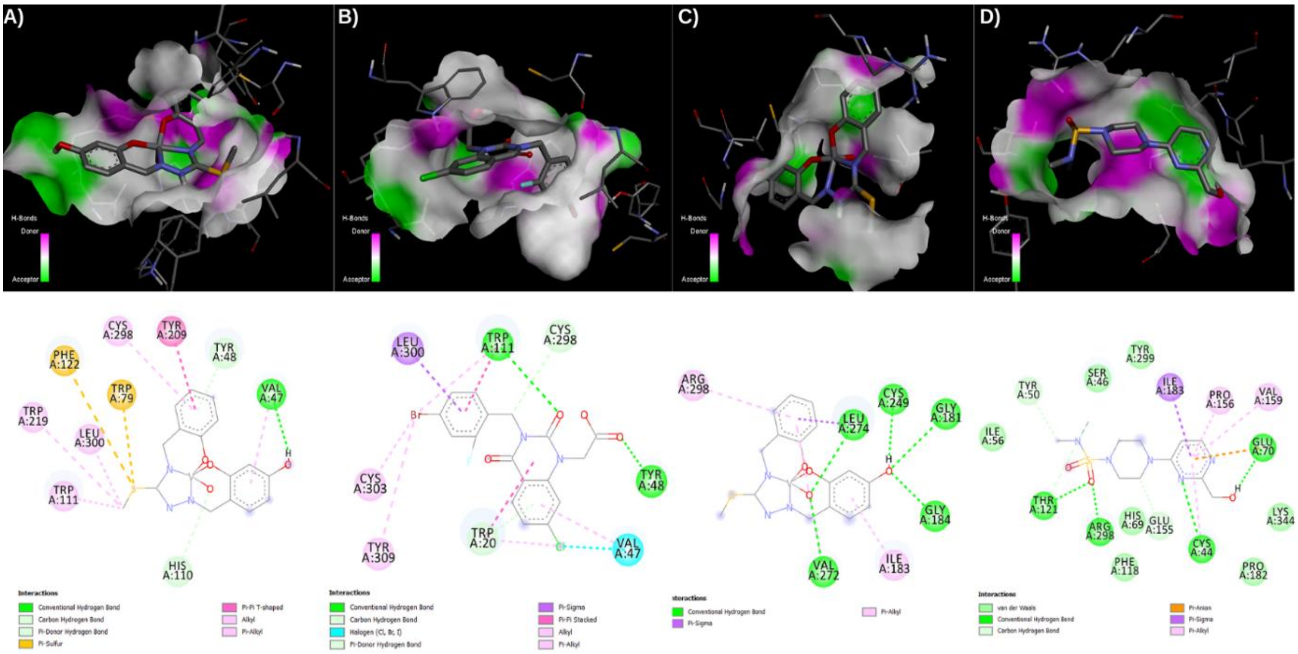

**Figure 3:** The 3D and 2D protein-ligand interactions with the target proteins. A) AR-VOL, B) AR-standard, C) SDH-VOL, D) SDH-standard complexes, respectively.

### 3.8. The Root Mean Square Fluctuation (RMSF) Analysis

RMSF, in terms of protein-ligand interactions, represents the average deviation or volatility of individual atoms in a molecule from their mean location over time.

RMSF is frequently employed in protein-ligand interactions to investigate the flexibility or dynamic behavior of a protein and its ligand complex during molecular dynamics simulations. RMSF offers information on whether parts of the protein or ligand are more flexible or stiff during the simulation. High RMSF values imply more flexibility, whilst low values indicate higher stiffness. This allows for a better understanding of the interactions between ligands and proteins (45).

The RMSF analysis graph and multimodal superimposed simulated structure of AR and ligand complexes are shown in Figure 4. It was observed that VOL increased the RMSF values in some regions and decreased them in other areas. When the RMSF averages were taken for AR, AR-VOL, and AR-STD, it was determined that they were 0.793±0.554, 0.841±0.656, and 0.838±0.573 Å, respectively.

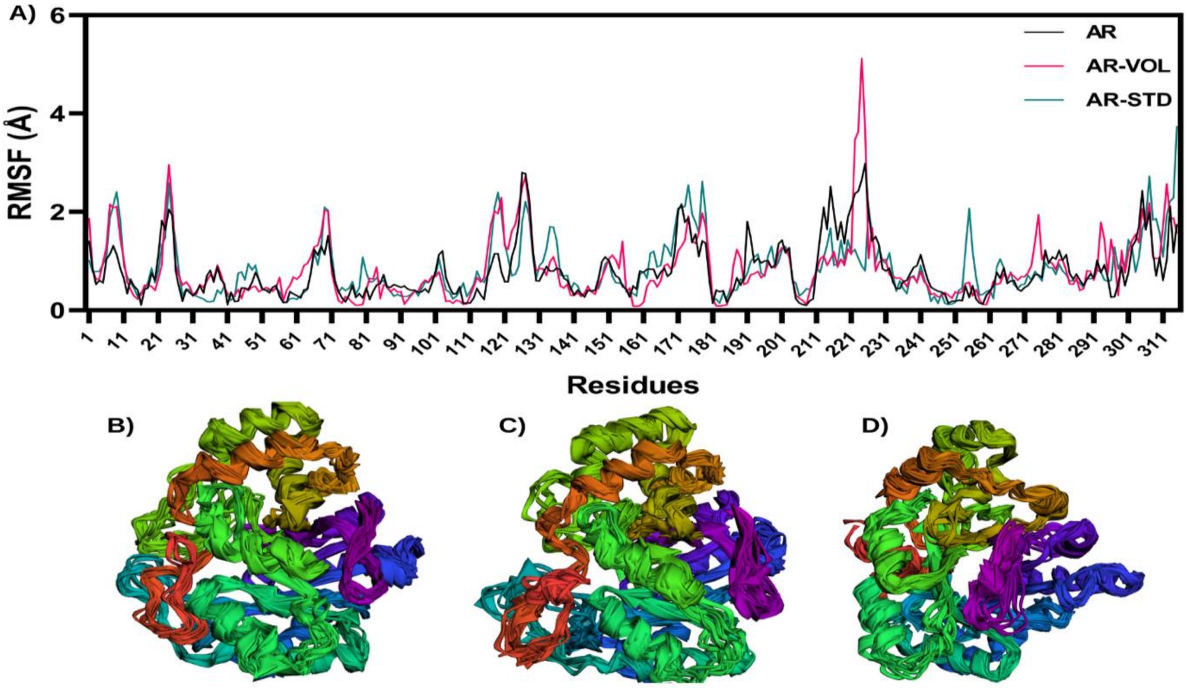

**Figure 4:** (A) The RMSF analysis of the protein-ligand complexes for AR and multimodel superimposed simulated structure of (B) AR, (C) AR-VOL, (D) AR-STD.

Diabetes mellitus (DM) is a chronic metabolic disorder marked by high blood glucose levels, which occur due to either insulin resistance or impaired insulin secretion. Failure of diabetic therapy to regulate abnormal glycemic control may enhance the risk of macrovascular and microvascular complications, such as diabetic foot, skin tissue, and retinopathy (46-48). Oxidative stress, occurring in the hyperglycemic organism, affects all systems with different mechanisms (49-52).

Studies have indicated that oxidative stress is a crucial factor in the development and progression of diabetes, contributing to pancreatic beta-cell dysfunction, insulin resistance, and various diabetic complications. Therefore, targeting oxidative stress has emerged as a promising therapeutic strategy for managing diabetes and its complications (48).

However, the proposed mechanism for vanadium compounds as an insulin mimic agent is that they enhance the activity of protein kinases in the insulin signal cascade. Also, several studies showed that some vanadium compounds protected beta cells by enhancing phosphorylation of a series of proteins in STZ-induced diabetic mice (53-58). A notable aspect during glucose regulation in the body is the recovery of glycogen synthesis, increased glucose uptake, and improved utilization. This has been observed in studies conducted on type 1 diabetes models treated with vanadium. It has been reported that significant increases in GLUT-4 expression result in improved insulin signaling pathways, leading to increased muscle and cardiac glycogen (59). These effects have led to an expansion in the use of metallotherapeutics today.

In the present study, besides the decreased GSH level, we observed increased LPO and advanced glycosylated end products (AGEs) content in the diabetic animals' lens and skin tissues. The increased polyol pathway enzyme activities and ROS production were also observed in the lens tissue. The decrease in GSH level in the diabetic lens and skin tissues increases the susceptibility to oxidative stress and the detoxification of $H_2O_2$ (60). The rise in MDA levels and NEG content in the studied two tissues of hyperglycemic animals, as compared to the control group, indicates both enhanced lipid peroxidation and protein oxidation (46,61). The elevated production of lipid peroxides in diabetes compromises the structural integrity of the lens tissue membrane, resulting in the inhibition of various membrane-bound enzymes. Additionally, lipid peroxidation is thought to contribute to the dysfunction of endothelial cells, changes in keratinocyte capillary permeability, and disturbances in fibroblast and collagen metabolism in skin tissue (62).

NEG is one of the post-translational modifications that negatively affect the structure and functions of proteins by cross-linking and aggregation in DM. In the hyperglycemic state, NEG also activates abnormal cellular signaling and transcription factors, as well as modifies gene expression profiles. AGEs are metabolic products that accumulate as a result of the NEG reaction (63). These effects of diabetes have drawn attention towards antioxidants and special metal-chelating compounds having anti-glycation activities, such as the administration of the VOL complex, which has cellular antioxidant properties. Besides that, our findings also support previous research on diabetic lenses and skin tissues (46,47,64-67).

The high production of ROS plays a key role in the initiation and progression of diabetic retinopathy and chronic hyperglycemia. The activation of secondary pathways triggered by hyperglycemic conditions leads to the formation of more ROS species, as well as to the reduction of antioxidant enzymes, thus further increasing damage (68-70). CAT and SOD, the main endogenous antioxidant enzymes, are responsible for protecting tissues from oxidative damage. They convert superoxide ions into hydrogen peroxide and then hydrogen peroxide to non-toxic peroxide compounds (71). More clearly, SOD converts the superoxide anion into $H_2O_2$ and $O_2$, while CAT detoxifies $H_2O_2$ (72). The increased production of $H_2O_2$ and $O_2^-$, resulting from the auto-oxidation caused by elevated glucose levels in the organism and the non-enzymatic glycation of proteins, leads to a decrease in the activities of the CAT and SOD enzymes (73,74). These enzyme activities can be partially inactivated by hydroxyl radicals and $H_2O_2$, as reported previously by Hodgson et al. (1975) and Pigeolet et al. (1990) (75,76). The reduced activities of SOD and CAT may result from the increased production of $H_2O_2$ and $O_2^-$, which occurs due to the auto-oxidation of excess glucose and the non-enzymatic glycation of proteins (77). We determined this from the significant increase in the activities of progression oxidative stress marker enzymes in diabetic lens and skin tissues treated with VOL. The ameliorated antioxidant defence system, in both tissues studied in our research, has been considered to be via the antioxidant capacity of oxovanadium complex. In fact, vanadium complexes are promising compounds due to their antidiabetic properties, as well as their antioxidant effect (78-80). Reports by Pranczk (2015) indicate that oxovanadium (IV) complex with iminodiacetate was found to scavenge superoxide free radicals ($O_2^{\cdot -}$) and organic radicals such as ABTS$^+$ and DPPH$^+$ (81). We observed a significant increase in the activities of progression oxidative stress marker enzymes in the lens and skin tissues of diabetic animals treated with VOL. Therefore, controlling the balance between oxidants/antioxidant status can be an effective strategy for attenuating the damage caused by diabetic retinopathy and dermopathy.

The polyol pathway has a major role in the development of opacity in the diabetic rat lenses (82). Increased AR activity under hyperglycemic conditions results in a reduction of NADPH rate, leading to a significant decrease in GSH concentration. The cellular antioxidant capacity is diminished by AR activity during hyperglycemia. The concurrent high activity of the SDH enzyme (excessive conversion of sorbitol to fructose) is among the causes of oxidative stress in lens tissue. Since the co-factor NAD$^+$ is reduced to NADH in this reaction, NADH causes the formation of ROS species, which are also considered as a starting molecule of NADH oxidase (83). The fructose produced from glucose in this pathway generates two metabolites (fructose-3-phosphate and 3-deoxyglucosone), which are more powerful non-enzymatic glycation agents than glucose. Therefore, the increased AGE formation is a result of glucose flux through the polyol pathway (1). The glucose flux-induced polyol pathway also causes tissue damage via sorbitol-induced osmotic stress. These osmatic changes also lead to degeneration of hydrophobic lens fibers, collapse and liquefaction of lens fibers, and consequently lens opacities and formation of diabetic cataracts (84,85). In the present study, we noted an increase in AR and SDH activities in hyperglycemic lens tissues. The decreased activities of these enzymes were observed upon treatment with vanadyl complex. This may be due to vanadium's insulin mimetic behavior, which provided a controlled normoglycemic state in the diabetic animals, and also the effective restoration of AR and SDH in the lens tissue (55,67).

As a result of *in vivo studies obtained for lens tissue, it was observed that AR and SDH target proteins increased in the diabetes group,* and VOL treatment reversed this increase, suggesting that VOL may be an inhibitor molecule for these target proteins. Therefore, computer-aided analyses, which have been included in studies in recent years, were performed to understand this situation. The binding affinities of VOL and target proteins were compared with molecular docking, and high binding affinities were found for both target proteins. In addition, DFT analyses made structural analysis possible for VOL. As a result, it was revealed that VOL is a potential inhibitor candidate for AR and SDH, which are target proteins for lens tissue in diabetes, especially in understanding the *in vivo* effects.

## 4. CONCLUSION

Diabetes is a complicated metabolic disorder that contributes to the progression of oxidative stress. In the study, we observed that oxidative stress caused deterioration of the physiology of the lens and skin tissues. Complex VOL conspicuously restored the integrity of lens and skin tissues via antioxidant and antihyperglycemic properties. It improved the tissues' metabolism by reducing oxidative stress in addition to DM therapy—the study gave promising results that require further research on DM therapy, both in vivo and in silico. By study, VOL is now an ingredient candidate for antidiabetic formulations. Moreover, it has been seen that the investigation of such thiosemicarbazone-based vanadium compounds is an important strategy in the development of drugs.

## 5. CONFLICT OF INTEREST

The authors declare that they have no conflict of interest.

## 6. ACKNOWLEDGMENTS

Research Fund of Istanbul University financed this study (Project No: BYP/3864 and Project No: BYP/37135).

## 7. REFERENCES

1. Geng X, Li Z, Yang Y. Emerging role of epitranscriptomics in diabetes mellitus and its complications. Front Endocrinol (Lausanne) [Internet]. 2022 May 27;13:907060. Available from: <URL>.

2. Darenskaya MA, Kolesnikova LI, Kolesnikov SI. Oxidative stress: Pathogenetic role in diabetes mellitus and its complications and therapeutic approaches to correction. Bull Exp Biol Med [Internet]. 2021 May 26;171(2):179–89. Available from: <URL>.

3. Gong W, Zhu G, Li J, Yang X. LncRNA MALAT1 promotes the apoptosis and oxidative stress of human lens epithelial cells via p38MAPK pathway in diabetic cataract. Diabetes Res Clin Pract [Internet]. 2018 Oct;144:314–21. Available from: <URL>.

4. Jain AK, Lim G, Langford M, Jain SK. Effect of high-glucose levels on protein oxidation in cultured lens cells, and in crystalline and albumin solution and its inhibition by vitamin B6 and N-acetylcysteine: Its possible relevance to cataract formation in diabetes. Free Radic Biol Med [Internet]. 2002 Dec;33(12):1615–21. Available from: <URL>.

5. Wan X, Gen F, Sheng Y, Ou M, Wang F, Peng T, et al. Meta-analysis of the effect of kangfuxin liquid on diabetic patients with skin ulcers. Chung YC, editor. Evidence-Based Complement Altern Med [Internet]. 2021 Jun 3;2021:1334255. Available from: <URL>.

6. Cheng B, Jiang Y, Fu X, Hao D, Liu H, Liu Y, et al. Epidemiological characteristics and clinical analyses of chronic cutaneous wounds of inpatients in China: Prevention and control. Wound Repair Regen [Internet]. 2020 Sep 25;28(5):623–30. Available from: <URL>.

7. Andrade TAM, Masson-Meyers DS, Caetano GF, Terra VA, Ovidio PP, Jordão-Júnior AA, et al. Skin changes in streptozotocin-induced diabetic rats. Biochem Biophys Res Commun [Internet]. 2017 Sep;490(4):1154–61. Available from: <URL>.

8. Makrantonaki E, Jiang D, Hossini AM, Nikolakis G, Wlaschek M, Scharffetter-Kochanek K, et al. Diabetes mellitus and the skin. Rev Endocr Metab Disord [Internet]. 2016 Sep 19;17(3):269–82. Available from: <URL>.

9. MW Hasanato R. Trace elements in type 2 diabetes mellitus and their association with glycemic control. Afr Health Sci [Internet]. 2020 Apr 20;20(1):287–93. Available from: <URL>.

10. Cancarini A, Fostinelli J, Napoli L, Gilberti ME, Apostoli P, Semeraro F. Trace elements and diabetes: Assessment of levels in tears and serum. Exp Eye Res [Internet]. 2017 Jan;154:47–52. Available from: <URL>.

11. Treviño S, Díaz A, Sánchez-Lara E, Sanchez-Gaytan BL, Perez-Aguilar JM, González-Vergara E. Vanadium in biological action: Chemical, pharmacological aspects, and metabolic implications in diabetes mellitus. Biol Trace Elem Res [Internet]. 2019 Mar 22;188(1):68–98. Available from: <URL>.

12. Tripathi D, Mani V, Pal RP. Vanadium in biosphere and its role in biological processes. Biol Trace Elem Res [Internet]. 2018 Nov 9;186(1):52–67. Available from: <URL>.

13. Harland BF, Harden-Williams BA. Is vanadium of human nutritional importance yet? J Am Diet Assoc [Internet]. 1994 Aug;94(8):891–4. Available from: <URL>.

14. Ścibior A, Pietrzyk Ł, Plewa Z, Skiba A. Vanadium: Risks and possible benefits in the light of a comprehensive overview of its pharmacotoxicological mechanisms and multi-applications with a summary of further research trends. J Trace Elem Med Biol [Internet]. 2020 Sep;61:126508. Available from: <URL>.

15. Lima LMA, Belian MF, Silva WE, Postal K, Kostenkova K, Crans DC, et al. Vanadium(IV)-diamine complex with hypoglycemic activity and a reduction in testicular atrophy. J Inorg Biochem [Internet]. 2021 Mar;216:111312. Available from: <URL>.

16. Irving E, Stoker A. Vanadium compounds as PTP inhibitors. Molecules [Internet]. 2017 Dec 19;22(12):2269. Available from: <URL>.

17. Semiz S. Vanadium as potential therapeutic agent for COVID-19: A focus on its antiviral, antiinflamatory, and antihyperglycemic effects. J Trace Elem Med Biol [Internet]. 2022 Jan;69:126887. Available from: <URL>.

18. Uprety B, Abrahamse H. Targeting breast cancer and their stem cell population through AMPK activation: Novel insights. Cells [Internet]. 2022 Feb 7;11(3):576. Available from: <URL>.

19. He Z, You G, Liu Q, Li N. Alzheimer's disease and diabetes mellitus in comparison: The therapeutic efficacy of the vanadium compound. Int J Mol Sci [Internet]. 2021 Nov 3;22(21):11931. Available from: <URL>.

20. He Z, Li X, Han S, Ren B, Hu X, Li N, et al. Bis(ethylmaltolato)oxidovanadium (IV) attenuates amyloid-beta-mediated neuroinflammation by inhibiting NF-κB signaling pathway via a PPARγ-dependent mechanism. Metallomics [Internet]. 2021 Jul 2;13(7):mfab036. Available from: <URL>.

21. He Z, Han S, Zhu H, Hu X, Li X, Hou C, et al. The protective effect of vanadium on cognitive impairment and the neuropathology of alzheimer's disease in APPSwe/PS1dE9 Mice. Front Mol Neurosci [Internet]. 2020 Mar 10;13:00021. Available from: <URL>.

22. Bal T, Atasever B, Solakoğlu Z, Erdem-Kuruca S, Ülküseven B. Synthesis, characterisation and cytotoxic properties of the N1,N4-diarylidene-S-methyl-thiosemicarbazone chelates with Fe(III) and Ni(II). Eur J Med Chem [Internet]. 2007 Feb;42(2):161–7. Available from: <URL>.

23. Atasever B, Ülküseven B, Bal-Demirci T, Erdem-Kuruca S, Solakoğlu Z. Cytotoxic activities of new iron(III) and nickel(II) chelates of some S-methyl-thiosemicarbazones on K562 and ECV304 cells. Invest New Drugs [Internet]. 2010 Aug 4;28(4):421–32. Available from: <URL>.

24. Yanardag R, Demirci TB, Ülküseven B, Bolkent S, Tunali S, Bolkent S. Synthesis, characterization and antidiabetic properties of N1-2,4-dihydroxybenzylidene-N4-2-hydroxybenzylidene-S-methyl-thiosemicarbazidato-oxovanadium(IV). Eur J Med Chem [Internet]. 2009 Feb;44(2):818–26. Available from: <URL>.

25. Melchior M, Rettig SJ, Liboiron BD, Thompson KH, Yuen VG, McNeill JH, et al. Insulin-enhancing vanadium(III) complexes. Inorg Chem [Internet]. 2001 Aug 27;40(18):4686–90. Available from: <URL>.

26. Junod A, Lambert AE, Stauffacher W, Renold AE. Diabetogenic action of streptozotocin: Relationship of dose to metabolic response. J Clin Invest [Internet]. 1969 Nov 1;48(11):2129–39. Available from: <URL>.

27. Relander A, Räihä CE. Differences between the enzymatic and O-Toluidine methods of blood glucose determination. Scand J Clin Lab Invest [Internet]. 1963 Jan 13;15(3):221–4. Available from: <URL>.

28. Beutler E. In: Bergmeyen HV, Ed., Red blood cell metabolism: a manual of biochemical methods, 2nd edition, Grune and Stratton, New York. 1975;112–4.

29. Ledwoż;yw A, Michalak J, Stępień A, Kądziołka A. The relationship between plasma triglycerides, cholesterol, total lipids and lipid peroxidation products during human atherosclerosis. Clin Chim Acta [Internet]. 1986 Mar;155(3):275–83. Available from: <URL>.

30. Parker KM, England JD, Da Costa J, Hess RL, Goldstein DE. Improved colorimetric assay for glycosylated hemoglobin. Clin Chem [Internet]. 1981 May 1;27(5):669–72. Available from: <URL>.

31. Lowry OH, Rosebrough NJ, Farr AL, Randall RJ. Protein measurement with the folin phenol reagent. J Biol Chem [Internet]. 1951;193(1):265–75. Available from: <URL>.

32. Aebi H. Catalase in vitro. In 1984. p. 121–6. Available from: <URL>.

33. Mylroie AA, Collins H, Umbles C, Kyle J. Erythrocyte superoxide dismutase activity and other parameters of copper status in rats ingesting lead acetate. Toxicol Appl Pharmacol [Internet]. 1986 Mar;82(3):512–20. Available from: <URL>.

34. Hayman S, Kinoshita JH. Isolation and properties of lens aldose reductase. J Biol Chem [Internet]. 1965 Feb;240(2):877–82. Available from: <URL>.

35. Barretto OCO, Beutler E. The sorbitol-oxidizing enzyme of red blood cells. J Lab Clin Med [Internet]. 1975 Apr 1;85(4):645–9. Available from: <URL>.

36. Frisch M, Trucks G, Schlegel HB, Scuseria GE, Robb MA, Cheeseman JR, et al. Gaussian 09, Revision d. 01; Gaussian, Inc.: Wallingford CT, USA. 2009.

37. Kinoshita T, Miyake H, Fujii T, Takakura S, Goto T. The structure of human recombinant aldose reductase complexed with the potent inhibitor zenarestat. Acta Crystallogr Sect D Biol Crystallogr [Internet]. 2002 Apr 1;58(4):622–6. Available from: <URL>.

38. Pauly TA, Ekstrom JL, Beebe DA, Chrunyk B, Cunningham D, Griffor M, et al. X-ray crystallographic and kinetic studies of human sorbitol dehydrogenase. Structure [Internet]. 2003 Sep;11(9):1071–85. Available from: <URL>.

39. Rappe AK, Casewit CJ, Colwell KS, Goddard WA, Skiff WM. UFF, a full periodic table force field for molecular mechanics and molecular dynamics simulations. J Am Chem Soc [Internet]. 1992 Dec 1;114(25):10024–35. Available from: <URL>.

40. Valdés-Tresanco MS, Valdés-Tresanco ME, Valiente PA, Moreno E. AMDock: A versatile graphical tool for assisting molecular docking with autodock vina and autodock4. Biol Direct [Internet]. 2020 Dec 16;15(1):12. Available from: <URL>.

41. Jamroz M, Kolinski A, Kmiecik S. CABS-flex: Server for fast simulation of protein structure fluctuations. Nucleic Acids Res [Internet]. 2013 Jul 1;41(W1):W427–31. Available from: <URL>.

42. Kmiecik S, Gront D, Kolinski M, Wieteska L, Dawid AE, Kolinski A. Coarse-grained protein models and their applications. Chem Rev [Internet]. 2016 Jul 27;116(14):7898–936. Available from: <URL>.

43. Gunasekaran S, Arun Balaji R, Kumaresan S, Anand G, Srini-Vasan S. Experimental and theoretical investigations of spectroscopic properties of N-acetyl-5-methoxytryptamine. Can J Anal Sci Spectrosc [Internet]. 2008;53(4):149–62. Available from: <URL>.

44. Buvaneswari M, Santhakumari R, Usha C, Jayasree R, Sagadevan S. Synthesis, growth, structural, spectroscopic, optical, thermal, DFT, HOMO–LUMO, MEP, NBO analysis and thermodynamic properties of vanillin isonicotinic hydrazide single crystal. J Mol Struct [Internet]. 2021 Nov 5;1243:130856. Available from: <URL>.

45. Sharma J, Kumar Bhardwaj V, Singh R, Rajendran V, Purohit R, Kumar S. An in-silico evaluation of different bioactive molecules of tea for their inhibition potency against non structural protein-15 of SARS-CoV-2. Food Chem [Internet]. 2021 Jun;346:128933. Available from: <URL>.

46. Tunali S, Yanardag R. Protective effect of vanadyl sulfate on skin injury in streptozotocin-induced diabetic rats. Hum Exp Toxicol [Internet]. 2013 Nov 26;32(11):1206–12. Available from: <URL>.

47. Tunalı S, Yanardağ R. The effects of vanadyl sulfate on glutathione, lipid peroxidation and nonenzymatic glycosylation levels in various tissues in experimental diabetes. İstanbul J Pharm [Internet]. 2021 Apr 30;51(1):73–8. Available from: <URL>.

48. Zhang P, Li T, Wu X, Nice EC, Huang C, Zhang Y. Oxidative stress and diabetes: antioxidative strategies. Front Med [Internet]. 2020 Oct 4;14(5):583–600. Available from: <URL>.

49. Kurt O, Ozden TY, Ozsoy N, Tunali S, Can A, Akev N, et al. Influence of vanadium supplementation on oxidative stress factors in the muscle of STZ-diabetic rats. BioMetals [Internet]. 2011 Oct 10;24(5):943–9. Available from: <URL>.

50. Tunali S, Gezginci-Oktayoglu S, Bolkent S, Coskun E, Bal-Demirci T, Ulkuseven B, et al. Protective effects of an oxovanadium(IV) complex with $N_2O_2$ chelating thiosemicarbazone on small intestine injury of STZ-diabetic rats. Biol Trace Elem Res [Internet]. 2021 Apr 9;199(4):1515–23. Available from: <URL>.

51. Akgün-Dar K, Bolkent S, Yanardag R, Tunalı S. Vanadyl sulfate protects against streptozotocin-induced morphological and biochemical changes in rat aorta. Cell Biochem Funct [Internet]. 2007 Nov 7;25(6):603–9. Available from: <URL>.

52. Tunali S, Yanardag R. Effect of vanadyl sulfate on the status of lipid parameters and on stomach and spleen tissues of streptozotocin-induced diabetic rats. Pharmacol Res [Internet]. 2006 Mar;53(3):271–7. Available from: <URL>.

53. Fantus IG, George R, Tang S, Chong P, Poznansky MJ. The insulin-mimetic agent vanadate promotes receptor endocytosis and inhibits intracellular Ligand-receptor degradation by a mechanism distinct from the lysosomotropic agents. Diabetes [Internet]. 1996 Aug 1;45(8):1084–93. Available from: <URL>.

54. Gao Z, Zhang C, Yu S, Yang X, Wang K. Vanadyl bisacetylacetonate protects β cells from palmitate-induced cell death through the unfolded protein response pathway. JBIC J Biol Inorg Chem [Internet]. 2011 Jun 22;16(5):789–98. Available from: <URL>.

55. Bolkent S, Bolkent S, Yanardag R, Tunali S. Protective effect of vanadyl sulfate on the pancreas of streptozotocin-induced diabetic rats. Diabetes Res Clin Pract [Internet]. 2005 Nov;70(2):103–9. Available from: <URL>.

56. Cam MC, Li WM, McNeill JH. Partial preservation of pancreatic β-cells by vanadian: Evidence for long-term amelioration of diabetes. Metabolism [Internet]. 1997 Jul;46(7):769–78. Available from: <URL>.

57. Pirmoradi L, Noorafshan A, Safaee A, Dehghani GA. Quantitative assessment of proliferative effects of oral vanadium on pancreatic islet volumes and beta cell numbers of diabetic rats. Iran Biomed J [Internet]. 2016;20(1):18–25. Available from: <URL>.

58. Mohammadi MT, Pirmoradi L, Mesbah F, Safaee A, Dehghani GA. Trophic Actions of Oral Vanadium and Improved Glycemia on the Pancreatic Beta-Cell Ultrastructure of Streptozotocin-Induced Diabetic Rats. J Pancreas [Internet]. 2014;15(6):591–6. Available from: <URL>.

59. Hiromura M, Nakayama A, Adachi Y, Doi M, Sakurai H. Action mechanism of bis(allixinato)oxovanadium(IV) as a novel potent insulin-mimetic complex: Regulation of GLUT4 translocation and FoxO1 transcription factor. JBIC J Biol Inorg Chem [Internet]. 2007 Oct 15;12(8):1275–87. Available from: <URL>.

60. Kahya MC, Nazıroğlu M. Melatonin reduces lens oxidative stress level in STZ-induced diabetic rats through supporting glutathione peroxidase and reduced glutathione values. J Cell Neurosci Oxidative Stress [Internet]. 2016 Dec 31;8(2):588–94. Available from: <URL>.

61. Sun L, Shi DJ, Gao XC, Mi SY, Yu Y, Han Q. The protective effect of vanadium against diabetic cataracts in diabetic rat model. Biol Trace Elem Res [Internet]. 2014 May 8;158(2):219–23. Available from: <URL>.

62. Altavilla D, Saitta A, Cucinotta D, Galeano M, Deodato B, Colonna M, et al. Inhibition of lipid peroxidation restores impaired vascular endothelial growth factor expression and stimulates wound healing and angiogenesis in the genetically diabetic mouse. Diabetes [Internet]. 2001 Mar 1;50(3):667–74. Available from: <URL>.

63. Kumar Pasupulati A, Chitra PS, Reddy GB. Advanced glycation end products mediated cellular and molecular events in the pathology of diabetic nephropathy. Biomol Concepts [Internet]. 2016 Dec 1;7(5–6):293–309. Available from: <URL>.

64. Tarwadi K V., Agte V V. Effect of micronutrients on methylglyoxal-mediated in vitro glycation of albumin. Biol Trace Elem Res [Internet]. 2011 Nov 17;143(2):717–25. Available from: <URL>.

65. Elosta A, Ghous T, Ahmed N. Natural products as anti-glycation agents: Possible therapeutic potential for diabetic complications. Curr Diabetes Rev [Internet]. 2012 Mar 1;8(2):92–108. Available from: <URL>.

66. Wu CH, Yen GC. Inhibitory effect of naturally occurring flavonoids on the formation of advanced glycation endproducts. J Agric Food Chem [Internet]. 2005 Apr 1;53(8):3167–73. Available from: <URL>.

67. Preet A, Gupta BL, Yadava PK, Baquer NZ. Efficacy of lower doses of vanadium in restoring altered glucose metabolism and antioxidant status in diabetic rat lenses. J Biosci [Internet]. 2005 Mar

1;30(2):221–30. Available from: <URL>.

68. Zhang L, Chu W, Zheng L, Li J, Ren Y, Xue L, et al. Zinc oxide nanoparticles from *Cyperus rotundus* attenuates diabetic retinopathy by inhibiting NLRP3 inflammasome activation in STZ-induced diabetic rats. J Biochem Mol Toxicol [Internet]. 2020 Dec 21;34(12):e22583. Available from: <URL>.

69. Giacco F, Brownlee M. Oxidative stress and diabetic complications. Schmidt AM, editor. Circ Res [Internet]. 2010 Oct 29;107(9):1058–70. Available from: <URL>.

70. Lu L, Lu Q, Chen W, Li J, Li C, Zheng Z. Vitamin D $_3$ protects against diabetic retinopathy by inhibiting high-glucose-induced activation of the ROS/TXNIP/NLRP3 inflammasome pathway. J Diabetes Res [Internet]. 2018 Feb 22;2018:8193523. Available from: <URL>.

71. Gong X, Zhang Q, Tan S. Inhibitory effect of r-hirudin variant III on streptozotocin-induced diabetic cataracts in rats. Galuppo M, Xi ZX, editors. Sci World J [Internet]. 2013 Jan 10;2013(1):630651. Available from: <URL>.

72. Zych M, Wojnar W, Kielanowska M, Folwarczna J, Kaczmarczyk-Sedlak I. Effect of berberine on glycation, aldose reductase activity, and oxidative stress in the lenses of streptozotocin-induced diabetic rats in vivo—A preliminary study. Int J Mol Sci [Internet]. 2020 Jun 16;21(12):4278. Available from: <URL>.

73. Siddiqui MR, Taha A, Moorthy K, Hussain ME, Basir SF, Baquer NZ. Amelioration of altered antioxidant status and membrane linked functions by vanadium andTrigonella in alloxan diabetic rat brains. J Biosci [Internet]. 2005 Sep 1;30(4):483–90. Available from: <URL>.

74. Aragno M, Brignardello E, Tamagno E, Gatto V, Danni O, Boccuzzi G. Dehydroepiandrosterone administration prevents the oxidative damage induced by acute hyperglycemia in rats. J Endocrinol [Internet]. 1997 Nov 1;155(2):233–40. Available from: <URL>.

75. Hodgson EK, Fridovich I. Interaction of bovine erythrocyte superoxide dismutase with hydrogen peroxide. Inactivation of the enzyme. Biochemistry [Internet]. 1975 Dec 1;14(24):5294–9. Available from: <URL>.

76. Pigeolet E, Corbisier P, Houbion A, Lambert D, Michiels C, Raes M, et al. Glutathione peroxidase, superoxide dismutase, and catalase inactivation by peroxides and oxygen derived free radicals. Mech Ageing Dev [Internet]. 1990 Feb;51(3):283–97. Available from: <URL>.

77. Sindhu RK, Koo J, Roberts CK, Vaziri ND. Dysregulation of hepatic superoxide dismutase, catalase and glutathione peroxidase in diabetes: response to insulin and antioxidant therapies. Clin Exp Hypertens [Internet]. 2004 Jan 29;26(1):43–53. Available from: <URL>.

78. Du J, Feng B, Dong Y, Zhao M, Yang X. Vanadium coordination compounds loaded on graphene quantum dots (GQDs) exhibit improved pharmaceutical properties and enhanced anti-diabetic effects. Nanoscale [Internet]. 2020;12(16):9219–30. Available from: <URL>.

79. Hadjiadamou I, Vlasiou M, Spanou S, Simos Y, Papanastasiou G, Kontargiris E, et al. Synthesis of vitamin E and aliphatic lipid vanadium(IV) and (V) complexes, and their cytotoxic properties. J Inorg Biochem [Internet]. 2020 Jul;208:111074. Available from: <URL>.

80. del Río D, Galindo A, Vicente R, Mealli C, Ienco A, Masi D. Synthesis, molecular structure and properties of oxo-vanadium(iv) complexes containing the oxydiacetate ligand. Dalt Trans [Internet]. 2003 Apr 17;(9):1813–20. Available from: <URL>.

81. Pranczk J, Jacewicz D, Wyrzykowski D, Wojtczak A, Tesmar A, Chmurzyński L. Crystal structure, antioxidant properties and characteristics in aqueous solutions of the oxidovanadium(IV) Complex [VO(IDA)phen]·$2H_2O$. Eur J Inorg Chem [Internet]. 2015 Jul 22;2015(20):3343–9. Available from: <URL>.

82. Smith DM, Sale GJ. Evidence that a novel serine kinase catalyses phosphorylation of the insulin receptor in an insulin-dependent and tyrosine kinase-dependent manner. Biochem J [Internet]. 1988 Dec 15;256(3):903–9. Available from: <URL>.

83. Morré DM, Lenaz G, Morré DJ. Surface oxidase and oxidative stress propagation in aging. J Exp Biol [Internet]. 2000 May 15;203(10):1513–21. Available from: <URL>.

84. Shibata M, Oshitari T, Kajita F, Baba T, Sato E, Yamamoto S. Development of macular holes after rhegmatogenous retinal detachment repair in japanese patients. J Ophthalmol [Internet]. 2012;2012:740591. Available from: <URL>.

85. Pradeep SR, Srinivasan K. Ameliorative influence of dietary fenugreek (*Trigonella foenum-graecum*) seeds and onion (*Allium cepa*) on eye lens abnormalities via modulation of crystallin proteins and polyol pathway in experimental diabetes. Curr Eye Res [Internet]. 2018 Sep 2;43(9):1108–18. Available from: <URL>.

JOURNAL of THE TURKISH CHEMICAL SOCIETY
SECTION: A
CHEMISTRY
TURKISH CHEMICAL SOCIETY

# Rational Design, Synthesis, and Comprehensive Characterization of Novel 1,4-Pentadien-3-one Derivatives Bearing Oxime Moieties

**Emine Vildan Burgaz[1*], Mahya Tanha[2], Seyed Armin Houshmand Kia[1,2]**

[1]Eastern Mediterranean University, Faculty of Pharmacy, Famagusta, North Cyprus, Mersin 10, Turkey
[2]Faculty of Pharmacy, International Final University, Kyrenia, North Cyprus, Mersin 10, Turkey.

**Abstract:** The purpose of this research is to synthesize a series of novel 1,4-pentadien-3-one oximes and 1,4-pentadien-3-one O-benzoyl oximes. In this work, new 1,4-pentadien-3-one derivatives with oxime moieties are logically designed, synthesized, and thoroughly characterized. Using a multi-step synthetic strategy, a number of 1,4-pentadien-3-one derivatives were created by functionalizing the core structure with oxime functionalities. The structures of the newly synthesized compounds were determined by several spectroscopic methods, including Nuclear Magnetic Resonance Spectroscopy ($^1$H NMR, $^{13}$C NMR) and Mass Spectroscopy.

**Keywords:** 1,4-pentadien-3-one, Curcumin, Synthesis, Chalcone, Oxime ether.

**Submitted:** July 5, 2025. **Accepted:** October 5, 2025.

**Cite this:** Burgaz EV, Tanha M, Kia SAH. Rational Design, Synthesis, and Comprehensive Characterization of Novel 1,4-Pentadien-3-one Derivatives Bearing Oxime Moieties. JOTCSA. 2025;12(4): 235-40.

**DOI:** https://doi.org/10.18596/jotcsa.1734865

***Corresponding author's E-mail:** vildan.burgaz@emu.edu.tr

## 1. INTRODUCTION

1,4-Pentadien-3-ones are curcumin derivatives that have garnered significant attention in organic chemistry due to their versatile reactivity and possible uses in materials science and medicine (1). These compounds, characterized by a conjugated diene and carbonyl group, serve as valuable intermediates to produce many functionalized compounds. Among the modifications of such derivatives, the formation of oximes and their subsequent O-acylation have proven to be particularly interesting, offering access to structurally diverse compounds with enhanced stability and functionality.

Curcumin (IUPAC name: (1E,6E)-1,7-bis(4-hydroxy-3-methoxyphenyl)-1,6-heptadiene-3,5-dione (2), derived from dried rhizomes of turmeric plants, is the active compound (3) (Figure 1). Turmeric belongs to the Curcuma longa species and the Zingiberaceae family. Curcumin is a natural curcuminoid that is responsible for the yellow color and most of its medicinal value (4).

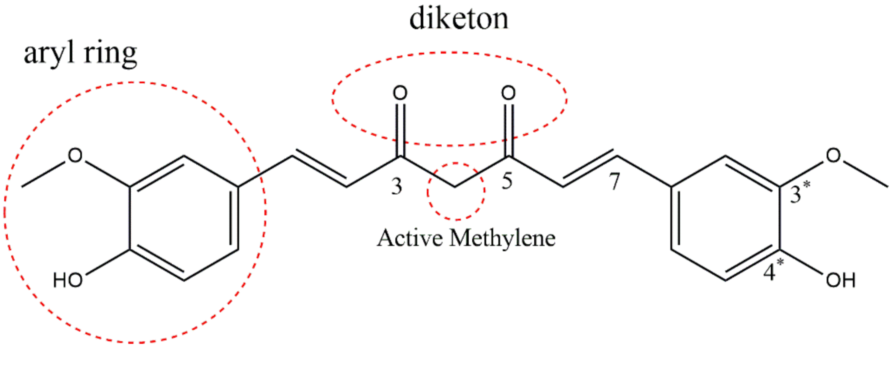

(1E,6E)-1,7-bis (4-hydroxy- 3-methoxyphenyl) -1,6- heptadiene-3,5-dione

**Figure 1:** Structure and SAR of Curcumin.

Numerous illnesses, such as coughs, diabetes, dermatological disorders, respiratory issues, cardiovascular and hepatobiliary diseases, arthritis, irritable bowel disease (IBS), peptic ulcers, psoriasis, and atherosclerosis, are treated with turmeric as a traditional medication (5). Curcumin exhibits diverse pharmacological properties. These include anti-inflammatory, hepatoprotective, antibacterial, antiviral (6), inflammatory bowel disease (7), anticancer, cholesterol-lowering (8), neuroprotective, and antioxidant, among others (9). It has been suggested that its antioxidant and anti-inflammatory activity is related, in fact, to its anticancer activity (10).

Oxime analogs have been explored as potential alternatives to curcumin and have demonstrated encouraging outcomes in combating several forms of cancer, such as colon cancer, prostate cancer, epithelial cancer, pancreatic cancer, breast cancer, lung cancer, and pancreatic carcinoma. Their significant antiproliferative activity evidences their efficacy against cancer cells (11). These derivatives show high antibacterial, antifungal, and antioxidant potency with a very low toxicity (12,13). Besides exhibiting a variety of biological activities, Oximes and their derivatives hold a prominent position in the field of organic chemistry, largely due to their versatility as synthetic intermediates. These compounds play a vital role in various chemical synthesis procedures, and they demonstrate significant industrial importance. The distinctive conjugated system of α,β-unsaturated ketones found in benzalacetones enhances their effectiveness as radical scavengers. This attribute highlights the potential of benzalacetone and its derivatives in showcasing antioxidant properties (14-16).

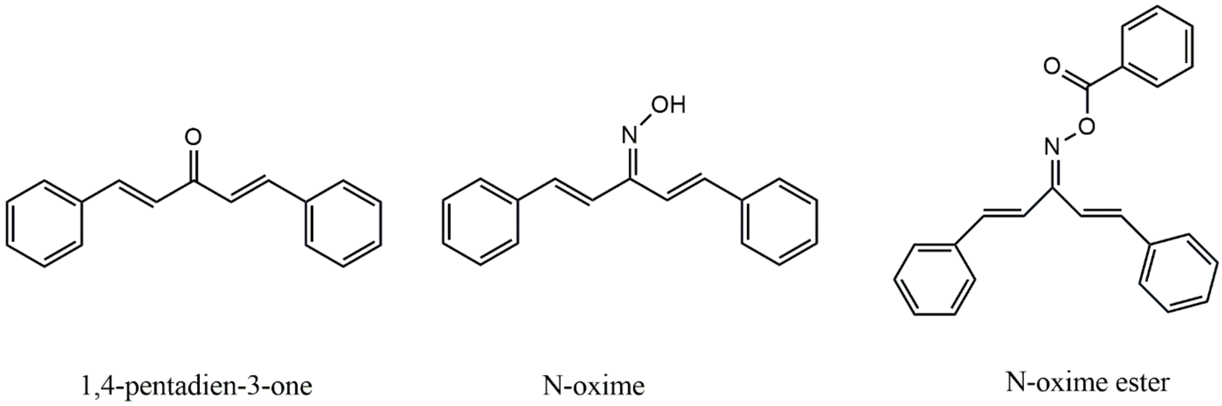

1,4-pentadien-3-one N-oxime N-oxime ester

**Figure 2:** General Chemical Structure of Oxime Analogs of Curcumin.

Oximes, derived from the reaction of carbonyl compounds with hydroxylamine, are well-known for their applications in coordination chemistry and analytical detection. They are also precursors in the synthesis of various bioactive molecules. Furthermore, O-acylated oximes, such as O-benzoyl oximes, have been extensively studied for their roles in medicinal chemistry, particularly as prodrugs, and in the development of novel materials with unique electronic properties (17).

Oxime formation, functionalization, and their potential applications have been widely studied. According to the literature, 1,5-diphenylpenta-1,4-dien-3-one was employed as a starting material for oxime synthesis, which subsequently led to the generation of O-benzoyl oximes. Several oxime derivatives exhibit significant medical benefits, such as anti-proliferative activities on cancer cells. Moreover, most O-benzoyl oxime derivatives possess antibacterial and antioxidant properties (17). Importantly, the ability to fine-tune their chemical properties by modifying the oxime or acyl group makes these compounds highly valuable in both fundamental and applied research.

This study aims to explore the synthesis of 1,4-pentadien-3-one oxime and its O-benzoyl derivatives, focusing on optimizing reaction conditions and characterization of the resulting compounds.

## 2. EXPERIMENTAL SECTION

### 2.1. Materials and Methods

p-Anisaldehyde, 4-fluorobenzaldehyde, p-tolualdehyde, o-anisaldehyde, thiophene-2-carboxaldehyde, 5-methylfurfural, sodium hydroxide, ethanol, hydroxyl amine hydrochloride, sodium sulphate, and benzoyl chloride were obtained from Sigma-Aldrich and Merck. Analytical grade chemicals were utilized unless otherwise specified. (1E,4E)-1,5-bis(4-methoxyphenyl)penta-1,4-dien-3-one (2a), (1E,4E)-1,5-bis(4-fluorophenyl)penta-1,4-dien-3-one (2b), (1E,4E)-1,5-di-p-tolylpenta-1,4-dien-3-one (2c), (1E,4E)-1,5-bis(2-methoxyphenyl)penta-1,4-dien-3-one (2d), (1E,4E)-1,5-di(thiophen-2-yl)penta-1,4-dien-3-one (2e), (1E,4E)-1,5-bis(5-methylfuran-2 yl)penta-1,4-dien-3-one (2f) intermediates were synthesis with appropriate methods. The $^1H$ and $^{13}C$ NMR spectra were acquired with TMS serving as the internal reference and $CDCl_3$ as the solvent. The measurements were carried out using a Bruker Avance 400 MHz Spectrometer. Using an Agilent 19091 N-136 GC–MS apparatus, the MS spectra were acquired.

### *2.1.1. General Procedure for the synthesis of 1,4-pentadien-3-one derivatives (**2a-f**)*

The α,β-unsaturated ketone compounds employed in this study were synthesized via a simple procedure based on the Claisen–Schmidt condensation (18-20). A solution containing sodium hydroxide (1 N, 1 mL) in distilled ethanol (5 mL) was stirred while the appropriate aldehyde (10 mmol) was added dropwise at an ice-cold temperature. After stirring for 15 minutes, acetone (5 mmol) was gradually introduced into the mixture with vigorous stirring at room temperature. Upon completion of the reaction, the mixture was quenched by the addition of cold water (10 mL) and stirred for an additional 10 minutes. The resulting precipitate was collected by filtration, thoroughly washed with cold water, and dried under high vacuum. Recrystallization from ethanol afforded the pure compound in moderate to excellent yields.

### *2.1.2. General Procedure for the synthesis of 1,4-pentadien-3-one oxime compounds (**3a-3f**)* (21)

A mixture of 1,4-pentadien-3-one derivatives (**2a-f**, 8 mmol), hydroxylamine hydrochloride (12 mmol), and sodium sulfate (8 mmol) was mixed in 50 mL of ethanol and refluxed for 4 hours. After the reaction was completed, the mixture was filtered, and the solvent was extracted under decreased pressure. The resultant residue was washed with water and extracted with dichloromethane. The organic layer was dried over anhydrous sodium sulfate, and the solvent was then evaporated under reduced pressure to obtain a crude product. This product was further purified using silica gel column chromatography with an eluent of hexane: ethyl acetate (10:1).

### *2.1.3. General Procedure for the synthesis of 1,4-pentadien-3-one O-benzoyl oxime compounds (**4a-e**) (14)*

The appropriate starting material was placed into a 100 mL flask. Then, 10 mL THF and 56 mg KOH were weighed and added. The mixture was stirred until the KOH completely dissolved. Subsequently, 140 mg of benzoyl chloride was added, upon which solid formation was immediately observed. After stirring at room temperature for 2 hours, the reaction was terminated. The solid and filtrate phases were separated, and the solid was recrystallized from ethanol.

## 3. RESULTS AND DISCUSSION

In this study, 1,4-pentadien-3-one compounds were strategically selected based on their molecular similarities to curcumin and their numerous biological activities in the literature (22-23). Su *et al.* mentioned that oxime and oxime ethers are a class of chemicals with high biological activity that have been widely used in medicine and insecticides (24). The aim of this study was to synthesize 1,4-pentadien-3-one oxime and O-benzoyl oxime derivatives. In this synthetic pathway, a total of eleven compounds were obtained, four of which have been previously reported in the literature (16,21), while the remaining seven are novel. The four known compounds were re-synthesized to serve as key intermediates for the subsequent synthesis of the final target molecules, namely the O-benzoyl oxime derivatives (**4a-e**).

The synthetic reaction of novel 1,4-pentadien-3-one oximes and 1,4-pentadien-3-one O-benzoyl oximes derivatives is shown in Scheme 1. As we previously described in our earlier study (18), the 1,4-pentadien-3-one derivatives (**2a–f**) were produced using a simple Claisen–Schmidt condensation with ethanolic NaOH acting as the catalyst and aromatic aldehydes with different substituents and acetone in a 2:1 molar ratio (Scheme 1). For compounds **2a–f**, the experimentally determined melting points were found to be in close agreement with those reported in the literature for structurally related analogues, further supporting the successful synthesis (25-26). After purifying the first step's product, the intermediate product was utilized for the second step, which involved adding sodium sulfate and hydroxylamine hydrochloride to ethanol to create 1,4-pentadien-3-one oxime compounds (**3a-f**). Benzoyl chloride, KOH, and tetrahydrofuran were then added to the second intermediate compound to form new 1,4-pentadien-3-one O-benzoyl oxime compounds (**4a-e**). Following column chromatography purification, spectrum analyses, including 1H NMR, 13C NMR, and mass spectra, were used to characterize the finished product (the spectra data are shown in the Supplementary Materials).

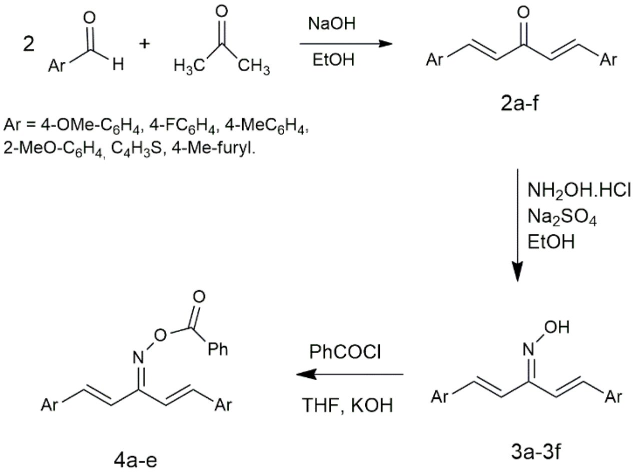

**Scheme 1:** Synthetic route of 1,4-pentadien-3-one oxime (3a-f) and O-benzoyl oxime (4a-e).

Compounds 3a-3f were produced via oximation of 1,4-pentadien-3-one derivatives in the presence of $NH_2OH.HCl$ and $Na_2SO_4$ in ethanol with moderate to good yields (58-81 %). O- benzoyl oxime derivatives 4a-4e were then created by treating the oximes with benzoyl chloride and KOH in THF. In compound 3d, the singlet at δ 11.45 ppm represents the hydroxide proton of the oxime group. This signal disappears after conversion to the O-benzoyl derivative 4d, showing that esterification was successful. Aromatic and olefinic protons emerge in multiplets between δ 7.80-6.90 ppm, indicating conjugated enone complexes. Compared to Erdoğan *et al*. (16), our compounds showed somewhat downfield-shifted olefinic proton signals due to the electron-withdrawing impact of the benzoyl group. The fluoro substituent on 4c may enhance lipophilicity and membrane permeability, while the electron-donating methoxy group on 4a may enhance conjugation and possible contact with biological targets. The molecular ion peak supports the suggested molecular formula of 4d $[M+H]^+$ seen in HRMS at m/z 375.1234 (calc. 375.1228). This study used a multi-step synthesis approach to create a series of 1,4-pentadien-3-one derivatives (3a-3f) and their corresponding O-benzoyl oxime ethers (4a-4e) from suitably substituted benzaldehydes and acetophenones.

### 3.1. Experimental Data

#### (1E,4E)-1,5-bis(2-methoxyphenyl)penta-1,4-dien-3-one oxime (3d)

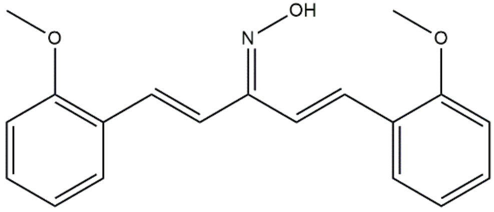

White solid (93%). Mp 182–188 °C. $^1$H NMR (400 MHz, DMSO, δ, ppm): 11.45 (1H, s, –O*H*), 7.67–7.62 (2H, m, Ar-*H*), 7.39–7.26 (5H, m, Ar-*H* and alkene-*H*), 7.04–6.94 (5H, m, Ar-*H* and alkene-*H*), 3.82 (6H, s, –C*H*$_3$). $^{13}$C NMR (100 MHz, CDCl$_3$, δ, ppm): 157.0 (*C*=O), 156.7, 153.2, 130.2, 130.1, 129.5, 127.1, 126.9, 126.7, 124.9, 124.7, 123.3, 120.8, 120.7, 117.7, 111.5, 111.4, 55.5, 55.5. MS: m/z 309 (310 $[M+1]^+$). Anal. calc. for $C_{19}H_{19}NO_3$ (309.14): C 73.77, H 6.19, N 4.53; found: C 73.71, H 6.22, N 4.56.

#### (1E,4E)-1,5-bis(5-methylfuran-2-yl)penta-1,4-dien-3-one oxime (3f)

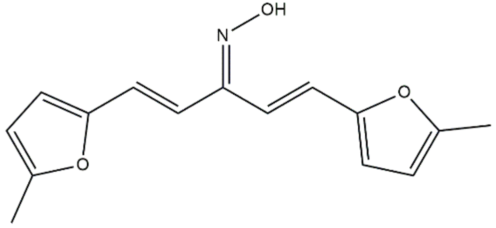

White solid (87%). Mp 152–158 °C. $^1$H NMR (400 MHz, DMSO, δ, ppm): 11.46 (1H, s, –O*H*), 7.04–6.94 (2H, m, Ar-*H*), 6.87–6.83 (1H, d, J = 16.0 Hz, alkene-*H*), 6.64–6.60 (1H, d, J = 16.0 Hz, alkene-*H*), 6.59–6.58 (1H, d, J = 3.6 Hz, Ar-*H*), 6.50–6.49 (1H, d, J = 3.6 Hz, Ar-*H*), 6.19–6.14 (2H, m, Ar-*H*), 2.32 (6H, s, –C*H*$_3$). $^{13}$C NMR (100 MHz, CDCl$_3$, δ, ppm): 153.5 (*C*=O), 152.6, 151.5, 150.8, 150.6, 122.9, 119.9, 118.7, 113.8, 112.8, 111.8, 108.7, 108.4, 13.5. MS: m/z 257.11 (258 $[M+1]^+$). Anal. calc. for $C_{15}H_{15}NO_3$ (257.11): C 70.02, H 5.88, N 5.44; found: C 69.98, H 5.91, N 5.45.

#### (1E,4E)-1,5-bis(4-methoxyphenyl)penta-1,4-dien-3-one O-benzoyl oxime (4a)

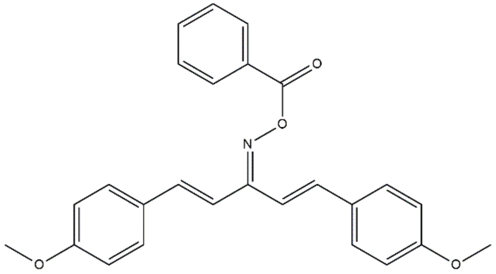

White solid (87%). Mp 159–163 °C. $^1$H NMR (400 MHz, DMSO, δ, ppm): 8.14–8.12 (2H, m, Ar-*H*), 7.64–7.60 (1H, m, Ar-*H*), 7.55–7.48 (6H, m, Ar-*H*), 7.35–7.31 (1H, d, J = 16 Hz, alkene-*H*), 7.26–7.19 (2H, m, Ar-*H*), 6.97–6.91 (5H, m, Ar-*H* and alkene-*H*), 3.86–3.84 (6H, s, –C*H*$_3$). $^{13}$C NMR (100 MHz, CDCl$_3$, δ, ppm): 163.9 (*C*=O), 161.9, 161.0, 160.5, 139.8, 138.6, 133.3, 129.7, 129.3, 129.1, 128.9, 128.6, 128.2, 118.6, 114.7, 114.5, 114.3, 55.4, 55.4. MS: m/z 413 (414 $[M+1]^+$). Anal. calc. for $C_{26}H_{23}N_2O_4$ (413.47): C 75.53, H 5.61, N 3.39; found: C 75.59, H 5.59, N 3.35.

#### (1E,4E)-1,5-bis(4-fluorophenyl)penta-1,4-dien-3-one O-benzoyl oxime (4b)

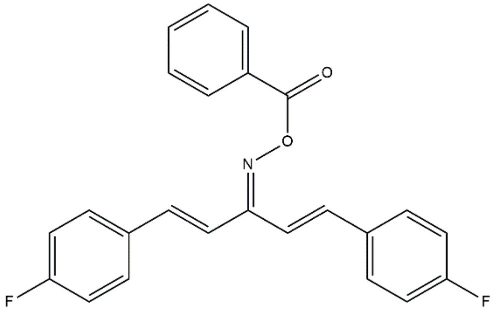

Yellow solid (89%). Mp 175–177 °C. $^1$H NMR (400 MHz, DMSO, δ, ppm): 8.12–8.10 (2H, m, Ar-*H*), 7.88–7.83 (4H, m, Ar-*H*), 7.76–7.72 (1H, m, Ar-*H*), 7.63–7.59 (2H, m, Ar-*H*), 7.49–7.48 (2H, m, Ar-*H*), 7.43–7.39 (1H, d, J = 16 Hz, alkene-*H*), 7.33–7.22 (5H, m, Ar-*H* and alkene-*H*). $^{13}$C NMR (100 MHz, CDCl$_3$, δ, ppm): 164.69 (*C*=O), 164.3, 163.5, 162.2, 161.9, 161.5, 140.0, 137.2, 134.2, 132.7, 132.5, 130.7, 130.7, 130.4, 130.3, 129.9, 129.5, 129.0, 120.8, 116.7, 116.5, 116.3, 116.3, 116.1. MS: m/z 389 (390 $[M+1]^+$). Anal. calc. for $C_{24}H_{17}F_2N_2O_2$ (389.39): C 74.03, H 4.40, F 9.76, N 3.60; found: C 74.01, H 4.35, F 9.79, N 3.64.

#### (1E,4E)-1,5-di-p-tolylpenta-1,4-dien-3-one O-benzoyl oxime (4c)

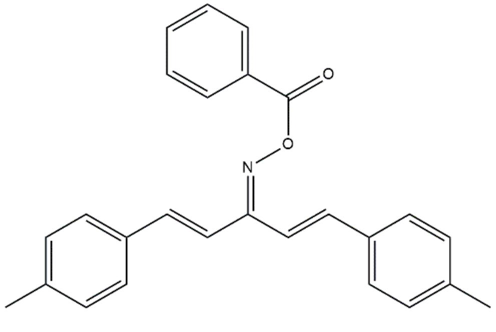

Yellowish solid (92%). Mp 164–167 °C. $^1$H NMR (400 MHz, DMSO, δ, ppm): 8.09–8.08 (2H, m, Ar-*H*), 7.87–7.86 (2H, m, Ar-*H*), 7.69–7.61 (4H, m, Ar-*H*), 7.43–7.41 (2H, m, Ar-*H*), 7.28–7.22 (7H, m, Ar-*H and* alkene-*H*), 2.33 (6H, s, –C*H*$_3$). $^{13}$C NMR (100 MHz, CDCl$_3$, δ, ppm): 169.1 (*C*=O), 163.0, 161.1, 141.3, 140.6, 139.8, 139.0, 137.7, 133.7, 132.9, 132.6, 129.6, 129.4, 129.3, 129.0, 128.2, 127.9, 127.7, 126.9, 119.3, 115.4, 21.0, 21.0. MS: m/z 381.47 (382 [M+1]$^+$). Anal. calc. for $C_{26}H_{23}NO_2$ (381.47): C 81.86, H 6.08, N 3.67; found: C 81.84, H 6.06, N 3.71.

### (1E,4E)-1,5-bis(2-methoxyphenyl)penta-1,4-dien-3-one O-benzoyl oxime (4d)

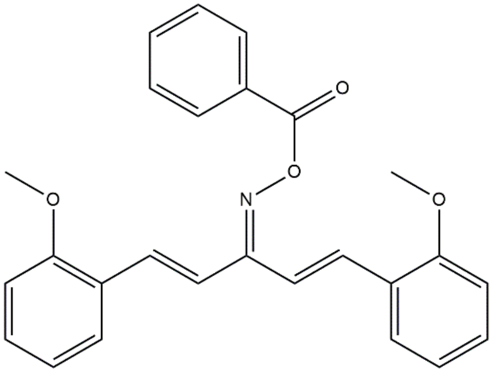

White solid (85%). Mp 165–169 °C. $^1$H NMR (400 MHz, DMSO, δ, ppm): 8.14–8.12 (2H, m, Ar-*H*), 7.64–7.60 (1H, m, Ar-*H*), 7.55–7.48 (6H, m, Ar-*H*), 7.35–7.31 (1H, d, J = 16 Hz, alkene-*H*), 7.26–7.19 (2H, m, Ar-*H*), 6.97–6.91 (5H, m, Ar-*H* and alkene-*H*), 3.86–3.84 (6H, s, –C*H*$_3$). $^{13}$C NMR (100 MHz, CDCl$_3$, δ, ppm): 162.9 (*C*=O), 161.9, 157.8, 157.2, 136.0, 133.8, 132.6, 131.4, 130.8, 129.2, 129.0, 129.0, 127.7, 123.9, 123.5, 120.9, 120.7, 120.4, 117.4, 111.8, 111.6, 55.6, 55.6. MS: m/z 413.47 (414 [M+1]$^+$). Anal. calc. for $C_{26}H_{23}NO_4$ (413.47): C 75.53, H 5.61, N 3.39; found: C 75.50, H 5.66, N 3.37.

### (1E,4E)-1,5-di(thiophen-2-yl)penta-1,4-dien-3-one O-benzoyl oxime (4e)

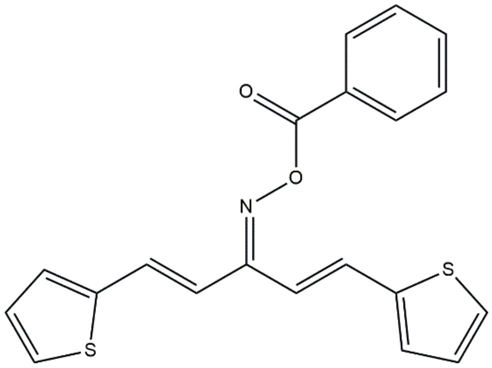

White solid (95%). Mp 188–192 °C. $^1$H NMR (400 MHz, DMSO, δ, ppm): 8.08–8.06 (2H, m, Ar-*H*), 7.76–7.62 (6H, m, Ar-*H*), 7.57–7.50 (3H, m, Ar-*H*), 7.20–7.14 (3H, m, Ar-*H* and alkene-*H*), 6.94–6.90 (1H, d, J = 16 Hz, alkene-*H*). $^{13}$C NMR (100 MHz, CDCl$_3$, δ, ppm): 163.2 (*C*=O), 160.7, 140.9, 140.8, 134.3, 134.2, 131.5, 131.4, 130.4, 129.7, 129.6, 129.1, 129.0, 128.8, 128.6, 119.0, 115.1. MS: m/z 365.05 (366 [M+1]$^+$). Anal. calc. for $C_{20}H_{15}NO_2S_2$ (365.05): C 65.73, H 4.14, N 3.83, S 17.55; found: C 65.70, H 4.17, N 3.80, S 17.58.

## 4. CONCLUSION

These novel compounds expand the chemical space of 1,4-pentadien-3-one derivatives and provide a platform for future biological evaluation. The O-benzoyl oxime derivatives synthesized in this study represent a new class of molecules that could be further investigated for potential medicinal or agrochemical applications. Future work may include detailed structure-activity relationship studies and exploration of alternative functionalization to optimize biological properties. Overall, this study provides both the practical synthetic route and a foundation for further research on the biological potential of these derivatives.

## 5. CONFLICT OF INTEREST

The author of the manuscript declares no conflicts of interest.

## 7. REFERENCES

1. Adams BK, Ferstl EM, Davis MC, Herold M, Kurtkaya S, Camalier RF, et al. Synthesis and biological evaluation of novel curcumin analogs as anti-cancer and anti-angiogenesis agents. Bioorg Med Chem [Internet]. 2004 Jul;12(14):3871–83. Available from: <URL>.

2. Priyadarsini K. The chemistry of curcumin: From extraction to therapeutic agent. Molecules [Internet]. 2014 Dec 1;19(12):20091–112. Available from: <URL>.

3. Weber WM, Hunsaker LA, Abcouwer SF, Deck LM, Vander Jagt DL. Anti-oxidant activities of curcumin and related enones. Bioorg Med Chem [Internet]. 2005 Jun;13(11):3811–20. Available from: <URL>.

4. Martín Ortega AM, Segura Campos MR. Medicinal plants and their bioactive metabolites in cancer prevention and treatment. In: Bioactive Compounds [Internet]. Elsevier; 2019. p. 85–109. Available from: <URL>.

5. El-Kenawy AEM, Hassan SMA, Mohamed AMM, Mohammed HMA. Tumeric or Curcuma longa Linn. In: Nonvitamin and Nonmineral Nutritional Supplements [Internet]. Elsevier; 2019. p. 447–53. Available from: <URL>.

6. Pandey P, Awasthi R, Dhiman N, Sharma B, Kulkarni GT. Ethnopharmacological reports on herbs used in the management of tuberculosis. In: Herbal Medicines [Internet]. Elsevier; 2022. p. 501–23. Available from: <URL>.

7. Dasgupta A. Antiinflammatory herbal supplements. In: Translational Inflammation [Internet]. Elsevier; 2019. p. 69–91. Available from: <URL>.

8. Malik D e shahwar, Pimentel TC, Mahmood NN, Farooqi AA. Antimetastatic effects of curcumin. In:

Unraveling the Complexities of Metastasis [Internet]. Elsevier; 2022. p. 249–58. Available from: <URL>.

9. Francieli da Silva G, Rocha LW, Quintão NLM. Nutraceuticals, dietary supplements, and functional foods as alternatives for the relief of neuropathic pain. In: Bioactive Nutraceuticals and Dietary Supplements in Neurological and Brain Disease [Internet]. Elsevier; 2015. p. 87–93. Available from: <URL>.

10. Huang MT, Lysz thomas, Ferrano T, Abidi TF, Laskin JD, Conney AH. Inhibitory effects of curcumin on *in vitro* lipoxygenase and cyclooxygenase activities in mouse epidermis. Cancer Res [Internet]. 1993;51(3):813–9. Available from: <URL>.

11. Noureddin SA, El-Shishtawy RM, Al-Footy KO. Curcumin analogues and their hybrid molecules as multifunctional drugs. Eur J Med Chem [Internet]. 2019 Nov 15;182:111631. Available from: <URL>.

12. Omidi S, Kakanejadifard A. A review on biological activities of schiff base, hydrazone, and oxime derivatives of curcumin. RSC Adv [Internet]. 2020 Aug 17;10(50):30186–202. Available from: <URL>.

13. Li SB, Song BA, Yang S, Jin LH, Xue W, Zeng S, et al. Synthesis and antifungal activity of novel 1,5-diphenyl- 1,4-pentadien-3-one oxime esters. Chinese J Org Chem [Internet]. 2008;28:311–6. Available from: <URL>.

14. Erdoğan T. The first synthesis of some novel 4-chloro chalcone based oxime Ethers: An experimental and computational study. SDÜ Fen Bilim Enstitüsü Derg [Internet]. 2016 Nov 24;20(3):475–89. Available from: <URL>.

15. Rayar A, Veitía MSI, Ferroud C. An efficient and selective microwave-assisted Claisen-Schmidt reaction for the synthesis of functionalized benzalacetones. Springerplus [Internet]. 2015 Dec 14;4(1):221. Available from: <URL>.

16. Erdogan T. Synthesis, characterization, DFT and molecular docking studies for novel 1,5-diphenylpenta-1,4-dien-3-one O-benzyl oximes. J Iran Chem Soc [Internet]. 2019 Oct 24;16(10):2243–55. Available from: <URL>.

17. Attia M, Zakaria A, Almutairi M, Ghoneim S. *In Vitro* anti-candida activity of certain new 3-(1*H*-Imidazol-1-yl)propan-1-one oxime esters. Molecules [Internet]. 2013 Sep 30;18(10):12208–21. Available from: <URL>.

18. Burgaz EV, Noshadi B, Yakut M. Synthesis, characterization, and optimization of novel furan-ring fused chalcones via radical cyclization of α,β-unsaturated ketones and cyclic ketone. Lett Org Chem [Internet]. 2024 Jun;21(6):534–40. Available from: <URL>.

19. Tang X, Su S, Li Q, He J, Chen M, Chen Y, et al. Synthesis and bioactivity evaluation of penta-1,4-diene-3-one oxime ether derivatives. J Pestic Sci [Internet]. 2019 Nov 20;44(4):242–8. Available from: <URL>.

20. Chen L, Wang X, Tang X, Xia R, Guo T, Zhang C, et al. Design, synthesis, antiviral bioactivities and interaction mechanisms of penta-1,4-diene-3-one oxime ether derivatives containing a quinazolin-4(3H)-one scaffold. BMC Chem [Internet]. 2019 Dec 25;13(1):34. Available from: <URL>.

21. Li JT, Zhai XL, Bai B, Liang YH. An efficient synthesis of 1,5-Diaryl-1,4-pentadien-3-one oxime in the presence of anhydrous sodium sulfate. Lett Org Chem [Internet]. 2010 Jun 1;7(4):323–6. Available from: <URL>.

22. Nasir Abbas Bukhari S, Jasamai M, Jantan I, Ahmad W. Review of Methods and Various Catalysts Used for Chalcone Synthesis. Mini Rev Org Chem [Internet]. 2013 Mar 1;10(1):73–83. Available from: <URL>.

23. Burgaz EV, Yakut M, Kunter İ. Efficient microwave synthesis and anti-cancer evaluation of new substituted 2,4-diazaspiro[5.5]undecane-1,5,9-trione (or 1,3,5,9-tetraone) derivatives. Joule JA, editor. Arkivoc [Internet]. 2024 Dec 9;2024(8). Available from: <URL>.

24. Su S, Chen M, Li Q, Wang Y, Chen S, Sun N, et al. Novel penta-1,4-diene-3-one derivatives containing quinazoline and oxime ether fragments: Design, synthesis and bioactivity. Bioorg Med Chem [Internet]. 2021 Feb;32:115999. Available from: <URL>.

25. Ferreira LOA, Valdo AKSM, Nascimento Neto JA, Ribeiro L, Silva JRD da, Queiroz LHK, et al. ss-NMR and single-crystal X-ray diffraction in the elucidation of a new polymorph of bischalcone (1 *E* ,4 *E* )-1,5-bis(4-fluorophenyl)penta-1,4-dien-3-one. Acta Crystallogr Sect C Struct Chem [Internet]. 2019 Jun 1;75(6):694–701. Available from: <URL>.

26. Naik N, Kumar HV, Swetha S. 1,5-diphenylpenta-1,4 dien-3-ones: A novel class of free radical scavengers. Bulg Chem Commun [Internet]. 2011;43(3):460–4. Available from: <URL>.

Özkan B. JOTCSA. 2025; 12(4): 241-248.

**RESEARCH ARTICLE**

JOURNAL of the Turkish Chemical Society Section: A Chemistry

TURKISH CHEMICAL SOCIETY

# Separation of $Ni^{2+}$ and $Co^{2+}$ Using Sorbitol–Stearic Acid-Derived Bio-Based Solvent: A Sustainable Solvent Extraction Approach

**Bekir Özkan**[1]*

[1]Institute of Nuclear Sciences, Ege University, 35100 Bornova–İzmir, Türkiye.

**Abstract:** The separation of $Ni^{2+}$ and $Co^{2+}$ is challenging due to their similar physicochemical properties. In industrial processes, solvent extraction is widely used for their refinement; however, the excessive use of petroleum-derived solvents poses significant environmental concerns. To address this, a greener approach was explored in this study by utilizing a bio-based solvent synthesized from sorbitol and stearic acid. The resulting solvent, Sorbitol: Stearic Acid ester (2: 1 molar ratio) (SSA2), was prepared via Fischer esterification and employed as the organic phase in solvent extraction experiments. After 5 hours of reaction, the acid value (AV) of SSA2 decreased roughly 87%, indicated ester bond formation and the reduction of carboxylic acid groups, confirming successful synthesis. Fourier transform infrared spectroscopy (FTIR) analysis confirmed the presence of ester bonds in SSA2, which are absent in the starting materials, sorbitol and stearic acid. The separation performance of SSA2 for $Ni^{2+}$ and $Co^{2+}$ was assessed by measuring the distribution coefficient ($K_D$) and separation factor (SF) values as functions of contact time and aqueous phase pH. SSA2 demonstrated higher selectivity towards $Co^{2+}$, achieving a maximum $SF_{Co^{2+}/Ni^{2+}}$ of 6.20 at pH 5. The highest $K_D$ values recorded were 75.6 and 12.2 for $Co^{2+}$ and $Ni^{2+}$ respectively.

**Keywords:** Solvent extraction, Bio-based solvent, Sorbitol-Stearic acid ester, Separation, Nickel and Cobalt ions.

**Submitted:** July 5, 2025. **Accepted:** October 28, 2025.

**Cite this:** Özkan B. Separation of $Ni^{2+}$ and $Co^{2+}$ Using Sorbitol–Stearic Acid-Derived Bio-Based Solvent: A Sustainable Solvent Extraction Approach. JOTCSA. 2025;12(4): 241-8.

**DOI:** https://doi.org/10.18596/jotcsa.1734826

***Corresponding author's E-mail:** bbekir.ozkan@gmail.com

## 1. INTRODUCTION

Metals are among the most abundant elements on Earth and are widely used across various industries due to their unique properties, often without viable alternatives. Although some mechanical properties of metals can be mimicked by polymeric or composite materials, most industries still rely heavily on metals. Particularly catalysts, batteries, alloys, and magnets depend significantly on metals like Ni and Co (1-3).

The primary sources of Ni and Co are ores and other naturally occurring resources, however they can also obtain via recycling scrap metals or spent batteries (4,5). Producing high-purity Ni and Co is crucial for industrial applications because their properties are highly dependent on their purity. As a result, both production routes face significant challenges in the individual separation of $Ni^{2+}$ and $Co^{2+}$ due to their physicochemical similarity (6). Several separation and purification techniques such as adsorption, ion exchange, electro-separation, membrane separation and solvent extraction can be used for the individual separation of $Ni^{2+}$ and $Co^{2+}$ (7-15). Among them solvent extraction stands out for its low operational cost, industrial compatibility and efficiency (16). Within this context numerous solvents and solvent mixtures have been employed for the separation and refinement of $Ni^{2+}$ and $Co^{2+}$ and have been reported in literature.

Parija and Sarma (2000) published a study for the separation of nickel from ammonium containing solutions using LIX84. They aim to separate $Ni^{2+}$ from loaded solvent via stripping and obtained 80% stripping efficiency at pH 1.5 (11). Zhang et al. (2012) benchmarked LIX®1104, LIX®1104SM and Versatic 10 containing LIX®1104 for the individual separation of $Ni^{2+}$ and $Co^{2+}$. The results from solvent extraction study indicated that the affinity towards metal ions can be ordered as Cu≫ Zn> Ni, Co≫ Mn≫ Mg, Ca (12). Nadimi et al. (2017) investigated the effect of citrate ion presence in D2EHPA on $Ni^{2+}$ and $Co^{2+}$ separation via solvent extraction. They reported that the presence of citrate ions in organic phase shifted the extraction to higher pH values. Additionally, increasing pH of aqueous phase increased the separation factor between $Ni^{2+}$ and $Co^{2+}$ (13). Virolainen et al. (2017) utilized cyanex 272 and PC-88A for the separation of $Ni^{2+}$ and $Co^{2+}$ from spent Li-ion batteries. Even though the presence of $Li^{+}$ ions aggravates the individual separation of $Ni^{2+}$ and $Co^{2+}$ they obtained Ni and Co with purity grades exceeding %99 (14). Hanada et al. (2022) synthesized amic-acid based extractants for the separation of $Ni^{2+}$ and $Co^{2+}$ from spent lithium-ion batteries. The separation factor for $Ni^{2+}$ and $Co^{2+}$ was reported to be 57.9 (15).

Solvent extraction techniques proven to be highly efficient for $Ni^{2+}$ and $Co^{2+}$ separation even in the presence of competing ions, however, they fail to address environmental concerns. The main problem with this technique is the excessive usage of petroleum derived solvents (17). This issue is raising environmental concerns because spent solvents are being incinerated in industry particularly in concrete plants (18,19). Industries that play a key role in ensuring a sustainable future, particularly those focused on renewable energy production, will be compelled to source critical raw materials such as Ni and Co with a lower carbon footprint, driven by global environmental policies such as the Green Deal (20-22). For this reason, a more sustainable, cost-effective, and eco-friendly Ni-Co refinement process must be developed (23). Ionic liquids are promising solvents for extraction and are considered environmentally friendly, they are expensive and often complicated to synthesize, which limits their practical application (24,25). In contrast, the utilization of bio-based solvents for the separation and purification of $Ni^{2+}$ and $Co^{2+}$ via solvent extraction offers a viable alternative. These solvents combine the advantages of solvent extraction with biodegradability, low environmental impact, and reduced costs (26). Several bio-based chemicals are already widely used in industries such as detergents, cosmetics, and food. Specifically, sorbitol-stearic acid esters are water-insoluble, chemically robust, and cost-effective materials suitable for solvent extraction. Their synthesis can be achieved through one-step Fischer esterification, further enhancing their economic viability (27-29). The long ester chains in their structure prevent water-solubility while allowing for diverse molecular polarity. Additionally, the partial negative charges on the oxygen atoms of hydroxyl and ester groups may facilitate the extraction of $Ni^{2+}$ and $Co^{2+}$ from aqueous solutions.

In this study we developed a cost-effective and environmentally friendly solvent for the separation of $Ni^{2+}$ and $Co^{2+}$. Within this scope, sorbitol - stearic ester in the molar ratio of 1:2 was synthesized via Fisher esterification in the presence of acidic catalyst and referred as SSA2. The melting point and density of SSA2 were measured, and the acid value (AV) was determined by titration method. The FT-IR diagram was taken and the characteristic peaks of ester bonds on SSA2 were underlined. The performance of the solvent on the individual separation of $Ni^{2+}$ and $Co^{2+}$ was investigated as a function of aqueous phase pH and contact time between organic-aqueous phase. The distribution coefficients ($K_D$) and separation factors (SF) for both $Ni^{2+}$ and $Co^{2+}$ were calculated and presented.

## 2. EXPERIMENTAL SECTION

### 2.1. Materials

The reagents used in the study were of analytical grade or chemical grade and used in the experiments without further purification. Granular shape sorbitol was purchased from ZAG. Stearic acid flakes and phenolphthalein were acquired from AFG Bioscience. Sulfuric acid (98%), potassium hydroxide, methanol and n-heptane were purchased from Merck. Nitrate salts of Ni and Co were obtained from Sigma and used for the preparation of aqueous phase. Ultrapure water (resistivity 18.2 MΩcm, TOC level 1–5 ppb) was prepared by the Millipore model water purification system.

### 2.2. Instrumentation

Perkin Elmer Optima DV 2000 model inductively coupled plasma optical emission spectrometry (ICP-OES) was employed for the determination of $Ni^{2+}$ and $Co^{2+}$ in aqueous solutions. pH adjustments were made using Mettler Toledo Seven Compact pH meter S210. FTIR diagrams of stearic acid, sorbitol and SSA2 were determined using Perkin Elmer Spectrum Two FTIR-ATR.

### 2.3. Synthesis of SSA2

2 moles of stearic acid was charged into 500 mL flask and melted at 60 °C, then 1-2 drops of 98% $H_2SO_4$ was added onto liquified stearic acid as a catalyst for Fisher esterification. The mixture was stirred for 5 min. and 1 mole of sorbitol powder was poured onto the mixture. The reaction temperature was set to 200 °C and samples were taken each hour to determine AV of SSA2. SSA2 then let to cool at ambient temperature after 5h of reaction time and filtered to eliminate the residual sorbitol. A schematic explanation of the synthesis equipment was given in Figure 1. The synthesis procedure was adopted from a previous study 27.

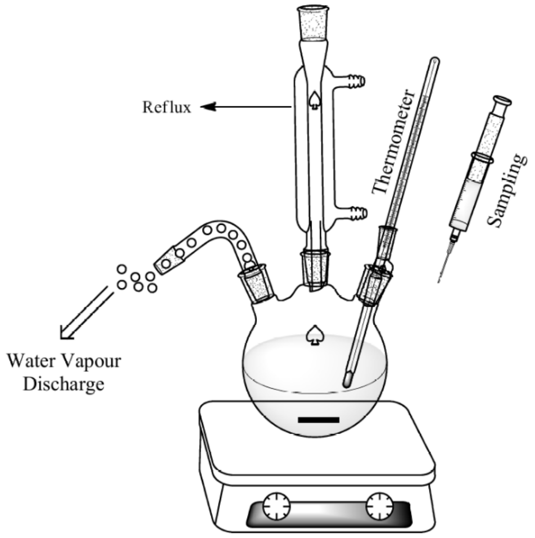

**Figure 1:** Schematic presentation of experimental setup for SSA2 synthesis (27).

## 2.4. Determination of Acid Value

Each hour a sample was taken from the synthesis chamber and 0.1 g of SSA2 was dissolved in 25 mL of n-heptane. Then, 3-4 drops of 1% phenolphthalein containing methanol were added onto the solution as an indicator. The sample was then titrated with methanol - KOH solution containing 0.02 mol/L KOH and when the color shift was observed the spent volume of titrator was noted and AV of the sample was calculated according to Eq. 1. The acid value of SSA2 was determined using a KOH titration method commonly employed for oil samples, following a similar approach reported by Luis et al. (2019) (30).

$$AV = (V_{eq} - V_{Beq})\ x\ N\ x\ \frac{56.1\ g/mol}{W_{SSA2}} \quad (1)$$

$V_{eq}$: Spent KOH solution volume for sample (mL)
$V_{Beq}$: Spent KOH solution volume for blank (without oil sample) (mL)
$N$: Normality of the KOH solution (N)
*56.1 g/mol*: molar mass of the KOH
$W_{SSA2}$: Mass of SSA2 (g)

## 2.5. Density Measurement

The density of SSA2 was measured using a pycnometer at 65 °C, corresponding to the temperature used in the solvent extraction experiments. 25 mL pycnometer weighed in a scale and then filled with deionized water at 65°C and weighed again. The exact volume of the pycnometer was calculated. Then the pycnometer was dried and filled with SSA at 65 °C and weighed once again and the density of SSA2 calculated using Eq. 2.

$$\text{SSA2 Density: } \frac{c-a}{PV} \quad (2)$$

$$\text{Pycnometer Volume (PV): } \frac{b-a}{d_{water}}$$

a: Mass of empty pycnometer (g)
b: Mass of water filled pycnometer (g)
c: Mass of SSA2 filled pycnometer (g)
$d_{water}$: Density of deionized water (g/mL)

## 2.6. Melting Point Determination

100 g of SSA2 was melted at 75 °C and put into freezer at -20 °C with an attached thermometer. Then a solidification was monitored and noted, the process was repeated 3 times, and the average melting point was given in result and discussion section.

## 2.7. Solvent Extraction Experiments

As an aqueous phase 50 mg/L $Ni^{2+}$ and $Co^{2+}$ containing solution was used. 80 mL of aqueous phase and 20 mL SSA2 as an organic phase were put into glass flask. The temperature was set to 65 °C and stirred with a mixer settler extraction apparatus. Samples were taken from aqueous phase and analyzed with ICP-OES to determine the concentration of $Ni^{2+}$ and $Co^{2+}$. In all solvent extraction experiments were carried out with 1:4 organic phase: aqueous phase ratio. The effects of contact time (5-120 min.) and aqueous phase pH (1-5) on KD and SF values were investigated. KD and SF values were calculated using Eq. 3 and Eq. 4 respectively.

$$K_D = \frac{C_0 - C_e}{C_e} \times \frac{V_{aq}}{V_{org}} \quad (3)$$

$$SF_{Co2+/Ni2+} = \frac{KD_{Co2+}}{KD_{Ni2+}} \quad (4)$$

$C_0$: Initial concentrations of metal ions (mg/L)
$C_e$: Equilibrium concentrations of metal ions (mg/L)
$V_{aq}$: Volume of the aqueous phase (mL)
$V_{org}$: Volume of the organic phase (mL)
$K_{DNi}$ and $K_{DCo}$: Distribution coefficients of $Ni^{2+}$ and $Co^{2+}$
$SF_{Co,Ni}$: Separation factor value used as an indicator in separating $Co^{2+}$ from $Ni^{2+}$

## 3. RESULTS AND DISCUSSION

## 3.1. Acid Value Determination

Samples were taken from synthesis medium for 60 min. intervals for 300min. and subjected to KOH titration to determine the AV of SSA2. In theory, Fisher esterification continues the -OH groups of sorbitol and -COOH group of stearic acid react to form ester group (-COOR) and $H_2O$ as byproduct. As a result, the acid value must decrease with the continuing reaction.

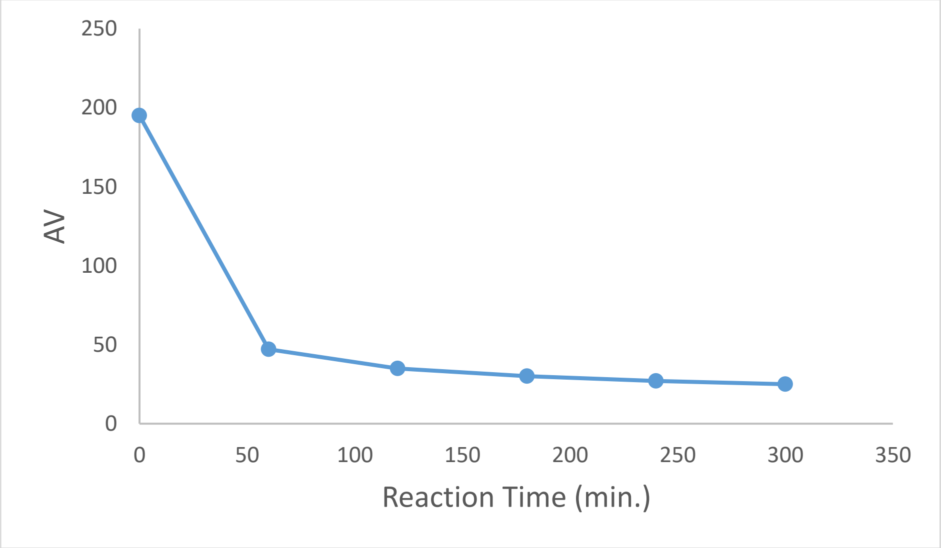

**Figure 2:** Acid value of SSA2 as a function of reaction time.

Figure 2 shows that there was a sharp decrease observed in AV within an hour of reaction at 200 °C. The decrease continued through the synthesis experiment since the reaction between stearic acid and sorbitol continues. However, due to lesser free stearic acid in the media and the formed ester groups on sorbitol started to slow down the reaction rate. At the beginning of the reaction the acid value was 195 and decreased to 25, which means more than 87% of stearic acid reacted with sorbitol. In further studies 120 min. reaction time might be more feasible to save energy.

### 3.2. FTIR Analysis of SSA2

The FT-IR diagram of SSA2 was presented in Figure 3 and comparable FTIR diagram that contains sorbitol, stearic acid, and SSA2 was given in Figure 4. In the FTIR diagram of SSA2 the peaks at 2920.8 cm$^{-1}$ and 2851.8 cm$^{-1}$ are attributed to C-H stretching and peak observed at 1467.9 cm$^{-1}$ could be belonging to $CH_2$ scissoring. The sharp peak at 1732.3 cm$^{-1}$ corresponds to C=O stretching of ester group and the peaks at 1168.2 cm$^{-1}$ and 1094.6 cm$^{-1}$ attributes to asymmetric stretching of C-O bonds in ester group. The peak at 723.9 cm$^{-1}$ belongs to O-C=O bending in SSA2's ester groups. Similar peaks were reported in a study published by Khan et al. (2015) (31).

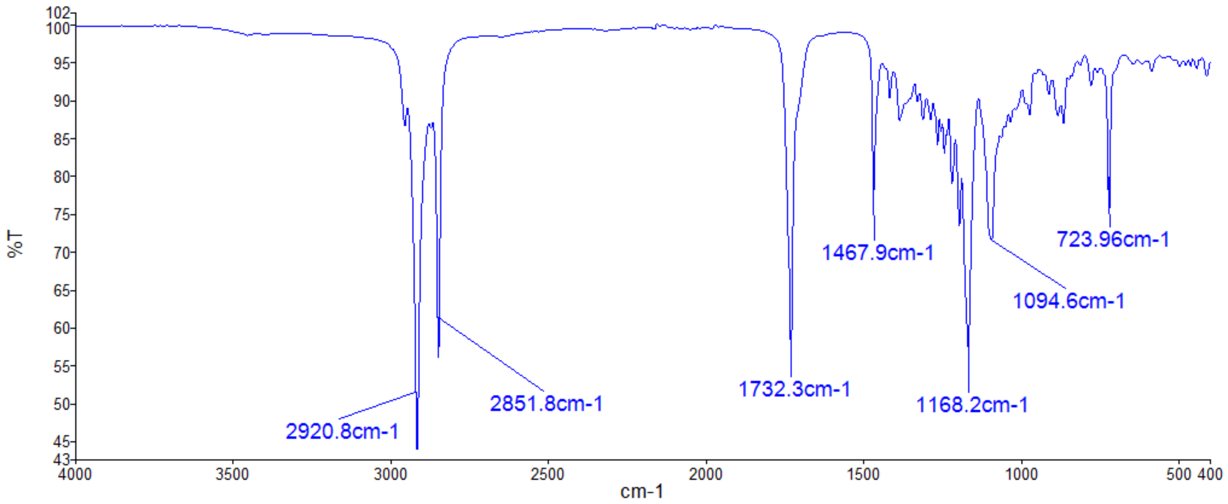

**Figure 3:** FTIR diagram of SSA2.

Figure 4 shows that characteristic peak of SSA2 between 1732 cm$^{-1}$ and 1172 cm$^{-1}$ are unique for SSA2 and can't be observed in stearic acid or in sorbitol. Therefore, it can be outlined that SSA2 was synthesized in ester form by reacting sorbitol and stearic acid via Fisher esterification.

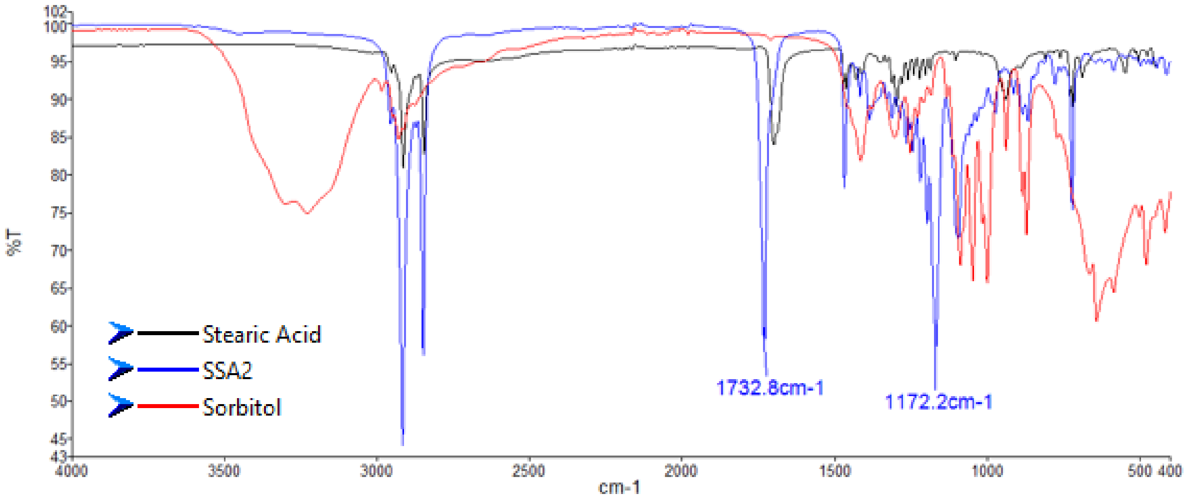

**Figure 4:** FTIR diagram of SSA2, sorbitol, and stearic acid.

### 3.2. Density Measurement and Melting Point

The density of SSA2 was determined at 65 °C and measured to be 0.919 g/mL. The melting point of SSA was determined from three repeated measurements as 48 ± 0.3 °C.

### 3.3. Solvent Extraction Studies

The initial pH of the aqueous phase was adjusted using ammonia or sulfuric acid solutions in 1 mol/L concentration. All solvent extraction experiments carried out at 65 °C temperature and 250 rpm mixing rate. The organic/aqueous phase ratio was set to 1:4 and kept constant for all extraction experiments. The $K_D$ values were investigated as a function of contact time and initial aqueous phase pH. The $K_D$ values of $Ni^{2+}$ and $Co^{2+}$ were presented in Figure 5 (a-e).

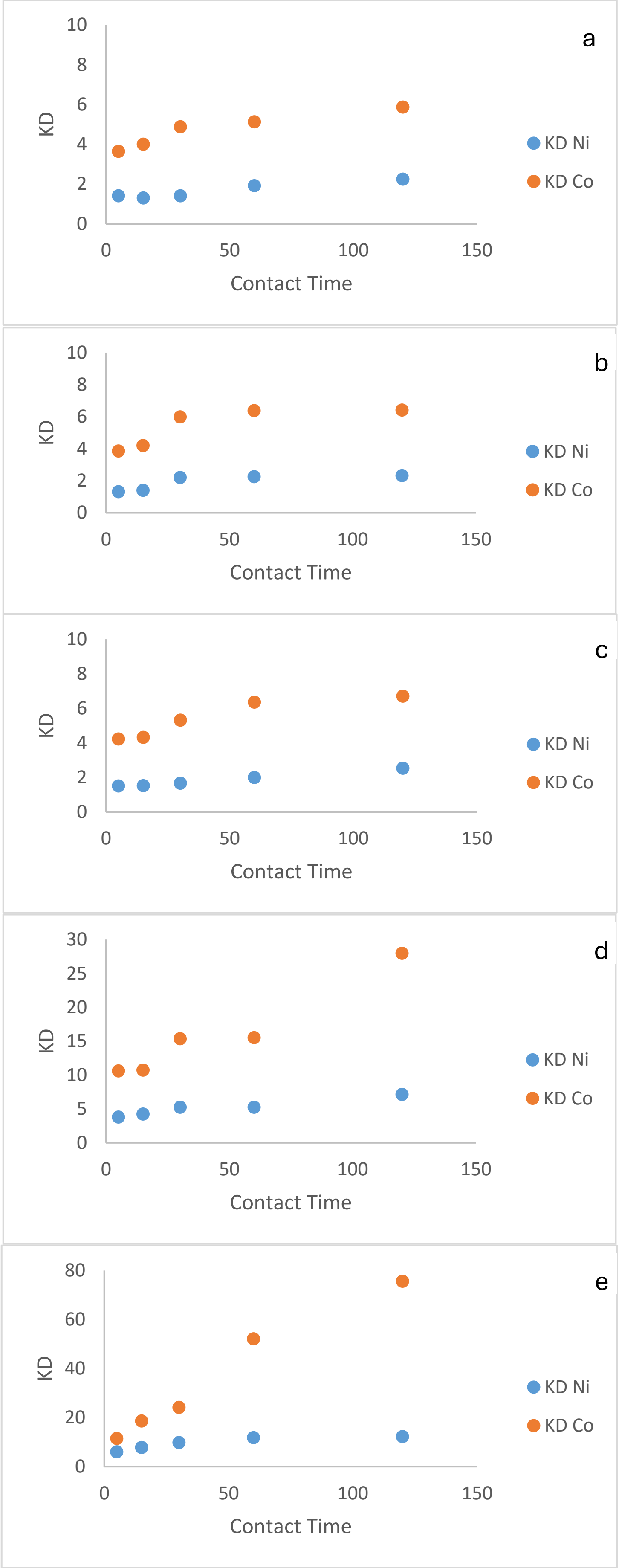

**Figure 5:** The KD values of $Ni^{2+}$ and $Co^{2+}$ as a function of contact time, a): pH 1, (b): pH 2, (c): pH 3, (d): pH 4 and (e): pH 5.

In the experiments, the $K_D$ values of $Ni^{2+}$ and $Co^{2+}$ showed an increasing trend over time. At pH 1, 2 and 3 the extraction of both $Ni^{2+}$ and $Co^{2+}$ nearly stabilized after 60 minutes of contact time. However, at pH 4 and 5 (as shown in Figure 5 (d–e)), the $K_D$ values for $Co^{2+}$ continued to rise even after 60 minutes. $K_D$ values of both $Ni^{2+}$ and $Co^{2+}$ demonstrated an increasing trend with increasing aqueous phase pH, potentially due to lower competition between $H^+$ ions and $Ni^{2+}/Co^{2+}$. Therefore, the highest $K_D$ values were obtained at pH 5. It can be observed that, this increasing effect was more pronounced for $Co^{2+}$, enabling effective separation of $Co^{2+}$ from $Ni^{2+}$ at pH 4-5 with a contact time of 120 minutes.

*Separation Factors*

The $SF_{Co^{2+}/Ni^{2+}}$ values are presented in accordance with pH values in Table 1. The data show that the highest separation factors were observed at pH 4 and pH 5 with a contact time of 120 minutes. This suggests that extraction of $Ni^{2+}$ ions are slower than $Co^{2+}$ ions and additionally, SSA2 is more selective towards $Co^{2+}$. Consequently, increasing the pH enhances the separation factor between $Ni^{2+}$ and $Co^{2+}$ in higher contact times.

**Table 1:** $SF_{Co^{2+}/Ni^{2+}}$ values in between pH 1–5.

| Contact time min. | pH 1 | pH 2 | pH 3 | pH 4 | pH 5 |
|---|---|---|---|---|---|
| 5 | 2.60 | 2.95 | 2.83 | 2.81 | 1.92 |
| 15 | 3.07 | 2.99 | 2.84 | 2.54 | 2.39 |
| 30 | 3.47 | 2.71 | 3.21 | 2.94 | 2.46 |
| 60 | 2.68 | 2.84 | 3.19 | 2.95 | 4.41 |
| 120 | 2.61 | 2.77 | 2.65 | 3.93 | 6.20 |

In the literature, various solvents and solvent systems have been investigated for the separation of $Ni^{2+}$ and $Co^{2+}$ ions. In this context, Sarangi et al. (1999) studied the separation performance of PC88A and Cyanex 272, reporting separation factors $SF_{Co^{2+}/Ni^{2+}}$ ranging from 12.3 to 71.8 for PC88A and 252 to 6972 for Cyanex 272 (32). Nadimi et al. (2017) evaluated the use of D2EHPA for $Ni^{2+}$ and $Co^{2+}$ separation, where $SF_{Co^{2+}/Ni^{2+}}$ values varied between 2 and 5.5 depending on the pH, specifically at pH values of 3 and 5 (13). Wellens et al. (2013) conducted separation experiments using ionic liquids, achieving $SF_{Co^{2+}/Ni^{2+}}$ values of 207 and 733 under optimized conditions (33). Similarly, Hereijgers et al. (2016) reported that Cyanex 272 exhibited separation factors around 1400, highlighting its high selectivity for $Co^{2+}$ over $Ni^{2+}$ (34). The separation factors obtained in the present study are comparable to those of D2EHPA but lower than those reported for Cyanex 272. The summary of the literature comparable with the manuscript is presented in Table 2.

**Table 2:** Comparison summary of $SF_{Co^{2+}/Ni^{2+}}$ between literature and SSA2.

| Solvent | Solvent Type | pH | Separation Factor | Reference No. |
|---|---|---|---|---|
| D2EHPA | Acidic | 4.5 | 5.5 | 13 |
| Na-PC88A | Ionic | 5.7 | 71.8 | 32 |
| Na-D2EHPA | Ionic | 5.2 | 12.3 | 32 |
| Na-Cyanex 272 | Ionic | 6.5 | 6972 | 32 |
| Cyphos IL 104 | Ionic | - | 207 | 33 |
| 1-ethyl-3-methylimidazolium chloride | Ionic | - | 733 | 33 |
| Cyanex 272 | Acidic | 6-7 | 1400 | 34 |
| SSA2 | Neutral | 5 | 6.2 | This Study |

## 4. CONCLUSION

In conclusion, SSA2 was synthesized with over 87% efficiency and made a valuable contribution to Ni–Co separation by promoting sustainable chemical practices. SSA2 demonstrated a higher affinity for $Co^{2+}$ than for $Ni^{2+}$ throughout the study. At lower pH values, the high concentration of $H^+$ ions limited the effective extraction of both metals. As the pH increased, the $K_D$ rose significantly, especially for $Co^{2+}$, with the highest value observed at pH 5. The maximum separation factor $SF_{Co^{2+}/Ni^{2+}}$ was achieved at pH 5, reaching 6.20 in favor of $Co^{2+}$. Due to the non-ionic nature of SSA2, its extraction capacity and SF in a single stage is relatively low; however, this limitation could be addressed by introducing carboxylic acid salts, such as sodium citrate into SSA2. Furthermore, structural modifications to SSA2 may enhance its selectivity for $Co^{2+}$, allowing its performance to approach that of commercial extractants like Cyanex 272. Future research should focus on employing bio-based solvents like SSA2 to help lower the carbon footprint of metal production, separation, and refinement processes.

## 5. CONFLICT OF INTEREST

The author would like to confirm that there is no conflict of interest.

## 6. ACKNOWLEDGMENTS

Author would like to thank TUBİTAK for the financial support of this work with Project No: 123C318. Additionally, author would like to thank Prof. Dr. Süleyman İNAN for his support and guidance.

## 7. REFERENCES

1. Alvial-Hein G, Mahandra H, Ghahreman A. Separation and recovery of cobalt and nickel from end of life products via solvent extraction technique: A review. J Clean Prod [Internet]. 2021 May;297:126592. Available from: <URL>.

2. Kerns J. Replacing metal with plastic. Mach Des [Internet]. 88(9):34–42. Available from: <URL>.

3. Cutler CP. Use of metals in our society. In: Metal Allergy [Internet]. Cham: Springer International Publishing; 2018. p. 3–16. Available from: <URL>.

4. Garrett RG. Natural sources of metals to the environment. Hum Ecol Risk Assess An Int J [Internet]. 2000 Nov;6(6):945–63. Available from: <URL>.

5. Meshram P, Abhilash, Pandey BD. Advanced review on extraction of nickel from primary and secondary sources. Miner Process Extr Metall Rev [Internet]. 2019 May 4;40(3):157–93. Available from: <URL>.

6. Taghdirian HR, Moheb A, Mehdipourghazi M. Selective separation of Ni(II)/Co(II) ions from dilute aqueous solutions using continuous electrodeionization in the presence of EDTA. J Memb Sci [Internet]. 2010 Oct;362(1–2):68–75. Available from: <URL>.

7. Sun P, Binter EA, Vo T, Benjamin I, Bera MK, Lin B, et al. Relevance of surface adsorption and aqueous complexation for the separation of Co(II), Ni(II), and Fe(III). J Phys Chem B [Internet]. 2023 Apr 20;127(15):3505–15. Available from: <URL>.

8. Juang RS, Wang YC. Use of complexing agents for effective ion-exchange separation of Co(II)/Ni(II) from aqueous solutions. Water Res [Internet]. 2003 Feb;37(4):845–52. Available from: <URL>.

9. Armstrong RD, Todd M, Atkinson JW, Scott K. Electroseparation of cobalt and nickel from a simulated wastewater. J Appl Electrochem [Internet]. 1997 Aug;27(8):965–9. Available from: <URL>.

10. Gega J, Walkowiak W, Gajda B. Separation of Co(II) and Ni(II) ions by supported and hybrid liquid membranes. Sep Purif Technol [Internet]. 2001 Mar 1;22–23(1–2):551–8. Available from: <URL>.

11. Parija C, Bhaskara Sarma PV. Separation of nickel and copper from ammoniacal solutions through co-extraction and selective stripping using LIX84 as the extractant. Hydrometallurgy [Internet]. 2000 Jan;54(2–3):195–204. Available from: <URL>.

12. Zhang W, Pranolo Y, Urbani M, Cheng CY. Extraction and separation of nickel and cobalt with hydroxamic acids LIX®1104, LIX®1104SM and the mixture of LIX®1104 and Versatic 10. Hydrometallurgy [Internet]. 2012 May;119–120:67–72. Available from: <URL>.

13. Nadimi H, Haghshenas Fatmehsari D, Firoozi S. Separation of Ni and Co by D2EHPA in the presence of citrate ion. Metall Mater Trans B [Internet]. 2017 Oct 1;48(5):2751–8. Available from: <URL>.

14. Virolainen S, Fallah Fini M, Laitinen A, Sainio T. Solvent extraction fractionation of Li-ion battery leachate containing Li, Ni, and Co. Sep Purif Technol [Internet]. 2017 May;179:274–82. Available from: <URL>.

15. Hanada T, Seo K, Yoshida W, Fajar ATN, Goto M. DFT-Based investigation of Amic–Acid extractants and their application to the recovery of Ni and Co from spent automotive Lithium–Ion batteries. Sep Purif Technol [Internet]. 2022 Jan;281:119898. Available from: <URL>.

16. Petrow HG. Solvent extraction. (No. TID-11938) National lead Co Inc raw materials development lab winchester mass. 1956.

17. Cvetanović A. Extractions without organic solvents: Advantages and disadvantages. Chem Africa [Internet]. 2019 Sep 15;2(3):343–9. Available from: <URL>.

18. Capello C, Hellweg S, Badertscher B, Betschart H, Hungerbühler K. Environmental assessment of waste-solvent treatment options. J Ind Ecol [Internet]. 2007 Oct 8;11(4):26–38. Available from: <URL>.

19. Luis P, Amelio A, Vreysen S, Calabro V, Van der Bruggen B. Life cycle assessment of alternatives for waste-solvent valorization: Batch and continuous distillation vs incineration. Int J Life Cycle Assess [Internet]. 2013 Jun 18;18(5):1048–61. Available from: <URL>.

20. Smol M, Marcinek P, Duda J, Szołdrowska D. Importance of sustainable mineral resource management in implementing the circular economy (CE) model and the european green deal strategy. Resources [Internet]. 2020 May 5;9(5):55. Available from: <URL>.

21. Petrova V. The european green deal and its impact on the raw material industry. Sustain Extr Process Raw Mater J [Internet]. 2021;2:47–53. Available from: <URL>.

22. An Z, Zhao Y, Zhang Y. Mineral exploration and the green transition: Opportunities and challenges for the mining industry. Resour Policy [Internet]. 2023 Oct;86:104263. Available from: <URL>.

23. Schuur B, Brouwer T, Smink D, Sprakel LMJ.

Green solvents for sustainable separation processes. Curr Opin Green Sustain Chem [Internet]. 2019 Aug;18:57–65. Available from: <URL>.

24. Flieger J, Flieger M. Ionic liquids toxicity—benefits and threats. Int J Mol Sci [Internet]. 2020 Aug 29;21(17):6267. Available from: <URL>.

25. Chiappe C, Pieraccini D. Ionic liquids: Solvent properties and organic reactivity. J Phys Org Chem [Internet]. 2005 Apr 21;18(4):275–97. Available from: <URL>.

26. Vovers J, Smith KH, Stevens GW. Bio-based molecular solvents. In: The Application of Green Solvents in Separation Processes [Internet]. Elsevier; 2017. p. 91–110. Available from: <URL>.

27. Özkan B, İnan S. Synthesis of bio-based solvents derived from sorbitol and stearic acid for the separation of Th, U, and REEs: A solvent extraction study. J Radioanal Nucl Chem [Internet]. 2025 Sep 4;334(9):6677–91. Available from: <URL>.

28. Ahsan F, Arnold JJ, Meezan E, Pillion DJ. Sucrose cocoate, a component of cosmetic preparations, enhances nasal and ocular peptide absorption. Int J Pharm [Internet]. 2003 Jan;251(1–2):195–203. Available from: <URL>.

29. Chansanroj K, Betz G. Sucrose esters with various hydrophilic–lipophilic properties: Novel controlled release agents for oral drug delivery matrix tablets prepared by direct compaction. Acta Biomater [Internet]. 2010 Aug;6(8):3101–9. Available from: <URL>.

30. Zhang J, Lu M, Ren F, Knothe G, Tu Q. A greener alternative titration method for measuring acid values of fats, oils, and grease. J Am Oil Chem Soc [Internet]. 2019 Oct 27;96(10):1083–91. Available from: <URL>.

31. Khan MI, Madni A, Ahmad S, Mahmood MA, Rehman M, Ashfaq M. Formulation design and characterization of a non-ionic surfactant based vesicular system for the sustained delivery of a new chondroprotective agent. Brazilian J Pharm Sci [Internet]. 2015 Sep;51(3):607–15. Available from: <URL>.

32. Sarangi K, Reddy BR, Das RP. Extraction studies of cobalt (II) and nickel (II) from chloride solutions using Na-Cyanex 272. Hydrometallurgy [Internet]. 1999 Jun;52(3):253–65. Available from: <URL>.

33. Wellens S, Thijs B, Möller C, Binnemans K. Separation of cobalt and nickel by solvent extraction with two mutually immiscible ionic liquids. Phys Chem Chem Phys [Internet]. 2013;15(24):9663–9. Available from: <URL>.

34. Hereijgers J, Vandermeersch T, Van Oeteren N, Verelst H, Song H, Cabooter D, et al. Separation of Co(II)/Ni(II) with Cyanex 272 using a flat membrane microcontactor: Extraction kinetics study. J Memb Sci [Internet]. 2016 Feb;499:370–8. Available from: <URL>.

Yıldız Akdağ B. JOTCSA. 2025; 12(4): 249-268. **REVIEW ARTICLE**

JOURNAL OF THE TURKISH CHEMICAL SOCIETY SECTION: A CHEMISTRY

TURKISH CHEMICAL SOCIETY

# Phase Separation Challenges in Borosilicate Nuclear Glasses and Strategies for Vitrification Improvement

**Berna Yıldız Akdağ**[1*]

[1]Turkish Energy, Nuclear and Mineral Research Agency.

**Abstract:** This review highlights three main topics: advancements in vitrification technology and associated issues like melter corrosion in global facilities, the chemistry and networking of glassy and frit forms of waste, and improvements in vitrified structures that enhance the properties of glass formulations. Borosilicate glass formulations offer various technical advantages for nuclear waste management, including effective bonding with fission products and actinides, resistance to radiation, simple and safe technology, and low leaching tendencies in aqueous environments. The maximum results indicate that the vitrification facility in Tarapur, India, 43.8% waste loadings with 6.4% $B_2O_3$ in the glass composition, while Savannah River Site in the USA processes waste loadings of up to 50 wt% with 6% $B_2O_3$ in the glass composition. In the IAEA-TECDOC, it is stated that considering spent fuel borosilicate glasses are suitable matrices for the immobilising up to 13 wt % of $UO_2$ or 6 wt % of $PuO_2$. However, borosilicate glasses may face issues when the molybdenum ratio in the waste exceeds certain limits, potentially leading to phase separation in the vitrified network. This review covers the importance of waste management policies and provides a historical overview of nuclear waste glass in different countries.

**Keywords:** Nuclear glass, Radioactive waste, Borosilicate.

**Submitted:** August 11, 2025. **Accepted:** November 2, 2025.

**Cite this:** Yıldız Akdağ B. Phase Separation Challenges in Borosilicate Nuclear Glasses and Strategies for Vitrification Improvement. JOTCSA. 2025;12(4): 249-68.

**DOI:** https://doi.org/10.18596/jotcsa.1760055

***Corresponding author's E-mail:** bernayildizakdag@gmail.com

## 1. INTRODUCTION

Management the waste of nuclear power plants is troublesome. Besides preservation of the recovering U and Pu radioisotopes for reuse; the high-level radioactive wastes (HLW) must be disposed of. This involves immobilisation the waste and deposition in safe places to protect both human and environmental health. Nuclear waste must be trapped in a matrix whose microstructure should be compatible with the waste formulation to bond and form a network. This is to avoid the leaching radioactive materials into the biosphere, harming human life, and polluting the environment on site of deposit. The best immobilization form is solid state. Glass is the best material of all options for vitrification or encapsulation of HLW because of its favourable chemical and radiation resistance, as well as thermal stability.

Based on the Power Reactor Information System Database (2022) gathered by the IAEA, 440 nuclear reactors are still functioning for energy production. There are an additional 54 plants under construction. Thus, radioactive waste is produced. Mainly, fission products, long-lived beta-particle and gamma-ray emitting (Se, Zr, Tc, Pd, I, and Cs) are decay radioisotopes in the inventory. Besides, Np, Am, Cm, and Cf are also present in the waste (1).

Countries started handle with the solidification processes and way out (2). In Europe, except Russia and Slovakia, more than 60,000 tons of spent nuclear fuel are deposited in varied forms. The EU countries' part is 57,000 tons. France alone stores 25% of the EU's spent nuclear fuel inventory. The second is Germany with 15% and the UK is third one with 14%. France, the UK, and Russia reprocessed their spent nuclear fuel, besides this, on behalf of most countries their spent nuclear fuel as well. In the 1990s, Russia first demanded that Hungary return residual radioactive waste generated during reprocessing. Vitrified waste (mostly high-level radioactive waste) is returned to the country of origin. To resolve this arisen problem, Hungary decided to construct a storage facility in 1993 due to

1,261 tons of spent nuclear fuel and 102 m³ of high-level radioactive waste to store (2016). Despite the signed long-term commercial agreement with Russia on reprocessing service, Bulgaria ceased all spent nuclear fuel shipments in 2014. The countries like Finland, had to deal with waste management strategy plans too (3).

A thermodynamic approach to predict metallic and oxide phase precipitations in nuclear waste glass melts was first presented at the 2nd International Summer School on Nuclear Glass Wasteform: Structure, Properties, and Long-Term Behaviour held in 2013 in France (4,5). This topic remained of significant interest and was revisited in the 2017 Joint ICTP–IAEA Workshop on Fundamentals of Vitrification and Vitreous Materials for Nuclear Waste Immobilisation, also in Marseille, France. During this workshop, thermodynamic modeling of nuclear waste glasses was identified as one of the core subjects. Particular attention was given to thermodynamic functions derived from relationships between fundamental thermodynamic quantities of glass, highlighting both experimental techniques for the determination of these quantities and computational approaches, such as the CALPHAD method, the Ideal Associated Solution Model, and other technical approximations.

Further advancements in this domain were featured in the 3rd Summer School on Nuclear and Industrial Glasses for Energy Transition, held in 2023 in Nîmes, France. It is emphasized modeling of both the thermodynamic and chemical mechanisms as well as the physico-chemical properties of glass and melt (6). Among the prominent issues discussed was the modeling of glass properties and their impact on glass production rate in electric melters. Key technological factors such as heat flux, gas bubbling, and foam layer parameters were identified as critical variables influencing the vitrification process (7).

Additionally, the phenomenon of phase separation, a central topic in this review, was discussed in detail. The 2023 Summer School addressed thermodynamic models for phase separation and crystallization in nuclear waste glasses, underscoring their importance for understanding glass stability and long-term performance (8,9).

Valuable studies aimed at understanding radiation effects and enabling predictive modeling of nuclear waste glass behaviour were presented at the 2nd SumGLASS School in 2013. One notable contribution is referenced in Weber's study (10). There are very few earlier foundational work such as that in Weber's another study (11). Prior to these, only a limited number of studies had been conducted in this area. More recently, the effects of gamma radiation on various properties of glass and glass-ceramic matrices used for nuclear waste immobilisation have been investigated. These include studies on ageing and gamma-induced structural changes, small density changes as a result of atomic displacements in nuclear glass as reported in references (12), (13) and (14), from research conducted across the globe.

Recently, description and modeling of chemical reactions in the feed of vitrification of high-level nuclear waste, (15) and the problems due to the sulphur solubility as $SO_3$ have been analysis at full speed (16,17). Improving the processes involved to minimize the waste form on Hanford tanks is an important issue that taken into consider in the review of Marcial et al. (18).

In the consideration of gap analysis in the research area, the structural improvement studies have been successfully conducted and are continuing without delay. However, a gap remains in the evaluation and "the comparison of high self-radiation stability of the glass with the recently proposed alternative matrices". It is necessary to further investigate and emphasize the material's radiation stability, particularly in comparison to alternative matrices such as geopolymers. Demonstrating a clear advantage in radiation resistance over other matrix materials will significantly strengthen the case for its application. Preliminary findings suggest that the self-radiation stability of the material surpasses that of alternative matrices, and this superior performance should be clearly validated and highlighted.

## 2. ASSESMENT OF METHODS AND RESULTS

The content of the review is branching as shown in Figure 1:

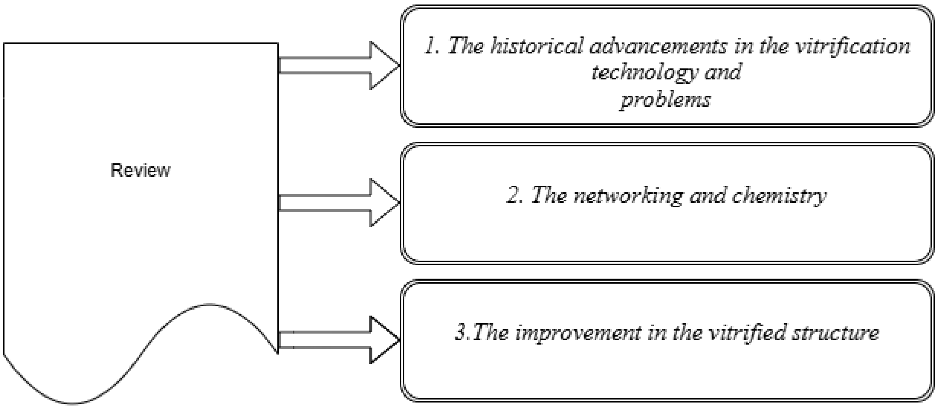

**Figure 1:** The branching of the content.

### 2.1. Historical Advancements in the Vitrification Technology and Problems

#### *2.1.1. The history of French vitrification advancements*

The criteria outlined for selecting countries and facilities act as the principal initiators of this process and its technologies, and they are the first to carry out the selection of these matrices. High-level nuclear waste vitrification in France started with the first radioactive glass at Saclay in 1957 (2).

PIVER facility at Marcoule processed 200 kg vitrified radioactive solutions in 1968 by a sol-gel process. Induction heating is used for the melting step of waste glass feed in a metal melter. Between 1969 and 1973, PIVER converted 25 m$^3$ of radioactive waste solution into 12 tons of glass by vitrification, earning the ANS Nuclear Historic Landmark Award of 1989 (2).

The two-step procedure model of calcination and vitrification, first developed in France, involved treating fission decay solutions in a calciner and melting the glass. This success led to construct a new plant with lines at La Hague. The British Nuclear Fuels Limited, (BNFL) adopted this two-step process for their Sellafield Vitrification Facility starting in 1990 (2).

Advancements in technology have continued, including the development of the Cold Crucible Induction Melter (CCIM), which allows the processing of highly corrosive solutions not manageable with traditional metallic melters at temperatures that exceed those achievable with metallic melter (2).

French R7T7, a type of nuclear glass which consists of more than thirty oxides, (see in Table 4) agreed upon that this type of trapping of fission products and simple actinide elements by bonding in the structure and immobilizing for long-term disposal (19).

#### *2.1.2. Nuclear waste vitrification processes with featured technological aspects*

The Environmental Protection Agency of the USA (EPA) stated that vitrification is the Best Demonstrated Available Technology with the aim of the disposal of HLW, in spite of high energy need for the treatment and producing volatile species. Vitrification of radioactive wastes into a glass is the right choice because the radioactive elements become atomically bonded within the glassy state. Hence, the waste forms remain highly durable over a long period. Joule heating and plasma technologies are both featured electric vitrification processings as well as former sol-gel process (20).

Sol-gel process: Typically, silicate glasses, which may include high-level nuclear waste components Cs, Sr, Co, and Nd (following actinides), are produced through a complex sol-gel process. An advantage of this approach is that some radioactive elements form resulting small volumes of mechanically robust waste inventory (21).

Joule-heated ceramic melter technology: Pd, Ru and Cu were recovered approximately 74%, 82%, and 93%, respectively, from the high level waste (HLW) using the canister to use Joule heating at process temperature 1473 K i n 1h. The glass formers, modifiers and radioactive waste were put into the canister (20).

55 million gallons of waste from recovery of the irradiated nuclear were at under ground of Hanford region, Washington State, by 2011. Joule-heated melter technology for the treatment and immobilization of low activity waste was developed. The waste is pretreated for Cs removing by ion exchange column before the transition to vitrification pool for melting. Table 1 has been created to show some critical aspects to consider and plan prevention actions considering the informations mentioned in the article of Kelly et al., 2011 (22).

**Table 1:** Critical aspects of joule-heated melter technology and risk management.

| No | Main Potential Risks of Process | Risk-based improvement plans |
|---|---|---|
| 1 | Leaks, spills and contamination risks for workers during waste transfer | Risk analysis and planning prevention actions (generate risk matrices and control the risks) |
| 2 | Gases from decomposition, oxidation and vaporization of feed content | |
| 3 | Flammable gas generation like hydrogen during | |
| 4 | Off-gas Release from Melter, toxic gases $NO_2$, NO | |
| 5 | Hg removing from Off-gas system | |
| 6 | Ammonia Release to workers or environment | |

The advantages of the Joule Heating Ceramic Melter (JHCM) and the zones in the vertical JHCM with cone-shaped bottom and cold-cap structure in horizontally oriented JHCM with flat bottom design are well-documented in practice for HLW vitrification in the paper of Yang et al. Boiling feed, reacting solids, compaction, formed foam and molten glass illustrated for clarify the zones inside (23).

Plasma technology for treatment and technical aspects and Plasma pilot plant: Plasma technology has 3 critical advantages: getting smaller gas flow rate to the environment, reaching high vitrification temperature with plasma and manage the release of toxic by-products. Nevertheless, in the plasma system design some vital improvements are needed. One of them is in air compressor pump for effective gas combustion, the second coming is in combustion chamber for good enough fully vacuum with negative pressure difference for prevent gas releases to out of the chamber system. Considering environment, the chimney height should be high enough in the waste treatment plant design. The power of exhaust fan is crucial, therefore improvement should done. Controlling of HEPA filter is another performance factor of the plasma system. Besides all, software validation and system measurement calibration should check periodically. Table 2 shows us that highly reachable vitrification temperatures is reachable with this process. It has been set up gathering the data of Salihuddin et al., to mark the high temperatures (24).

**Table 2:** Vitrification temperatures in plasma technology depending on current.

| Current | Voltage | Plasma jet temperature |
|---|---|---|
| minimum 100 A | 300 V | 3161 °C |
| maximum 160 A | 300 V | 3360 °C |

Institute of Nuclear Energy Research of the Republic of China, started to use the plasma technology with a capacity of 250 kg/h and operation at 1700 °C plasma melter for treatment technique of low level waste at 1994 (25).

With plasma technology removal efficiencies of Cd, Cs, and Hg were shown in Figure 2 respectively. It has been constructed using the dataset provided by the article Sanito et al., 2022 (20).

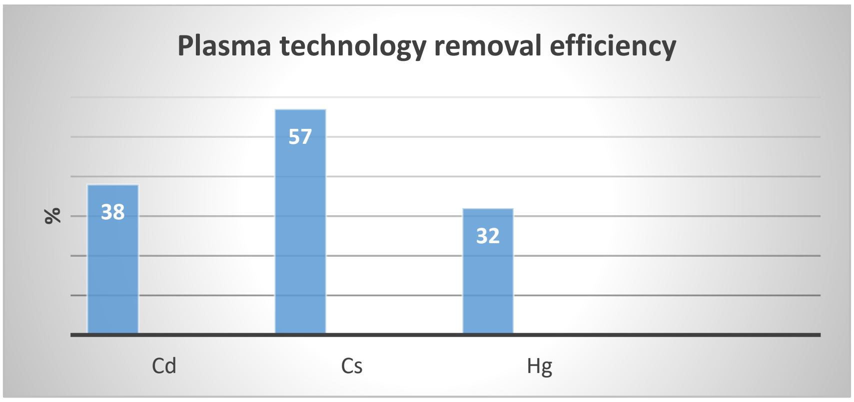

**Figure 2:** Removal effiency of Plasma technology in the vitrification process.

### *2.1.3. Waste minimization programme performance*

Waste minimization programs have reached a tenfold reduction in LLW generation, bringing LLW volumes down to approximately 100 m$^3$ annually per 1 GW (26).

In the vitrification process, radioactive waste is not only encapsulated by the glass but also each waste atom is individually bound in the glass molecular structure chemically with definite exceptions, e.g., ruthenium and palladium (27).

Ion exchange and dissolution of the matrix result in the creation of top coating consisting of multiple porous layers featuring a varied mixture of both crystalline and amorphous components within the glass.

In 1984, a three-year research of six US laboratories was performed on the leaching behaviour of HLW in borosilicates glass and solubility in the surface layers produced at Marcoule, (France) in collaboration with Japan, Sweden, and Switzerland (28).

### *2.1.4. The history of the Indian vitrification technology*

In India, borosilicate glass matrix has been implemented in three vitrification facilities. The first is in Tarapur, the second is at Bhabha Atomic Research Centre, and the third is at Kalpakkam (29).

The composition of (HLW) varies based on parameters such as the reactor's processing steps, and the recovery chemistry. This waste includes long-and short-lived fission elements, actinides, unrecovered Pu/U, and chemicals used in the treatment steps, as well as corrosion byproducts from the storage tanks and tubing, exist in the waste content. While americium, neptunium, and curium are the main actinides, the chemicals present are nitric acid and sodium nitrate. HLW at Trombay generated from the recovery of research reactor's output emits radiation of 0.27- 0.37 TBq/L (29).

In PUREX (Plutonium URanium EXtraction) process which used to recover the uranium and plutonium through liquid-liquid solvent extraction by tributyl phosphate as the organic solvent, a nitric acid-based liquid waste flux is derived as a by-product (30).

### *2.1.5. History of HLW vitrification advancements in the UK nuclear power*

The UK's WVP at Sellafield constructed its first two lines in 1990, and a third line was implemented in 2002. The WVP employs the French two-stage calcination-melting operation to handle 25 kg/h of waste. High-level waste glass have been yielded and stored until final deep geological disposal (30).

### *2.1.6. Vitrification Facilities in the World and Waste Inventories*

Some notable properties and glass formulations around the World were selected and tabulated. Two remarkable points exist on the list of Table 3. One is the highest waste loading capacity obtained with the glass composition with MnO. The highest waste loading capacity on the list is received from India's Tarapur facility, 43.8%. Interestingly, this facility is the only one that includes manganese oxide in its glass composition of the original list. MnO content does not appear in any glass composition of any other country's facility on the list. This glass composition has high MnO content (9%) and relatively low $B_2O_3$ content (6.4%). The second remarkable point is with high $P_2O_5$ content, Russia's Mayak facility. $P_2O_5$ content is 52.0%, very high, and there is no $B_2O_3$ content in the glass composition. Its waste loading is quite good (≤33%). This means up to 33% is obtained without $B_2O_3$ in this composition. It is clear that $P_2O_5$ is a suitable glass former for waste loading as well. In Table 3, this point is made obvious (31). The notable results selected from the article of Thorpe et al., 2021 to discuss.

**Table 3:** The selected results on the world waste glasses and their capacities (Thorpe et al. ,2021).

| Country: vitrification facilities | Waste category - glass name | $SiO_2$ | $P_2O_5$ | $B_2O_3$ | $Al_2O_3$ | CaO | MgO | $Na_2O$ | Other | Significant Other | Waste Loading |
|---|---|---|---|---|---|---|---|---|---|---|---|
| India: Tarapur | HLW-IR111 | 34.1 | - | 6.4 | - | 2 | - | 0.2 | 59.3 | MnO (9%) | 43.8% |
| Slovakia: VICHR, Bohunice | HLW-Chrompik III | 54.8 | - | 13.9 | 5.0 | - | - | 8.0 | 18.3 | $Fe_2O_3$ (4.3%) | 3-10 % |
| Russia: Mayak | HLW | - | 52.0 | - | 19.0 | - | - | 21.2 | 7.8 | - | ≤33% |
| UK: Sellafield | HLW-CaZn Magnox | 34.4 | 0.51 | 16.3 | 5.6 | 4.6 | 2.9 | 6.9 | 28.8 | - | ~28% |

Japan, Korea, China, and one of the UK's facilities have $P_2O_5$ content of less than 1% in their glass composition, besides $B_2O_3$ (10.6-16.3%). The UK has three facilities with six types of glass compositions; one glass includes $P_2O_5$ as 1.9% in its composition, besides 2.0% $B_2O_3$.

The UK's Sellafield facility has the higher $B_2O_3$ content in the glass composition on the list (16.3-16.4%), and 26-30% waste loading is obtained. One of three UK glasses has CaO content (4.6%) as extra.

The lowest waste loading is in Slovakia, Bohunice. The difference in composition from the others is $Fe_2O$ content 3% and the result is 3-10% (31).

The waste's physical shape with its structural characteristics and engineered barrier are crucial in determining glass durability. According the data on glass corrosion and dissolution kinetics vitrified LAW will not include longer-lived and radiotoxic actinides (e.g., U, Np) still, it will immobilise a mixture of short and long-lived fission. ASTM, EPA, and ANSI standard methods have been used for glass dissolution and leaching tests since 1981. Finland and Sweden are progressing in their pattern for directly disposing of used fuel and have chosen their sites in Sweden. The USA has decided Yucca Mountain in Nevada as the site for its repository. Additionally, vitrification plants in the UK and Belgium have been in operation for over forty years (31).

Commercial nuclear fuel reprocessing facilities with high level waste are based on 3 main Technologies. Facilities sites are located in India, Japan, France, China, Russia and the United Kingdom. JHCM: Joule-heated ceramic-lined melter; HWIM: Hot-walled induction melter; CCIM: Cold-crucible induction melter. German Vitrification Plant's melter technology is also under review from a technological perspective. Vitrification technologies used in spent fuel reprocessing are plotted as percentages in Figure 3 based on the informations from the article of Vienna et al., 2010 (32).

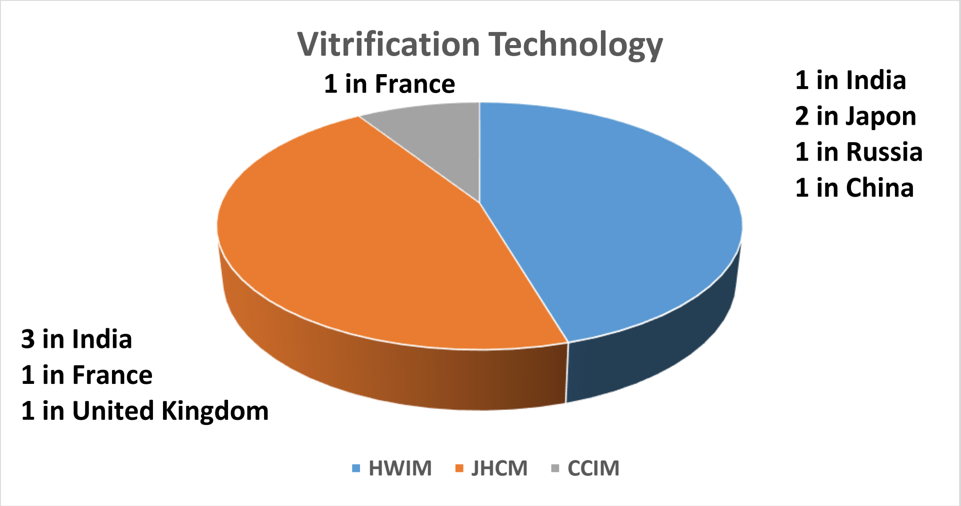

**Figure 3:** Vitrification technologies used in spent fuel reprocessing.

Two main factors exist to be considered in the storage conditions. First, decay heat from radionuclides with a half-life of 30 years ($^{134}Cs$, $^{137}Cs$, $^{90}Sr$, decay) will heat the glass during the time in the repository. When the temperature gets close to the glass transition temperature, phase changes may take place in the glass, impacting its long-term performance. The second one is that Pd, Ru, and Rh are rare soluble in alkali-boro-silicate waste glasses and will remain insoluble solids within the melt (32).

The most extensive nuclear waste vitrification facility in the USA is in the Savannah River. Mainly these are removed from the used fuel to allow for the recycling of U and Pu. The vitrified HLW is encapsulated into stainless steel cylinders, kept for final deep geological disposal (31).

A safe geological disposal design with "multiple barriers" is essential to prevent significant environmental releases for thousands of years (26,31). Taking advantage of clay adsorption of the radioactive waste, by groundwater elution. Figure 4 illustrates the same technical recommendation (33).

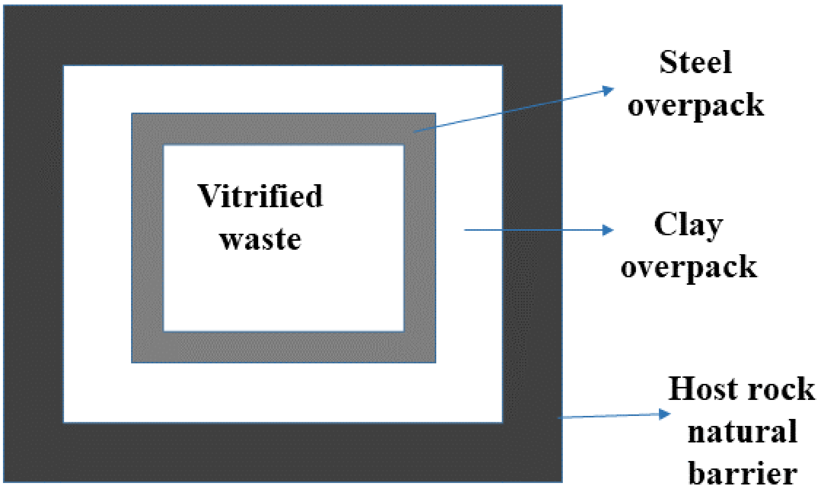

**Figure 4:** The recommended multiple barrier system for the disposal of nuclear glass.

Some examples of glass formulation from the World is seen in the Table 4 (34).

**Table 4:** Waste classes and the glass formulations of some countries (34).

| Code of glass and waste class | Country | Formula of the Glass |
|---|---|---|
| Magnox, HLW | UK | $47.2SiO_2$-$16.9B_2O_3$-$4.8Al_2O_3$-5.3MgO-$8.4Na_2O$-17.4Others |
| R7T7, HLW | France | $45.5SiO_2$-$14B_2O_3$-$4.9Al_2O_3$-$9.9Na_2O$-$2.9Fe_2O_3$-22.8Others |
| K26, LILW | Russia | $48.2SiO_2$-$7.5B_2O_3$-$2.5Al_2O_3$-$16.1Na_2O$-15.5CaO-10.2Others |
| CCM, HLW | Russia | $52P_2O_5$-$19Al_2O_3$-$21Na_2O$-7.8Others |
| DWPF, HLW | United States | $50SiO_2$-8B2O3-$4Al_2O_3$-$8.7Na_2O$-1.4 MgO-27.9Others |
| PAMELA, HLW | Germany-Belgium | $52.7SiO_2$-$13.2B_2O_3$-$2.7Al_2O_3$-$5.9Na_2O$-4.6CaO-20.9Others |

### *2.1.7. Nuclear waste treatment and melter corrosion*

It has been faced with some technologycal problems with the glass-contact refractory in the nuclear waste vitrification melters. According to the review encountered about correlation of corrosion data versus melter life considering melters, after being closed down, the melter lining was taken apart, and the examination revealed refractory melt line indicated a material loss of around 10–13 cm. was discovered to have infiltrated the cracks on the external layers of the refractory. The overall details related with the problems encountered regarding the process were summarized in Table 5 based on the information provided the articles of Jin et al., 2023 and Guillen et al., 2020 (35,36).

**Table 5:** The main corrosion and circuit problems in vitrification process steps.

| The reason | The results and observations | Facility, glass type |
|---|---|---|
| High melting temperature need in Joule-heated ceramic melter (JHCM) | The glass feed is heated by an electric current between electrodes immersed in the glass pool to melt.<br>Decrease in melter life. | New York, US, 1995-2002, 2200 $m^3$ high level waste, 0.7-1.2 ton of daily glass production |
| Borax migration and electrical shorts | Refractory corrosion.<br>Damages to the refractory and leakage of melt from assembly joints. | South Carolina, US, 1996-1999<br>2500 $m^3$ low level waste, 5-15 tons of daily glass production |
| Salt phase such as sulphate and chloride | Greater corrosion depth.<br>melt line material lost with 10-13 cm gap, the cracks. | 1998-2003,<br>Low Pilot Melter |
| Controling of oxidation state and the solubility of molybdenum, chromium, iron ions in inventory | Corrosion of the melter refractory based on their oxidation related with high heating.<br>Fe(III)/Fe≈0.5 at 500 °C;≈0.7 at 700 °C.<br>Rearrangement from octahedral to tetrahedral. | LLW-E-M09 glass type,<br>NG-$Fe_2$ glass type |

The insoluble part and the unwanted layers formed in the glass matrix serve the purpose of creating a barrier that prevents contact with the melter. Some examples that providing advantages were given in Table 6. This Table created based on the cases mentioned in the articles of Jin et al., 2023, Guillen 2020 et al., Crum et al., 2023 (35-37).

**Table 6:** Some advantages of layers produced during the vitrification on melter life.

| Factor | Benefit for corrosion | Result | Facility |
|---|---|---|---|
| Molybdenium dissolution in the glass feed | Due to the dissolution of molybdenum and no leakage on the melter floor. It is an advantage. No problem in contact with glass and the refractory lining layer. | Increase of service life of the melter; Refractory still on service. | Facility in Ohio, US, 1996, daily 1 ton of glass production |
| Layer of eskolaite ($CrO_3$) on corrosion resistance | A Protective layer of 22 μm-33 μm. Crystals will slow the corrosion because of its high melting point of 2435 °C providing the corrosion resistance. | It is a proposal of improvement to reduce corrosion of refractory. | In refractories |

Gray $Cr_2O_3$ crystals present intensly at the side wall and at the bottom of the crucible areas. Increasing the use of $Cr_20_3$ works to reduce corrosion of refractory materials (22,37).

There is a directly relationship between the chromium and increasing of viscosity. The reason are the crystalline chromium mineral phases which built up in air-quenched melts. In the melt form, these crystals bring additional friction through shear movements (27).

### *2.1.8. Platinum group metals in Japanese HLW vitrification, Rokkasho Reprocessing Plant*

Rokkasho vitrification facility situated in Northern Japan was completed in 2013. Liquid Fed Ceramic Melter that uses Joule heating through direct electrification is adopted.

In addition to the yellow phase components (primarily molybdenum and sulphur), the noble metals group—particularly ruthenium (Ru), rhodium (Rh), and palladium (Pd)—poses significant challenges in HLW borosilicate glass melts due to their high electrical conductivity which can interfere with melter operation. These problematic elements are typically present as compound forms such as $RuO_2$, $Rh_2O_3$, PdO appearing as needle-like or spheres. They are the noble metals which are located at the bottom of the melter as sedimentation (38). It should be noted Platinum group metals in one ton of SNF; ruthenium is 3.04 kg, rhodium 0.60 kg and palladium 1.94 kg (39).

### *2.1.9. $RuO_2$ Sphere Formation and Their Contribution to Short-Circuiting Failure Risk*

$RuO_2$ can markedly influence the electrochemical characteristics of nuclear waste glass melts due to their higher conductivity. Platinum group metals such as ruthenium, rhodium, and palladium, exhibit extremely low solubility in glass. Ruthenium typically forms $RuO_2$ crystals, while palladium and rhodium form spherical Pd-Rh-Te alloys, all of which are present as agglomerates in the nuclear glass melts causing issues such as electrode short-circuiting or even damage to the furnace, ruthenium's behaviour should be considered (40).

### *2.1.10. Vitrified HLW storage in the savannah river site location in the United States*

The Savannah River Site, recognized as the largest radioactive waste vitrification facility globally, currently manages high-level liquid radioactive waste containing an estimated total activity of 332 million curies. This waste is stored in underground stainless steel canister containing the glass (41). Notably, one of the earliest publications addressing the borosilicate glass waste loading capacity for this facility was released in 1983 up to 50 wt% (42) Leaching rates of borosilicate glass containing radioactive wastes from the Savannah River Plant have been evaluated over a 900-day period based on $^{90}$Sr and $^{137}$Cs analyses, with particular emphasis on the influence of pH (43) In the review of Hossen, it is underlined the alkaline conditions improve uranium and technetium leaching at significiant degree at above pH 9 (44).

Average Composition of Savannah River Site Vitrified High-Level Waste is presented in the report of U.S. Nuclear Waste Technical Review Board as 6% $B_2O_3$ (41) In the report of Savannah River National Laboratory 2014, ruthenium, rhodium, and palladium crystals are included in crystallization data (45).

Selected Chemical Engineering Applications in NucleaWaste Processing in Savannah River Site studied in the review of Crouse et al. and illustrated via Fishbone diagram based on recent conceptual developments at the site recently. The primary processes implemented as improvements include filtration, evaporation, solvent extraction of cesium, acid addition methods, the introduction of antifoam agents to prevent foam layer formation, and mercury separation (46). Engineered Multibarrier system for Storage Of Savannah River Plant Waste is illustrated in 1980's (47).

Construction and Design principles of the were discussed in the facility of Savannah earlier articles (48)

## 2.2. Networking and Chemistry

### *2.2.1. Melting-quenching method: Glass formation and glass-ceramic matrix*

Boron has a field strength of 1.63 with 3 coordination number; phosphorus has a field strength of 2.1 with 4 coordination number. Their role is acting as network formers, formation of the backbone and location in the polyhedrals. Fundamental "glassformers" are $B_2O_3$, $SiO_2$, $GeO_2$, and $P_2O_5$, which have the ability to form glasses on their own and high field strength (F). In contrast, oxides like $TeO_2$, $SeO_2$, $MoO_3$, $WO_3$, $Bi_2O_3$, $Al_2O_3$, $Ga_2O_3$, $TiO_2$, and $V_2O_5$ do not form glass by themselves, they are modifiers. Modifiers require second oxide for transforming into the glass and are located in the holes of the network randomly (22,27). Glass formation is a kinetically controlled process (26). It is essential for long-term durability that the glass does not crystallize during cooling and remains stable (2).

Quenching is cooling the melt by bringing it to a fast cooling rate. When the melt is quenched, a glass structure is formed. On the other, glass-ceramic formation occurs by internal crystallization and encapsulation method under slow and controlled cooling conditions of melt that allow at first nucleation; then crystals form in the glass matrix where the glass either binds crystalline particles or distributes crystalline particles in the vitreous phase (21,34).

### *2.2.2. Borosilicate glass as a network matrix*

The basic structural unit of the glass framework consists of Si with four adjacent oxygen-forming tetrahedra. Adjacent silicate groups are linked to each other through oxygen atom bondings. It is strong ionic or covalent bridging. The binding of $B^{3+}$, $Fe^{2+}$, $Fe^{3+}$, rare earths, or actinides occurs also via oxygen bondings, through similar bonding mechanisms. Binding of low-valence ions, i.e., $Na^+$, $Cs^+$, $Sr^{2+}$, occurs via nonbridging oxygen bonds based on the fitness of the ion's size and voids in the network (27).

Researching of the doping of alkali and alkaline-earth cations in standard borosilicate glass calcium doped formulation, (BSNC), $10B_2O_3 \cdot 15Na_2O \cdot 15CaO \cdot 60SiO_2$ were examined to compare. BSNC has shown differences in viscosity and structural properties compared to standard borosilicate glass, neutralizing the charge, and enhancing the ionic mobility in the network. The presence of $Ca^{2+}$ affects the field strength and density of the glass, which influences its properties (49).

### *2.2.3. Analysis of crystallization mechanism and glass-ceramics*

The study of barium borosilicate glass–ceramics at varying heating rates and particle sizes by Li et al. demonstrated that the various heating rates and particle size range do not induce a notable impact regarding the glass transition temperatures ($T_g$) (50).

### *2.2.4. Matrix development and formulation: The advantages of borosilicates*

Borosilicate glasses have some technical advantages comparing with silica glass. The difficulty of high temperatures, keeping the melting process temperature at the range of 1100 °C-1250 °C is crucial for to prevent the volatilisation bring handicap for silica glasses. The waste loading capacity is low (51).

Four hundred seventy-nine glass formulations have been achieved via matrix development to immobilize radioactive wastes (1). Within Borosilicate, silicon and boron are formers of geometry positioned centrally within oxygen polyhedra, silicon in tetrahedra, and boron in triangles. On the other hand, in sodium borosilicate structure, boron oxide is also present in the tetrahedral matrix. Sodium balances negativity in the network (29). These polyhedra are connected to each other by sharing common corner atoms. The distinction in dimensionality helps explain the significant variation in glass transition temperatures ($T_g$) with $B_2O_3$ at approximately 260 °C while that of vitreous silica at around 1100 °C (51). The positioning of numerous ions in this three-dimensional network of HLW is related to the electronegativity, ionic size, and field strength (52). Sodium borosilicate, lead borosilicate, and barium borosilicate glass types matrix are at Tarapur and Trombay. Some of their mechanical, thermal, and chemical properties vary (29). Cooling of high viscosity melt, some crystalline microstructures formed could surface disruption causing a decrease in waste loading.

### *2.2.5. Surface chemistry of nuclear glass*

The performance of borosilicate model nuclear waste is the result of its chemistry. For glass modifier structure, for example, in the case of formulation of (mol%) of $60.2SiO_2-16.0B_2O_3-12.6Na_2O_3.8Al_2O_3-5.7CaO-1.7ZrO_2$ sodium ions tend to accumulate at the surface of borosilicate glass. This enrichment of sodium on a glass surface increases the number of ion-exchange probability, accelerating the initial dissolution of glass. It is found that the mol % of $Na_2O$ is 12.7 in bulk, whereas it is 17.4 at surface composition. Due to its lower charge and smaller ionic radius, $Na^+$ has a lower diffusion energy barrier and higher self-diffusion coefficient (53).

### *2.2.6. Structural function of molybdenum in glass network and utilizing phosphorus*

If the amount of $MoO_3$ in the inventory exceeds its solubility limit, phase separation and crystal formation step could occur in molten glass. Molybdenum may form crystalline molybdates, known as "yellow phases" when combined with alkaline and alkali-earth ions. These phases can potentially decrease the durability of the glass. The report presented for Commissariat a L'énergie Atomique (CEA) underlines the structural point of view for the behaviour of molybdenum oxide. In the basic high-level waste (HLW), the spheres have a diameter of 15 µm in the glasses bearing 3% mol $MoO_3$. At a rapid cooling (quenching) rate $10^4$ °C/min, a heterogenous matrix is observed with 2.5 mol % $MoO_3$ in places. It becomes an opalescent glass with a crystal phase with 3% $MoO_3$ in the microstructure. It is concluded slow cooling rates of crystalline structure formation starts earlier (54).

The molybdate anionic groups location in the borosilicate was revealed by increasing either $MoO_3$ or $B_2O_3$ contents. The results make clear that there are two regions in the borosilicate structure. One of two which is depolymerised region, is in the middle. The second is either on both sides called the polymerized network. Molybdate anionic structures are located in depolymerised areas, where non-bridging oxygen atoms are abundant and alkali and alkaline-earth cations to balance the negative charge, without linking directly to the silicate network (Figure 5). The figure was inspired by Caurant et al. (2010) in its design (55).

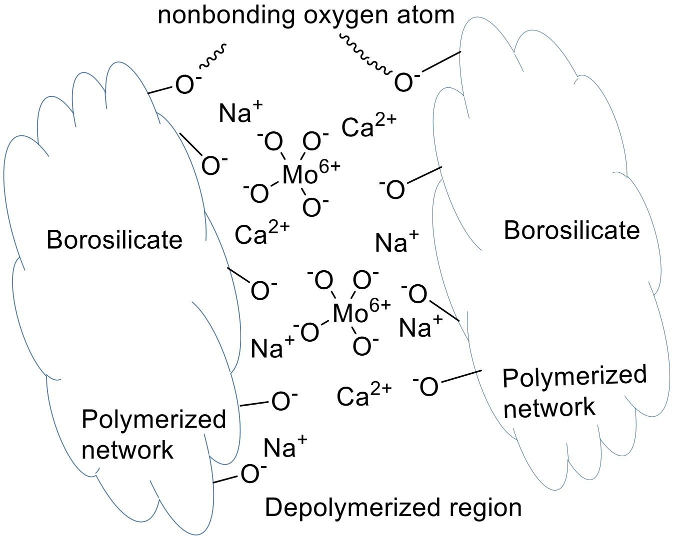

**Figure 5:** The location of the molybdate anionic groups in the borosilicate glass structure causes crystalline phases.

Borosilicate glasses may consist of over 30 elements, including fission products like molybdenum which pose difficulties for inclusion in nuclear waste glasses. Molybdenum slightly soluble in borosilicates, typically less than 1 wt% $MoO_3$ while elements such as zinc and zirconium are consistently integrated into the borosilicate framework with a notable involvement of silicon.

Calas et al. confirms the article of Caurant et al. working with $MoO_3$ incorporated five oxide glasses. Analysis confirms that $[MoO_4]^{2-}$ tetrahedra do not directly link to the vitrous bonding. Alkalis, alkaline-earths or lanthanide cations present in the nuclear glasses may be the responsable for the 60 wt% part of the spherical crystalline phases. The identified yellow phase is Na-molybdate (56).

Mo isotopes present in the waste forming complex molybdate with very high radioactive $^{135}Cs$,$^{137}Cs$, and $^{90}Sr$ radioisotopes as named "yellow phase". As long as they remain unbound, these radioactive crystalline phases exhibits good solubility in water and could leach into the environment if exposed to water at a geological repository site. It means a risk for human health. Due to the its low solubility in borosilicates, $MoO_3$ is a key factor limiting the nuclear-waste loading capacities of borosilicate glasses. Nevertheless, homogeneous glasses, with no separated crystalline phases seen as long as the $MoO_3$ loading limit is kept below 1.5 mol % (57).

Using phosphorus is a way to increase the solubility of the contents in borosilicate-based nuclear glasses. In the waste inventory with both molybdenum and phoshorus, molybdenum phase separation mechanism varies depending on parameters such as cooling rate of melt, method or conditions too.

The advantage of phosphorus seems to stem from its high cation field strength, which facilitates a more balanced sharing of oxygens with $Mo^{6+}$ and $S^{6+}$ compared to the lower field-strength cations e.g. silicon, boron, and aluminum (57).

Phase separation mechanism and immiscibility of borosilicate bearing molybdenum and phosphorus oxides analysed with discussions concerning the glass transformation temperature. The glass formulation consists of $SiO_2$, $CaCO_3$, $Na_2CO_3$, $H_3BO_3$, $MoO_3$, $Al_2O_3$, ZnO, $ZrO_2$, and $Nd_2O_3$. Initially, the melt is homogeneous at the vitrification temperature, 1250 °C. During the cooling process, separated phase formation appears between 1200 °C and 1150 °C. These spherical phases are rich in molybdenum, calcium, and phosphorus oxides. The transformations between the liquids are observed at intervals of 1150 °C and 1100 °C and the separated phases tend to grow. The partial crystallization of the seperated phases are $CaMoO_4$.

Morover, samples were taken from separated phases at temperatures 1150 °C, 1100 °C, 1050 °C. Mol content % of $ZrO_2$ are 0.0 in the separeted phase samples. It is obvious that $ZrSiO_4$ crystals are in the residual matrix, and are not present in the separeted phases (58).

Sugawara et al. performed several calculations on the dissolution behaviour of $MoO_3$ in Japanese simulated HLW glasses via using a thermodynamic database. CALculation of PHAse Diagrams methodology, CALPHAD, used via thermodynamic database to improve chemical durability of HLW glass especially for the exhibition of liquid–liquid phase separation of molybdenum-bearing silicate melt. The effect of $SiO_2/B_2O_3$ mol fraction on molybdate behaviour is examined. The draw of liquids phase diagram of HLW glass as function of $CaO/Na_2O$ and $SiO_2/B_2O_3$ ratios when $MoO_3$ content is 4.0 wt% is clear. Different glass composition circles at different temperatures represent for clarification of thermodynamic behaviour (59).

### *2.2.7. Deviation of the glassy structure*

The incorporation of $Li_2O$ and $Na_2O$ significantly influences the performance of borosilicate glasses for high-level liquid waste (HLLW), particularly with respect to structural homogeneity, metal oxide retention capacity, elution behaviour, and mechanical stability (60). The incorporation of iron oxides into the glass leads to rearrangement of the atomic structure. Contrary to previous studies, T(g) increases with rising of $Fe_2O_3$ content. As the concentration of iron oxide increases, $Na^+$ content correspondingly decreases, indicating a diminished role of $Na_2O$ as both a network former and modifier due to the its reduced presence. In place of the glass network contributes to the structural polymerization of the glass network (61).

### *2.2.8. Chemistry: Zirconolite, perovskite, and baddeleyite crystalline phases in barium borosilicate matrix*

Crystalline phases of barium borosilicate glass-ceramics detected by back scattered electron (BSE). In BSE images of the glass-ceramics bearing 0-20 wt% HLLW the crystals are zirconolite. In EDX analysis the dendritic structures correspond to zirconolite. With increasing the loading ratio of HLLW, perovskite peaks intensified, while the peaks of zirconolite decrease. They are needle-shaped crystals. Glass ceramics had pores and cracks. The peak noticed in DTA analysis for the glass loading 30 wt% HLLW belongs to perovskite. A little of nepheline phase is detected in the formulation with 30 wt % HLLW. Besides, traces of baddeleyite phase exist always for all of samples. White particles appear on the zirconolite crystals match up with baddeleyite (62).

There are works through improvement of sulphate solubility in the borosilicate. Kaushik et al. found that incorporating BaO as a modifier in borosilicate glass significiantly enhanced the sulphate solubility. The barium borosilicate glass with the composition $BaO\text{-}Na_2O\text{-}B_2O_3\text{-}SiO_2$ can be loaded up to 23 wt % sulphate containing waste oxide uniformly. Above 23 wt% waste oxide loading, the barium borosilicate glass matrix turned heterogeneous due to the development of yellow phase consist of basically consists of element Na which is 290 mg/g (63).

This yellow-colored mass primarily consists of $Na_2SO_4$, (thenardite). This phase, being less dense than the bulk, floats on the surface of molten vitreous bulk. It builds a block to prevent releasing the gas bubbles exit at the vitrification step. Viscosity difference creates a manufacturing problem pouring of borosilicate melt to the canister. Yellow phase presence with great solubility in water could facilitate the easy release of $^{137}Cs$ and $^{90}Sr$ isotopes into environment. To inhibit the yellow phase in the glass, it is preferable incorporation of charcoal, sucrose, and similar materials into the vitreous melts, facilitating the reduction of sulphate to sulphite through carbon and lower oxidation state of sulphur. This type of formulation, SB-44 type, has been safely used for isolation of 11 000 kg of vitrified waste containing $10^7$ GBq of radioactivity. This process offers a range of of advantageous features, like no excessive foaming and prevention of growth of yellow phase (63).

### *2.2.9. Operation Conditions: Experimental sample preparations and formation of glasses*

Operation conditions for vitrification are varried. In the article of Magnin et al., chemical powders of two series of glasses were melted in platinum or gold pots at 1300 °C for 3 h. Each molten matrix was cooled by quenching within two copper sheets at a cooling step of $10^4$ °C/min or 1 °C/min. $Nd_2O_3$ (0.15 mol%) was added to the following composition $64.76SiO_2 – 10.48B_2O_3 – 13.68Na_2O – 8.43CaO – 2.5MoO_3$ (in mol%) recipe (64). In another French nuclear waste vitrification procedure for uranium–molybdenum recovery, and handling with (>6 mol%) of molybdenum and phosphorus (2 mol%) are crucial in order to control phases formed. The glass matrix was formed by using starting materials: $SiO_2$, $CaCO_3$, $Na_2CO_3$, $H_3BO_3$, $MoO_3$, $Al_2O_3$, ZnO, $ZrO_2$ and $Nd_2O_3$. The feed powder was blended and melted in a platinum–rhodium pot with mechanically stirring. After heating at a rate of 10 °C/min, for 3 h at 1250 °C, then plate-quenched at a rate of $10^3$ °C/min. about 800 g of glass was obtained (58).

### *2.2.10. Vitrified Borosilicate glass chemistry: Ion exchange mechanism*

Glass dissolution and ion exchange are related to diffusion including transportation of molecules, ion movement. The release rate of boron is critical for network endurance-this helps the ion exchange mechanism of glass for leaching test and matrix durability. As temperature changes from 26 to 40 °C, the rate of boron increases roughly 20 times. Besides temperature, the size and pH conditions are basic parameters (65).

### *2.2.11. Octahedral Zr position on the boron glassy network*

When it comes to Zr chemistry, In the study of borosilicate glasses, including zirconium (Zr) plays a notable role in altering the glass network. When zirconium is introduced, octahedral geometry around Zr ions is noticed. However, according to the high polarizability, additional $Na^+$ and $Ca^{2+}$ ions are needed to balance the charge of the $ZrO_6$ units, which each carry two negative charges (66).

Alkali-earth, $Ca^{2+}$ ions, do not enter the four-layer boron glass due to its high polarisation and the low possibility of linking $BO_4$ groups. $Ca^{2+}$ cations only form non-bonding oxygens (NBO) within the silicate framework and the charge compensation with aluminum-based repetitive units (66). Zirconium retains its charge-balancing cations at the expense of boron (67).

## 2.3. Improvement in The Vitrified Structure

### *2.3.1. Improvements in vitrification*

In general, research and developments in this area are based on three fundamental pillars: (2). The first is the “ability to accommodate the waste.” The experiments diverge into a) Solubility (Cr, Ru, Rh, Pd, Ce, Pu, $SO_4$, Cl), b) Phase formation (Mo, $SO_4$, Cl, P), c) Devitrification (Mo, P, F, Mg) d) Highest waste load.

The second is “Process / Technology”. Key aspects are: a) melting temperature suitable for processing, b) viscosity, c) reactivity, d) residence time, e) electrical conductivity, f) thermal conductivity, and g) additives for improvement.

The last pillar is “glass performance”. This splits into; a) Convenience for storage and disposal, b) Thermal stability, c) Chemical durability, d) Ability to resist self irradiation, e) Mechanical performance (2).

### *2.3.2. Required qualifications for vitrified waste*

The solidified waste form needs specific features: it must be suitable for long-term storage, economical and environmentally preferable. Key attributes include proper chemical stability and integrity, low leachability with the groundwater, resistance to radiations alpha, beta, and gamma, capability to load quantity of waste, ensuring capacity of volume reduction (20).

Table 7 provides a summary the improvements and potential negative effects of oxides. The relevant factors are discussed in the text of this review (see Table 7).

**Table 7:** Effect of oxide incorporation on glass properties.

| Oxide | Observed Effect |
|---|---|
| $Na_2O$ | Increases glass surface area |
| $Nd_2O_3$ | Enhances molybdenum solubility in glass |
| $ZrO_6$ | Modifies (alters) the glass network structure |
| $Y_2O_3$ | Improves radiation shielding ability |
| $V_2O_5$ | Enhances thermomechanical performance and increases sulphur solubility |
| $Al_2O_3$ | Improves elastic properties and overall glass durability, reduce the volatility |
| $Gd_2O_3$ | Inhibits powellite crystal formation |
| CaO / $Na_2O$ | Enhances $MoO_3$ solubility and suppresses phase separation |
| $Ba(NO_3)_2$ | Acts as a pretreatment agent, reducing yellow phase formation |
| $Li_2O$, $Na_2O$, $K_2O$ | Negatively affect glass durability |
| $SiO_2$ | Reduces the volatility |
| $B_2O_3$ | Increases the volatility |
| CaO | Affects the field strength and density of the glass |
| $CrO_3$ | Increases the viscosity |

The volatility of borosilicate glasses increased with the addition of boric oxide, $B_2O_3$. However, high ratio of $SiO_2$ and $Al_2O_3$ content is reducing the volatility. The role of these components in the melt is to transform the more volatile components into less mobile by preventing their mobilities in the network spaces (27).

### *2.3.3. Radiation Effects and the addition of $Y_2O_3$ on shielding effect during Glass-ceramics preparation*

Radiation effects on glass structure were examined as "an aging effect". Glasses with short-lived actinides ($^{244}$Cm, $^{238}$Pu) enable "accelerated aging," which allows the radiation effects to be simulated in a few years, which would take results 10,000 years to manifest (2). Internal radiation sources in HLW include alpha decay from actinides, up to 5 MeV energy release per decay, and β decay from fission products which release 1 MeV energy. The primary sources of α-decay are isotopes of uranium, neptunium, plutonium, americium, and curium (27).

Shielding ability is a plus of glass characteristics for protecting human and next-generation health through the environmental medium. In a study by A.F. Abd El-Rehim et al., borosilicate glass-ceramics were developed showing improvements in physical properties and glass formation capacity as a result of the $Y_2O_3$ doping. The addition of $Y_2O_3$ improves the shielding effectiveness of the glasses (68,69).

This is because such glasses are durable and can inhibit the escape of volatile elements in the waste inventory, e.g., Cs and Ru, at higher temperatures.

Glass-ceramics made from borosilicate glasses doped with Yttrium were produced and Crystalline phases of yttrium silicate, $Y_2SiO_5$, were noticed. The sample productions of waste glasses were carried out in Şişecam (70).

### *2.3.4. Improvement in the vitrified structure: Durability of vitrified waste*

In Tarapur, durability experiments were conducted for more than 700 days to evaluate the effect of repository components, such as granite, back-fill material, and corrosion products, on the leach rate of vitrified matrix (29).

The exchange of $B_2O_3$ by $SiO_2$ enhances the abundance of nonbridging oxygens and alters the molecular proportion of $BO_4$ and $BO_3$. The high density, glass forming capacity, and fragility of the sample with 5 mol % $B_2O_3$ caused the conversion of $BO_3$ to $BO_4$ structure (52).

When leaching behaviour versus additive of oxides examined, $Al_2O_3$ addition passes the leaching tests. Leaching resistance is quite good for borosilicate glasses with alumina and glass durability is high while it is very negatively affected with the addition of some oxides $Li_2O$, $Na_2O$ and $K_2O$ (27).

### *2.3.5. Structure-property relationship of silica glass framework and the role of Zn for mechanical properties*

In terms of chemistry, in glassy silica, Zn-O-Si angles are narrower than Si-O-Si angles. The repulsive force between cations is rather low, reducing the rings' dimensions in the glassy repetitive unit. $Na^+$ balances the charge of oxygen atoms bonded to both Zn and Si (71). Nuclear glass cations occupy the network-forming position, which clarifies how Zn improves the mechanical characteristics and the chemical stability of glasses (72).

### *2.3.6. Improving the thermomechanical performance of borosilicate glass: Incorporation of $V_2O_5$*

Waste inventory with high-sulphate content typically include residues from exchanging resins. Throughout the waste vitrification procedure an immiscible sulphate layer which is on the surface of the borosilicate molten phase. The task of vanadium incorporation in the borosilicate matrix is to accelerate the kinetics of sulphur integration into the glass and its release into the gas phase and increasing sulphur solubility within the vitreous melt of the borosilicate. $V^{5+}$ ions can be distributed in the spaces in boron–silicon–oxygen network, loosening it and facilitate the contribution of sulphate ions. The structural behaviour behind is likely forming proper spaces within the glassy matrix and depolymerising the borate units (73).

The impact of vanadium oxide incorporation on improving the thermomechanical performance of high crack-resistant borosilicate glasses in nuclear waste disposal is pretty noticeable.

When 8.0 mol% $V_2O_5$ was added to borosilicate composition Bulk, Young's and shear modulus decreased by ~17%, ~29%, and ~32%, respectively, the addition of $V_2O_5$ significantly improved the crack resistance of ISG. The cracks mean extra surfaces that can promote corrosion in geological disposal. The addition of $V_2O_5$ to ISG, inelastic deformation on all sides of indentation, leading to high crack initiation forces for glasses with high $V_2O_5$ ratios (74).

A second suggestion is given as the reason for this, regarding the behaviour of $V_2O_5$ doped glass. Given that vanadium ions exhibits multiple oxidation states, have different function and big impact on structural and physical properties of glass network, bulk and surface. The presence of $V^{3+}$ and $V^{4+}$ ions might transform $[BO_4]^{1-}$ to $[BO_3]$. This fact improves crack resistance, because $BO_3$ triangle structures can move by sliding and creates elastic form (74).

### *2.3.7. Improvement in the vitrified glass chemistry: Gadolinium effect on powellite crystallization*

In the powellite topic, the sizes and distributions of the formed crystals in both the surface and bulk are influenced primarily by the heat treatment applied and the gadolinium mole ratio. Glass-ceramic formulations $SiO_2$–$B_2O_3$–$Na_2O$–CaO–$Al_2O_3$–$MoO_3$–$Gd_2O_3$ synthesised by varying heating methods. For the glasses with $[MoO_3]$ = 1.5 mol% at low gadolinium content, powellite crystals after single step heat treatment were too tiny, after triple step of heat predominantly take the form of bipyramids. In contrast, at high content of Gd, by single step of heat mainly micrometer-sized cross-shaped crystals, upon triple step of heating treatment at high ratio spherical particles are noticed (75).

In the lower Mo concentration, dendrite structures appear either on the surface or within the bulk during at one step heat treatment, while they are found only on the surface by triple step of heat treatment. One step of heat treatment results in a uniform size distribution, while the triple step of heating causes a broad distribution of crystal sizes (75).

The XRD findings indicated that an increase in the amount of $Gd_2O_3$ prevented the powellite crystals. Confirming the article of Caurant et al. 2010, the $Gd^{3+}$ ions in the depolymerised regions abundant in $MoO_4^{2-}$ species may enhance the Mo dissolvability at remaining glass site (75).

The results verify gadolinium contributes to be brought under control of $MoO_4^{2-}$ ionic groups. Powellite crystals is suppressed by stabilisation $MoO_4^{2-}$ with $Gd^{3+}$ ions, anionic group is surrounded. In that case, what is noticed is that $Gd^{3+}$ ions prevent powellite crystal formation (75).

At slower cooling rates, sodium molybdates could crystallize in the bulk (75).

In alumino-borosilicate glasses, molybdenum crystallizes as either $CaMoO_4$ (powellite) or $Na_2MoO_4$. The rare earth proportion acts a crucial influencer in molybdenum solubility in glass thus, powellite crystallization. Despite of molybdenum is a nonradioactive fission element, exist in high level inventory, would result in phase separation throughout the cooling step of the molten matrix. The separated phase, the "yellow phase" may bear radioisotopes like $^{137}Cs$, is a risk due to durability reasons. A piece containing radioactivity separated from the glass can be transported more easily to the environment, meaning a greater risk (75).

At standard canister cooling step of melt, to prevent a free Mo-including phase, the limit of 1 and 3 wt% $MoO_3$ is suitable. These glasses typically have adequate cation, allowing the immiscible separation of Mo-containing liquid to be followed by crystallization into powellite ($CaMoO_4$) (32) The formation of the yellow phase leads to reduced chemical stability of the glassy waste form (27).

Crystallization of alkaline molybdates, like $CsNaMoO_4.2H_2O$ and $Na_2MoO_4.2H_2O$, of the model nuclear glasses increases sharply for 2.5 and 5 mol% $MoO_3$. It is noticed that $MoO_3$ crystallines accumulated in distinct phase which exist as monodisperse droplets in a remaining amorphous matrix site in the SEM images.

The maximum amount of $Na_2MoO_4.2H_2O$ hydrated crystalline formed at slow cooling rate (76).

### *2.3.8. Nd enrichment of borosilicates glass-ceramics and vitrification operating conditions*

The existance of $Nd_2O_3$ in the composition results in the changes of crystalline phases, microstructure, and chemical stability of barium borosilicate glass-ceramics. The formulation chosen as $SiO_2–B_2O_3–Na_2O–BaO–CaO–TiO_2–ZrO_2–Nd_2O_3$ with 2–6 wt% of $Nd_2O_3$ consist of primary zirconolite and titanite phases and a small extent baddeleyite phase in bulk. In the glass-ceramics with 6 wt% $Nd_2O_3$, Nd elements uniformly distributed in zirconolite, titanite, as well as remaining glass structure. Additionally, these glass-ceramics exhibit lower leaching rates (LR), for the glass with 8 wt% $Nd_2O_3$. 42 days later, $LR_B$ and $LR_{Nd}$ of the Nd-6 glass-ceramics were given in Table 8. The leaching rates of B and Nd selected to discuss and tabulate from the article of Wu et al., 2016 (77).

**Table 8:** The leaching rates of elements in barium borosilicate glass-ceramics.

| Element | Leaching rate |
|---|---|
| B | $LR_B = 6.8 \times 10^{-3}$ g·m⁻²·d⁻¹ |
| Nd | $LR_{Nd} = 4.4 \times 10^{-6}$ g·m⁻²·d⁻¹ |

Besides this property of Nd, its presence in the glass structure has a crucial role. Its integration into the glass matrix has a major structural significance. In the experiments of Chouard et al., when there is no neodymium in the glass composition (NdO sample), 1.2 mol% $MoO_3$ soluble in this glass, corresponding 80%. Then, when $Nd_2O_3$ is added, the solubility of molybdenum in the glass progressively increases with increasing $Nd_2O_3$ content. Almost solubility is reached with 8–10 wt.% $Nd_2O_3$ samples (78).

### *2.3.9. Improvement in borosilicate glass: Elastic material properties based on the $Al_2O_3$ content in the borosilicates*

Sodium borosilicate glass modified by adding up to 4.0 mol% $Al_2O_3$. Based on Raman and $^{11}B$ NMR, the conversion from four-fold-coordinated boron to three-fold geometry is noticed. The reason for the planar boroxole unit models is the high amount of $Al_2O_3$ in the network, resulting in the shear softening effect that appears by the decrease in glass hardness. Elastic modulus and hardness are inversely proportional with the further quantity of more elastic trigonal borate units. This means losing the network because of its planar geometry. It enables a more extensive free volume for $B^{3+}$ to decrease the hardness of the glass network, and the glass softens (79).

### *2.3.10. Innovative approachment for developing of borosilicate glass formulations for waste immobilization based on Ce in China and confirming publications*

A radioisotope with low solubility can not be dispersed homogenously in the form of a glass network; it can break away from the structure and be transported to the environment, which may pose a risk to the protection of human health. Improvement in the solubility of the long-lived radioactive elements in glass is a particularly important issue. Np, Pu, Cm, and Am actinides have low solubility and long life, which are disadvantages for glass waste. Cerium is a simulation of the actinides for research due to the analogical chemical features of cerium and actinide.

When the doped amount is 30%, a new spherical second phase, the $CeO_2$ crystalline phase, appears in the image. These glasses exhibit good thermal stability and leaching resistance, making them effective for immobilizing simulated actinide Ce. Following the 28 days, mass loss in leaching tests the leadership belongs to Ca. Then B and after them Si is in the turn. This means Ce's networking building block is quite strong. Raman spectroscopy results show that adding Ce causes depolymerization of the glass network, and Ce is adsorbed into the gaps in the glass network (80).

The study's notable findings are that the actinide surrogates solubility limits increase with the heating temperature, and $Ce^{3+}$ is more soluble than $Ce^{4+}$ in this borosilicate glass. Plutonium, cerium, and hafnium in borosilicate glass were compared to make clear their loading capacities. The results indicate that Pu is more soluble in their trivalent than tetravalent form. Besides this, Hafnium oxide crystals and gray hafnium silicate crystals, $HfO_2$ and $HfSiO_4$, in the glass were analysed (81).

A theoretical study by N. Karpuz on the glass with a composition of $40MgO–30SiO_2 – (30-x)B_2O_3–xLa_2O_3$, where x = 0, 2.5, 5, 7.5 (mol%) was carried out Lanthanum (III) oxide improve the radiation-shielding properties of innovative types of glasses. This type of glass composition with La, provided the experiments are carried out, could also be a new opportunity for nuclear waste glass (82).

### *2.3.11. Glass corrosion in geological media under repository -Saponite formation*

Ion migration, ion exchange and diffusion are fundamental to leaching behaviour as well as corrosion. In Marcoule's SON68 glass (France) the $Na^+$ and $Li^+$ separation from the glass matrix causes $Mg^{2+}$ to be released into the solution, too. The solution was monitored. After 2291 days, below a pH of 7.0, silicate containing Mg did not precipitate. As the medium pH reaches 7.2 to 7.6, precipitation of secondary phases occurs due to initially fast glass corrosion (83).

$$3Mg^{2+} + 0.34Na^+ + 0.34Al^{3+} + 3.66H_4SiO_4 \rightarrow \text{Saponite} + 7.36H^+ + 2.64H_2O$$

Considering the formulation of hydrated saponite is ($Na_{0.34}Mg_3Al_{0.34}Si_{3.66}O_{10}(OH)_2.3.84H_2O$), the diffusive gradient of $Mg^{2+}$ and $Fe^{2+}$ between the glass and its medium shows that their conversion is slow. When magnesium concentration in the solution is decreased, the glass-corrosion rate increases. When $Mg^{2+}$ stabilizes, the equilibrium is reached, and the glass-corrosion rate sharply decreases. The sorption in clay runs in two stages: first, adsorption, followed by incorporation, where boron (B) can replace silicon (Si) and aluminum (Al) at tetrahedral positions. The reference indicates that clays could soup as much as 110 ± 22 μg of B for 1 g of rock (83).

### *2.3.12. Role of $Ba(NO_3)_2$ pretreatment in reducing the yellow phase formation*

The waste loading capacity of pretreated high-level waste (HLW) glass can reach up to 23 wt%, which is notably higher than that of non-pretreated HLW glass (~18 wt%) following melting at 1050 °C for 4 hours. Across the temperature range of 850 °C to 1100 °C, all pretreated glass compositions demonstrate a greater capacity for waste incorporation compared to their untreated counterparts. The largest disparity is observed at 850 °C. Additionally, the yellow phase is no longer observed when the temperature exceeds 1150 °C, regardless of pretreatment. This phenomenon is attributed to the volatilization of the primary constituents of the yellow phase, namely alkaline metal sulphates, at elevated temperatures and the small amount of molybdates and chromates in the yellow phase may enter into the glassy network (84).

## 3. CONCLUSION

This review aims to underline the importance of waste management policy with data on the history of nuclear waste glass in many countries. Considering the countries' 2023 nuclear electricy supplied by United States that is 779.2 billion kWh, by China that is 406.5 billion kWh, by France that is 323.8 billion kWh and by Russia 204.0 billion kWh (85). As a result the waste treatment become vital day by day based on nuclear industry performance as global highlights. When viewed top 6 countries by percentage of electricity generated by nuclear in 2023; France is coming first with 64.8%, Slovakia is second with 61.3%; Hungary is third with 48.8%, Finland is coming fourth with 42.0%. Then Belgium is coming with 41.2% and Czech Republic with 40.0%. IAEA-TECDOC indicates considering spent fuel borosilicate glasses formulations have also been developed for the immobilization of 13 wt % of $UO_2$ or 6 wt % of $PuO_2$ considering durability (86).

This review provides a historical perspective on nuclear waste vitrification in countries with chemical insights. Furthermore, atomic treatment paths, methods, and capacities are included. Nuclear glasses were found to be not as formulations incorporating boron compounds can be preferred for glass vitrification matrices. These formulations should be developed to mimic natural states, ensuring compatibility with the chemical formula of nuclear waste types and reactor fuel.

The experimental part delves into the effects of additives on glass compositions, encompassing alterations in chemical structure, physical parameters, and the formation of secondary phase crystals. Additionally, it explores the use of appropriate chemicals to prevent undesired outcomes such as glass corrosion in disposal areas and melter corrosion.

The benefits of vitrification include enhanced physical properties such as fracture resistance, elasticity, durability, and leachability, alongside the flexibility to prepare new compositions. However, materials inside the melter must exhibit sufficient chemical resistance. For the first part, within the vitrification technology and problems part, corrosion in the melter due to borax migration at high temperatures presents a significant challenge, leading to electrical shorts and damage to refractory materials. Control over Mo, Cr, Mn, and Fe oxidation states is essential to mitigate melter floor and lining hazards. Additionally, addressing solubility changes with ion oxidation states is manageable, albeit ongoing efforts are required to resolve melter floor coating issues completely.

Boric acid is used to regulate the reactivity rate and manage the power output of the reactor pressurized water. Borosilicate vitrification can immobilize boron waste in a glassy form; nonetheless, it is quite expensive due to the high temperature treatment involved (1000–1200 °C).

Formulation and optimization of high-level waste glass, particularly regarding the incorporation of molybdenum and rare earth elements, pose significant challenges due to limited solubility and potential induced amorphisation from self-irradiation. Addressing these challenges may involve the development of glass composite materials with a residual glassy phase depleted in crystalline constituents.

For the second part, the networking and chemistry part, the results shows us that crystals observed as secondary phases within barium borosilicate matrices encompass powellite, $Na_2MoO_4$, $Na_2MoO_4.2H_2O$, $CsNaMoO_4.2H_2O$, $Cs_3Na(MoO_4)_2$, zirconolite, perovskite, baddeleyite, hafnium oxide, and gray hafnium silicate crystals. Notably, the challenge of low Mo solubility in borosilicate can be addressed through Nd or Gd addition, with secondary phase formation largely dependent on cooling rates during vitrification. The effect of each chemical element on glass quality was discussed.

In situations where $MoO_3$ presents or some elements like lanthanides in the waste inventory, due to their low solubilities, especially $MoO_3$, it is inevitable for the formation of second phase as a crystalline form. It causes to move away of single phase glass structure by limiting waste loading of borosilcate glass. As appropriate according to the waste inventory, replacement of borosilicate glass; glass-ceramics is a potential opportunity waste form. In recent studies the rare earth elements have a crucial function on molybdenum solubility developing glass ceramics. The main task is fairly increasing the solubility as double. Glass ceramics, like apatites or zirconolite, are more suitable structures for some specific elements immobilization.

Among various glass microstructures, the highest waste loading quantity achieved is 43.8% by weight, correlating with a Mn content of 9% in borosilicate glass. Further analyses, such as SEM and Raman spectroscopy, are necessary to elucidate the role of Mn in the network structure.

For the third part, discussions were on improvement in the vitrified structure in the other words, on doping effects on glass structure are comprehensive within the experimental realm. These include the impact of molybdenum on borosilicate structure, the incorporation of $V_2O_5$ to enhance crack resistance, $Nd_2O_3$ enrichment to prevent crystal formation, alterations in elasticity. Besides this, the properties with varying $Al_2O_3$ ratios, Ce-doped glasses' resistance into leaching tests, the influence of gadolinium on solubilities, the role of Zn in mechanical properties, and overall durability of vitrified waste were among the issues discussed.

In terms of the gap analysis, the effect of self-irradiation is one of the major factors on the durability of glasses. The degradation of nuclear waste borosilicate and phosphate glasses doped with strong alpha-emitter $^{238}$Pu doped at a specific activity of 6.33 x $10^5$ MBq/g and containing beta- and gamma-emitters radionuclides such as $^{134}$Cs and $^{137}$Cs. It is concluded that alkali-aluminophosphate glass is less chemically durable than the borosilicate (87). $^{244}$Cm is used for self-radiation tests of Malkovsky's review. As a result of collisions with atoms of structural elements of glass, the α particle is decelerated and neutralized, and it turns into a helium atom. Most of helium formed bubbles; migrates to the glass surface and leaves it (88). Alkali-borosilicate glasses are used for vitrification of HLW except Russia that uses as sodium aluminum-phosphate glasses as industrially HWL matrix (87, 88). $^{238/239}$Pu-doped SON68 type glass blocks studied to simulate high alpha dose rates for glass durability (89).

The review highlights the novel advancement and gaps in the technique with the aim of opening avenues for further research. As a result at first coming inferences for on-going experiments that it will be better that these two points will be highlightened:

Firstly, the advantage of borosilicate glasses in terms of radiation durability over alternative industrial matrices, including geopolymers and aluminum-phosphate glasses, should be emphasised by means of planned self-irradiation experiments and the comparison test with the other matrices. Borosilicates is over the other matrices, this topic should further corroborated by the comparision with the other matrices in the literature. SON68 nuclear glass doped with a short-lived actinide $^{244}$Cm, of $4 \times 10^{18}$ $\alpha\ g^{-1}$ exhibits a reduction in density only 0.6%. The SEM and TEM analysis confirmed that the glass remains homogeneous. No evidence of phase separation, crystallization or bubbles was observed, even at alpha decay dose equivalent to several thousand years of disposal of nuclear glass canister (90).

Secondly, it should be considered that the geochemical properties of the groundwater at the disposal facility such as composition is a critical determinant of ionic mobility in leaching tests. Accordingly, researchers should treat this factor with due care, and perform experiments using several distinct groundwater compositions.

## 4. REFERENCES

1. Nascimento MLF, Cassar DR, Ciolini R, Souza SO, d'Errico F. Radioactive waste immobilization using vitreous materials for facilities in a safe and resilient infrastructure classified by multivariate exploratory analyses. Infrastructures [Internet]. 2022 Sep 13;7(9):120. Available from: <URL>.

2. Vernaz É, Bruezière J. History of nuclear waste glass in France. Procedia Mater Sci [Internet]. 2014 Jan 1;7:3–9. Available from: <URL>.

3. Besnard M. The world nuclear waste report 2019: Focus europe. 2019.

4. Gossé S, Guéneau C, Bordier S, Schuller S, Laplace A, Rogez J. A thermodynamic approach to predict the metallic and oxide phases precipitations in nuclear waste glass melts. Procedia Mater Sci [Internet]. 2014 Jan 1;7:79–86. Available from: <URL>.

5. Benigni P, Rogez J, Schuller S. Experimental determination of thermodynamical quantities in oxide mixtures and glasses. Procedia Mater Sci [Internet]. 2014 Jan 1;7:138–47. Available from: <URL>.

6. Hrma P, Ferkl P, Pokomy R. Modeling of glass properties and their effect on glass production rate in an electric melter. In: 3rd Summer School on nuclear and industrial glasses for energy transition (SUMGLASS 2023). 2023.

7. Hrma P, Ferkl P, Pokorný R, Kruger AA. Glass production rate in an electric melter: Melting rate correlation and primary foam stability. Mater Lett [Internet]. 2024 Aug 15;369:136689. Available from: <URL>.

8. Benigni P. Thermodynamic modeling of nuclear glasses and glass forming liquids. In: 3rd Summer School on nuclear and industrial glasses for energy transition (SUMGLASS 2023). 2023.

9. Gossé S, Fossati P, Dupin N, Deshkar A, Schuller S. Thermodynamic models for phase separation and crystallization in nuclear glasses. In: 3rd Summer School on nuclear and industrial glasses for energy transition (SUMGLASS 2023). 2023.

10. Weber WJ. Radiation and thermal ageing of nuclear waste glass. Procedia Mater Sci [Internet]. 2014 Jan 1;7:237–46. Available from: <URL>.

11. Weber WJ. Effects of beta/gamma radiation on nuclear waste glasses. In: CEA/Valrho summer session Glass scientific research for high performance containment [Internet]. Mejannes-Le-Clap (France); 1997. p. 194–209. Available from: <URL>.

12. Al-Mashhadani AH. Study the effect of gamma radiation on the some properties of glass and glass-ceramic immobilize nuclear waste. Iraqi J Phys [Internet]. 2019 Feb 24;11(21):75–83. Available from: <URL>.

13. Kumar A, Nayak C, Rajput P, Mishra RK, Bhattacharyya D, Kaushik CP, et al. Investigation of gamma radiation induced changes in local structure of borosilicate glass by TDPAC and EXAFS. Hyperfine Interact [Internet]. 2016 Dec 6;237(1):143. Available from: <URL>.

14. Mir AH, Jan A, Delaye JM, Donnelly S, Hinks J, Gin S. Effect of decades of corrosion on the microstructure of altered glasses and their radiation stability. npj Mater Degrad [Internet]. 2020 Apr 15;4(1):11. Available from: <URL>.

15. Sauvage E, Schuller S, Nabyl Z, Podor R, Lautru J, Benigni P, et al. Liquid feed vitrification of high-level nuclear waste: Description and modeling of chemical reactions. J Nucl Mater [Internet]. 2025 Mar 1;607:155688. Available from: <URL>.

16. Xu X, Han T, Huang J, Kruger AA, Kumar A, Goel A. Machine learning enabled models to predict sulfur solubility in nuclear waste glasses. ACS Appl Mater Interfaces [Internet]. 2021 Nov 17;13(45):53375–87. Available from: <URL>.

17. Vienna JD, Kim D, Muller IS, Piepel GF, Kruger AA. Toward understanding the effect of low-activity waste glass composition on sulfur solubility. Jantzen C, editor. J Am Ceram Soc [Internet]. 2014 Oct 24;97(10):3135–42. Available from: <URL>.

18. Marcial J, Riley BJ, Kruger AA, Lonergan CE, Vienna JD. Hanford low-activity waste vitrification: A review. J Hazard Mater [Internet]. 2024 Jan 5;461:132437. Available from: <URL>.

19. Bouty O. Application of the empirical potential structure refinement technique to a borosilicate glass of nuclear interest. Procedia Mater Sci [Internet]. 2014 Jan 1;7:32–7. Available from: <URL>.

20. Sanito RC, Bernuy-Zumaeta M, You SJ, Wang YF. A review on vitrification technologies of hazardous waste. J Environ Manage [Internet]. 2022 Aug 15;316:115243. Available from: <URL>.

21. Deptuła A, Miłkowska M, Łada W, Olczak T, Wawszczak D, Smolinski T, et al. Sol-gel processing of silica nuclear waste glasses. New J Glas Ceram [Internet]. 2011;01(03):105–11. Available from: <URL>.

22. Kelly SE. A joule-heated melter technology for the treatment and immobilization of low-activity waste [Internet]. Richland, WA (United States); 2011 Apr. Available from: <URL>.

23. Yang Y, Wang F, Kang L, Zhou H, Wang D, Fan Z. Research progress on high-level waste vitrification based on Joule heating ceramic melter. Ann Nucl Energy [Internet]. 2025 Jun 15;216:111273. Available from: <URL>.

24. Salihuddin R, Baan R, Zakaria N, others and. Radioactive waste treatment and conditioning using plasma technology pilot plant: Testing and commissioning. In: Research and Development Seminar 2016 (R&D Seminar 2016) [Internet]. Bangi (Malaysia); 2016. Available from: <URL>.

25. Tzeng CC, Kuo YY, Huang TF, Lin DL, Yu YJ. Treatment of radioactive wastes by plasma incineration and vitrification for final disposal. J Hazard Mater [Internet]. 1998 Feb 1;58(1–3):207–20. Available from: <URL>.

26. Ojovan MI, Lee WE. An introduction to nuclear waste immobilisation [Internet]. 2nd Edition. Elsevier; 2014. Available from: <URL>.

27. Manaktala HK. An assessment of borosilicate glass as a high-level waste form. San Antonio, Texas;

1992.

28. Hench LL, Clark DE, Harker AB. Nuclear waste solids. J Mater Sci [Internet]. 1986 May;21(5):1457–78. Available from: <URL>.

29. Kaushik CP. Indian program for vitrification of high level radioactive liquid waste. Procedia Mater Sci [Internet]. 2014 Jan 1;7:16–22. Available from: <URL>.

30. Harrison MT. Vitrification of high level waste in the UK. Procedia Mater Sci [Internet]. 2014;7:10–5. Available from: <URL>.

31. Thorpe CL, Neeway JJ, Pearce CI, Hand RJ, Fisher AJ, Walling SA, et al. Forty years of durability assessment of nuclear waste glass by standard methods. npj Mater Degrad [Internet]. 2021 Dec 20;5(1):61. Available from: <URL>.

32. Vienna JD. Nuclear waste vitrification in the United States: Recent developments and future options. Int J Appl Glas Sci [Internet]. 2010 Sep 16;1(3):309–21. Available from: <URL>.

33. Yıldız B, Erten HN, Kış M. The sorption behavior of $Cs^+$ ion on clay minerals and zeolite in radioactive waste management: Sorption kinetics and thermodynamics. J Radioanal Nucl Chem [Internet]. 2011 May 12;288(2):475–83. Available from: <URL>.

34. Pilania RK, Dube CL. Matrices for radioactive waste immobilization: A review. Front Mater [Internet]. 2023 Sep 28;10:1236470. Available from: <URL>.

35. Jin T, Hall MA, Vienna JD, Eaton WC, Amoroso JW, Wiersma BJ, et al. Glass-contact refractory of the nuclear waste vitrification melters in the United States: A review of corrosion data and melter life. Int Mater Rev [Internet]. 2023 Nov 29;68(8):1135–57. Available from: <URL>.

36. Guillen DP, Lee S, Hrma P, Traverso J, Pokorny R, Klouzek J, et al. Evolution of chromium, manganese and iron oxidation state during conversion of nuclear waste melter feed to molten glass. J Non Cryst Solids [Internet]. 2020 Mar 1;531:119860. Available from: <URL>.

37. Crum J V., Vienna JD, Riley BJ, Silverstein JA, Kissinger RM, Neeway JJ, et al. Formulation and testing of a high-tin borosilicate nuclear waste glass for in-can melting. J Nucl Mater [Internet]. 2023 Nov 1;585:154643. Available from: <URL>.

38. Sakai A, Ishida S. Reflective reviews on Japanese high-level waste (HLW) vitrification – Exploring the obstacles encountered in active tests at Rokkasho. Ann Nucl Energy [Internet]. 2024 Feb 1;196:110175. Available from: <URL>.

39. Kovalev N V., Prokoshin AM, Davydova P V., Korolev VA. Radiation characteristics of reactor grade platinum group metals. Nucl Energy Technol [Internet]. 2025 Mar 7;11(1):55–8. Available from: <URL>.

40. Duan X, Zhang Q, Liu X, Qian Z, Zhang K, Zhu G, et al. The influence of $RuO_2$ crystal morphology on the conductivity of glass melts during vitrification process. J Nucl Mater [Internet]. 2025 Oct 1;616:156068. Available from: <URL>.

41. Vitrified high-level radioactive waste. U.S. nuclear waste technical review board, revision 1. 2017.

42. Rankin WD, Wicks GG. Chemical durability of savannah river plant waste glass as a function of waste loading. J Am Ceram Soc [Internet]. 1983 Jun 2;66(6):417–20. Available from: <URL>.

43. Walker DD, Wiley JR, Dukes MD, LeRoy JH. Leach rate studies on glass containing actual radioactive waste. Nucl Chem Waste Manag [Internet]. 1982 Jan 1;3(2):91–4. Available from: <URL>.

44. Hossen A, Rayhan MM, Sarker MSA, Saha A, Hamrani A, McDaniel D. A systematic review on grout in nuclear waste management: Advancement, composition and performance. Nucl Eng Des [Internet]. 2025 Nov 1;443:114281. Available from: <URL>.

45. Dukes MD, Mosley WC, Rankin WN, Tennant MH, Wiley JR. Multibarrier storage of savannah river plant waste. In Springer, Boston, MA; 1980. p. 231–8. Available from: <URL>.

46. Crouse SH, Prasad R, Maharjan N, Ocampo VC, Woodham WH, Lambert DP, et al. Selected chemical engineering applications in nuclear-waste processing at the savannah river Site. Annu Rev Chem Biomol Eng [Internet]. 2025 Jun 9;16(1):349–70. Available from: <URL>.

47. Hobbs DT, Walker DD. Chemical pretreatment of savannah river site nuclear waste. In: 204 American Chemical Society (ACS) national meeting [Internet]. Washington, DC (United States): American Chemical Society; 1992. p. 613–613. Available from: <URL>.

48. Weismanl AF, Knightz JR, Mclntoshz GL, Papouchado LM. High level waste vitrification at the SRP (DWPF Summary). In: Waste Management '88. 1988.

49. Michel F, Cormier L, Lombard P, Beuneu B, Galoisy L, Calas G. Mechanisms of boron coordination change between borosilicate glasses and melts. J Non Cryst Solids [Internet]. 2013 Nov 1;379:169–76. Available from: <URL>.

50. Li H, Wu L, Wang X, Xu D, Teng Y, Li Y. Crystallization behavior and microstructure of barium borosilicate glass–ceramics. Ceram Int [Internet]. 2015 Dec 1;41(10):15202–7. Available from: <URL>.

51. Shelby JE. Introduction to glass science and technology. Second edition. Cambridge, UK: The Royal Society of Chemistry; 2005.

52. Kashif I, Sakr EM, Soliman AA, Ratep A. Influence of $SiO_2$ substitution for $B_2O_3$ on the properties of borosilicate glasses. Phys Chem Glas - Eur J Glas Sci

Technol Part B [Internet]. 2013;54(1):35–41. Available from: <URL>.

53. Lu X, Ren M, Deng L, Benmore CJ, Du J. Structural features of ISG borosilicate nuclear waste glasses revealed from high-energy X-ray diffraction and molecular dynamics simulations. J Nucl Mater [Internet]. 2019 Mar 1;515:284–93. Available from: <URL>.

54. Magnin M. Etude Des Processus De Démixtion et De Cristallisation Au Sein De Liquides Fondus Borosilicatés Riches En Oxyde De Molybdene, Commissariat a L'énergie Atomique, Direction De L'energie Nucleaire Départment D'études Du Traitement et Du Conditionnement Dés Déchets, 2010, Rapport, CEA-R-6237 (in French)

55. Caurant D, Majérus O, Fadel E, Quintas A, Gervais C, Charpentier T, et al. Structural investigations of borosilicate glasses containing $MoO_3$ by MAS NMR and Raman spectroscopies. J Nucl Mater [Internet]. 2010 Jan 1;396(1):94–101. Available from: <URL>.

56. Calas G, Le Grand M, Galoisy L, Ghaleb D. Structural role of molybdenum in nuclear glasses: An EXAFS study. J Nucl Mater [Internet]. 2003 Oct 1;322(1):15–20. Available from: <URL>.

57. Krishnamurthy A, Kroeker S. Improving molybdenum and sulfur vitrification in borosilicate nuclear waste glasses using phosphorus: Structural insights from NMR. Inorg Chem [Internet]. 2022 Jan 10;61(1):73–85. Available from: <URL>.

58. Schuller S, Pinet O, Penelon B. Liquid–liquid phase separation process in borosilicate liquids enriched in molybdenum and phosphorus oxides. J Am Ceram Soc [Internet]. 2011 Feb 14;94(2):447–54. Available from: <URL>.

59. Sugawara T, Ohira T, Owaku K, Kanehira N, Tsukada T. CALPHAD optimization of $SiO_2$-$B_2O_3$-$Al_2O_3$-ZnO-CaO-$Na_2O$-$Li_2O$-$MoO_3$ system and their applications to high-level radioactive waste vitrification. Mater Lett [Internet]. 2025 Aug 15;393:138540. Available from: <URL>.

60. Motokawa R, Kaneko K, Oba Y, Nagai T, Okamoto Y, Kobayashi T, et al. Nanoscopic structure of borosilicate glass with additives for nuclear waste vitrification. J Non Cryst Solids [Internet]. 2022 Feb 15;578:121352. Available from: <URL>.

61. Maity S, Ghosh C, Srihari V, Pan S, Selvakumar J, Suneel G, et al. $Fe_2O_3$ solubility and structural investigation in simulated high-level liquid waste vitrified $Na_2O$-$TiO_2$-$Fe_2O_3$ -$B_2O_3$-$SiO_2$ glass system. Ceram Int [Internet]. 2025 Aug 1;51(20):31009–20. Available from: <URL>.

62. Wu L, Xiao J, Wang X, Teng Y, Li Y, Liao Q. Crystalline phase, microstructure, and aqueous stability of zirconolite–barium borosilicate glass-ceramics for immobilization of simulated sulfate bearing high-level liquid waste. J Nucl Mater [Internet]. 2018 Jan 1;498:241–8. Available from: <URL>.

63. Kaushik CP, Mishra RK, Sengupta P, Kumar A, Das D, Kale GB, et al. Barium borosilicate glass – a potential matrix for immobilization of sulfate bearing high-level radioactive liquid waste. J Nucl Mater [Internet]. 2006 Nov 30;358(2–3):129–38. Available from: <URL>.

64. Magnin M, Schuller S, Angeli F. Study of molybdenum incorporation in nuclear waste glasses: Effect of compositional variations in borosilicate glasses rich in $MoO_3$. In: Proceedings of Global 2009 [Internet]. Paris, France; 2009. p. 9288. Available from: <URL>.

65. Lonergan CE, Neeway JJ. A critical review of ion exchange in nuclear waste glasses to support the immobilized low-activity waste integrated disposal facility rate model [Internet]. Richland, WA (United States); 2017 Sep. Available from: <URL>.

66. Bouty O, Delaye JM, Beuneu B, Charpentier T. Modelling borosilicate glasses of nuclear interest with the help of RMC, WAXS, neutron diffraction and 11B NMR. J Non Cryst Solids [Internet]. 2014 Oct 1;401:27–31. Available from: <URL>.

67. Quintas A, Charpentier T, Majérus O, Caurant D, Dussossoy JL, Vermaut P. NMR study of a rare-earth aluminoborosilicate glass with varying CaO-to-$Na_2O$ ratio. Appl Magn Reson [Internet]. 2007 Dec;32(4):613–34. Available from: <URL>.

68. El-Rehim AFA, Zahran HY, Yahia IS, Wahab EAA, Shaaban KS. Structural, elastic moduli, and radiation shielding of $SiO_2$-$TiO_2$-$La_2O_3$-$Na_2O$ glasses containing $Y_2O_3$. J Mater Eng Perform [Internet]. 2021 Mar 16;30(3):1872–84. Available from: <URL>.

69. Singh S, Kalia G, Singh K. Effect of intermediate oxide ($Y_2O_3$) on thermal, structural and optical properties of lithium borosilicate glasses. J Mol Struct [Internet]. 2015 Apr 15;1086:239–45. Available from: <URL>.

70. Al-Buriahi MS, Kırkbınar M, İbrahimoğlu E, Çalışkan F, Alrowaili ZA, Olarinoye IO, et al. Recycling of optical borosilicate waste glasses by $Y_2O_3$ doping for radiation shielding applications. Optik (Stuttg) [Internet]. 2023 Feb 1;273:170399. Available from: <URL>.

71. Calas G, Galoisy L, Cormier L, Ferlat G, Lelong G. The structural properties of cations in nuclear glasses. Procedia Mater Sci [Internet]. 2014 Jan 1;7:23–31. Available from: <URL>.

72. Calas G, Cormier L, Galoisy L, Jollivet P. Structure–property relationships in multicomponent oxide glasses. Comptes Rendus Chim [Internet]. 2002 Dec 1;5(12):831–43. Available from: <URL>.

73. Manara D, Grandjean A, Pinet O, Dussossoy JL, Neuville DR. Sulfur behavior in silicate glasses and melts: Implications for sulfate incorporation in nuclear waste glasses as a function of alkali cation and $V_2O_5$ content. J Non Cryst Solids [Internet]. 2007 Jan 1;353(1):12–23. Available from: <URL>.

74. Lu X, Sun R, Huang L, Ryan J V., Vienna JD, Du

J. Effect of vanadium oxide addition on thermomechanical behaviors of borosilicate glasses: Toward development of high crack resistant glasses for nuclear waste disposal. J Non Cryst Solids [Internet]. 2019 Jul 1;515:88–97. Available from: <URL>.

75. Taurines T, Boizot B. Microstructure of powellite-rich glass-ceramics: A model system for high level waste immobilization. Pinckney L, editor. J Am Ceram Soc [Internet]. 2012 Mar 10;95(3):1105–11. Available from: <URL>.

76. Kroeker S, Schuller S, Wren JEC, Greer BJ, Mesbah A. $^{133}$Cs and $^{23}$Na MAS NMR spectroscopy of molybdate crystallization in model nuclear glasses. Jantzen C, editor. J Am Ceram Soc [Internet]. 2016 May 3;99(5):1557–64. Available from: <URL>.

77. Wu L, Li H, Wang X, Xiao J, Teng Y, Li Y. Effects of Nd content on structure and chemical durability of zirconolite–barium borosilicate glass-ceramics. Vance E, editor. J Am Ceram Soc [Internet]. 2016 Dec 10;99(12):4093–9. Available from: <URL>.

78. Chouard N, Caurant D, Majérus O, Dussossoy JL, Ledieu A, Peuget S, et al. Effect of neodymium oxide on the solubility of $MoO_3$ in an aluminoborosilicate glass. J Non Cryst Solids [Internet]. 2011 Jul 1;357(14):2752–62. Available from: <URL>.

79. Bruns S, Uesbeck T, Weil D, Möncke D, van Wüllen L, Durst K, et al. Influence of $Al_2O_3$ addition on structure and mechanical properties of borosilicate glasses. Front Mater [Internet]. 2020 Jul 28;7:525928. Available from: <URL>.

80. Yang L, Zhu Y, Huo J, Cui Z, Zhang X, Dong X, et al. Solubility and valence variation of Ce in low-alkali borosilicate glass and glass network structure analysis. Materials [Internet]. 2023 Jul 18;16(14):5063. Available from: <URL>.

81. Lopez C, Deschanels X, Bart JM, Boubals JM, Den Auwer C, Simoni E. Solubility of actinide surrogates in nuclear glasses. J Nucl Mater [Internet]. 2003 Jan 1;312(1):76–80. Available from: <URL>.

82. Karpuz N. Effect of $La_2O_3$ on magnesium borosilicate glasses glass for radiation shielding materials in nuclear application. Radiat Phys Chem [Internet]. 2024 Jan 1;214:111305. Available from: <URL>.

83. Debure M, Linard Y, Martin C, Claret F. In situ nuclear-glass corrosion under geological repository conditions. npj Mater Degrad [Internet]. 2019 Oct 31;3(1):38. Available from: <URL>.

84. Lei J, Wang B, Xu L, Teng Y, Li Y, Deng H, et al. Role of $Ba(NO_3)$ pretreatment in reducing the yellow phase formation during vitrification of nuclear waste. J Nucl Mater [Internet]. 2021 Nov 1;555:153121. Available from: <URL>.

85. World nuclear association, information library, nuclear generation by country, updated 6. 2024.

86. IAEA (International Atomic Energy Agency). Spent fuel and high level waste: Chemical durability and performance under simulated repository conditions. Vienna, Austria; 2007.

87. Zubekhina BY, Burakov BE, Ojovan MI. Surface alteration of borosilicate and phosphate nuclear waste glasses by hydration and irradiation. Challenges [Internet]. 2020 Jul 23;11(2):14. Available from: <URL>.

88. Malkovsky VI, Yudintsev S V., Ojovan MI, Petrov VA. The influence of radiation on confinement properties of nuclear waste glasses. Sci Technol Nucl Install [Internet]. 2020 Aug 1;2020(1):875723. Available from: <URL>.

89. Tribet M, Marques C, Mougnaud S, Broudic V, Jegou C, Peuget S. Alpha dose rate and decay dose impacts on the long-term alteration of HLW nuclear glasses. npj Mater Degrad [Internet]. 2021 Jul 7;5(1):36. Available from: <URL>.

90. Peuget S, Cachia JN, Jégou C, Deschanels X, Roudil D, Broudic V, et al. Irradiation stability of R7T7-type borosilicate glass. J Nucl Mater [Internet]. 2006 Aug 1;354(1–3):1–13. Available from: <URL>.

# Design, Synthesis, and Biological Evaluation of Schiff Base and Azo Derivatives of Cefixime: Antibacterial, Antifungal, Antioxidant, ADMET, and Docking Studies

**Aqeel Sami Majeed[1]*, Mohammed Rifaat Ahmad[1]**

[1]University of Baghdad, Collage of Sciences, Department of Chemistry, Baghdad, Iraq.

**Abstract:** The development of new antibiotics is imperative due to the increasing resistance of bacteria to existing drugs. This study aimed to synthesize Schiff bases and azo derivatives of cefixime, a third-generation cephalosporin, and to evaluate their antimicrobial and antioxidant activities. The antibacterial activity of the synthesized compounds was assessed against *Candida albicans* and various Gram-positive and Gram-negative pathogens. Several derivatives exhibited potent antibacterial and antifungal activities, with compounds C6 and C9 demonstrating superior efficacy compared to standard antibiotics. Furthermore, molecular docking simulations revealed favorable interactions between these derivatives and beta-lactamase enzymes as well as penicillin-binding proteins, providing insights into their mechanism of action. Despite some limitations in bioavailability, the ADMET analysis clarified their pharmacokinetic profiles and confirmed their potential for systemic administration. These findings highlight the potential of cefixime-derived azo compounds and Schiff bases as novel strategies to overcome antibiotic resistance. Notably, compounds C9 and C6 differentiated themselves through enhanced antibacterial and antioxidant properties, making them promising candidates for further research, including preclinical and clinical evaluations following comprehensive pharmacological and therapeutic assessments.

**Keywords:** Cefixime, Schiff-base, Azo-derivatives, Antimicrobial, Molecular docking, PDP receptors, β-lactamase.

**Submitted:** July 10, 2025. **Accepted:** October 3, 2025.

**Cite this:** Majeed AS, Ahmad MR. Design, Synthesis, and Biological Evaluation of Schiff Base and Azo Derivatives of Cefixime: Antibacterial, Antifungal, Antioxidant, ADMET, and Docking Studies. JOTCSA. 2025;12(4): 269-86.

**DOI:** https://doi.org/10.18596/jotcsa.1739097

***Corresponding author's E-mail:** aqeel.sami@sc.uobaghdad.edu.iq

## 1. INTRODUCTION

Antimicrobial resistance (AMR) is among the greatest global public health challenges of the twenty-first century. The increasing prevalence of multidrug-resistant (MDR) bacteria is drastically threatening the efficacy of existing antibiotics, resulting in enhanced morbidity and mortality, and imposing substantial healthcare costs around the world (1-3). As a result, it is imperative to intensify research efforts and continue developing new antimicrobial agents with novel mechanisms of action to address these evolving threats (4-6).

For years, β-lactam antibiotics, particularly cephalosporin-type antibiotics such as cefixime, have dominated antibacterial therapy due to their ability to inhibit the synthesis of bacterial cell walls (7). This inhibition relies on the formation of a strong peptidoglycan layer, a complex polymer consisting mainly of a chain of alternating N-acetylglucosamine (NAG) and N-acetylmuramic acid (NAM) units cross-linked by short peptides. Penicillin-binding proteins (PBPs) are a group of bacterial enzymes that catalyze these cross-linking reactions within the peptidoglycan, forming the structural backbone of the bacterial cell wall, and are among the molecular targets of β-lactam antibiotics. Inhibition of this process, particularly the late transpeptidation step catalyzed by PBPs, is generally bactericidal to bacteria in vivo (8-14).

Nonetheless, the resistance to cefixime increased at a rapid rate, despite its effectiveness in treating a variety of bacterial infectious diseases in both pediatric and adult patients (15). Bacteria have evolved a broad array of resistance mechanisms, including the expression of beta-lactam-destroying enzymes, beta-lactamases, which cleave the beta-lactam ring and thereby render the antibiotic inactive (16-18). Moreover, efflux pumps in Gram-negative organisms can pump the drug out of the cell, and bacterial PBPs have been shown to undergo structural changes, resulting in a decrease in binding affinities for beta-lactam-based antibiotics (19).

As a result, there is an urgent need for alternative therapies that are not solely dependent on beta-lactams or that minimally utilize them (20,21). In this context, the synthesis of Schiff bases and azo compounds has received considerable attention in drug discovery, as they possess potent biological activity. Quinazoline and its derivatives have garnered significant attention due to their potent antimicrobial activity (22,23). Schiff bases possess physicochemical properties and have the potential to modify biological activity. Schiff's bases, which are derived from the condensation of an aldehyde or a ketone with a primary amine, possess a (C=N) imine bond, which imparts enhanced solubility and modification of biological activity (24-29).

In addition, azo compounds have garnered significant attention in recent years due to their diverse biological activities, including effective antimicrobial properties against certain Gram-positive and Gram-negative bacteria, as well as fungi (30,31). These molecules interact with DNA, produce reactive oxygen species, and perturb key metabolic networks. In fact, their potential matches well with that of most of the classical drugs, with the added advantage of their conversion to active species due to the metabolic activation of azo compounds in the biological system (27,32,33).

The search for new chemical scaffolds with proven antimicrobial potential, such as Schiff bases and azo compounds, is imperative due to the growing problem of antimicrobial resistance and the urgent need for new therapeutic options. The structural flexibility and the easy access to these types of compounds make them a good choice for drug design and for researchers to develop new antimicrobial agents. This review provides a comprehensive description of the antimicrobial and antioxidant effects of certain Schiff bases and azo derivatives of cefixime, including their mechanisms of synthesis, potential biological applications, ADMET properties, and molecular docking evaluations at penicillin receptors. It justifies their compliance with the five Lipinski rules for drug-like properties.

## 2. EXPERIMENTAL SECTION

### 2.1. Chemistry

The high-purity reagents and anhydrous solvents used in this study were all obtained from Sigma Aldrich, Riedel-de Haen, Merck (Germany), BDH (England), and CDH (China). Infrared (FT-IR) recordings, obtained using an FT-IR-6100 Type A infrared spectrometer combined with potassium bromide tablets, were employed to identify the chemicals. (1H-NMR and 13C-NMR) were performed using a Bruker 400 MHz spectrometer at Al-Basara University.

*2.1.1. Synthesis of schiff base and azo derivatives (C1-C9)* (34,35)

Schiff base derivatives were synthesized by reacting cefixime with various aromatic aldehydes in ethanol under microwave irradiation. In contrast, azo derivatives were prepared by diazotization of cefixime followed by coupling with phenolic compounds. The products were purified by column chromatography. As shown in Scheme 1.

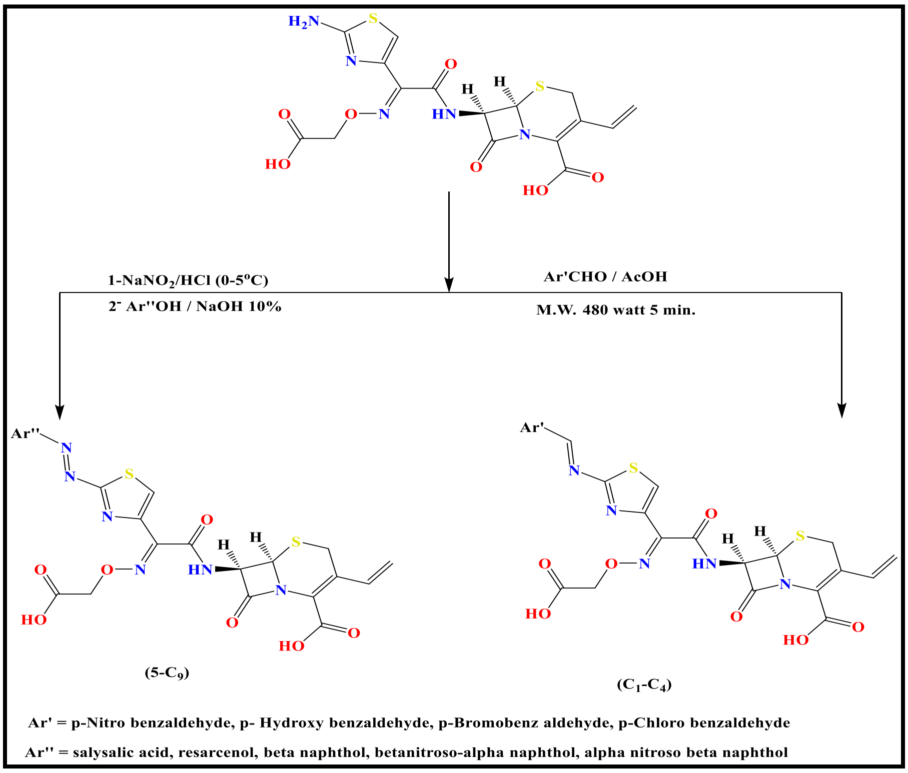

**Scheme 1:** General Procedure to Prepare Schiff Bases and Azo Compounds.

### 2.2. ADMET Procedure

The ligands (C1-C9) were generated using ChemDraw 15 and subsequently transformed into SMILE format using the Swiss ADME site (http://www.swissadme.ch/) (36). This tool forecasted the ligands' physicochemical and pharmacokinetic characteristics. The ProTox-3 (https://tox.charite.de/protox3/) (37). The site was used to predict toxicity for all compounds under study.

### 2.3. Molecular Docking

*2.3.1. Ligands and protein receptor preparation*

The Protein Data Bank supplied the crystal structures of three penicillin-binding proteins from various bacteria: *Staphylococcus pneumoniae* and *Staphylococcus aureus* (PBP2a (1VQQ) (38), PBP-2B (2WAE) (39), PBP2x (1PYY) (40), and β-Lactamase Toho-1 (1IYS) (41) *Escherichia coli.*

Compounds were drawn, and their energies were optimized using ChemDraw and Chem3D to determine the minimum energy required for the synthesized compounds.

*2.3.2. Docking protocols*

Molecular docking was performed using AutoDock4 (42). To prepare the receptors for the docking procedure. Protein residues within a 40 Å radius of the reference ligands derived from the downloaded protein structure complexes were classified as part of the binding region for bulk docking. They were utilized for docking purposes. Graphics were generated using PyMOL and Discovery Studio to illustrate the amino acid residues associated with the ligands, and the distances between the ligands and the receptor were computed.

### 2.4. Antimicrobial Activity (43)

The Agar Diffusion method was employed to investigate the antibacterial efficacy of synthesized cefixime derivatives against various bacterial strains, utilizing cefixime and ampicillin as reference agents. Nutrient agar medium, dimethyl sulfoxide sample solution, and sample quantities for all examined chemicals were utilized, with the sample volume established at 0.02 M. The beakers were emptied of the agar medium into a pre-prepared Petri plate containing bacteria. 0.1 ml of the test compound solution was introduced into the beakers, and the Petri dishes were incubated at 37°C for 48 hours. The zones of inhibition produced by each chemical were quantified in millimeters, and the results are presented in Table 12 and Figure 4.

### 2.5. Antioxidant Activity (44)

Four milligrams of DPPH were dissolved in 100 milliliters of ethanol, and the solution was shielded from light by covering the containers with aluminum foil. Various concentrations (100, 50, 25, 12.5, and 6.25 ppm) were prepared from C1-C9 by dissolving 1 mg of the chemical in 10 ml of ethanol to produce a 100-ppm solution, which was further diluted to obtain the other concentrations. Various concentrations (100, 50, 25, 12.5, and 6.25 ppm) were prepared from C1-C9 by dissolving 1 mg of the chemical in 10 ml of ethanol to produce a 100-ppm solution, which was further diluted to achieve the other concentrations.

- Ascorbic acid (vitamin C): Equivalent quantities of the synthesised compounds were prepared.

Procedure: The efficacy of the stable free radical DPPH in neutralizing deleterious chemicals was assessed to evaluate the antioxidant capacity of the plant methanol extract and conventional vitamin C. In a test tube, 1 ml of the diluted or standard solution (100, 50, 25, 12.5, or 6.25 ppm) was mixed with 1 ml of DPPH solution. The absorbance of each solvent was measured with a spectrophotometer at 517 nm. Thereafter, incubation occurred at 37°C for one hour. Three measurements were conducted using the equation to assess the capacity to eliminate DPPH.

$$I\% = \frac{(AB - AS)}{AB} \times 100$$

## 3. RESULTS AND DISCUSSION

### 3.1. Chemistry (34,35,45)

Schiff Base Derivatives (C1–C4): We have retained the basic Cefixime structure with an adequate orientation of the beta-lactam ring, thereby maintaining its antibacterial activity. The FTIR band of the sample detected peaks assigned as O-H and N-H (3323–3421 cm$^{-1}$), β-lactam carbonyl (1733–1747 cm$^{-1}$), and carboxylic acid carbonyl groups (1670–1701 cm$^{-1}$). Halogen substituents (C–Br at 555 cm$^{-1}$ and C–Cl at 719 cm$^{-1}$) at C3 and C4 in derivatives may affect stability and the pharmacological potential. The appearance of C=N (imine) groups (1556–1681 cm$^{-1}$) may contribute to the increased structural stability and recognition of the receptor. In general, these compounds retain the antibacterial β-lactam, but small changes in the functional groups enable a wide range of variation in physicochemical properties. All FTIR spectral data are found in Table 1.

Azo Derivatives (C5–C9) Azo (N=N) groups are present in these derivatives (1398–1413 cm$^{-1}$), which provide new chemical properties that may be associated with photoreactivity and potentially better biological profiles. The large peaks of the β-lactam and carboxylic acid carbonyl groups are seen at 1718–1730 cm$^{-1}$ and 1668–1679 cm$^{-1}$, respectively. The (N=O) groups will provide specific (N=O) features at 1523 and 1344 cm$^{-1}$, which might affect stability and therapeutic efficacy. The Aromatic (C=C) stretching (1556 1633 cm$^{-1}$) indicates the involvement of aromatic cycles in the network. Derivative C7, which exhibits an extra broad hydroxyl absorption band at 3394 cm$^{-1}$, can be suggested to contain additional hydroxyl groups or hydrogen bonding. All FTIR spectral data are found in Table 1.

Finally, the cefixime backbone system structure of Schiff base derivatives is retained with minimal halogen substitutions, exhibiting good antibacterial potential and improved physicochemical properties. Azo derivatives can provide azo and nitro groups that further enhance their functional diversity, offering potential improvements in chemical and biological properties due to their potential photo-responsive capabilities, while retaining functional heterocyclic pharmacophores. FTIR unequivocally confirms these structural changes and their implications for the biological activities and applications of Cefixime analogues.

**Table 1:** FTIR Spectral Data for Compounds (C1-C9).

| Com. ID | FTIR spectral data v / cm$^{-1}$ | | | | | | | |
|---|---|---|---|---|---|---|---|---|
| | **OH** | **NH** | **C=O beta lactam** | **C=O acid** | **C=N** | **N=N** | **C=C** | **Other bands** |
| **C1** | 3400 | 3336 | 1742 | 1701 | 1681 | -- | 1556 | $NO_2$ 1523 & 1344 |
| **C2** | 3323 | 3292 | 1745 | 1679 | 1600 | -- | 1581 | Overlapped |
| **C3** | 3390 | 3325 | 1741 | 1680 | 1652 | -- | 1556 | C-Br 555 |
| **C4** | 3421 | 3392 | 1747 | 1677 | 1654 | -- | 1556 | C-Cl 719 |
| **C5** | 3371 & 3390 | 3296 | 1733 | 1718 & 1670 | -- | 1402 | 1556 | |
| **C6** | 3232 | 3199 | 1731 | 1668 | -- | 1404 | 1595 | |
| **C7** | 3427 | 3373 | 1737 | 1679 | -- | 1402 | 1633 | 3394 |
| **C8** | 3411 | 3361 | 1741 | 1677 | -- | 1398 | 1629 | N=O 1515 & 1317 |
| **C9** | 3301 | 3240 | 1730 | 1676 | -- | 1413 | 1539 | N=O 1523 & 1373 |

**Compound C1** was prepared from cefixime and p-nitrobenzaldehyde; pale yellow; m.p. 133-135°C; (87%) yield. IR (KBr, cm-1) v = 3400 (OH), 1742 β-lactam (C=O), 1681 (C=N), 1523 & 1344 ($NO_2$); $^1$H NMR (400 MHz, DMSO) δ 13.07 (s, 1H), 9.64 – 9.57 (m, 1H), 9.05 (s, 1H), 8.44 (s, 2H), 8.43 (d, *J* = 8.6 Hz, 1H), 8.18 (dd, *J* = 8.8, 2.4 Hz, 2H), 7.67 (d, *J* = 16.8 Hz, 2H), 6.98 – 6.79 (m, 2H), 5.82 (dd, *J* = 8.2, 4.7 Hz, 1H), 5.60 (d, *J* = 17.5 Hz, 1H), 5.32 (d, *J* = 11.4 Hz, 1H), 5.22 (d, *J* = 4.9 Hz, 1H), 4.63 – 4.56 (m, 3H), 3.94 – 3.81 (m, 1H); $^{13}$C NMR (101 MHz, DMSO) δ 181.00, 171.59, 168.95, 164.06, 163.70, 162.94, 150.33, 132.45, 131.13, 129.51, 126.01, 124.76, 124.64, 124.22, 116.86, 110.80, 78.96, 71.12, 59.34, 58.14, 32.01.

**Compound C2** was prepared from cefixime and p-hydroxybenzaldehyde; orange; m.p. 168-170°C; (80%) yield. IR (KBr, cm-1) v = 3323 (OH), 1745 β-lactam (C=O), 1600 (C=N); $^1$H NMR (400 MHz, DMSO) δ 12.55 (s, 1H), 9.67 (s, 1H), 9.17 (d, *J* = 56.5 Hz, 1H), 7.69 (dd, *J* = 9.2, 2.6 Hz, 4H), 6.78 (dd, *J* = 9.3, 2.6 Hz, 3H), 6.66 (d, *J* = 17.8 Hz, 1H), 6.33 – 5.64 (m, 2H), 5.07 (s, 1H), 4.90 – 4.41 (m, 1H), 4.18 (s, 2H), 3.88 (d, *J* = 32.3 Hz, 2H), $^{13}$C NMR (101 MHz, DMSO) δ 190.33, 172.52, 166.68, 163.28, 161.67, 158.89, 154.65, 143.14, 139.73, 136.25, 132.01, 128.73, 124.97, 120.85, 117.99, 115.48, 114.23, 111.51, 73.77, 64.01, 59.99, , 34.13, 29.50, 29.21.

**Compound C3** was prepared from cefixime and p-bromobenzaldehyde; Yellow; m.p. 123-125°C; (77%) yield. IR (KBr, cm-1) v = 3323 (OH), 1745 β-lactam (C=O), 1652 (C=N); $^1$H NMR (400 MHz, DMSO) δ 12.64 (s, 1H), 11.84 (s, 1H), 9.99 (s, 1H), 9.16 (d, *J* = 8.5 Hz, 2H), 9.08 (s, 1H), 7.84 (s, 3H), 7.78 (s, 1H), 7.51 (s, 3H), 7.27 (d, *J* = 12.9 Hz, 5H), 7.08 (s, 1H), 6.95 – 6.79 (m, 2H), 6.04 (s, 1H), 5.97 (d, *J* = 7.0 Hz, 2H), 5.81 (s, 1H), 5.59 (d, *J* = 17.1 Hz, 1H), 5.08 (s, 6H), 4.56 (s, 4H), 4.16 (s, 9H), 3.91 (s, 2H). $^{13}$C NMR (101 MHz, DMSO) δ = 192.52, 182.03, 174.99, 171.28, 170.85, 169.31, 168.87, 162.65, 159.30, 150.17, 147.57, 142.75, 135.58, 134.12, 132.78, 132.16, 131.72, 129.09, 115.95, 113.66, 111.93, 103.19, 73.53, 61.78, 57.54, 29.48.

**Compound C4** was prepared from cefixime and p-chloroybenzaldehyde; Yellow; m.p. 118-120°C; (79%) yield. IR (KBr, cm-1) v = 3421 (OH), 1747 β-lactam (C=O), 1654 (C=N); $^1$H NMR (400 MHz, DMSO) δ 12.64 (s, 1H), 11.85 (s, 1H), 10.87 (s, 1H), 9.99 (s, 1H), 8.68 – 8.22 (m, 1H), 8.15 – 6.93 (m, 3H), 6.64 (dt, *J* = 54.8, 13.7 Hz, 1H), 6.42 – 5.58 (m, 1H), 5.52 (d, *J* = 7.3 Hz, 1H), 5.28 – 4.99 (m, 1H), 4.17 (s, 1H), 3.81 (dd, *J* = 30.5, 8.4 Hz, 2H); $^{13}$C NMR (101 MHz, DMSO) δ 171.79, 169.26, 156.40, 152.51, 148.67, 140.11, 139.33, 136.68, 129.89, 129.52, 129.22, 128.76, 128.66, 128.53, 128.28, 128.05, 127.52, 123.24, 68.40, 58.22, 37.74, 34.23, 31.77, 30.19, 29.50, 29.19, 29.05.

**Compound C5** was prepared from cefixime and salicylic acid; Red; m.p. 202-204°C; (53%) yield. IR (KBr, cm-1) v = 3371 & 3390 (OH), 1733 β-lactam (C=O), 1402 (N=N); $^1$H NMR (400 MHz, DMSO) δ 12.64 (s, 1H), 11.85 (s, 1H), 10.87 (s, 1H), 9.99 (s, 1H), 8.68 – 8.22 (m, 1H), 8.15 – 6.93 (m, 3H), 6.64 (dt, *J* = 54.8, 13.7 Hz, 1H), 6.42 – 5.58 (m, 1H), 5.52 (d, *J* = 7.3 Hz, 1H), 5.28 – 4.99 (m, 1H), 4.17 (s, 1H), 3.81 (dd, *J* = 30.5, 8.4 Hz, 2H); $^{13}$C NMR (101 MHz, DMSO) δ 180.78, 174.99, 172.37, 171.03, 169.72, 169.66, 161.58, 155.73, 148.71, 136.10, 132.44, 130.73, 130.43, 129.61, 119.89, 119.63, 119.33, 118.36, 117.54, 113.36, 112.17, 71.40, 65.75, 58.03, 34.14, 31.74, 29.01.

**Compound C6** was prepared from cefixime and resorcinol; Red; m.p. 182-184°C; (81%) yield. IR (KBr, cm-1) v = 3232 (OH), 1731 β-lactam (C=O), 1404 (N=N); $^1$H NMR (400 MHz, DMSO) δ 11.78 (s, 1H), 11.62 (s, 1H), 10.17 (s, 0H), 7.87 (d, *J* = 45.3 Hz, 1H), 7.62 (d, *J* = 7.3 Hz, 2H), 7.56 (d, *J* = 7.0 Hz, 3H), 7.39 – 7.26 (m, 4H), 6.72 (q, *J* = 10.1 Hz, 2H), 6.61 – 6.44 (m, 3H), 5.80 (d, *J* = 7.9 Hz, 1H), 5.65 (t, *J* = 8.6 Hz, 1H), 5.34 (q, *J* = 11.4 Hz, 1H), 5.07 (d, *J* = 9.4 Hz, 1H), 4.09 (s, 1H), 3.83 – 3.73 (m, 1H), 3.63 (dd, *J* = 17.1, 6.9 Hz, 1H), 3.42 (d, q, *J* = 12.9, 7.1 Hz, 3H), 3.24 (dd, *J* = 15.7, 8.9 Hz, 1H); $^{13}$C NMR (101 MHz, DMSO) δ 142.62, 140.41, 139.35, 137.09, 131.97, 131.86, 130.69, 130.23, 129.65, 129.44, 129.14, 127.41, 123.56, 121.87, 121.53, 63.55, 56.51, 52.58, 52.35, 34.92, 33.14, 30.32, 19.04, 169.15, 164.12, 161.20, 157.09.

**Compound C7** was prepared from cefixime and β-naphthol; Red; m.p. Decomposed at 73°C; (60%) yield. IR (KBr, cm-1) ν = 3427 (OH), 1737 β-lactam (C=O), 1398 (N=N); $^{1}$H NMR (400 MHz, DMSO) δ 11.50 (s, 1H), 10.43 (d, *J* = 15.5 Hz, 1H), 10.09 (s, 0H), 8.03 – 7.91 (m, 3H), 7.75 (dt, *J* = 26.6, 8.6 Hz, 4H), 7.64 – 7.54 (m, 1H), 7.04 – 6.92 (m, 2H), 6.73 – 6.58 (m, 5H), 6.47 – 6.39 (m, 4H), 5.90 (s, 1H), 5.38 (s, 1H), 5.08 (s, 1H), 4.69 (s, 3H), 3.61 (s, 5H), 3.56 (s, 1H); 13C NMR (101 MHz, DMSO) δ = 172.91, 167.32, 163.99, 160.43, 156.33, 153.00, 150.67, 143.35, 129.97, 128.28, 121.27, 114.03, 113.02, 110.65, 72.83, 65.60, 58.70.

**Compound C8** was prepared from cefixime and β-nitroso-α-naphthol; Red; m.p. Decomposed at 88°C; (61%) yield. IR (KBr, cm-1) ν = 3411 (OH), 1741 β-lactam (C=O), 1402 (N=N), 1515 & 1317 (N=O); $^{1}$H NMR (400 MHz, DMSO) δ 12.27 (s, 1H), 10.98 (s, 1H), 9.71 (d, *J* = 7.6 Hz, 1H), 8.21 (s, 0H), 7.54 – 7.44 (m, 2H), 7.12 – 6.86 (m, 1H), 6.60 (t, *J* = 10.3 Hz, 1H), 6.11 (d, *J* = 14.6 Hz, 1H), 5.97 (s, 0H), 5.33 (d, *J* = 11.3 Hz, 1H), 5.07 (s, 1H), 4.78 (s, 1H), 4.64 (d, *J* = 10.9 Hz, 2H), 3.70 – 3.52 (m, 1H); $^{13}$C NMR (101 MHz, DMSO) δ 176.97, 175.02, 171.29, 170.37, 169.75, 168.63, 164.97, 163.64, 162.05, 158.38, 154.29, 153.46, 149.13, 136.09, 129.28, 125.20, 116.40, 116.39, 112.48, 110.61, 71.25, 63.44, 59.37, 34.13, 31.76, 29.17.

**Compound C9** was prepared from cefixime and α-nitroso-β-naphthol; Red; m.p. Decomposed at 75°C; (65%) yield. IR (KBr, cm-1) ν = 3301 (OH), 1730 β-lactam (C=O), 1413 (N=N), 1523 & 1337 (N=O); 1H NMR (400 MHz, DMSO) δ 11.55 (s, 1H), 11.34 (s, 1H), 9.53 (s, 1H), 8.12 – 8.03 (m, 2H), 8.01 (s, 1H), 7.95 (d, J = 5.8 Hz, 1H), 7.47 – 7.33 (m, 1H), 7.16 (s, 1H), 6.85 – 6.71 (m, 2H), 6.71 – 6.64 (m, 1H), 6.58 – 6.50 (m, 1H), 6.47 (d, J = 5.4 Hz, 1H), 5.96 – 5.88 (m, 1H), 5.78 (d, J = 12.5 Hz, 1H), 5.68 (d, J = 7.4 Hz, 1H), 5.54 (d, J = 5.9 Hz, 1H), 5.44 (d, J = 5.8 Hz, 1H), 5.28 (d, J = 5.3 Hz, 1H), 5.17 (d, J = 4.9 Hz, 1H), 4.27 (s, 0H), 13C NMR (101 MHz, DMSO) δ 188.50, 180.69, 174.58, 170.47, 170.11, 168.27, 165.57, 165.00, 163.10, 161.11, 157.16, 152.09, 150.33, 149.55, 149.31, 149.10, 148.39, 148.25, 144.84, 125.79, 122.65, 121.78, 116.00, 115.86, 110.12, 109.53, 108.66, 56.04, 55.99, 36.82, 36.51, -15.24.

## 3.2. ADMET Analysis

The ADMET (absorption, distribution, metabolism, excretion, and toxicity) properties of the compounds (C1-C9) were studied to determine the drug-likeness of these compounds in comparison with the standard antibiotics amoxicillin, cefixime, and metronidazole. Key PK parameters, including GI, BBB, P-gp, substrate status, CYP inhibition, and predicted toxicities in various organs, are analyzed. The study also evaluates other chemical properties such as skin permeability, water solubility, molecular weight, and predicted toxicity class. As shown in Tables 2, 3, 4, and 5.

### *3.2.1. Pharmacokinetic and toxicological analysis*

The low gastrointestinal absorption of the compounds (C1-C9) indicates that their absorption in the gastrointestinal tract will be limited. This makes oral formulations challenging, and alternative methods of administration (e.g., topical or intravenous) are necessary to achieve sufficient bioavailability. In contrast, none of these compounds exhibited permeability across the BBB, implying that the CNS might be left unaffected. This may be advantageous in preventing CNS effects, although it may also limit their usefulness for disease modulation in the CNS. As shown in Table 2.

Several of them, C1, C5, C6, C8, and C9, are known to be P-glycoprotein (P-gp) substrates. That is, these compounds are recognized by the P-gp transporter, which pumps drugs out of cells, potentially reducing their bioavailability. As a result, this could result in reduced therapeutic efficacy when P-gp-mediated efflux is involved. As shown in Table 2.

All compounds (C1–C9) exhibited a weak ability to inhibit major CYP enzymes (CYP1A2, CYP2C19, CYP2C9, CYP2D6, and CYP3A4), indicating a low probability of interaction with other drugs that require metabolism via these enzymes. This property is advantageous as it minimizes the risk of potential drug-drug interactions when used in combination therapies, as shown in Table 2.

Skin Permeability In the skin permeating experiments, C9 has a low skin permeability (Log Kp -8.34 cm/s), suggesting limited topical absorption. Nevertheless, systemic application may remain a highly potent therapeutic option. C6 and C1 both exhibit low skin permeability, indicating that they may not be suitable candidates for topical delivery; however, they are preferred for systemic delivery. As shown in Table 2.

### *3.2.2. Physicochemical properties*

The molecular weights of the compounds varied between 453.45 g/mol (for cefixime) and 637.60 g/mol (for C8, C9). Higher molecular weights may influence the cellular permeability and solubility, and hence their rate of absorption in the body. Compounds with higher molecular weights may fail to be absorbed through the gastrointestinal tract. As shown in Table 3.

The compounds (C1-C9) have a moderate number of rotatable bonds (9–14), suggesting a degree of flexibility in their structure. Thus, this flexibility, which is crucial for interactions with biological targets, may affect the bioactivity of molecules. Moreover, all the compounds contain sufficient H-bond acceptors and donors that can facilitate biological receptor interaction and enhance their therapeutic potential. As shown in Table 3.

In terms of solubility in water, most of the compounds are of poor solubility, except for C2, which is of moderate solubility. Low solubility can lead to reduced oral bioavailability and may require advanced formulation approaches, such as nanoparticle technology, to enhance absorption and bioavailability. As shown in Table 3.

The Log Po/w values vary from -1.07 to 1.23, where negative indicates better hydrophilicity (water solubility) and positive indicates better lipophilicity (fat solubility). These properties may influence tissue distribution, cellular uptake, and bioavailability, favouring adipose deposition for lipophilic compounds. As shown in Table 3.

### *3.2.3. Predicted toxicity and safety profile*

Predicted toxicities of compounds C1 to C9 are overall low to moderate, indicating their relative safety for therapeutic use. These compounds show less hazardous predictions for clinical toxicity and are therefore less likely to elicit a high level of adverse effects during clinical trials; nevertheless, additional studies are needed to confirm their safety.

In accordance with the specific organ, these compounds present low toxic risks. Hepatotoxicity predictions are inactive or of low risk, suggesting a relatively low potential for liver toxicity. Likewise, all the compounds exhibit inactive neurotoxicity, which implies that the nervous system is not at major risk. The nephrotoxicity of most compounds is not active, ie, their nephrotoxic potential is negligible. Predictions for respiratory toxicity and cardiotoxicity are mostly inactive, suggesting low effects for respiration and the heart.

There is no evidence of carcinogenicity for any of the compounds. Furthermore, the inactive immunotoxicity and mutagenicity predictions of the compounds imply a low risk to the immune system and no genotoxicity. Cytotoxicity. All the complexes demonstrated weak cytotoxicity and are not likely to be cytotoxic. As shown in Table 4.

The LD50 of all the substances is 10,000 mg/kg, and they are categorised as toxicity class 6, which represents slight toxicants. These findings indicate that these agents may be safely utilised in clinical settings at therapeutic concentrations. As shown in Table 5

In conclusion, Compounds C9 and C6 have emerged as the best candidates because they are minimally toxic, display potent antimicrobial activity, and possess moderate to low preclinical toxicity against different organs. In view of their low intestinal absorption and skin permeability, combined with their high PBP2a and β-lactamase Toho-1-binding affinities,51 these agents are promising candidates for systemic treatment.

C1, C2, C3, C5, C7, and C8, with different bioavailability and toxicity, have similar TEFs; the PO-LCETs of C1 and C5 are higher than those of the others, which indicates that C9 and C6 might be safer and more effective in the clinic. Additional preclinical as well as clinical studies are necessary to confirm the safety and effectiveness of these compounds before being used as a potential therapeutic approach.

**Table 2:** Pharmacokinetics & Lipinski Violation for Cefixime and its Derivatives (C1-C9).

| **Com.** | **GI absorption** | **BBB permeant** | **P-gp substrate** | **CYP1A2 inhibitor** | **CYP2C19 inhibitor** | **CYP2C9 inhibitor** | **CYP2D6 inhibitor** | **CYP3A4 inhibitor** | **Log Kp (skin permeation) cm/s** | **Bioavailability Score** | **Lipinski violation** |
|---|---|---|---|---|---|---|---|---|---|---|---|
| **Ce** | Low | No | No | No | No | No | No | No | -9.55 | 0.11 | Yes,1 |
| **C1** | Low | No | Yes | No | No | No | No | No | -9.08 | 0.11 | No, 2 |
| **C2** | Low | No | No | No | No | No | No | No | -9.03 | 0.11 | No, 2 |
| **C3** | Low | No | No | No | No | No | No | No | -8.67 | 0.11 | No, 2 |
| **C4** | Low | No | No | No | No | No | No | No | -8.44 | 0.11 | No, 2 |
| **C5** | Low | No | Yes | No | No | No | No | No | -8.91 | 0.11 | No, 2 |
| **C6** | Low | No | Yes | No | No | No | No | No | -9.05 | 0.11 | No, 2 |
| **C7** | Low | No | No | No | No | No | No | No | -8.12 | 0.11 | No, 2 |
| **C8** | Low | No | Yes | No | No | No | No | No | -8.34 | 0.11 | No, 2 |
| **C9** | Low | No | Yes | No | No | No | No | No | -8.34 | 0.11 | No, 2 |

**Table 3:** Physicochemical Properties, Lipophilicity, and Water Solubility for Cefixime and its Derivatives (C1-C9).

| Com. | M.Wt. g/mol | rotatable bonds | H.B. acceptors | H.B. donors | M.R. | TPSA /Å² | Water Solubility | Log Po/w (MLOGP) |
|---|---|---|---|---|---|---|---|---|
| **Ce** | 453.45 | 9 | 9 | 4 | 109.91 | 238.05 | Soluble | -1.07 |
| **C1** | 586.55 | 12 | 12 | 3 | 148.02 | 270.21 | Poorly soluble | -0.17 |
| **C2** | 557.56 | 11 | 11 | 4 | 141.22 | 244.62 | Moderately soluble | 0.16 |
| **C3** | 620.45 | 11 | 10 | 3 | 146.90 | 224.39 | Poorly soluble | 1.23 |
| **C4** | 576.00 | 11 | 10 | 3 | 144.21 | 224.39 | Poorly soluble | 1.12 |
| **C5** | 602.55 | 12 | 14 | 5 | 145.11 | 294.28 | Poorly soluble | 0.04 |
| **C6** | 574.54 | 11 | 13 | 5 | 140.17 | 277.21 | Poorly soluble | -0.18 |
| **C7** | 608.60 | 11 | 12 | 4 | 155.65 | 256.98 | Poorly soluble | 0.95 |
| **C8** | 637.60 | 12 | 14 | 4 | 161.11 | 286.41 | Poorly soluble | 0.50 |
| **C9** | 637.60 | 12 | 14 | 4 | 161.11 | 286.41 | Poorly soluble | 0.50 |

**Table 4:** Organ and Endpoint Toxicities for Cefixime and Derivatives (C1-C9).

| | Organ toxicity | | | | | Toxicity endpoints | | | | |
|---|---|---|---|---|---|---|---|---|---|---|
| **Comp. ID** | **Hepatotoxicity** | **Neurotoxicity** | **Nephrotoxicity** | **Resnratory toxicity** | **Cardiotoxicity** | **Carcinogenicity** | **Immunotoxicity** | **Mutagenicity** | **Cytotoxicity** | **Clinical toxicity** |
| **Ce** | In | In | Ac | Ac | In | In | In | In | In | Ac |
| **C1** | In | In | Ac | Ac | In | Ac | In | Ac | In | In |
| **C2** | In | In | Ac | Ac | In | In | In | In | In | Ac |
| **C3** | In | In | Ac | Ac | In | In | In | In | In | Ac |
| **C4** | In | In | Ac | Ac | In | In | In | In | In | Ac |
| **C5** | In | In | Ac | Ac | In | In | In | In | In | Ac |
| **C6** | In | In | Ac | Ac | In | In | In | In | In | Ac |
| **C7** | In | In | Ac | Ac | In | In | In | In | In | Ac |
| **C8** | In | In | Ac | Ac | In | In | In | In | In | Ac |
| **C9** | In | In | Ac | Ac | In | In | In | In | In | Ac |

In =Inactive, Ac = Active

**Table 5:** Predicted LD50, Predicted Toxicity Class, Average Similarity %, Prediction Accuracy % for Cefixime and its Derivatives (C1-C9).

| Comp. ID | Predicted LD50 mg/kg | Predicted Toxicity Class | Average similarity % | Prediction accuracy % |
|---|---|---|---|---|
| **Ce** | 10000 | 6 | 100 | 100 |
| **C1** | 10000 | 6 | 81.31 | 70.97 |
| **C2** | 10000 | 6 | 81.51 | 70.97 |
| **C3** | 10000 | 6 | 80.66 | 70.97 |
| **C4** | 10000 | 6 | 81.23 | 70.97 |
| **C5** | 10000 | 6 | 75.46 | 69.26 |
| **C6** | 10000 | 6 | 79.08 | 69.26 |
| **C7** | 10000 | 6 | 79.36 | 69.26 |
| **C8** | 10000 | 6 | 77.23 | 69.26 |
| **C9** | 10000 | 6 | 76.46 | 69.26 |

### 3.3. Molecular Docking (46)

In molecular docking experiments, we investigate the interactions of cefixime-related drugs (C1–C9) and four primary receptor targets: β-Lactamase Toho-1 (1IYS), PBP2a (1VQQ), PBP-2B (2WAE), and PBP2x (1PYY). The reference drug, cefixime (Ce), helps us understand these new molecules' binding and interaction properties.

Using cefixime (Ce), the reference ligand, we contextualise these new derivatives' binding affinities and interaction characteristics. An overview of binding affinity and interaction profiles. For all receptor complexes, binding energies (B.E.) define ligand affinity; larger negative values suggest higher binding. Some compounds show binding affinities on par with or better than cefixime, suggesting enhanced functioning or new interactions. Show Table 6 and Figure 1.

**Table 6:** Binding Energies for Cefixime and its Derivatives (C1-C9) with Receptors.

| **Com.** | **Binding Energies Kcal/mol** | | | |
|---|---|---|---|---|
| | **PBP2a (1VQQ)** | **PBP2b (2WAE)** | **PBP2x (1PYY)** | **β-Lactamase Toho-1 (1IYS)** |
| **C1** | -1.67 | -0.65 | 0.59 | -1.5 |
| **C2** | -0.98 | -0.91 | -0.05 | -2.25 |
| **C3** | -1.46 | 0.53 | -0.42 | -3.12 |
| **C4** | -1.98 | -0.35 | 0.74 | -1.86 |
| **C5** | -0.6 | 0.51 | 1.49 | -1.52 |
| **C6** | -0.55 | 0.47 | 1.55 | -1.65 |
| **C7** | -0.36 | -0.24 | -0.13 | -0.52 |
| **C8** | -1.05 | 0.33 | 0.05 | -1.91 |
| **C9** | -0.27 | 0.40 | 0.21 | -3.34 |
| **Ce** | -1.97 | -1.06 | 0.23 | -1.61 |

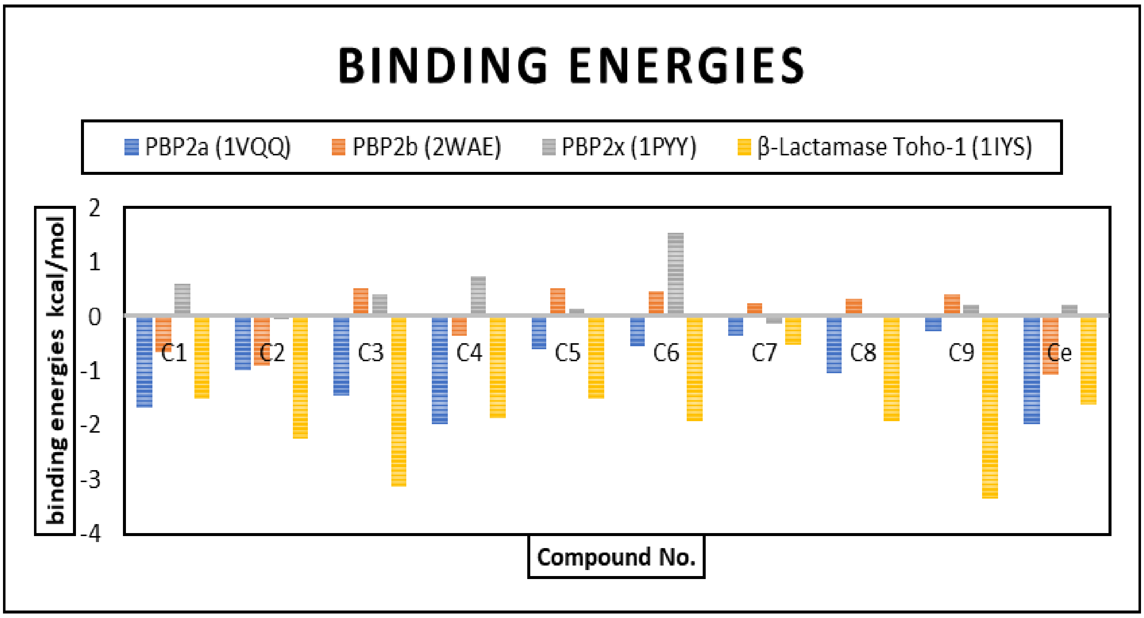

**Figure 1:** Diagram of Binding Energies for Cefixime and Derivatives (C1-C9).

### 3.4. Discussion of Binding Interactions and Binding Energies for Compounds (C1-C9) Compared to Cefixime (Ce) (47)

Cefixime was chosen as the standard compound to test how well its designed derivatives bind to it. The docking results showed that the four receptors being studied had very different binding energies and interaction patterns.

For **PBP2a (1VQQ),** cefixime had a binding energy of −1.97 kcal/mol and made six hydrogen bonds with ASN415, LYS417, LYS477, LYS478, and LYS481. Cefixime was very stable, but compound C4 was even more stable, with a binding energy of −1.98 kcal/mol. This derivative formed four hydrogen bonds with LYS273 and LYS316, as well as four additional non-hydrogen contacts, including π–sigma, π–sulfur, alkyl, and π–alkyl interactions. These made it more stable overall. In contrast, compound C9 had the weakest binding, with an energy of −0.27 kcal/mol. It was held together by only three hydrogen bonds and one alkyl interaction. As shown in Table 7.

Cefixime was the strongest binder for **PBP2b (2WAE),** with an energy of −1.06 kcal/mol. Its stability was supported by three hydrogen bonds with ALA419 and LYS426, as well as two non-hydrogen contacts of the π–sigma and π–alkyl types. With a performance of −0.91 kcal/mol, compound C2 formed three hydrogen bonds and one π–sigma interaction. Compound C3, on the other hand, was the weakest. It had a positive binding energy of +0.53 kcal/mol and was held together by only two hydrogen bonds and one π-alkyl contact. Compound C9 had a more varied interaction profile, with two hydrogen bonds and four non-hydrogen interactions. However, its energy value of +0.40 kcal/mol indicated that cefixime remained the most stable with this receptor. As shown in Table 8.

Cefixime had a weak binding energy of +0.23 kcal/mol for **PBP2x (1PYY)**. It only had one hydrogen bond with LYS121 and two alkyl contacts. Compound C3 was the best binder among the derivatives, with a value of −0.42 kcal/mol. Even though it only made one hydrogen bond with TYR129, it also made seven other contacts that weren't hydrogen bonds, such as π-stacked, alkyl, and π-amide interactions. These contacts significantly stabilized the molecule.

In contrast, compound C6 demonstrated the weakest binding affinity, with a binding energy of +1.55 kcal/mol. This reduced stability is attributable to the presence of three hydrogen bonds, which were insufficient to sustain a robust interaction within the complex, as detailed in Table 9.

Cefixime had a moderate affinity for **β-lactamase Toho-1 (1IYS)**, binding with an enthalpy change of −1.61 kcal/mol through three hydrogen bonds with GLU96 and HIS141, as well as two alkyl interactions. In contrast, compound C9 was much stronger, with a binding energy of −3.34 kcal/mol. This was due to two hydrogen bonds with LYS191 and TRP251, as well as three other non-hydrogen interactions of the alkyl and π-alkyl types. Compounds C5 and C6 also did better than cefixime, with energies of −1.52 and −1.65 kcal/mol, respectively. Several hydrogen bonds and π-alkyl interactions held both together. C7 was the weakest derivative because it only had two hydrogen bonds and three weak alkyl contacts to hold it together. As shown in Table 10 and Figure 2.

In conclusion, cefixime was a good standard for all receptors. Compound C4 was slightly stronger than cefixime against PBP2a, as it had more non-hydrogen contacts. Cefixime itself was still the strongest against PBP2b, showing that, in this case, the reference compound was superior to its derivatives. Compound C3 was the most stable with PBP2x, and compound C9 was the best with β-lactamase, having the lowest binding energy and a well-balanced network of interactions. These results indicate that specific changes, particularly those in C9, can enhance cefixime's effectiveness in combating bacterial strains resistant to it.

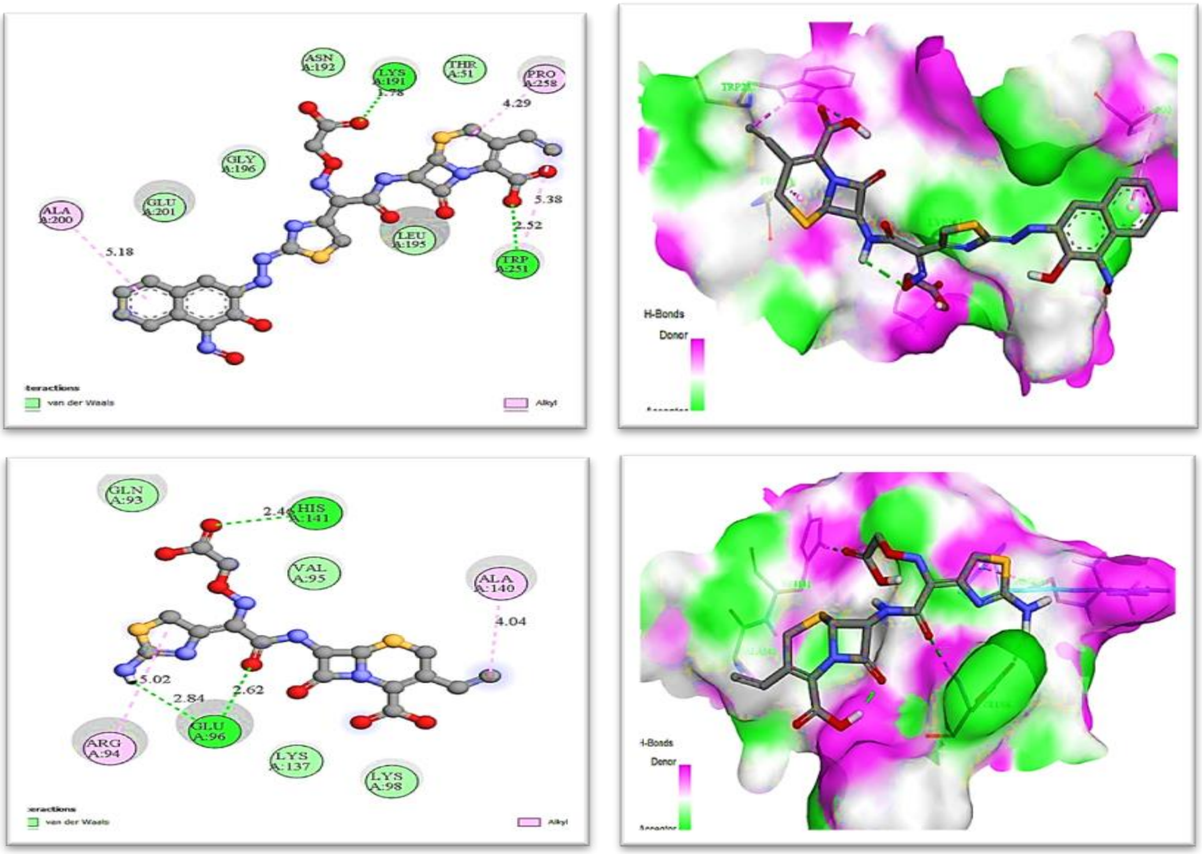

**Figure 2:** 2D & 3D for C9 and Cefixime with β-Lactamase Toho-1 (1IYS).

**Table 7:** Hydrogen and Non-Hydrogen bond Interactions for Cefixime and Derivatives (C1-C9) with PBP2a (1VQQ).

| | **Hydrogen bond interaction** | | | **Non-hydrogen bond interaction** | | | |
|---|---|---|---|---|---|---|---|
| **Com. ID** | **Bonds No.** | **Residue** | **Distance** | **Bonds No.** | **Type** | **Residue** | **Distance** |
| **C1** | 4 | LYS 477, LYS 477, LYS 478, LYS 560 | 5.74, 6.10, 4.26, 4.80 | 1 | π-alkyl | LYS 560 | 6.08 |
| **C2** | 4 | THR 344, THR 398, THR 398, GLU 523 | 2.61, 2.65, 2.77, 2.30 | 3 | alkyl | LEU 525, LEU 603, LYS 604 | 4.90, 4.14, 4.14 |
| **C3** | 1 | LYS 322 | 2.02 | 3 | t-shaped alkyl π π-alkyl | TYR 272 ALA 276 TYR 272 | 5.48, 3.38, 2.72 |
| **C4** | 4 | LYS 273, LYS 316 | 1.98, 3.05 2.73, 2.82 | 4 | π-sigma π-sulfur alkyl π-alkyl | LYS 317 TYR 297 LYS 317 TYR 105 | 3.75, 5.89, 4.45, 4.70 |
| **C5** | 2 | LYS 290, LYS 554 | 3.87, 1.96 | 1 | π-sigma | LYS 290 | 3.87 |
| **C6** | 4 | LYS 318, ASP 320, LYS 321, LYS 322 | 2.80, 2.10, 3.77, 2.59 | 4 | alkyl | LYS 317, LYS 319, LYS 322 | 5.12, 4.82, 4.24, 4.06 |
| **C7** | 4 | ARG 110, HIS 311, LEU 313, LYS 317 | 2.40, 2.05, 2.68, 2.40 | 1 | alkyl | LYS 317 | 4.63 |
| **C8** | 3 | LYS 554, VAL 557, LYS 560 | 2.11, 3.25, 3.23 | 1 | π-alkyl | LYS 556 | 4.64 |
| **C9** | 3 | GLU 315, LYS 316 | 3.08, (2.09, 3.21) | 1 | alkyl | LYS 316 | 4.45 |
| **Ce** | 6 | ASN 415, LYS 417, LYS 477, LYS 478, LYS 481 | 3.61, 2.04, 1.81, (2.24 2.72), 2.96 | 0 | -- | -- | -- |

**Table 8:** Hydrogen and Non-Hydrogen Bond Interactions for Cefixime and Derivatives (C1-C9) with PBP2b (2WAE).

| | **Hydrogen bond interaction** | | | **Non-hydrogen bond interaction** | | | |
|---|---|---|---|---|---|---|---|
| **Com. ID** | **Bonds No.** | **Residue** | **Distance** | **Bonds No.** | **Type** | **Residue** | **Distance** |
| C1 | 3 | LYS 338, LEU 365, LYS 366 | 2.07, 2.97, 1.83 | 2 | T-shaped π-alkyl | TYR 339 HIS 653 | 5.33 3.97 |
| C2 | 3 | LYS 426, LEU 427, PRO 597 | 1.88, 2.66, 2.25 | 1 | π - sigma | ALA 428 | 3.84 |
| C3 | 2 | LYS 254, LEU 253 | 2.05, 3.45 | 1 | π-alkyl | PHE 187 | 5.49 |
| C4 | 2 | LYS 254, LYS 255 | 1.97, 1.72 | 3 | alkyl | LYS 279 ARG 280 VAL 282 | 4.67, 4.11, 5.30 |
| C5 | 3 | LYS 426, ASN 463 | 2.32, (2.56, 2.66) | 2 | alkyl,π-alkyl | PRO 420 VAL 414 | 3.59 5.28 |
| C6 | 6 | GLY 501, LEU 502, VAL 503, LYS 505 | 2.36, 3.54, 2.60, (1.81, 1.83, 2.86) | 0 | -- | -- | -- |
| C7 | 3 | THR 600, THR 658, LYS 659 | 2.47, 2.19, 1.80 | 2 | π -stacked | TRP 424 | (4.88, 5.36) |
| C8 | 2 | LYS 426 | (1.62, 2.90) | 3 | π -cation alkyl π -alkyl | LYS 426 LEU 657 LEU 657 | 2.75 4.67 5.36 |
| C9 | 2 | TRP 424, LEU 427 | 2.98, 1.82 | 4 | π -sigma alkyl π -alkyl | LEU 657 LEU 657 LYS 426 | (3.79, 3.84) 4.47 4.42 |
| Ce | 3 | ALA 419, LYS 426 | 2.42, (1.96, 3.6) | 2 | π -sigma π- alkyl | ILE 421 ALA 419 | 3.80 4.82 |

**Table 9:** Hydrogen and Non-Hydrogen Bond Interactions for Cefixime and Derivatives (C1-C9) with PBP2x (1PYY).

| | Hydrogen bond interaction | | | Non-hydrogen bond interaction | | | |
|---|---|---|---|---|---|---|---|
| **Com. ID** | **Bonds No.** | **Residue** | **Distance** | **Bonds No.** | **Type** | **Residue** | **Distance** |
| **C1** | 2 | LYS 121, MET 164 | 2.91, 3.33 | 5 | п-sulfur alkyl п-alkyl | PHE 126 VAL 125 ALA 98, VAL 122 | 5.83 (4.13 4.72) 5.49, 4.47 |
| **C2** | 2 | LYS 121, ASN 162 | 1.73, 2.29 | 4 | п-sigma t-shaped alkyl п-alkyl | VAL 125 TYR 129 LYS 128 TYR 129 | 3.93 4.73 3.71 5.05 |
| **C3** | 1 | TYR 129 | 2.28 | 7 | п-stacked amide п-stacked alkyl п-alkyl | MET 163 TYR 129 VAL 96, LEU 130, ILE 158 VAL 125, PHE 126 | 4.91 4.91 4.49, 4.37, 4.98 5.05, 4.89 |
| **C4** | 2 | TYR 97 | 2.64, 2.74 | 5 | t-shaped alkyl п-alkyl | PHE 126 VAL 125, MET 163 VAL 96, PHE 126 | 5.68 4.23, 5.40 5.31, 5.13 |
| **C5** | 3 | TYR 528, GLY 533, LYS 534 | 2.23, 2.14, 2.18 | 2 | alkyl п-alkyl | VAL 523 TYR 524 | 3.89 5.49 |
| **C6** | 3 | LYS 128, TYR 129 | (2.08, 2.52), 2.82 | 4 | unfura.п-sulfur п-stacked alkyl | TYR 129 TYR 129 TYR 129 ALA 161 | 2.01 4.45 4.16 3.83 |
| **C7** | 2 | LYS 121 | 2.37, 2.38 | 1 | п-alkyl | MET 163 | 4.98 |
| **C8** | 0 | -- | -- | 5 | п-stacked- t-shaped amide-п-stacked п-alkyl | MET 163 TYR 129 PHE 126 VAL 125 | 4.40, 4.59, 4.94, 5.97, 5.17 |
| **C9** | 1 | LYS 121 | 1.96 | 1 | п-alkyl | VAL 125 | 4.77 |
| **Ce** | 1 | LYS 121 | 1.98 | 2 | alkyl | LYS 121 | 3.81, 4.22 |

### 3.5. Antioxidant Activity (44)

The table presents the reactions of various samples (C1 to C9) with differing concentrations, utilising ascorbic acid as the standard antioxidant reference in a linear experiment. This study employs DPPH (2,2-diphenyl-1-пcrylhydrazyl) as a free radical scavenger. The essential parameters, including IC50 values, linear equations, and R2 values, allow the comparison of the antioxidant activities of these samples with those of ascorbic acid.

#### *3.5.1. Discussion of antioxidant activity for compounds (C1-C9) compared to ascorbic acid*

The table (10) presents the IC50 values for the antioxidant activity of compounds (C1-C9) compared to ascorbic acid (vitamin C). The IC50 value represents the concentration at which 50% of the antioxidant activity is inhibited, providing a key measure of the compound's potency. Lower IC50 values indicate stronger antioxidant activity. Show Table 11 and Figure 3.

In conclusion, C6 emerges as the most potent antioxidant, with the lowest IC50, making it highly effective at neutralizing oxidative stress. This high potency aligns with its strong binding to PBP2a and β-lactamase Toho-1, positioning C6 as a promising candidate for applications in both antibacterial therapy and oxidative stress management.

Compound C9 closely follows C6, demonstrating significant antioxidant activity with an IC50 value of 6.78 μg/mL, supporting its potential therapeutic use.

Compounds C1 and C8 exhibit moderate antioxidant activity, whereas C2, C3, and C4 manifest comparatively weaker activity, with C3 being the least effective. However, their potential as antibacterial agents or in other therapeutic areas should not be overlooked.

Overall, C6 and C9 represent the most promising antioxidant candidates, with C6, in particular, exhibiting potential to exceed the clinical efficacy of ascorbic acid. Further rigorous investigations are warranted to optimize the therapeutic potential of C6 and C9 in the management of oxidative stress-related pathologies.

**Table 10:** Hydrogen and Non-hydrogen Bond Interactions for Cefixime and Derivatives (C1-C9) with β-Lactamase Toho-1 (1IYS).

| Com. ID | Hydrogen bond interaction | | | Non-hydrogen bond interaction | | | |
|---|---|---|---|---|---|---|---|
| | **Bonds No.** | **Residue** | **Distance** | **Bonds No.** | **Type** | **Residue** | **Distance** |
| **C1** | 3 | PRO 145, ASP 146, ARG 153 | 3.10, 2.11, 2.53 | 3 | unv. π-anion alkyl | ASP 146<br>ASP 146<br>PRO 145 | 2.58<br>4.17<br>4.57 |
| **C2** | 3 | ASP 146, LYS 147, ARG 153 | 2.32, 3.00, 1.98 | 0 | -- | -- | -- |
| **C3** | 2 | ASP 146, LYS 147 | 2.32, 2.87 | 2 | π-cation<br>π-alky | ARG 153<br>ALA 150 | 3.48<br>5.27 |
| **C4** | 2 | ASP 146, LYS 147 | 2.46, 2.16 | 2 | Alkyl<br>π-alkyl | ARG 164<br>ALA 140 | 4.81<br>4.35 |
| **C5** | 5 | PRO 226, LYS 227, LYS 284, HIS 288, GLY 289 | 3.33, 2.14, 3.15, 2.87, 3.05 | 2 | π-alkyl | LYS 227, HIS 288 | 4.21, 4.99 |
| **C6** | 4 | ARG 94, GLU 96 | (2.45, 2.76, 2.77)1.93 | 3 | π-cation<br>π-alkyl | ARG 94<br>ARG 94, VAL 95 | 3.91<br>4.21, 5.03 |
| **C7** | 2 | ASP 101, LYS 137 | 2.96, 1.79 | 3 | Alkyl<br>π-alkyl | ALA 140<br>PRO 145 | 3.88<br>3.86, 4.35 |
| **C8** | 3 | ARG 94, LYS 137 | (2.26, 3.01) 2.56 | 3 | π-sigma<br>alkyl<br>π-alkyl | GLN 93<br>ALA 140<br>ARG 94 | 3.93<br>3.96<br>4.73 |
| **C9** | 2 | LYS 191, TRP 251 | 1.78, 2.52 | 3 | Alkyl<br>π-alkyl | TRP 251<br>ALA 200<br>PRO 258 | 5.38<br>4.29, 5.18 |
| **Ce** | 3 | GLU 96, HIS 141 | (2.62, 2.84) 2.46 | 2 | alkyl | ARG 94, ALA 140 | 5.02, 4.64 |

**Table 11:** Antioxidant Activities for Ascorbic Acid and Derivatives (C1-C9).

| **Com. ID** | **100 µg/ml** | **50 µg/ml** | **25 µg/ml** | **12.5 µg/ml** | **6.25 µg/ml** | **linear eq.** | **$R^2$** | **IC50** |
|---|---|---|---|---|---|---|---|---|
| **C1** | 84.44 | 72.53 | 61.01 | 50.51 | 42.02 | y = 0.4229x + 45.715 | 0.9063 | 10.13 |
| **C2** | 78.99 | 64.85 | 48.69 | 39.19 | 34.75 | y = 0.4714x + 35.025 | 0.9513 | 31.76 |
| **C3** | 48.69 | 41.82 | 33.94 | 30.71 | 27.47 | y = 0.2214x + 27.946 | 0.9549 | 99.61 |
| **C4** | 68.48 | 43.23 | 31.92 | 30.71 | 25.66 | y = 0.4477x + 22.652 | 0.988 | 61.08 |
| **C5** | 65.86 | 55.96 | 50.51 | 44.85 | 41.82 | y = 0.2465x + 42.247 | 0.9684 | 31.45 |
| **C6** | 91.52 | 74.55 | 65.25 | 52.12 | 46.06 | y = 0.4613x + 48.022 | 0.941 | 4.28 |
| **C7** | 69.70 | 49.29 | 40.00 | 34.95 | 31.72 | y = 0.4x + 29.63 | 0.9994 | 50.92 |
| **C8** | 87.07 | 70.71 | 58.59 | 45.05 | 37.37 | y = 0.5034x + 40.253 | 0.9294 | 19.36 |
| **C9** | 98.59 | 97.78 | 88.28 | 74.34 | 64.44 | y = -9.1717x + 112.2 | 0.9407 | 6.78 |
| **A.A.** | 90.17 | 72.57 | 60.6 | 51.89 | 45.69 | y = 0.4644x + 46.43 | 0.9941 | 7.68 |

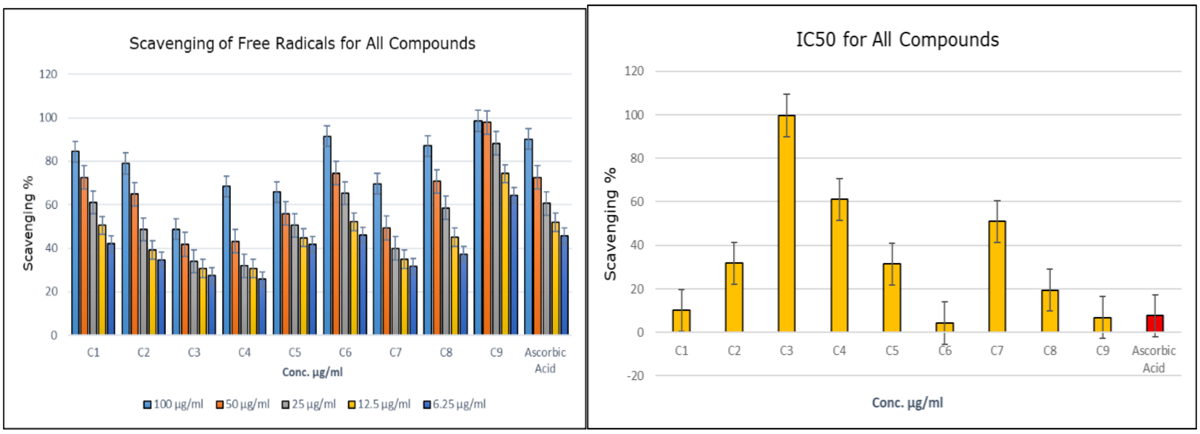

**Figure 3:** Histogram of Antioxidant Activities and IC50 for Compounds (C1-C9).

### 3.6. Antimicrobial Activity (48)

#### *3.6.1. Compounds (C1–C9) vs conventional antibiotics for antimicrobial activity*

Compounds C1–C9 were also tested for their antimicrobial activity against a range of bacteria and fungi, including *E. coli, P. mirabilis, S. aureus, B. cereus*, and *C. albicans*. The inhibition zones were compared to those of standard antibiotics such as Ampicillin, Cefixime, and Metronidazole, which are widely used in clinical settings. The detailed data is presented in Table 12.

#### *3.6.2. Results of antimicrobial testing*

C9 showed the strongest antimicrobial activity among the tested compounds, with inhibition zones of 31 mm against Proteus mirabilis and *E. coli*, 35 mm against *Candida albicans*, and 33 mm against *Bacillus cereus*. Moderate activity was also recorded against *Staphylococcus aureus* (at 27 mm).

C6 showed strong inhibition of Bacillus cereus (31 mm) and *Candida albicans* (28 mm), in addition to demonstrating strong antioxidant activity (IC50 value = 4.28 µg/mL), which enhances its therapeutic potential in treating both bacterial and fungal infections. C6 also exhibited activity against *Proteus mirabilis* (at 22 mm) and *Staphylococcus aureus* (at 19 mm), and 27 mm against *E. coli*.

C4 was more active against *E. coli* and *Staphylococcus aureus* (both 35 mm) compared to *Candida albicans* (10 mm), indicating a selective antimicrobial effect. C4 showed no significant activity against *Proteus mirabilis* or *Bacillus cereus*.

C2 exhibited moderate activity against *Staphylococcus aureus* (30 mm) and *Bacillus cereus* (35 mm) but weak activity against *Proteus mirabilis* (11 mm) and *Candida albicans* (15 mm), suggesting that it has a broad spectrum of activity against some bacteria.

C3 exhibited good activity against *Staphylococcus aureus* (35 mm) but weak activity against *Proteus mirabilis* (12 mm) and *Candida albicans* (15 mm), indicating a selective antibacterial effect.

C7 demonstrated good activity against *Bacillus cereus* (34 mm) and *Candida albicans* (27 mm). Still, it was less effective against other bacterial strains, with values of 33 mm against *E. coli* and 16 mm against *Staphylococcus aureus*.

C8 exhibited strong antibacterial activities against *Bacillus cereus* (33 mm) and *E. coli* (34 mm). However, its activity against *Staphylococcus aureus* (14 mm) and *Candida albicans* (21 mm) was less effective compared to other compounds in this study.

#### *3.6.3. Comparison with traditional antibiotics*

Cefixime demonstrated strong antimicrobial activity against *E. coli, P. mirabilis*, and *S. aureus* (all 35 mm). Still, moderate activity against *C. albicans* (15 mm), indicating that while Cefixime is effective against some bacterial strains, it has limited activity against fungal infections.

Metronidazole showed significant activity against *Staphylococcus aureus* (30 mm), but no activity against the other bacterial and fungal strains, indicating a narrow spectrum of activity compared to the compounds tested here. As shown in Table 12, Figure 4, and Figure 5.

#### *3.6.4. Conclusion*

In conclusion, C9 is the most superior compound in this study in terms of antimicrobial activity, exhibiting strong activity against most of the bacteria and fungi tested. However, C6 demonstrated the strongest antioxidant activity among all the compounds. This dual action makes C9 and C6 promising candidates for development as drugs against both antibiotic-resistant bacteria and fungal infections.

C6 is also a promising candidate due to its broad activity spectrum and high antioxidant activity. C9 came in second in terms of antioxidant activity, with an IC50 value of 6.78 µg/mL, indicating that it can also be used as both an antimicrobial and antioxidant agent. Both C9 and C6 may serve as promising antibiotics for infections caused by antibiotic-resistant microorganisms. Further preclinical and clinical research is needed to validate the therapeutic efficacy and safety of these compounds in treatments.

## 4. CONCLUSION

The Schiff base and azo derivatives of cefixime synthesized in this study exhibit promising antimicrobial and antioxidant activities. C9 and C6, in particular, demonstrated excellent efficacy in inhibiting bacterial growth, surpassing traditional antibiotics like cefixime, and exhibited strong antioxidant potential. Molecular docking studies further support these findings, highlighting the potential of these derivatives as inhibitors of β-lactamase and PBPs. These results suggest that Schiff base and azo derivatives of cefixime could be developed as novel therapeutic agents to combat antimicrobial resistance and oxidative stress.

## 5. ACKNOWLEDGEMENT

We would like to thank the Head of the Chemistry Department / College of Science / University of Baghdad and the staff of the service laboratory, especially Hajjah Munira. I would also like to thank everyone who helped me or facilitated my work.

**Table (12):** Antimicrobial Activities Compounds (C1-C9).

| Compound ID | *E. coli* | *Proteus mirabilis* | *Staphylococcus aureus* | *Bacillus cereus* | *Candida albicans* |
|---|---|---|---|---|---|
| **C1** | 20 | 11 | 20 | 9 | 15 |
| **C2** | 25 | 11 | 30 | 9 | 15 |
| **C3** | 31 | 12 | 35 | 10 | 15 |
| **C4** | 35 | 10 | 35 | 10 | 10 |
| **C5** | 25 | 14 | 15 | 27 | 26 |
| **C6** | 27 | 22 | 19 | 31 | 28 |
| **C7** | 33 | 16 | 13 | 34 | 27 |
| **C8** | 34 | 11 | 14 | 33 | 21 |
| **C9** | 31 | 30 | 27 | 33 | 35 |
| **Ampicillin** | 30 | 20 | 20 | 35 | 10 |
| **Cefixime** | 35 | 35 | 35 | 30 | 15 |
| **Metronidazole** | 20 | -- | 30 | -- | -- |

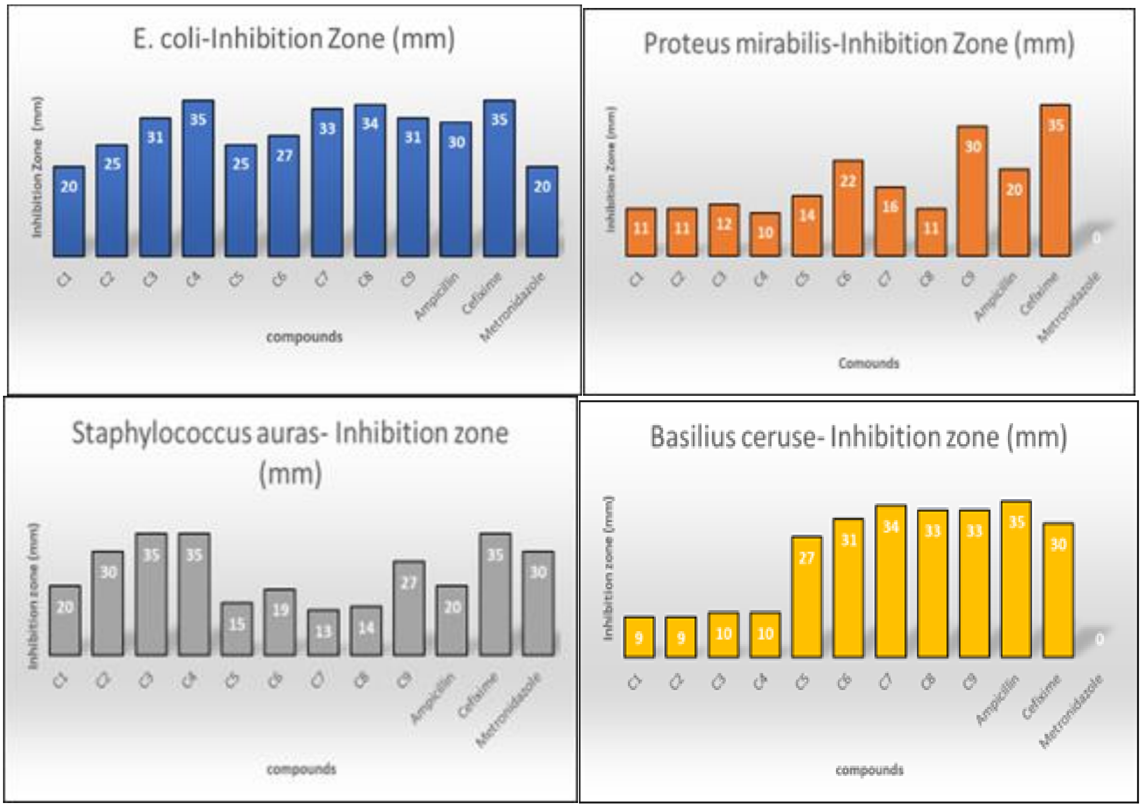

**Figure 4:** "Inhibition Zones of *E. coli, Proteus mirabilis, Staphylococcus aureus,* and *Bacillus cereus* Under the Effect of Different Compounds.

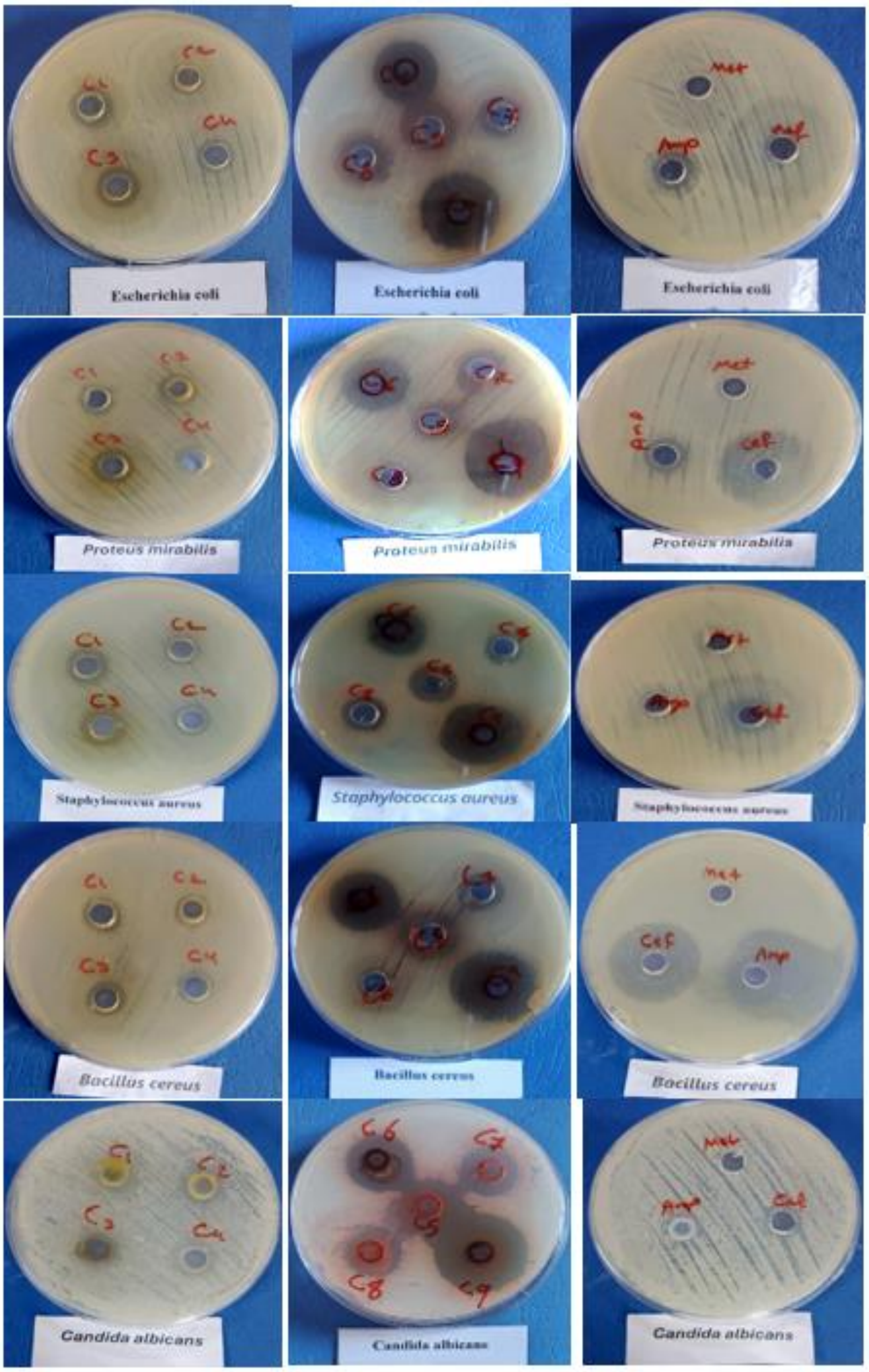

**Figure 5:** "Comparative Study of the Effect of Prepared Compounds (C1-C9) and Antibiotics (Cefixime, Ampicillin) on Bacterial and Fungal Sensitivity Using the Agar Diffusion Method".

## 6. REFERENCES

1. Aslam B, Khurshid M, Arshad MI, Muzammil S, Rasool M, Yasmeen N, et al. Antibiotic resistance: One health one world outlook. Front Cell Infect Microbiol [Internet]. 2021 Nov 25;11:771510. Available from: <URL>.

2. Piergiacomo F, Brusetti L, Pagani L. Understanding the interplay between antimicrobial resistance, microplastics and xenobiotic contaminants: A leap towards one health? Int J Environ Res Public Health [Internet]. 2022 Dec 20;20(1):42. Available from: <URL>.

3. Santra H, Bhadury P. Prevalence of antimicrobial resistance in fecal coliforms in wastewater settings: Challenges and way forward from the perspective of global south. In Springer, Singapore; 2024. p. 3–32. Available from: <URL>.

4. Bharadwaj A, Rastogi A, Pandey S, Gupta S, Sohal JS. Multidrug-resistant bacteria: Their mechanism of action and prophylaxis. Kaushik S, editor. Biomed Res Int [Internet]. 2022 Jan 5;2022(1):5419874. Available from: <URL>.

5. Terreni M, Taccani M, Pregnolato M. New antibiotics for multidrug-resistant bacterial strains: Latest research developments and future perspectives. Molecules [Internet]. 2021 May 2;26(9):2671. Available from: <URL>.

6. Brüssow H. The antibiotic resistance crisis and the development of new antibiotics. Microb Biotechnol [Internet]. 2024 Jul 5;17(7):e14510. Available from: <URL>.

7. Abbas AT, Salih HA, Hassan BA. Review of Beta lactams. Ann Rom Soc Cell Biol [Internet]. 2022;26(1):1863–81. Available from: <URL>.

8. Gupta R, Gupta N, Bindal S. Bacterial cell wall biosynthesis and inhibitors. In: Fundamentals of Bacterial Physiology and Metabolism [Internet]. Singapore: Springer Singapore; 2021. p. 81–98. Available from: <URL>.

9. Torrens G, Cava F. Mechanisms conferring bacterial cell wall variability and adaptivity. Biochem Soc Trans [Internet]. 2024 Oct 30;52(5):1981–93. Available from: <URL>.

10. Aliashkevich A, Cava F. LD-transpeptidases: The great unknown among the peptidoglycan cross-linkers. FEBS J [Internet]. 2022 Aug 22;289(16):4718–30. Available from: <URL>.

11. Vacariu CM, Tanner ME. Recent advances in the synthesis and biological applications of peptidoglycan fragments. Chem – A Eur J [Internet]. 2022 Aug 16;28(43):e202200788. Available from: <URL>.

12. Orsini Delgado ML, Gamelas Magalhaes J, Morra R, Cultrone A. Muropeptides and muropeptide transporters impact on host immune response. Gut Microbes [Internet]. 2024 Dec 31;16(1). Available from: <URL>.

13. Dabhi M, Patel R, Shah V, Soni R, Saraf M, Rawal R, et al. Penicillin-binding proteins: The master builders and breakers of bacterial cell walls and its interaction with β-lactam antibiotics. J Proteins Proteomics [Internet]. 2024 Apr 6;15(2):215–32. Available from: <URL>.

14. Liu X, den Blaauwen T. NlpI-Prc proteolytic complex mediates peptidoglycan synthesis and degradation via regulation of hydrolases and synthases in *Escherichia coli*. Int J Mol Sci [Internet]. 2023 Nov 15;24(22):16355. Available from: <URL>.

15. Arumugham VB, Gujarathi R, Cascella M. Third-Generation Cephalosporins. StatPearls [Internet]. 2023 Jun 4; Available from: <URL>.

16. Zaragoza G, Pérez-Vázquez M, Villar-Gómara L, González-Prieto A, Oteo-Iglesias J, Alós JI. Community emergence of cefixime-resistant *Escherichia coli* belonging to ST12 with chromosomal AmpC hyperproduction. Antibiotics [Internet]. 2024 Feb 27;13(3):218. Available from: <URL>.

17. Mora-Ochomogo M, Lohans CT. β-Lactam antibiotic targets and resistance mechanisms: from covalent inhibitors to substrates. RSC Med Chem [Internet]. 2021 Oct 20;12(10):1623–39. Available from: <URL>.

18. Bush K, Bradford PA. β-Lactams and β-Lactamase inhibitors: An overview. Cold Spring Harb Perspect Med [Internet]. 2016 Aug 1;6(8):a025247. Available from: <URL>.

19. Baquero F, Cantón R, Pérez-Cobas AE, Coque TM, Levin B, Rodríguez-Beltrán J. Antechodynamics and antechokinetics: Dynamics and kinetics of antibiotic resistance biomolecules. Biomolecules [Internet]. 2025 Jun 5;15(6):823. Available from: <URL>.

20. Karvouniaris M, Almyroudi MP, Abdul-Aziz MH, Blot S, Paramythiotou E, Tsigou E, et al. Novel antimicrobial agents for gram-negative pathogens. Antibiotics [Internet]. 2023 Apr 16;12(4):761. Available from: <URL>.

21. Gajic I, Tomic N, Lukovic B, Jovicevic M, Kekic D, Petrovic M, et al. A comprehensive overview of antibacterial agents for combating multidrug-resistant bacteria: The current landscape, development, future opportunities, and challenges. Antibiotics [Internet]. 2025 Feb 21;14(3):221. Available from: <URL>.

22. Cook MA, Wright GD. The past, present, and future of antibiotics. Sci Transl Med [Internet]. 2022 Aug 10;14(657). Available from: <URL>.

23. Bhattacharjee R, Negi A, Bhattacharya B, Dey T, Mitra P, Preetam S, et al. Nanotheranostics to target antibiotic-resistant bacteria: Strategies and applications. OpenNano [Internet]. 2023 May 1;11:100138. Available from: <URL>.

24. Hamad AA, Omer RA, Kaka KN, Abdulkareem EI, Rashid RF. Biological activities of metal complexes with schiff base. Rev Inorg Chem [Internet]. 2025 Sep 25;45(3):543–52. Available from: <URL>.

25. Al-Mosawy M. Review of the biological effects of schiff bases and their derivatives, including their synthesis. Med Sci J Adv Res [Internet]. 2023 Jul 31;4(2):67–85. Available from: <URL>.

26. Alsantali RI, Raja QA, Alzahrani AYA, Sadiq A, Naeem N, Mughal EU, et al. Miscellaneous azo dyes: A comprehensive review on recent advancements in biological and industrial applications. Dye Pigment [Internet]. 2022 Mar 1;199:110050. Available from: <URL>.

27. Banaszak-Leonard E, Fayeulle A, Franche A, Sagadevan S, Billamboz M. Antimicrobial azo molecules: A review. J Iran Chem Soc [Internet]. 2021 Nov 22;18(11):2829–51. Available from: <URL>.

28. Tuna Subasi N. Overview of schiff bases. In: Akitsu T, editor. Schiff Base in Organic, Inorganic and Physical Chemistry [Internet]. IntechOpen; 2023. p. 15–36. Available from: <URL>.

29. Jorge J, Del Pino Santos KF, Timóteo F, Piva Vasconcelos RR, Ignacio Ayala Cáceres O, Juliane Arantes Granja I, et al. Recent advances on the

antimicrobial activities of schiff bases and their metal complexes: An updated overview. Curr Med Chem [Internet]. 2024 May 24;31(17):2330–44. Available from: <URL>.

30. Razali NA, Jamain Z. Synthesis, chemical identification and biological application of Azo-based molecules containing different terminal group: A review. J Mol Struct [Internet]. 2023 Jul 15;1284:135329. Available from: <URL>.

31. Prasad Mishra D, Kumar Sahu P, Acharya B, Prasad Mishra S, Bhati S. A review of the synthesis and application of azo dyes and metal complexes for emerging antimicrobial therapies. Results Chem [Internet]. 2024 Aug 1;10:101712. Available from: <URL>.

32. Trivedi HD, Patel BY, Patel PK, Sagar SR. Synthesis, molecular modeling, ADMET and fastness studies of some quinoline encompassing pyrimidine azo dye derivatives as potent antimicrobial agents. Chem Data Collect [Internet]. 2022 Oct 1;41:100923. Available from: <URL>.

33. Mustapha B, Saleh AA, El-Seifat R, Bufarwa S, Hasan H, Moustafa D. Exploring the antituberculosis, anti-inflammatory, and antimicrobial activities and computational potential of quinoline-8-ol azo dye complexes. Appl Organomet Chem [Internet]. 2025 Aug 20;39(8):e70310. Available from: <URL>.

34. Al-Hiyari BA, Shakya AK, Naik RR, Bardaweel S. Microwave-assisted synthesis of schiff bases of isoniazid and evaluation of their anti-proliferative and antibacterial activities. Molbank [Internet]. 2021 Feb 4;2021(1):M1189. Available from: <URL>.

35. Benkhaya S, M'rabet S, El Harfi A. Classifications, properties, recent synthesis and applications of azo dyes. Heliyon [Internet]. 2020 Jan 1;6(1):e03271. Available from: <URL>.

36. Daina A, Michielin O, Zoete V. SwissADME: A free web tool to evaluate pharmacokinetics, drug-likeness and medicinal chemistry friendliness of small molecules. Sci Rep [Internet]. 2017 Mar 3;7(1):42717. Available from: <URL>.

37. Banerjee P, Kemmler E, Dunkel M, Preissner R. ProTox 3.0: A webserver for the prediction of toxicity of chemicals. Nucleic Acids Res [Internet]. 2024 Jul 5;52(W1):W513–20. Available from: <URL>.

38. Lim D, Strynadka NCJ. Structural basis for the β lactam resistance of PBP2a from methicillin-resistant *Staphylococcus aureus*. Nat Struct Biol [Internet]. 2002 Oct 21;9(11):870–6. Available from: <URL>.

39. Contreras-Martel C, Dahout-Gonzalez C, Martins ADS, Kotnik M, Dessen A. PBP active site flexibility as the key mechanism for β-Lactam resistance in pneumococci. J Mol Biol [Internet]. 2009 Apr 10;387(4):899–909. Available from: <URL>.

40. Chesnel L, Pernot L, Lemaire D, Champelovier D, Croizé J, Dideberg O, et al. The structural modifications induced by the M339F substitution in PBP2x from *Streptococcus pneumoniae* further decreases the susceptibility to β-Lactams of resistant strains. J Biol Chem [Internet]. 2003 Nov 7;278(45):44448–56. Available from: <URL>.

41. Ibuka AS, Ishii Y, Galleni M, Ishiguro M, Yamaguchi K, Frère JM, et al. Crystal structure of extended-spectrum β-Lactamase toho-1: Insights into the molecular mechanism for catalytic reaction and substrate specificity expansion. Biochemistry [Internet]. 2003 Sep 1;42(36):10634–43. Available from: <URL>.

42. Bitencourt-Ferreira G, Pintro VO, de Azevedo WF. Docking with AutoDock4. In: Methods in Molecular Biology [Internet]. Humana, New York, NY; 2019. p. 125–48. Available from: <URL>.

43. Hossain TJ. Methods for screening and evaluation of antimicrobial activity: A review of protocols, advantages, and limitations. Eur J Microbiol Immunol [Internet]. 2024 May 14;14(2):97–115. Available from: <URL>.

44. Maged AS, Ahamed LS. Synthesis and applications of new heterocyclic derivatives from 2-furyl methanethiol Synthesis of new heterocyclic derivatives from 2-furyl methanethiol and study their applications. Eurasian Chem Commun [Internet]. 2021;3:461–76. Available from: <URL>.

45. Silverstein RM, Bassler GC. Spectrometric identification of organic compounds. J Chem Educ [Internet]. 1962 Nov 1;39(11):546. Available from: <URL>.

46. Zapun A, Contreras-Martel C, Vernet T. Penicillin-binding proteins and β-lactam resistance. FEMS Microbiol Rev [Internet]. 2008 Mar 1;32(2):361–85. Available from: <URL>.

47. Agu PC, Afiukwa CA, Orji OU, Ezeh EM, Ofoke IH, Ogbu CO, et al. Molecular docking as a tool for the discovery of molecular targets of nutraceuticals in diseases management. Sci Rep [Internet]. 2023 Aug 17;13(1):13398. Available from: <URL>.

48. Latief BH, Al-Azzawi AM. Synthesis and antimicrobial activity screening of new cyclic imides comprising antipyrine and oxazole cycles. Biochem Cell Arch [Internet]. 2019 Oct 1;19(2):4419–24. Available from: <URL>.